ALMA MATER STUDIORUM
UNIVERSITÀ DI BOLOGNA

DOTTORATO DI RICERCA IN

FISICA

Ciclo 36

Settore Concorsuale: 02/A1 - FISICA SPERIMENTALE DELLE INTERAZIONI FONDAMENTALI

Settore Scientifico Disciplinare: FIS/01 - FISICA SPERIMENTALE

THE XENONNT NEUTRON VETO: DESIGN, CONSTRUCTION AND PERFORMANCE

Presentata da: Andrea Mancuso

Coordinatore Dottorato

Alessandro Gabrielli

Supervisore

Marco Selvi

Co-supervisore

Maurizio Spurio

Esame finale anno 2024

This page intentionally left blank.

ABSTRACT

The universe, as suggested by abundant and convincing evidence, is predominantly composed of Dark Energy and a non-luminous and non-relativistic matter called Dark Matter (DM). This dual influence has become a focal point of theoretical and experimental pursuits, standing at the forefront of modern astrophysics' greatest enigma. The quest to unveil the nature of DM, which manifests only through gravitational and possibly weak interactions, presents formidable challenges. Among the myriad of potential DM candidates, Weakly Interacting Massive Particles (WIMPs) stand out, emerging from the realms of theories beyond the Standard Model of particle physics. The most effective detectors focused on DM direct search have the common features of being constructed from ultra-pure materials and situated in underground locations to minimize cosmic ray interference. The XENON Dark Matter Project, located at the INFN Laboratori Nazionali del Gran Sasso (LNGS), exemplifies this approach. This cutting-edge multi-stage experiment employs a dual-phase xenon time projection chamber (TPC) designed to directly detect WIMPs. It aims to enhance the sensitivity to WIMP-nucleon elastic scattering by both increasing the target mass and reducing backgrounds. The current phase of the project, XENONnT, was installed in 2020 and has been actively collecting data so far. Building upon its predecessor, XENONnT features an enlarged TPC with a total sensitive liquid xenon (LXe) mass of 5.9 tons. A novel addition to this phase is the integration of a Gadolinium-loaded water Cherenkov neutron veto (NV), installed within the existing water Cherenkov Muon Veto from XENON1T. The NV has been the focus of my research, from its initial conception to its construction, commissioning, and data acquisition, and is the main topic of this PhD thesis. A critical challenge in DM detection is distinguishing WIMP-induced nuclear recoils (NRs) from the backgrounds, dominated by electronic recoil (ER) interactions. However, neutrons emitted by the detector materials can mimic WIMP signals by undergoing single scatters inside the TPC, thus posing a significant threat to the sensitivity to DM detection. The NV plays a crucial role in mitigating this background by tagging the escaping neutrons through their delayed neutron capture in water. Thus, in this work, we delve into the performance of the NV and its impact in the first WIMP search science runs. The NV surrounds the cryostat, it is optically separated from the Muon Veto with highly reflective panels and is instrumented with 120 photomultiplier tubes (PMTs), supported by a light stainless steel structure. These PMTs are instrumental in detecting the Cherenkov photons emitted following the neutron captures inside the NV volume. In the first two science runs of the experiment, the NV was operated with demineralized water, with neutrons being captured on hydrogen with consequent emission of a single 2.2 MeV gamma ray. In this setup, the NV achieved a neutron tagging efficiency of (53 ± 3)%, the highest ever recorded in a water Cherenkov detector, estimated through calibration with an Americium-Beryllium (AmBe) source. The NV excellent performances are largely attributed to its careful design inducing a very low background from the NV materials, the high single-photoelectron acceptance of the PMTs, and the outstanding optical properties of the detector itself, including water transparency and reflectivity of the surfaces. The NV contributed significantly to the WIMP analysis in the first XENONnT science run (SR0). A blind analysis over a total exposure of 1.1 tonne-year revealed no significant excess over the expected backgrounds, establishing the lowest upper limit to the WIMP-nucleon spin-independent cross section of 2.58×10^{-47} cm^2 for WIMPs of 28 GeV/c^2 mass at a 90% confidence level, improving upon the final XENON1T results.

Since October 2023, the NV performance has been further improved via Gd-doping of the water. With the current Gd concentration of 500 ppm, the neutron tagging efficiency is enhanced to (77 ± 3)%. This further suppresses the neutron background by a factor of 2 compared to previous science runs, and improves the XENONnT sensitivity to WIMP search in the future.

Keywords: Dark Matter, XENONnT, Neutron Veto, Gadolinium

This page intentionally left blank.

CONTENTS

List of Figures xi

List of Tables xxxi

Introduction 1

1 The quest for dark matter 4

1.1 Evidence of Dark Matter 5

1.1.1 Dark Matter Dynamics: Galaxies and Clusters 5

1.1.2 Cosmological evidence 8

1.2 Dark Matter Candidates: Particle Dark Matter 10

1.3 Detection of Dark Matter 11

1.3.1 Dark Matter in The Milky Way 15

1.3.2 Direct Detection 16

2 The XENONnT Experiment **20**

2.1 The XENON Dark Matter Project 20

2.2 Particle Detection in a Xenon Dual Phase Time Projection Chamber 23

2.2.1 Liquid Xenon 23

2.2.2 Dual Phase TPC 25

2.3 The Experiment 28

2.3.1 Status of the Experiment 33

2.4 Backgrounds 35

2.4.1 Electronic recoil background 36

2.4.2 Nuclear recoil background 36

2.5 Future Prospects in LXe-based DM Research 38

3 The Neutron Veto of XENONnT **40**

3.1 Detection principle 41

3.1.1 Impact of Gadolinium 43

3.1.2 Gd-Water Purification System (GdWPS) 46

3.2 Detector design 53
3.3 Installation 55
3.4 Light Calibration Tool 58
3.5 Data Acquisition and Reconstruction 61
3.5.1 Electronics & DAQ 61
3.5.2 Data Processing 64

4 Neutron Veto Characterization and Performances 67
4.1 The Neutron Veto PMTs 68
4.1.1 Fundamental characteristics of PMTs 70
4.1.2 SPE Models 72
4.1.3 PMT Performances 76
4.2 NV Optical Properties and Stability 79
4.2.1 Transparency and Reflectivity 81
4.2.2 The Neutron Veto background events 84

5 Calibration of NV efficiency 92
5.1 Thorium Calibration 93
5.2 AmBe Calibration 94
5.2.1 AmBe Source 94
5.2.2 AmBe Spectrum 97
5.3 Neutron Tagging Efficiency 100
5.4 Detection Efficiency 107
5.5 MC-Data Matching - Hitlet Simulator 109

6 XENONnT DM search and the impact of the Neutron Veto 119
6.1 Science Run 0 120
6.1.1 Search for New Physics in ER Data 121
6.1.2 First Dark Matter Search with NR data 124
6.1.3 Impact of the Neutron Veto 127
6.2 Science Run 1 131
6.3 Towards Science Run 2 132

7 Summary and Outlook 145

Bibliography 152

This page intentionally left blank.

List of Figures

1.1 Analysis of M33 Rotation Curve, highlighting the discrepancy between measured rotation velocities (comprising ionized gas and neutral hydrogen data) and those predicted by baryonic matter alone (stars and gas). To reconcile this difference, a DM contribution is essential. The figure combines the rotational influences of total gas, the stellar bulge, the stellar disc, and the DM halo, which are collectively integrated in quadrature to form the best-fit model (represented by the solid red line) to the observed data. Data from [6]. 6

1.2 Composite Image of the Bullet Cluster (1E0657-558), as seen by the Hubble and Magellan optical telescopes. It features a colorized overlay highlighting mass distributions: the red regions represent data from X-ray spectroscopy conducted by the Chandra Observatory [10], while the blue areas indicate mass distributions derived from gravitational lensing measurements. Picture from [9]. 7

1.3 Temperature Power Spectrum of the Cosmic Microwave Background. The blue line represents the optimal fit to the Planck 2018 data release [16]. 9

1.4 Schematic showing the couplings of a WIMP χ to ordinary matter p, with the corresponding detection technique. The annihilation of DM particles (downward arrow) would produce a pair of SM particles and this is exploited by the indirect detection technique. On the other hand, the collision of SM particles at colliders (upward arrow) could produce DM particles. Their missing or unbalanced energy is usually searched. Finally, the elastic scattering of DM off nuclei (rightward arrow) is exploited in the direct detection technique. 11

1.5 Rotation curve of the Milky Way with all the different components represented. Data from [60] plotted using the mw-plot and galpy python package [61, 62]. 15

1.6 Spectra of Nuclear Recoils generated by a WIMP with a mass of $m_\chi = 100$ GeV/c^2 interacting with different commonly used target materials, under the assumption of a spin-independent WIMP-nucleon cross-section ($\sigma_{SI} = 1 \times 10^{-47} cm^2$). The interaction rate for spin-independent processes shows a preference for heavier materials, scaling with A^2. However, for larger nuclei such as Xenon, the interaction rate diminishes at higher energies due to form factor suppression. Plot from [67]. 18

1.7 Exclusion limits on the SI DM-nucleon cross-section as a function of DM particle mass m_χ. One of the main features of this plot is the neutrino fog representation, as it is depicted as a function of the index n, present in the relation between the limit and the number of background events, as $\sigma \propto N^{-1/n}$. Here the neutrino fog is defined to be the region in which n>2. In this way, it is underlined that the CEνNS is not a strict limit which makes the WIMP direct detection search impossible, but rather a background source that makes it more challenging. Plot from [68]. 19

2.1 Overview of the XENON program detectors, showcasing the TPCs of varying dimensions and with the construction year noted. Displayed in blue are the active LXe masses within the TPCs. The orange indicator represents the low-energy ER background level, set at ≤ 20 keV. The rate for XENONnT, marked with an asterisk, represents the targeted performance and purity goals of the experiment. Figure re-adapted from [71]. 21

2.2 A view of the XENONnT experiment located in hall B at LNGS. Prominently featured in the background is the water tank, serving both as a passive shield and an active water Cherenkov MV. At the heart of the water tank, the TPC stands as depicted on the overlaying poster. In the foreground, the service building is visible, housing the various subsystems of the experiment including cryogenics, Xe purification, distillation, recovery, and the DAQ system. 22

2.3 Energy depositions in LXe lead to the formation of observable scintillation and ionization signals, as well as to non-observable energy loss to heat. Atom excitation and ion-electron recombination form the prompt scintillation signal, referred to as S1. The ionization electrons are drifted and extracted by the application of electric fields, forming a proportional scintillation signal, S2. The dashed grey line depicts the process of superelastic collisions between electrons and singlet states, forming triplet molecular states. Schematic re-adapted from [87]. 24

2.4 Schematic illustrating a particle interaction within the XENONnT TPC. When a particle collides with the LXe, it imparts energy to either a xenon nucleus or an electron. This interaction results in immediate scintillation light, captured by the PMT arrays positioned at both the top and bottom of the TPC, known as the S1 signal. Additionally, the collision produces quasi-free electrons. These electrons are guided upwards to the liquid surface by the E_{drift} electric field. Here, a more intense field, $E_{exctraction}$, propels them into the GXe layer above. The ensuing interactions with xenon atoms in this layer generate a secondary scintillation signal, called S2. The horizontal (x, y) position of the interaction is deduced from the pattern of S2 detected by the top PMT array (illustrated in the bottom right), while the vertical (z) coordinate is determined by measuring the time interval between the S1 and S2 signals 26

2.5 Determination of ER (top - blue) and NR (bottom - red) bands in the (cS1 area, cS2 area) parameter space during XENONnT SR0 [86]. The ^{220}Rn and ^{241}AmBe calibration data were used to identify the bands, whose median (solid line) and $\pm 2\sigma$ percentile are depicted for both types of interaction. The dotted grey lines in the plots show the respective ER and NR energies. 27

2.6 Schematic View of the XENONnT Experiment and its main subsystems. 28

2.7 CAD rendering of the XENONnT dual-phase TPC. The zoomed insets show details about the field cage, the electrode at the top and bottom of the TPC, and the PMT arrays. 29

2.8 CAD rendering showing the various components inside the XENONnT water tank, including the central cryostat, the NV, the MV, and the calibration systems. In blue is the I-belt, used for moving the tungsten collimator. In purple, the L-shaped beam for neutron calibrations, and in red and green, the two U-tubes that embrace the cryostat. 34

3.1 Kinetic energy distribution of the recoil electrons after the Compton scattering by gamma rays of different energies. For MeV energy photons, the electrons have ~MeV kinetic energies. Plot re-adapted from [102]. 42

3.2 Cross section of the interaction between neutrons and ^{1}H / ^{155}Gd / ^{157}Gd as a function of the neutron kinetic energy (MeV). The neutron-H interaction can occur as elastic scattering (orange line) or as (n, γ) (blue line). On the other hand the dominant process with the Gd isotopes is the (n, γ) (green and red lines). The cross-section for the Gd decreases with the energy but for values $\mathcal{O}$(10 eV) presents some resonant states. Data from IAEA ENDF Database [106]. 44

3.3 Fraction of neutron captures on Gd as a function of the Gd concentration. With a $\sim$ 0.1% in mass of Gd, the $\sim$ 90% of neutrons are captured by the Gd, while 10% are captured by protons as shown in Eq.(3.9). Plot re-adapted from [110]. 46

3.4 Picture of the EGADS facility, in the Kamioka mine. Key features of EGADS include a 200-ton water Cherenkov detector equipped with 20-inch PMTs (of the SK model), a pre-treatment system with a 15-ton tank for dissolving and mixing $Gd_2(SO_4)_3$ into the water, a main Gd-water circulation system, and the UDEAL (**U**nderground **D**evice **E**valuating **A**ttenuation **L**ength) device for automatic measurement of water transparency. A primary objective of EGADS is to assess the transparency of ultra-pure water versus water doped with gadolinium sulfate. The monitor is performed with the dedicated UDEAL device. For the XENONnT NV, water transparency (coupled with the reflectivity of the panels) is monitored internally within the detector itself using a dedicated reflectivity monitor (section 3.4) 48

3.5 Picture of the Gadolinium-water purification system, placed close to the 700 t XENON water tank. 49

3.6 Piping and Instrumentation Diagram (P&ID) of the GdWPS. All the relevant circulation elements (such as pumps and valves), filters, and sensors are reported. 51

3.7 (a) Technical drawing of the NV support structure, showcasing also design of the supports for the reflective panels. (b) Technical drawing of the ePTFE panel assembly constituting the reflective surface of the NV. 53

3.8 (a) Technical drawing of the ePTFE panels composing the NV floor. (b) Technical drawing of the ePTFE panels composing the NV ceiling. 54

3.9 CAD rendering of the NV installed in the center of the 700 t water tank: support structure (grey), reflector panels (white), 120 PMTs (yellow). The main components of the calibration system entering the NV are also shown: neutron generator pipe (purple), I-belt (blue), U-tubes (red and green). The reflector mounted to the cryostat has been deliberately removed in this CAD drawing. . . . 55

3.10 (a) Picture taken during the wrapping of the cryostat with the ePTFE foils. (b) Picture from inside the NV structure, during the installation of the NV lateral panels 56

3.11 View of the NV from below. The picture was taken before the installation of the NV floor panels. 57

3.12 Picture of the NV wall with the PMTs mounted, and the optical fibers coupled to each PMT through PTFE rods. Just as reference, the photocathode diameter is about 200 mm and the PMT is less than 300 mm long. 58

3.13 View of the PTFE rod and nozzle coupled with the optical fiber. The light from the OF is reflected by the nozzle and hit the photocathode. 59

3.14 Picture of one of the four diffuser balls installed in the NV. They are anchored to the cryostat stiffening ring. 60

3.15 Left: picture and CAD rendering of the support element for the Reflectivity Monitor, with the labels of the four channels: channels 1 and 3 look upward while channels 2 and 4 look downward. Right: position of the Reflectivity Monitor support on the lateral wall of the NV, compared to the PMTs positions 60

3.16 NV DAQ scheme. PMT signals are digitized by the V1730S modules with a sampling rate of 500 MSamples/s. Data is read from the digitizers by the reader server and written to a common (Ceph) storage disk available to the event-builder processing. The busy logic and the acquisition monitor functionalities are handled by V1495 and V1724 modules, respectively. Schematic and caption from [113]. 61

3.17 Waveform of a SPE signal recorded in PMT 2054. The black solid and dashed lines represent the baseline of the waveform as estimated by the digitizer and processing software respectively. The black-shaded region indicates the baseline RMS. The orange horizontal line shows the hit-finder threshold which is set to 20 ADC counts above baseline. All consecutive samples below this line are marked as a hit. The orange shaded region indicates the hit including the left and right extension which is referred as to “`hitlet`" in the straxen framework. 65

3.18 Interactive event display of a neutron-capture event recorded during the AmBe calibration. The top figure shows a two-dimensional projection of the NV with the outer wall of the TPC cryostat shown as a black circle. The blue circles indicate the location of the four diffuser balls. The position of the NV reflector walls is displayed as a black octagon. Each circle next to the octagon represents one of the NV PMTs. The size of the dot indicates the integrated charge detected by the PMT in the displayed event. The color code encodes the arrival time of the detected photon. The bottom panel shows the arrival time of the individual hitlets for the given event, where the color code indicates the charge of each hitlet. . . 66

4.1 (Left) Picture of a R5912 PMT. (Right) Schematic of the PMT and its socket structure. Both figures are taken from [117]. 69

4.2 Average quantum efficiency of the 120 PMTs. The maximum average value stands at ~ 39% for a wavelength of 350 nm. 69

4.3 Charge spectrum measured in one PMT during the LED calibration. The fit function with contributions of pedestal, single, and 2 photo-electrons is superimposed. The light blue full histogram corresponds to the signals surviving the digitizer’s threshold, applied offline. In the top panel are shown the normalized residuals. 74

4.4 Charge spectrum for one PMT during the LED calibration. The fit function with contributions of pedestal, single, and 2 photoelectrons is superimposed. The orange full histogram corresponds to the signals surviving the digitizer's threshold, applied offline. In the top panel are shown the normalized residuals. 75

4.5 Distribution of the Dark Rate of the 120 PMTs. The mean DR is $\langle R \rangle_{\mathrm{DR}} = (960 \pm 4)$ Hz. 77

4.6 Evolution of the dark rate of six PMTs during SR0. The temperature measured inside the demineralized water purification plant is shown with the blue-dashed line. 77

4.7 Evolution of the gain of six PMTs during SR0. Some of the points are the result of the weekly LED calibration performed during SR0; in the case of missing runs, the gain values have been inferred through the Savitzky-Golay filter. 78

4.8 Distribution of the SPE acceptance of the 120 NV PMTs. 79

4.9 Gain distribution for a SR0 and a SR1 LED calibration run. The mean gain for SR0 stands at $\mu_G^{SR0} = (7.2 \pm 0.7) \times 10^6$ while for SR1 stands at $\mu_G^{SR1} = (11.2 \pm 1.4) \times 10^6$. 80

4.10 Evolution of the gain of six PMTs during SR1. Some of the points are the result of the weekly LED calibration performed during SR1; in the case of missing runs the gain values have been inferred through the Savitzky-Golay filter. 80

4.11 Measurement of reflectivity of the ePTFE installed in the NV, as a function of the incident wavelength. 81

4.12 Reconstructed average position of the detected events in the four channels of the reflectivity monitor. 82

4.13 Arrival time spectra of all PMTs for an injected light signal using one channel (the 4^{th}) of the reflectivity monitor. The solid lines show the best-fit model. The bottom panel indicates the residuals of the fit. 82

4.14 Trend of the time decay parameter τ estimated from the fit of the time distribution in reflectivity monitor runs for the four different channels, in one year of data taking starting from the end of SR0. The linear fit performed on channel 4 data reveals a slightly decreasing trend of < 0.5 ns/y. However, this decrease does not significantly affect the light collection efficiency. 84

4.15 Trend of the time decay parameter τ estimated from the fit of the time distribution in reflectivity monitor runs for the four different channels, during SR1. 84

4.16 Evolution of the 4-, 6-, and 10-fold coincidence rate during the commissioning of the NV. The trend has been fitted with an exponential function on top of a flat one. The obtained time decay constant is in agreement with the decay of Rn present in water at the beginning of the water tank filling. 85

4.17 Evolution of the 4- and 10-fold coincidence rate during SR0. Each point corresponds to a run. The 4-fold trend is slightly decreasing due to the PMT dark rate evolution. This plot also enters the NV data-quality selection. 86

4.18 Evolution of the 4- and 10-fold coincidence rate during SR1. Each point corresponds to a run. The 4-fold trend is slightly decreasing due to the PMT dark rate evolution. This plot also enters the NV data-quality selection. In this case, few outliers have been found in the data-taking period, which will be excluded from the analysis. For this plot only science runs have been considered; the empty periods are indeed related to detector calibration runs. 86

4.19 Spectrum of background events in NV during SR0. The purple line represents all background signals with an area exceeding 3 PE and involving at least 3 PMTs. The orange curve further refines this selection to include only events within the central 95% contour of the center-time distribution in Fig. 4.20. 87

4.20 Distribution of center-time vs. event area for NV events during SR0: The top figure presents the background data of the NV, while the bottom figure displays data from the AmBe calibration. The bottom figure has undergone bin-wise background subtraction based on the top figure. The background data can be categorized into five distinct components, two of which are also observable in the AmBe calibration data. The various contributions are associated to: (1) AC of PMTs' dark counts; (2 & 4) Cherenkov signals; (3) Afterpulses + Dark Counts or β-decays close to the PMT; (5) Un-identified background component. Plot from [126]. . 88

4.21 Number of contributing PMTs Vs event area for SR0 NV background events, with the color scale representing the center-time parameter. Events with a smaller number of contributing PMTs typically belong to the third population of Fig. 4.20. 89

4.22 Reconstructed position of the events of the 5^{th} component outlined in Fig. 4.20. 90

4.23 Area distribution of the events of the 5^{th} component outlined in Fig. 4.20 before (purple) and after (yellow) the cut in the z-position shown in Fig. 4.22, which reveals a peak-like structure with an average area of around 120 PE. 91

5.1 Schematic of the U-tubes embracing the cryostat, as it results from the detector geometry implemented in the Geant4 simulation framework. 93
5.2 Hit map for one Thorium run with the source located at the Bottom U-tubes (position CW6d). Each square/bin represents one NV PMT. We have 20 columns, each having 6 PMTs (called levels here). The color map represents the number of hitlets in 10 minutes of run. 94
5.3 Event area distribution for one background run (orange) and one Thorium run before (green) after (purple) the background subtraction. 95
5.4 Schematic of the energy levels involved in the ^{9}Be$(\alpha, n)^{12}$C reaction. The maximum kinetic energy of the ^{241}Am alpha particles is indicated by an additional energy level 5.5 MeV above the ground state of ^{9}Be. Blue arrows represent transitions via internal conversion, while the red arrow indicates a transition via gamma emission. The energy levels and the transition properties of ^{12}C are sourced from [129]. 95
5.5 The neutron energy spectrum of Am-Be source. Plot re-adapted from [130]. 96
5.6 Background subtracted spectra for the center-time cut space (left) for the top CW5d9m position. The gray lines indicate the boundaries of the center-time cut. 97
5.7 Background subtracted spectra for the spatial cut for the top CW5d9m position. The red dashed lines show the cut boundaries for the spatial distribution. The center-time cut shown in figure 5.6 has been applied to obtain this plot. 98
5.8 Best fit of the NV AmBe energy spectrum taken at the bottom CW5d9m source position. The bottom panel shows the fit residuals. The individual fit components are also shown in different colors 98
5.9 Detected neutron rate (circles) and fraction of high-energy neutron capture events (triangles) as a function of the radial distance from the cryostat. 100

5.10 Schematic showing the measurements of the NV tagging efficiency with the AmBe calibration. We search for the time-coincidence between the 4.4 MeV gamma in the NV (yellow) and the S1 signal of the NR in the TPC (green), then we look for the 2.2 MeV gamma of neutron capture in the NV (light blue). 101

5.11 cS2 versus cS1 space showing all NR single-scatter events within the 90 % contour of the NR band. 102

5.12 Distribution of the time difference between NV events and the triggering single-scatter nuclear-recoil S1 signal in the TPC. The small gray vertical lines indicate the individual time differences. The purple line shows the best fit of the time distribution. The purple and orange areas indicate the ROI and background reference regions explained in the text. The black histogram shows a binned representation of the data whereas the gray-shaded part indicates bins excluded from the fit region. The bottom panel shows the residuals of the best fit with the binned data. 103

5.13 Event area distribution for the signal (in purple) and background (in orange) reference region of Fig. 5.12. The error bars indicate the statistical uncertainties in each bin. 104

5.14 Best fit of the hit time distribution in AmBe calibration runs, zoomed in the [0, 600] μs region. The gray part of the histogram indicates the data in the initial time region excluded from the fit represented by the purple line. The bottom panel shows the residuals of the fit. 105

5.15 Tagging efficiency of the NV in SR0. The red and blue data show the tagging efficiency for a 250 μs and 600 μs veto-window, respectively. In both cases, it was required that at least 5 PMTs contribute to an NV event. 106

5.16 Schematic showing the measurements of the NV detection efficiency with the AmBe calibration. We search for the 4.4 MeV gamma in the TPC (yellow), and then we look for the 2.2 MeV gamma of neutron capture in the NV (light blue). 108

5.17 Distribution in the corrected S1-S2 space of the full absorption of the AmBe γ-ray detected in the TPC. The black contours show the 1 to 5σ regions of the ellipse of the best fit. Only fully colored events inside 3σ were selected. 109

5.18 Distribution of the time difference between NV events and the 4.44 MeV gamma-ray S1 signals recorded in the TPC. The color code is the same as in Fig. 5.12. 109

5.19 Detection efficiency of the NV in SR0. The red and blue data show the detection efficiency for a 250 μs and 600 μs veto-window, respectively. In both cases, it was required that at least 5 PMTs contribute to an NV event 110

5.20 Schematic of the concept and working principle behind the Hitlet Simulator. Geant4 takes care of all the physics processes to be simulated (blue box). Epix (Electron and Photon Instructions generator for XENON) [137] uses XENONnT Geant4 MC data to produce inputs to the TPC waveform-simulator (Wfsim) and thus to start the "processing"-chain of the simulated data into the TPC. Once the photon hits the PMT photocathode, the HitSim is used (orange box). In the HitSim, we determine if the photon is converted into a photoelectron and detected using the QE and the SPE acceptance of each PMT. For each photoelectron generated, the charge is sampled from a pre-defined PDF. The hits, with their charge in PE and their timing, are then clustered into straxen hitlets and events. 111

5.21 Quantum efficiency curve of one PMT overlapped and convoluted to the energy spectrum of the Cherenkov photon hits from the Geant 4 output. The model of the water absorption length used in the simulation is also reported and is convoluted to the Cherenkov Spectrum and to the QE. The two dashed thin black lines refer to the wavelength of the Reflectivity Monitor and Diffuser Ball lasers used for the light calibrations. 112

5.22 Charge distribution used for the sampling in the HitSim for the two science runs. Both are a combination of the data with the 15 ADC count amplitude threshold applied (orange distribution) and of the SPE fit function (dashed thin black line). Up to the first intersection point (marked with the solid vertical line), the distribution follows the data, then it continues with the fit function. The final model is shown with the solid green line. 114

5.23 Position of the 4.4 MeV (left) and 2.2 MeV (right) peaks in the simulated AmBe charge spectrum varying the Collection Efficiency in the range [0.7, 0.8]. From the intersection of the linear fit (dashed thin blue line) and the position of the peaks (red/blue lines) we determined the best CE for the match. The best CE from the two plots do not differ significantly; however, we decided to rely on the one inferred from the 4.4 MeV match since the data are less affected by the low-charge noise and threshold effects. In the bottom panels, the reduced χ^2 of the fit of the simulated spectra are shown. 115

5.24 Position of the 4.4 MeV (left) and 2.2 MeV (right) peaks in the simulated AmBe charge spectrum varying the Collection Efficiency in the range [0.7, 0.8] for SR1. The procedure to determine the CE is the same as the one reported in figure 5.23. 115

5.25 (Left) Drawing of the U-tubes, the TPC and the NV PMTs with the position of the source indicated by the red dot. (Right) Event area distribution from simulated AmBe neutron captures events with the source located in the Bottom CW6d0m position and with the NV in the Water (blue) and Gd-Water [500ppm] (red) configurations. To highlight the impact of captures on Gd, the neutron emission without an associated 4.4 MeV γ are considered here. The number of generated primaries is the same for the two dataset. 116

5.26 (Left) Drawing of the U-tubes, the TPC and the NV PMTs with the position of the source indicated by the red dot. (Right) Event area distribution from simulated AmBe neutron captures events with the source located in the Top CW7d8m position and with the NV in the Water (blue) and Gd-Water [500ppm] (red) configurations. To highlight the impact of captures on Gd, the neutron emission without an associated 4.4 MeV γ are considered here. The number of generated primaries is the same for the two dataset. 117

5.27 Time distribution of the simulated neutron captures, identified by their flags in the MC-truth. The distribution is shown for several position and with a comparison with the pure-Water configuration; with the current Gd concentration we expect to halve the average capture time (estimated here with an exponential fit of the distribution). 117

5.28 Tagging efficiency computed from simulating radiogenic neutrons emitted from the cryostat, for different Gd concentrations as a function of the n-fold coincidence requirement . The NV selection cut used in the data analysis is applied. 118

6.1 NR and ER calibration data from ^{241}AmBe (orange), ^{220}Rn (blue) and ^{37}Ar (black). The median and the ±2 σ contours of the NR and ER model are shown in blue and red respectively. The gray dash-dotted contour lines show the reconstructed NR energy (keV$_{NR}$). Only the not-shaded events up to a cS1 of 100 PE are considered in the response model fits. Plot from [85]. 121

6.2 ER background fits for XENONnT [85] and XENON1T [139]. The XENONnT ER background is $\sim 5\times$ lower than that of XENON1T. No excess with respect to the background model is observed in the XENONnT data. 122

6.3 Distributions of coincident ER events between TPC and NV. The cuts applied on the selection for TPC events are the standard ones (BASICS) and the Fiducial Volume (FV) cut. The selection of NV events requires a 3-fold PMT coincidence and a 5 PE threshold. The time window for coincidence is ±300 ns. The left-bottom plot is the 2D distribution of coincident events between TPC-NV (with energy in the TPC up to 3 MeV). The left-middle plot is the energy distribution of CES before (blue) and after (yellow) the NV-coincidence cut. The left-top plot is the ratio of the yellow and blue histograms in the left-middle figure, showing the fraction of ER events tagged by the NV. In the right plot, the projection of the NV-tagged event area is shown. 123

6.4 Efficiency for detecting and selecting NR events in the WIMP search, plotted against NR recoil energy. The overall efficiency within the WIMP search region (black line) is primarily influenced by detection efficiency (green line) at lower energies and by event selection criteria (blue line) at higher energies, up to the boundary of the ROI. The normalized recoil spectra for WIMPs with masses of 10, 50, and 200 GeV/c^2 are depicted as orange dashed lines. Plot from [86]. 125

6.5 Data from the WIMP search displayed in the cS1-cS2 space, where each event is visualized as a pie chart. These charts represent the fraction of the best-fit model at the event location, including the expected number of 200 GeV/c^2 WIMPs (shown in orange). The size of each pie chart is scaled to match the signal model prediction at that specific position. Background probability density distributions are illustrated as 1σ (darker regions) and 2σ (lighter regions) contours, as identified in the legend for ERs in blue, ACs in purple, and surface events (green, labeled as "wall"). The neutron background, indicated in yellow in the pie charts, shares a distribution similar to the WIMP signal, which is represented by the orange-filled area marking the 2σ region. An orange dashed contour outlines a signal-like region, designed to encompass 50% of a 200 GeV/c^2 WIMP signal, optimized for the highest signal-to-noise ratio. Plot from [86]. 126

6.6 Upper limit on the spin-independent WIMP-nucleon cross-section at a 90% confidence level (represented by the full black line) as a function of the WIMP mass. This limit is constrained to remain at or above the median unconstrained upper limit through a power constraint. The dashed lines depict the upper limit without the power constraint applied. The 1σ (green) and 2σ (yellow) sensitivity bands are illustrated as shaded areas, with lighter shades indicating the range of potential downward fluctuations. The result from the XENON1T experiment [79] is also included for comparison, shown in blue, with the same power constraint applied. Plot from [86]. 127

6.7 Upper limits on SI WIMP-nucleon cross-section at 90% confidence level for this work (black lines), LZ [141] (purple lines), PandaX-4T [142] (red lines) and XENON1T [79] (blue lines). For PandaX and LZ, dashed lines represent their published result, for XENON results the dashed lines represent limits without a power constraint applied. Full lines for each experiment represent a limit that is power-constrained to always lie at or above the median un-constrained limit. 128

6.8 NV-tagged events within the WIMP ROI from SR0 data are depicted here. Round markers symbolize multi-scatter events identified by the NV, while diamonds represent the single-scatter event that was tagged. The color coding of these markers corresponds to the event ID, consistent with the color scheme used in subsequent figures, specifically Fig. 6.9 and Fig. 6.10. The gray-shaded area highlights the blinded region of SR0, where neutron and WIMP signals are predicted to appear. Gray dots represent all events located within the WIMP ROI, but outside the blinded region. Additionally, events tagged by the NV that fall outside the blinded region are marked with colored triangles. 129

6.9 Area of NV-tagged events plotted against the time delay between the S1 signal and the NV signal. Dashed lines represent the threshold and the duration of the tagging window implemented in SR0. Black contours and gray vertical lines delineate the 50%, 70%, 90%, and 95% quantiles for NV neutron-capture signals and background signals, respectively. These quantiles are derived from the purple and orange area distributions in Fig. 5.12, and the expected time distribution, which follows an exponential pattern for capture signals and a uniform distribution for background signals. The events are denoted using the same color coding and marker types as in Fig. 6.8. 130

6.10 Spatial correlation between TPC and NV events, with marker sizes representing the positions of the largest and second-largest S2 signals for each event. The color-shaded wedges depict the reconstructed azimuthal angle of the NV events, with the angular span of each wedge corresponding to the average 1 sigma contour of the AmBe calibration distributions. The red event is marked by two wedges, each corresponding to one of the NV events shown in Fig. 6.9. 131

6.11 Evolution of the data rate during the Gd-loading operations. This plot covers the entire timeline from the first loading of 1.5 kg in October 2023 up to the goal concentration achieved in December. Each step is represented by a different color. For the first loading only (red region), the Gd-Water injection occurred also directly in the NV. After observing a sudden increase in the rate, we decided to adopt in the following insertions a more gradual procedure by injecting the water only at the bottom of the water tank. Therefore, from the orange region onwards, the rate increase does not immediately follow the operation, but occurs a few days later, the time needed for the concentrated Gadolinium solution to also spread into the NV. Most of the spikes observed are associated with optical calibrations (using laser) to regularly monitor the optical properties during operations. These calibrations are linked to a constant rate of $\sim$ 30 MB/sec, defined by the trigger rate that characterizes data acquisition. Some of the smaller spikes, however, are associated with regular AmBe calibrations. These lead to a more modest increase in the data rate, due to an increase in the rate of physical events. 134

6.12 Zoom of the plot in Fig. 6.11, corresponding to the initial steps of Gd loading into the water tank. In this plot, each step is identified by a colored vertical dashed line. In addition to the moments when Gd salt was added to the system, the plot also marks the time when the water injection into the NV was turned off to control the rapid increase in rate following the very first loading on October 5^{th}. 135

6.13 CAD rendering of the water tank and NV with the sampling points where the Gd-water solution is extracted for further analyses. The 4 sampling points are reported with different colors, matching the scheme of figure 6.14. For the NV port there are two colors indicating that for those samples the measurements of the concentration are performed with two different methods (conductivity and ICP-MS). The flow of the Gd-Water is also reported. The GdWPS line is positioned on the top of the water tank since the solution flows in the GdWPS from that spot. 136

6.14 Evolution of the measured Gd concentration of the solution extracted from various sampling points arranged as shown in figure 6.13. The different steps of Gd-loading are represented by various background colors. The expected values based on the amount of added GdSO are marked with the black dashed horizontal lines. The concentration was primarily estimated using the conductivity measured at the 4 sampling points. Additionally, the Gd concentration of the sample collected from the NV (green dots) was also measured using ICP-MS (yellow dots). The values estimated with these different methods agree with each other. The continuous trend outlined by the pink line represents the concentration measured directly with the conductivity sensors in the GdWPS. In this case, the delay between the insertion and the achievement of the concentration plateau is associated with the diffusion of the doped water throughout the water tank, since the system collects the water from the top of the water tank. 137

6.15 Evolution of the average time parameter τ estimated from the fit of the time distribution of the daily reflectivity monitor runs taken during the Gd-loading operation. Each GdSO insertion step is marked by a different color. 138

6.16 Energy spectrum in the NV during AmBe calibration for different GdSO concentration - (a) Demineralized water (as the one already shown in figure 5.8) - (b) 32.5 kg of GdSO (corresponding to $\sim$ 50 ppm). (c) 152.5 kg of GdSO (corresponding to $\sim$ 200 ppm) - (d) 352.5 kg of GdSO (corresponding to $\sim$ 500 ppm). The bottom panels of all the plots show the fit residuals. The individual fit components are also shown in different colors. For all the plots with Gd an additional Gaussian component (shown in red solid line) has been added to take into account the contribution of neutron captures on Gd. 139

6.17 (Top Panel) Time evolution of the mean values of the Gaussian corresponding to H captures and ^{12}C de-excitation, normalized to their initial value. (Bottom panel) Time evolution of the rate of n capture for H (blue), Gd (brown) and the ^{12}C de-excitation (light-blue). The open diamonds represent the values obtained without considering the threshold, while the solid points show the results above the 5 PE threshold. Also, the total number of captures (the sum of the H and the Gd captures) is shown for reference. 141

6.18 Distribution of the time difference between the triggering nuclear-recoil S1 signal in the TPC and the neutron capture event in the NV: in demi-water (blue) and with 500 ppm of GdSO (red). . . . 142
6.19 Event area distribution of AmBe calibration after the 4.4 MeV γ subtraction (this contribution has been estimated with the usual fit described in 5.2.2), for demineralized water (blue) and 500 ppm GdSO-water solution (red). 143
6.20 Tagging Efficiency measured with an AmBe calibration with the source positioned close to the cryostat (Top CW7d8m). The tagging efficiency is displayed here for the time window of [0,250]μs which is the one used in Science Runs analysis (section 5.3). With the current configuration (500 ppm GdSO concentration, in red) we observe an improvement of $+\sim 24\%$ (absolute value) in the tagging efficiency with respect to SR0 with demi-water (blue). . . 143

This page intentionally left blank.

List of Tables

2.1 Natural xenon composition. Only two of the natural isotopes are unstable but with half-life greater than the age of the Universe. For the stable isotopes, $^{128..131}$Xe, the overall abundance is reported. 23

2.2 Estimated ER background event rates in a 4 t fiducial volume. The energy ROI in which the event rates are integrated is (1, 13) keV [91]. The assumption for the ^{222}Rn activity concentration is of 1 μBq/kg and 0.1 ppt (mol/mol) for ^{nat}Kr/Xe. The background contributions from Xe isotopes are determined assuming the natural abundances of ^{136}Xe and ^{124}Xe. 37

2.3 Estimated NR background event rates in a 4 t fiducial volume. The energy ROI in which the event rates are integrated is (4, 50) keV. Table from [91]. 38

3.1 Thermal neutron capture cross sections of the various Gd isotopes, with their natural abundance. The two isotopes which are exploited for their high (n, γ) cross section are the ^{155}Gd and ^{157}Gd. Table from [105]. 44

4.1 Overview of experimental phases in XENONnT. It details the start and end dates of each phase, noting that the commissioning phase lacks precise dates due to the asynchronous commissioning of detectors (e.g., the TPC commissioning occurred while the NV was in its final step of installation - DAQ cabling etc.). The table also highlights the main research activities and operations conducted during each phase. 68

4.2 Comparison between the values of the PMT radioactivity reported by Hamamatsu [117] and measured with the Ge detector available at LNGS. In particular, the glass of two broken PMTs (featuring different glass materials) was isolated from the PMT body for the measurement. The values, expressed in [Bq/PMT], for the ^{40}K and the U/Th-series are shown. The employment of a low radioactivity glass in the NV PMTs mitigates the radioactive background. The uncertainties of the measured value, of less than 10%, are not reported in the table. 70

6.1 Sequence of GdSO insertion steps. 136

This page intentionally left blank.

INTRODUCTION

Over the past century, a growing number of astrophysical and cosmological observations has increasingly supported the existence of Dark Matter (DM) in the cosmos. According to the ΛCDM model, the standard cosmological framework, DM is believed to make up over 85% of the universe's matter. Among various hypotheses posited to explain DM, the Weakly Interacting Massive Particles (WIMPs) has emerged as one of the most promising candidates. The search for WIMPs encompasses a wide array of experimental approaches, including collider experiments like those at the LHC, indirect detection through astrophysical observations, and direct search experiments. The first chapter of this thesis provides a comprehensive overview of the DM puzzle, the exact nature of which remains unknown, and the ongoing experimental efforts to detect WIMPs. In the quest to directly detect DM, the focus is on measuring the energy released from the nuclear recoil of target nuclei following interactions with WIMPs. Given the expected low event rate (less than a few events per ton per year), this pursuit hinges on massive, ultra-pure detectors situated in environments with minimal radioactivity and shielded from cosmic rays, typically underground. Chapter 2 delves into the XENON project which, with its series of increasingly sophisticated dual-phase liquid-gas xenon Time Projection Chambers (TPC), stands as the frontrunner in the direct detection of DM, mainly targeting WIMPs. Situated deep underground at the INFN Laboratori Nazionali del Gran Sasso in Italy, these detectors have evolved through various stages, each marked by a significant increase in active mass and a background reduction. The latest phase, XENONnT, commissioned in 2020, is an upgrade of XENON1T and has already completed its first science runs (SR0-1). Xenon choice as the target medium is due to its excellent scintillation and ionization properties, making it ideal for detecting rare particle interactions. The scintillation light is revealed by Photomultiplier Tubes (PMTs) positioned at the TPC top and bottom edges. An internal electric field drifts ionization electrons toward the gas region above, where they generate a secondary signal through proportional scintillation. The power of this technology lies in its ability to use both ionization and scintillation signals to differentiate WIMP interactions from background events, achieving significant background reduction. A critical aspect of WIMP searches in a liquid Xe (LXe) TPC is distinguishing between electronic (ER) and nuclear (NR) recoil backgrounds. In previous experiments like XENON1T, ER backgrounds, primarily from intrinsic beta decays of ^{214}Pb were the main concern. However, Monte Carlo simulations indicated that with the reduction of its parent nuclide ^{222}Rn in XENONnT, neutron-induced NR backgrounds become increasingly significant. These NR backgrounds, resulting from neutrons elastically scattering off nuclei, mimic the signals expected from WIMP interactions, necessitating further effective mitigation strategies. To address this challenge, XENONnT introduced a novel system, the Neutron Veto (NV), a Gadolinium-loaded water Cherenkov detector designed to tag neutrons inducing background events in the TPC. This system is crucial for reducing NR backgrounds, particularly those induced by radiogenic or cosmogenic neutrons. The NV, comprising 120 PMTs and high-reflectivity ePTFE panels, is strategically positioned within a 700-tonne water tank that also houses the TPC. This setup not only serves as a passive shield against environmental radiation but also actively detects neutrons emitted from the radioactivity of detector materials. These neutrons, after being moderated by the water, are captured and emit gamma rays, which are then detected through the Cherenkov photons produced by Compton (scattered) electrons. Initially, the NV was operated with demineralized water, enabling neutron tagging through hydrogen capture, a technique previously employed in experiments like Super-Kamiokande and SNO. To enhance the NV performance the water is doped with Gd, precisely with $Gd_2(SO_4)_3$. This addition improves neutron tagging efficiency by increasing the energy released upon neutron capture; additionally, the Gd-loading reduces the neutron capture time and, in turn, the induced dead time in the TPC.

Chapter 3 provides an in-depth description of the NV, covering its detection principles, design, installation, and operational aspects. The key role of the Gd in enhancing neutron detection efficiency is also highlighted. To achieve an optimal concentration that maximizes the NV detection efficiency without compromising its optical properties, and to prevent the loss of valuable and costly Gd salt during water purification, a dedicated Gd Water Purification System (GdWPS) was installed. This system demonstrated excellent performance throughout its commissioning phase.

Chapter 4 delves into the key ingredients that contribute to the high neutron detection efficiency observed in the NV. These include the optical properties of the detector, such as surface reflectivity and water transparency, and the performance of the PMTs. The PMTs used in the NV are Hamamatsu R5912, chosen for their high quantum efficiency, low radioactivity, low dark rate, high gain, and excellent single photoelectron (SPE) acceptance. A significant portion of my research work has been focused on characterizing these PMTs, and monitoring their performance as well as the optical properties of the detector. The excellent 'low-level' performances (related to the PMTs, reflectivity, and water transparency) observed during the data acquisition phase of the experiment, have led to outstanding 'high-level' detector performances. These are characterized by the tagging and detection efficiency, related to the fraction of emitted neutrons detected by the NV.

Both efficiencies were evaluated during scientific runs through calibrations with neutron sources, particularly Americium-Beryllium (AmBe): the corresponding analyses are described in Chapter 5. Additionally, it is described the Hitlet Simulator, an effective tool for simulating signals observed with the NV detector. This simulator enables the accurate estimation of the NV tagging efficiency under different detector conditions, including the efficiency in the presence of Gd. This is of particular interest as, in the ongoing Science Run 2 (SR2), the NV is operating with a Gd-sulphate concentration of 500 ppm.

In Chapter 6, the focus shifts to the scientific runs of the XENONnT experiment. This chapter highlights the substantial impact of the NV on these searches, particularly in the first science run (SR0), in reducing neutron background and enhancing the experiment sensitivity. The blinded analysis conducted over (1.09±0.03) t·y exposure showed no significant excess of WIMP signals. This result led to an improvement in the upper limit on the spin-independent WIMP-nucleon cross section previously set by XENON1T, with a minimum at 2.58×10^{-47} cm^2 for WIMPs of mass of 28 GeV/c^2 at 90% confidence level. The performances of the NV in SR1, with increased single-photoelectron acceptance of the PMTs and the consequent increase in neutron tagging efficiency, are briefly presented. The chapter ends with a description of the most recent phase of the experiment, where 350 kg of Gd-salt was added to the system at the end of 2023, reaching a 500 ppm concentration. The preliminary behaviour of the system in terms of concentration, data rate, and optical performances is described, together with a first look at the NV spectrum of detected neutron captures on Gd, performed with the same AmBe neutron source. This new phase of the Gd-doped NV will allow for a further reduction of the neutron background, and thus increasing the sensitivity to WIMPs in the next XENONnT science runs.

1

THE QUEST FOR DARK MATTER

In the grand narrative of the cosmos, dark matter (DM) plays the role of an enigmatic protagonist, whose presence, though inferred, remains shrouded in mystery. Though ordinary baryonic matter constitutes less than 20% of the universe total mass, the predominant portion remains an enigma, unknown and unseen. This chapter embarks on a journey into the quest for DM, a pursuit that intertwines the realms of astrophysics, cosmology, and particle physics. The story begins with the astrophysical anomalies that first hinted at DM existence, such as the rotational speeds of galaxies observed by Vera Rubin and others, which defied expectations based on visible matter alone. Similarly, gravitational lensing effects and the dynamics of galaxy clusters, exemplified by observations of the Bullet Cluster, provided compelling evidence for an unseen mass exerting its influence on cosmic structures. Transitioning from an astrophysical puzzle to a fundamental component of the universe architecture, DM is revealed to play a key role in the Cosmic Microwave Background (CMB) radiation, the large-scale structure of the universe, and in the formation and evolution of galaxies. The Lambda Cold Dark Matter (ΛCDM) model, which aligns closely with cosmological observations, positions DM as a crucial ingredient in the universe composition. Yet, as the pursuit of DM true nature intensifies, the field of potential candidates broadens. The standard model of particle physics, while a triumph in its domain, fails to account for DM characteristics. This inadequacy has spurred a diverse array of hypotheses, with theoretical physicists proposing numerous exotic particles as potential DM constituents. Among these, Weakly Interacting Massive Particles (WIMPs) have garnered significant attention. These hypothetical particles emerge naturally in several models extending beyond the standard model. Their search not only represents a significant experimental challenge but also a gateway to new physics. In the first chapter, we walk through the history, the compelling evidence, the theoretical candidates, and the cutting-edge detection methods of DM.

1.1 Evidence of Dark Matter

Dark matter, an enigmatic constituent of the universe, remains one of the most intriguing and elusive subjects in astroparticle physics. Despite being invisible and undetectable through direct electromagnetic observations, its existence is deeply rooted in observations that date back to the early 20th century. The underpinning of DM existence lies in the discrepancies observed between the gravitational effects in the universe and the predictions made by the standard model of particle physics and cosmology. It was Fritz Zwicky's 1933 study of the Coma Galaxy Cluster [1] that provided a groundbreaking empirical basis for the existence of DM. His observations and analysis revealed a discrepancy between the mass of the visible components of the cluster and the gravitational effects they exhibited. By applying the virial theorem, Zwicky estimated the total mass of the cluster and discovered that the visible matter accounted for only a fraction of the total mass needed to cause the observed gravitational effects. This led to his hypothesis of the existence of unseen matter, which he termed "dunkle Materie" or dark matter. These inconsistencies manifest in various scales and contexts, demanding an explanation beyond the realm of ordinary baryonic matter. The following subsections delve into the evidences at a galactic level, exploring the rotational curves of galaxies, gravitational lensing effects, and the dynamics of galaxy clusters. Furthermore, at a cosmological scale, we discuss the cosmic microwave background radiation, large-scale structure formation, and the role of DM in the evolution of the universe.

1.1.1 Dark Matter Dynamics: Galaxies and Clusters

The enigma of DM, a key component in our understanding of the universe, has been substantially informed by observations at galactic and extra-galactic scales. Zwicky's approach on the study of the galaxies of the Coma Cluster was based on the virial theorem [2]. The theorem connects, for a gravitationally bound system like the cluster, its total kinetic energy K and gravitational potential energy U.For a system in equilibrium, the theorem simplifies to $U = -2K$. In a cluster modeled as a sphere, the gravitational potential energy U is expressed as $\frac{GM^2}{R}$, with M representing the cluster total mass and R its radius. Thus, the mass of the cluster can be calculated using the formula:

$$M = \frac{3R\langle v_{\parallel}^2 \rangle}{G} \tag{1.1}$$

In this equation, $\langle v_{\parallel}^2 \rangle$ denotes the velocity dispersion of galaxies along the line of sight. Zwicky's initial measurements in the Coma Cluster indicated a velocity dispersion significantly higher than expected based on visible matter alone, pointing towards the existence of a much larger, unseen mass. Despite its implications, Zwicky's hypothesis did not gain immediate acceptance in the scientific community. It was not until the late 1970s, with the work of V. C. Rubin and others on the rotation curves of spiral galaxies, that the existence of DM began to be widely recognized. In the 1970s, Vera Rubin and Kent Ford's detailed study of the Andromeda Galaxy (M31) [3] and the Triangulum Galaxy (M33) studied by Kenneth Freeman [4] further solidified the DM hypothesis. They observed that the galaxy rotation velocity $v(r)$ remained unexpectedly constant even at large radii r, where luminous matter diminishes [5]. Kepler's laws suggest that the velocity $v(r)$ of stars orbiting at a distance r from the galactic center should depend on the mass $M(r)$, scaling like $v(r) \propto \sqrt{M(r)/r}$. This implies that the orbital velocity should decrease as $v(r) \propto r^{-1/2}$, due to the diminishing density of stars and gas. However, observations of galaxies like M31 and M33 reveal a different reality, showing an approximately constant rotational velocity in the outermost regions, indicative of an additional non-luminous mass component. Figure 1.1 shows the rotational velocity profile of M33.

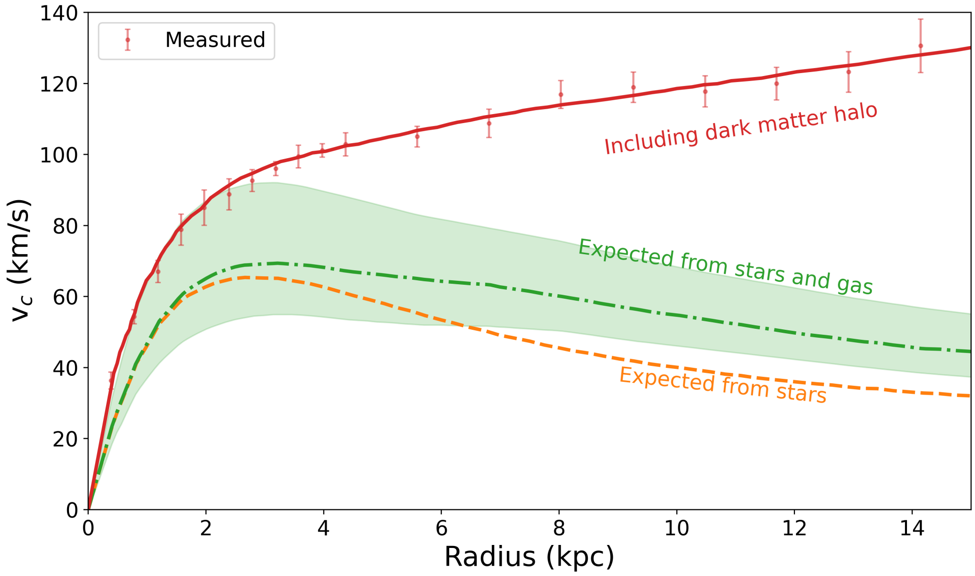

Figure 1.1: *Analysis of M33 Rotation Curve, highlighting the discrepancy between measured rotation velocities (comprising ionized gas and neutral hydrogen data) and those predicted by baryonic matter alone (stars and gas). To reconcile this difference, a DM contribution is essential. The figure combines the rotational influences of total gas, the stellar bulge, the stellar disc, and the DM halo, which are collectively integrated in quadrature to form the best-fit model (represented by the solid red line) to the observed data. Data from [6].*

To reconcile these observations with the existing understanding of galactic dynamics, the hypothesis of a DM halo was introduced. This halo, consisting of invisible matter, extends well beyond the distribution of visible matter in the galaxy. The proposed density profile for such a dark halo to align these observations with the DM hypothesis is the Navarro–Frenk–White (NFW) mass profile [7]:

$$\rho(r) = \frac{\rho_0 R_s^3}{r(r + R_s)^2} \tag{1.2}$$

where $\rho(r)$ is the halo density as a function of radius r, ρ_0 is the characteristic density, and R_s is the scale radius. The study of galactic rotation curves has significantly deepened our understanding of DM within individual galaxies [8]. However, the pursuit of DM mysteries extends beyond the galactic boundaries, finding implications in extra-galactic phenomena. A notable instance of this is the study of gravitational lensing, especially in the context of the Bullet Cluster (1E0657-558), which provides compelling extra-galactic evidence for DM [9].

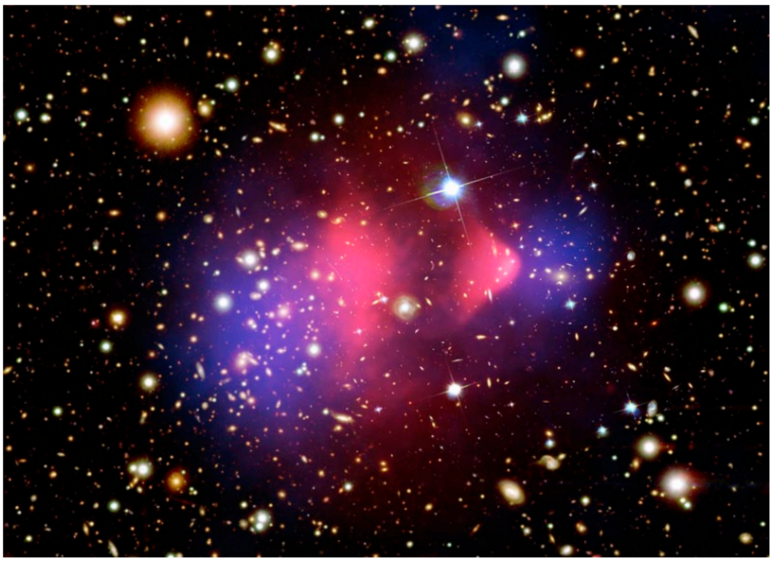

Figure 1.2: *Composite Image of the Bullet Cluster (1E0657-558), as seen by the Hubble and Magellan optical telescopes. It features a colorized overlay highlighting mass distributions: the red regions represent data from X-ray spectroscopy conducted by the Chandra Observatory [10], while the blue areas indicate mass distributions derived from gravitational lensing measurements. Picture from [9].*

The Bullet Cluster, consisting of two colliding galaxy clusters, offers a unique opportunity to observe the interplay between baryonic and DM. The majority of the baryonic mass within these clusters exists as sparse intergalactic gas, heated during the collision and emitting intensely in the X-ray spectrum. This emission has been vividly captured by the Chandra X-ray Observatory [10] for the Bullet Cluster (1E0657-558) [11], delineating the distribution of the hot, shocked gas in detail (the pink region in figure 1.2). In contrast to the bright X-ray emitting gas, the galaxies within the Bullet Cluster continued their paths relatively undisturbed, following nearly unaltered ballistic trajectories through the collision. The total mass of the Bullet Cluster is inferred through weak gravitational lensing techniques. The *gravitational lensing* [12] mentioned here is a phenomenon predicted by Einstein's theory of General Relativity for which both clusters possess enough mass to significantly distort the space-time, acting as gravitational lenses [13]. The mass distribution, inferred from imaging distant objects lensed by the clusters, reveals the presence of a substantial mass (depicted in blue in figure 1.2) where no luminous matter is observed.

1.1.2 Cosmological evidence

On the cosmological scale, the Cosmic Microwave Background [14] provides profound insights into the existence and role of DM in the universe. The CMB, a relic radiation from the early universe, exhibits a nearly perfect black-body spectrum with a temperature $T_0 = (2.7255 \pm 0.0006)\mathrm{K}$ [15] with small anisotropies $\mathcal{O}(10^{-5})$, which are key to understanding the composition and evolution of the cosmos. High-precision observations, such as those by the Planck collaboration [16], have meticulously mapped these anisotropies, which are caused by density perturbations in the early universe. These fluctuations, influenced by the interplay between baryonic matter, DM, and radiation, are crucial for understanding the universe matter and energy budget.

The ΛCDM (Lambda Cold Dark Matter) model, supported by CMB observations, describes a universe that is flat, homogeneous, isotropic, undergoing accelerated expansion due to the presence of dark energy (Λ) and permeated with cold DM (CDM). This model aligns with the observed large-scale structure and galaxy formation processes, effectively explaining the temperature anisotropies in the CMB, and predicts a total energy density Ω_{total} given by the following contributions:

$$\Omega_{\mathrm{total}} = \Omega_{\Lambda} + \Omega_{\mathrm{DM}} + \Omega_{\mathrm{baryon}} \approx 1 \tag{1.3}$$

where Ω_{baryon}, Ω_{DM}, Ω_{Λ} represent the energy density of baryonic matter, DM and "Dark Energy" respectively. The decomposition of the CMB temperature fluctuations into spherical harmonics is a powerful technique used to further understand the anisotropies. The temperature fluctuations can be expressed as a function of the multipole moment ℓ, where increasing values of ℓ correspond to smaller angular scales. The power spectrum of this multipole expansion provides a critical tool for testing the ΛCDM model, as the exact locations of the peaks in the power spectrum depend on the intricate interaction of radiation, matter, and DM. Recent results from the Planck collaboration [16], as shown in Fig. 1.3, present the multipole expansion of the CMB temperature anisotropy measurements, with an excellent fit for the ΛCDM model.

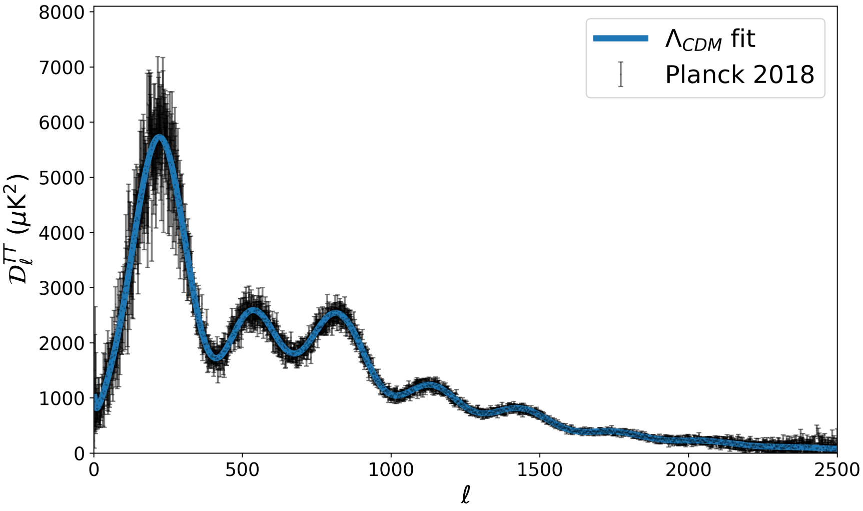

Figure 1.3: *Temperature Power Spectrum of the Cosmic Microwave Background. The blue line represents the optimal fit to the Planck 2018 data release [16].*

The model fit yields the following contributions to the energy density of the present-day universe:

$$\begin{aligned} \Omega_{\Lambda,0} &= 0.691 \pm 0.006, \\ \Omega_{M,0} &= 0.309 \pm 0.006, \\ \Omega_{R,0} &\approx 10^{-4}, \\ \Omega_{b,0} &= 0.049 \pm 0.003, \\ \Omega_{c,0} &= 0.259 \pm 0.002 \end{aligned}$$

These parameters reveal that DM constitutes approximately 84% of the mass content of the universe ($\Omega_{c,0}$ to $\Omega_{M,0}$), emphasizing its dominant role in the cosmos.

Big Bang nucleosynthesis (BBN) [17] and N-body simulations of structure formation [18] lend further support to the DM hypothesis. BBN, responsible for the formation of light nuclei, aligns with the baryon density inferred from CMB observations. Similarly, N-body simulations, which often use CMB-derived density fluctuations as initial conditions, show remarkable agreement with observed galaxy distributions. The simulations highlight DM crucial role in cosmic structure formation, serving as seeds for the aggregation of baryons into the large-scale structures we observe today; all these hints are considered the most convincing evidence supporting the model and undermining alternative theories such as modified gravity models [19].

1.2 Dark Matter Candidates: Particle Dark Matter

The quest to identify the constituents of DM has led to a diverse range of hypotheses. However, according to the paradigm of the ΛCDM model, the potential candidates for the non-baryonic DM must adhere to several key properties inferred from astronomical and cosmological observations. DM particles should be electrically neutral, either long-lived or stable, as evident from DM presence across all time scales of the universe. Observations of cluster collisions and structure formation suggest that DM has a small self-interaction cross-section. These candidates must not violate the observed baryon density from BBN and the CMB, implying a non-baryonic nature.

The broad landscape of DM candidates consists of particles and astrophysical objects whose masses range nearly over 50 orders of magnitude, from 10^{-21} eV (fuzzy DM [20]) up to 10^{27} eV (primordial black holes [21]). In this context, the Weakly Interacting Massive Particles (WIMPs) emerge as one of the most prominent candidates. These hypothetical particles arise naturally from theories BSM of particle physics, as supersymmetry (SUSY). WIMPs are especially appealing because they are theorized to be non-relativistic (*'cold'*), non-baryonic, neutral, stable or extremely long-lived, and massive, aligning with the gravitational effects we observe on cosmic scales. They are predicted to weakly interact with baryonic matter and themselves, explaining the mass distributions observed in galaxy cluster collisions. The WIMP hypothesis is underpinned by the concept of *'freeze-out'*, a mechanism that could produce the correct relic abundance of DM. In the early and hot stage of the Universe (radiation era) the production of WIMPs happened through the collision between SM particles, with the latter being produced through WIMP annihilation, leading to a thermal equilibrium regime. The interaction rate is given by:

$$\Gamma_A = n_\chi^{eq} \langle \sigma_A v \rangle \tag{1.4}$$

where n_χ^{eq} is the WIMP density at the time of the equilibrium, σ_A is the annihilation cross-section, and v is the WIMP velocity. As the Universe expanded and cooled, this equilibrium was broken, leading to a decrease in WIMP density through self-annihilation. When the self-annihilation rate dropped below the expansion rate of the Universe, the WIMP density 'froze out' leaving a relic abundance that we can still observe today [22]. The so-called *'WIMP miracle'* refers to the coincidence that a thermally averaged self-annihilation cross-section of approximately $\langle \sigma v \rangle \approx 3 \times 10^{-26}$ cm^3/s and a WIMP mass around 100 GeV/c^2 would yield the correct DM abundance [23]. The predicted WIMPs masses range is between 1 to 10^5 GeV, with interaction cross sections between 10^{-41} cm^2 and

10^{-51} cm^2. Besides WIMPs, axions and axion-like particles (ALPs) are another important class of DM candidates. These hypothetical particles are theorized to be much lighter than WIMPs and could solve the strong CP problem in quantum chromodynamics [24]. Axions, if they exist, would also be non-baryonic and non-relativistic, potentially contributing to the DM content of the Universe [25]. While the WIMP and axion hypotheses are compelling, alternative theories exist. One notable alternative is Modified Newtonian Dynamics (MOND) [26, 27], which proposes modifications to Newton's laws at very low accelerations. Although MOND can explain some galactic-scale observations, it struggles to account for all the experimental evidence, particularly on larger scales, such as the Bullet Cluster and CMB anisotropies. Several experimental efforts are employed to cover the broad spectrum of DM candidates, ranging from telescopes and particle detectors to collider experiments and direct DM detection experiments.

1.3 Detection of Dark Matter

The detection of DM is pursued through three main experimental approaches (Fig.1.4), each one aiming to offer unique insights into the elusive nature of DM.

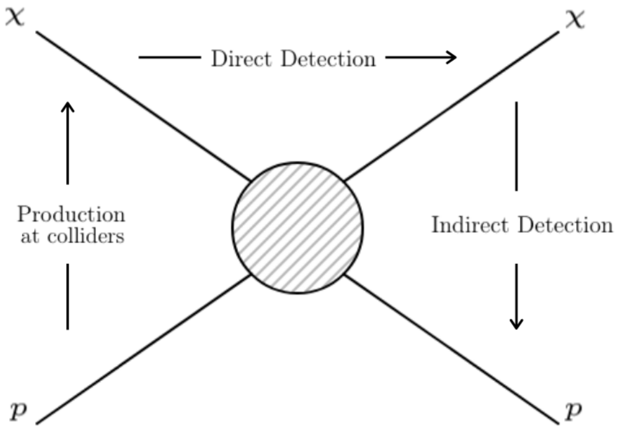

Figure 1.4: *Schematic showing the couplings of a WIMP χ to ordinary matter p, with the corresponding detection technique. The annihilation of DM particles (downward arrow) would produce a pair of SM particles and this is exploited by the indirect detection technique. On the other hand, the collision of SM particles at colliders (upward arrow) could produce DM particles. Their missing or unbalanced energy is usually searched. Finally, the elastic scattering of DM off nuclei (rightward arrow) is exploited in the direct detection technique.*

Indirect Detection: This method seeks for signatures of self-annihilating DM which may either be produced directly or via loop diagrams. The DM annihilation can take place in specific regions where the density of DM is higher than the froze-out relic density, i.e. close to the galactic center, near (primordial) black holes etc. The resulting SM particles could reach one of the various telescopes and observatories, offering indirect evidence of DM. Searches for anomalies in charged cosmic rays are made with balloon-type detectors (HEAT [28]), ground-based telescopes (Pierre Auger Observatory [29], Tescope Array [30]) and experiments on satellites (PAMELA [31], AMS [32],Fermi-LAT [33]). For instance, Fermi-LAT detected an excess of gamma rays around $\mathcal{O}(10\text{ GeV})$ [34]; considered at first to be a potential signature of DM self-annihilation, it has been finally interpreted as an excess in the form of un-modeled backgrounds or point-like sources (es millisecond pulsars) [35]. In various DM models, neutrinos are often produced in particle cascades resulting from DM annihilation or decay. As DM particles accumulate within galactic centers, their annihilation products that move slower than the escape velocity are trapped, while neutrinos can escape and be detected. This phenomenon provides a distinct signature for DM searches [36]. Water Cherenkov neutrino telescopes, such as ANTARES [37], IceCube [38], and Super-Kamiokande [39], have made significant experimental advancements, enabling them to set the most stringent constraints on the WIMP-nucleon spin-dependent cross-section, based on the upper limits of neutrino fluxes emanating from DM annihilation. Future improvements in DM detection are anticipated from upcoming neutrino telescopes like Hyper-Kamiokande [40], and KM3Net [41].

Gamma-ray emission is also a product of DM annihilation, characterized either by a continuous spectrum resulting from the decay, hadronization, and final state radiation of SM particles produced during annihilation, or by distinct spectral features such as mono-energetic lines or internal bremsstrahlung gammas. The search for gammas, particularly those coming from the galactic center, presents a complex background that must be carefully considered. Direct gamma-ray observations are conducted using space telescopes, while ground-based observatories detect Cherenkov light from secondary particle showers created by gamma-rays interacting with the Earth atmosphere. Also in this context, Fermi-LAT, exploiting pair conversion within a tracking detector and an electromagnetic calorimeter plays a significant role. Ground-based Imaging Air Cherenkov Telescopes (IACTs) such as MAGIC [42], VERITAS [43], and the upcoming next-generation telescope CTA [44] are also leading the DM indirect searches panorama. While IACTs have a higher energy threshold compared to space detectors, they benefit from observing a much larger effective area.

Production at colliders: In high-energy particle collisions, such as those conducted at the Large Hadron Collider (LHC), DM particles might be produced. ATLAS or CMS could detect these particles indirectly through missing transverse momentum. Another channel for DM detection is the search for mediators between SM and DM particles through the resonance at the "dark" mediator mass. While this approach avoids astrophysical uncertainties, it faces challenges in ensuring that the detected particles are indeed the constituent of the DM component in galaxies and not other long-lived particles that could escape detection. In fact, the vast majority of the searches for new physics at the LHC are designed to look for events that, besides the rich hadronic/leptonic activity emerging from the decay chain of the produced visible particle, are also characterized by a large amount of missing energy. In this sense, then, the discovery of one or more visible particles in a channel characterized by highly energetic jets or leptons, and large missing momentum, would also imply the discovery of a neutral and stable (at least within the detector bounds) particle, which could be part of the DM or even all of it. In many scenarios, however, WIMPs are considered as the only new field around the electroweak scale, while additional visible particles, if existing, remain beyond the reach of the detector. In these cases, the detection strategy involves isolating one or a few highly energetic objects, like jets, gauge bosons, or leptons, produced in the scattering event due to initial state radiation (ISR). These searches, commonly known as Mono-X, have generated significant excitement in recent years [45].

Although the LHC Mono-X search results have been adapted to various models with electroweak DM interactions and have been valuable for investigating compressed spectra in supersymmetry, limits that are competitive with the one estimated with direct and indirect detection have predominantly been presented by ATLAS and CMS using two preferred frameworks: Effective Field Theory (EFT) and simplified model spectra (SMS). It's important to note that mono-jet bounds are exceptionally competitive for the lower range of the DM mass spectrum, as the probability of emitting a high-pT jet significantly decreases when the DM mass approaches the pT cut.

Direct Detection: This technique, which is the primary focus of this section, involves searching for interactions between DM particles and SM particles within Earth-based detectors. The principle is to detect the energy deposited by the scattering of DM particles off atomic nuclei or electrons in a detector. This energy can be transformed into heat, light, or charge, and the detector is designed to be sensitive to one or more of these signals. The experiments are conducted in deep underground laboratories to minimize interference from cosmic rays and require meticulous selection of materials to reduce background radiation; while the primary backgrounds, gamma (γ), beta (β), and alpha (α) radiation, as well as neutrinos, typically result in recoils of atomic electrons, DM can potentially interact with both electrons and atomic nuclei. The interaction of DM, especially with typical WIMP masses in the range of $10 - 100\,\mathrm{GeV/c^2}$, is more likely to involve nuclear rather than electronic recoils due to kinematic constraints. This difference in scattering mechanisms provides a key method for differentiating DM signals from the background. The direct detection landscape includes a variety of technologies, with experiments that implement various techniques to distinguish nuclear recoils (NR) from electronic recoils (ER). For instance, dual-phase xenon Time Projection Chambers (TPC) like XENONnT and LZ [46] utilize both scintillation and ionization signals to discern between these interactions. Similarly, cryogenic bolometers employing semiconductors (or light detectors), such as SuperCDMS [47] (COSINUS [48]), combine phonon detection methods with charge (light) collection, being particularly sensitive to low-mass WIMPs due to their low energy thresholds. Additionally, experiments must contend with other background sources like neutrons, which can mimic DM interactions by scattering off nuclei. Neutron backgrounds are often mitigated by identifying and vetoing multiple scatter events, as neutrons are more likely than DM particles to scatter multiple times; to address this, advanced DM detection experiments incorporate also neutron veto systems. Concerning neutrinos, they present a unique challenge; they can cause also nuclear recoils, indistinguishable from WIMP interactions, through CEνNS.

Future DM detectors, such as DARWIN [49], are expected to reach sensitivity levels to probe the challenging region where neutrino interactions will become a significant background (the so-called *neutrino floor* or *fog*).

Noble liquid or gas detectors, using elements like xenon and argon, are prominent in the direct detection field. They are very good scintillators and require relatively low energy for electron-ion pair production. Detectors like DEAP-3600 [50] operate in scintillation mode, while others like DarkSide-50 [51], LUX [52], and the XENON [53] experiments combine both light and charge readout. These technologies benefit from their self-shielding feature due to high density and can distinguish particle types effectively using the charge-to-light ratio or pulse shape analysis of scintillation signals.

Despite the advanced technologies and methods employed, no experiment to date has observed a signal that can be definitively attributed to DM particle interactions. The DAMA/LIBRA experiment [54], which uses thallium-doped sodium iodide crystals, sees evidence of a modulating signal that can be attributed to DM interaction [55], but this finding is in tension with other experimental results and is still a subject of debate within the scientific community.

Given the breadth and rapid evolution of the direct detection field, it is hard (and beyond the purpose of this thesis) to provide a complete, updated overview of all the experiments and techniques. A comprehensive view can be found in [56] and [57].

In the upcoming sections, we will delve deeper into more technical concepts around direct detection.

1.3.1 Dark Matter in The Milky Way

Of particular significance to Earth-based DM searches is the observed discrepancy between the expected velocity distribution based on the baryonic matter and the observed velocity distribution in our galaxy. To calculate the interaction probability of DM within a detector on Earth, it is important to estimate the abundance of the DM. Recent advancements in astrophysical observations, particularly the data released from the GAIA satellite [58], have significantly refined our comprehension of DM distribution and structural dynamics within our galaxy. To model the Milky Way, an adjusted NFW halo profile is employed [59]. Figure 1.5 shows the model of the rotation curve within the Milky Way together with data inferred from the Gaia satellite [60].

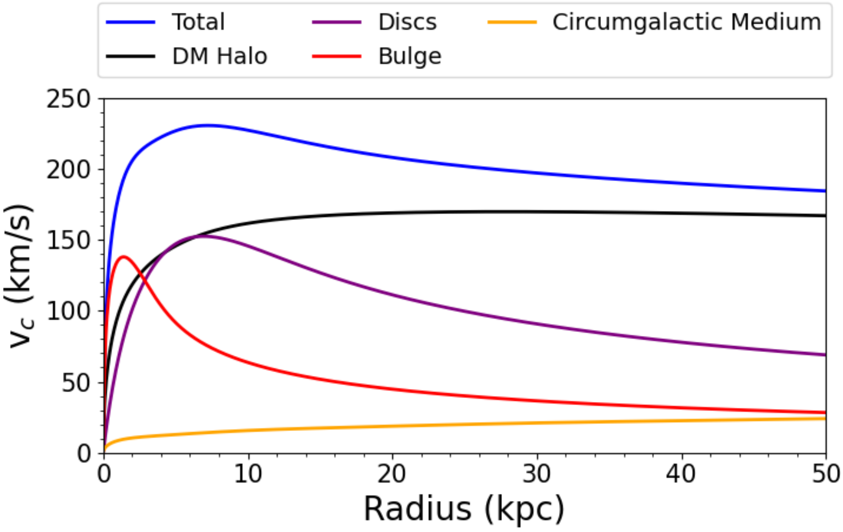

Figure 1.5: *Rotation curve of the Milky Way with all the different components represented. Data from [60] plotted using the mw-plot and galpy python package [61, 62].*

As a result of this improved model, the DM density at the Sun location is now estimated to be approximately ~0.43 GeV/cm^3 [63]. Complementary analyses offer a range of 0.3 to 0.5 GeV/cm^3. The Standard Halo Model used to define the WIMP velocity distribution is based on a Maxwell-Boltzmann velocity distribution:

$$f(v\chi) = \frac{1}{\sqrt{2\pi}\sigma} \exp\left\{\frac{-|v_\chi|^2}{2\sigma^2}\right\} \tag{1.5}$$

where v_χ represents the DM velocity and σ the dispersion velocity which is related to the circular velocity through $\sigma = \sqrt{3/2}\, v_c$ with v_c being usually assumed to be 220 km/s [64]. For velocities exceeding a certain threshold DM particles would not remain gravitationally bound to the galaxy. Consequently, the velocity distribution is truncated at the local escape velocity, often taken as $v_{\mathrm{esc}} = 544\,\mathrm{km/s}$ [65]. Furthermore, the motion of Earth in relation to the Sun trajectory through the DM halo introduces an additional variable. This relative motion causes a modulation in the WIMP velocity, subsequently affecting the rate at which WIMPs are detected. Such a modulation could give a strong hint in confirming the presence of a DM signal.

1.3.2 Direct Detection

Given all the astrophysical inputs in the previous section, it is possible to estimate the expected interaction between WIMPs in the halo of our galaxy and the target nuclei of an earth-based experiment. Considering the typical velocity of WIMPs around 220 km/s at the solar orbit radius and their mass range from a few GeV to TeV, it is reasonable to assume that WIMPs travel at non-relativistic speeds. This results in typical kinetic energies in the range of a few keV, which are significantly lower than the nuclear binding energies of heavier nuclei. Thus, the collisions between DM particles and target nuclei will be elastic, largely independent of the specific WIMP candidate [66]. The interaction is expected to generate a nuclear recoil whose energy is dependent on the WIMP and target nucleus masses and on the WIMP velocity. The formula is given by:

$$E_r = 2v^2 \frac{\mu}{m_N} \times \cos^2\theta_r \tag{1.6}$$

where μ is the WIMP-nucleus reduced mass, $\mu = \frac{m_N m_\chi}{m_N + m_\chi}$, m_N and m_χ the target nucleus and WIMP masses, v the WIMP velocity and θ_r the WIMP-nucleus recoiling angle. The recoil energy is expected to be in the low-energy range of $(1-100)$ keV. The rate of interactions in any direct detection experiment, per unit energy, is proportional to the target atom density N_T, DM particle flux ϕ_χ, and interaction cross-section σ. This rate can be expressed as:

$$\frac{dR}{dE_r} = \frac{\rho_0 M}{m_N m_\chi} \int_{v_{min}}^{v_{esc}} v f(v) \frac{d\sigma_{\chi,N}}{dE_r} dv \tag{1.7}$$

Here, M represents the total target mass, m_N the mass of a single nucleus, $d\sigma_{\chi,N}/dE_R$ the differential DM-nucleus cross-section, and v_{min} the minimum velocity required to produce a detectable signal. The latter, for a nucleus of given mass m_N:

$$v_{min} = \sqrt{\frac{E_r m_N}{2\mu^2}} \tag{1.8}$$

Above the escape velocity, v_{esc}, WIMPs will no longer be bound to the gravitational potential well of the galaxy. Therefore the integration is done over the v_{min} and v_{esc} bounds. Many terms in equation 1.7 depend on the detector's physical properties and astrophysical DM model; however, the last term relies on inputs from particle physics. The interaction cross-section is generally considered as the sum of spin-independent (SI) interaction, described by a scalar or vector effective Lagrangian, and a spin-dependent (SD) interaction described by an axial-vector effective Lagrangian. Therefore, the cross-section can be represented as:

$$\frac{d\sigma_{\chi,N}}{dE_r} = \frac{m_N}{2v^2\mu^2}\left[\sigma_0^{SI}F_{SI}^2(E_r) + \sigma_0^{SD}F_{SD}^2(E_r)\right] \tag{1.9}$$

In this expression σ_0^i denotes the spin-dependent and independent cross-sections at zero momentum transfer, and F_i are the form factors accounting for momentum transfer and nuclear structure. In SI interactions, the form factor F_{SI} is commonly described by the Helm parametrization, and the cross-section is given by:

$$\sigma_0^{SI} = \sigma_n \frac{\mu^2}{\mu_n^2}\frac{\left(f_p Z + f_n\left(A - Z\right)\right)^2}{f_n^2} = \sigma_n \frac{\mu^2}{\mu_n^2}A^2 \tag{1.10}$$

where f_i is the contribution from neutron and proton couplings to the total cross-section, σ_n the cross-section of a single nucleon, and μ_n the WIMP-nucleon reduced mass. The de Broglie wavelength of an elastically scattered WIMP on a xenon nucleus typically exceeds the nucleus size, it is assumed that $f_p = f_n$, leading to coherent scattering where $\sigma_{SI}^0 \propto A^2$. The implication of this is that experiments using heavier target nuclei are more appealing for the search of SI interactions, at low momentum transfer. On the other hand, for larger momentum transfers the form factor starts to play a role, implying an event rate drop for heavier nuclei. This is shown in figure 1.6 for various common target materials.

In SD interactions, the cross-section directly depends on the nuclear angular momentum j and nucleon spins $\langle S_i \rangle$. Unlike SI interactions, the SD case exhibits more variation among different isotopes, even with similar atomic masses. The SD cross-section can be expressed as:

$$\sigma_0^{SD} = \frac{32G_F^2\mu^2}{\pi}\frac{J+1}{J}\left[a_p\langle S_P\rangle + a_n\langle S_n\rangle\right]^2 \tag{1.11}$$

where G$_F$ is the Fermi coupling constant and a_i the effective proton and neutron couplings. Although xenon does not have an unpaired proton it is thus still sensitive to SD proton couplings, with its isotopes ^{129}Xe and ^{131}Xe. However, the expected rates compared to SI interactions are much lower as the $\propto A^2$

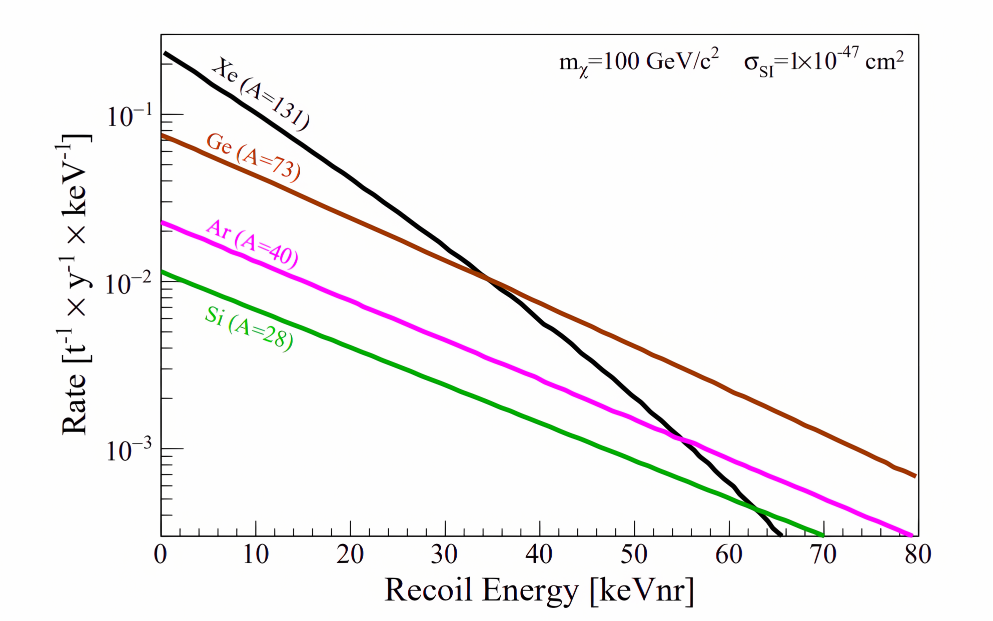

Figure 1.6: *Spectra of Nuclear Recoils generated by a WIMP with a mass of* $m_\chi = 100$ *GeV/c*^{2} *interacting with different commonly used target materials, under the assumption of a spin-independent WIMP-nucleon cross-section* ($\sigma_{SI} = 1 \times 10^{-47} cm^2$)*. The interaction rate for spin-independent processes shows a preference for heavier materials, scaling with* A^2*. However, for larger nuclei such as Xenon, the interaction rate diminishes at higher energies due to form factor suppression. Plot from [67].*

enhancement is missing. As discussed before, depending on the target material and detector technology, DM particle signals are detected through photons, charge carriers, phonons (heat), or a combination thereof. Liquid noble gas detectors, like dual-phase TPCs detecting charge and light signals, are at the forefront of DM searches in the mass range of 1 GeV/c^2 to several TeV/c^2, while cryogenic bolometers are more sensitive to lower mass WIMPs due to their ultra-low energy threshold. The state-of-the-art of direct search for spin-independent WIMP-nucleon interactions is represented in figure 1.7.

The small DM masses below ∼ 1 GeV/c^2 are best probed by experiments like CRESST-III [69], which measure DM signals through photons and heat. The mid-range masses are dominated by experiments like DarkSide-50, with higher mass ranges being the focus of XENON and LZ. The following chapter will provide a more detailed discussion of the LXe dual-phase TPC experimental approaches and the main results achieved with the experiments of the XENON project.

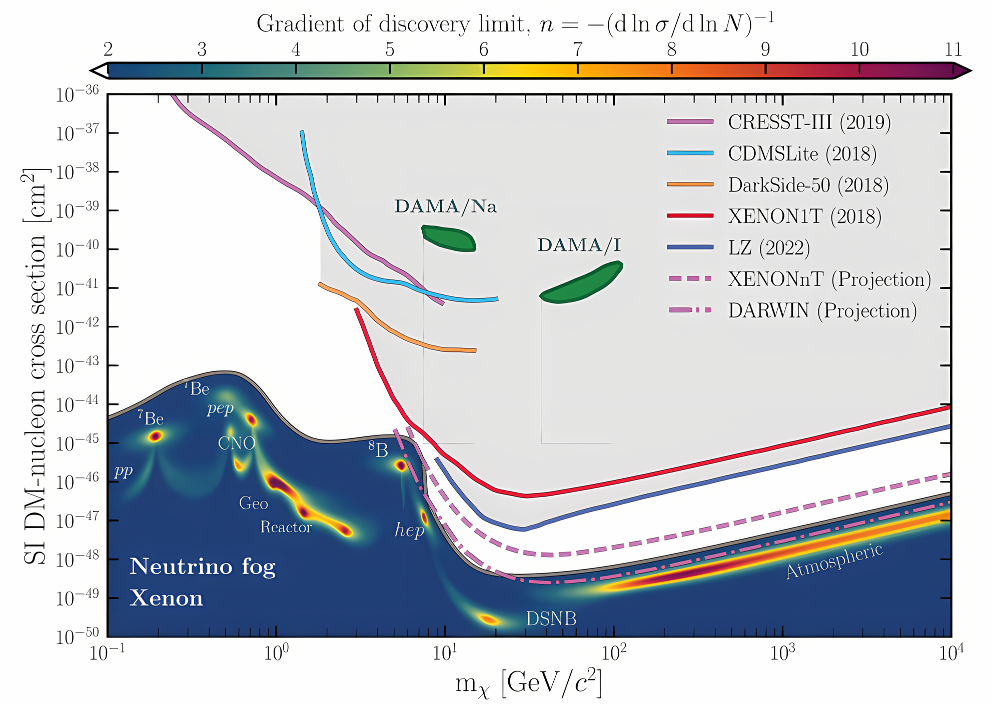

Figure 1.7: *Exclusion limits on the SI DM-nucleon cross-section as a function of DM particle mass* m_χ. *One of the main features of this plot is the neutrino fog representation, as it is depicted as a function of the index* n, *present in the relation between the limit and the number of background events, as* $\sigma \propto N^{-1/n}$. *Here the neutrino fog is defined to be the region in which n>2. In this way, it is underlined that the CEνNS is not a strict limit which makes the WIMP direct detection search impossible, but rather a background source that makes it more challenging. Plot from [68].*

2

The XENONnT Experiment

The quest to unravel the mystery of Dark Matter has led to the development of sophisticated detectors and experiments. This chapter delves into the details of the XENONnT experiment, a cutting-edge dual-phase xenon Time Projection Chamber (TPC), designed with the primary objective of detecting WIMPs (Section 2.2). We start by exploring the fundamental principles behind particle interactions with liquid xenon and the operational mechanics of a dual-phase xenon TPC. This sets the stage for a comprehensive overview of the XENONnT experiment, including its intricate design elements aimed at minimizing background, a key challenge in direct DM detection. The XENONnT experiment is the newest phase of the international XENON collaboration extensive DM direct detection program. The detector not only significantly contributes to the search for DM, consistently demonstrating exceptional sensitivity, but also allows for the study of other rare physics events, such as the search for two-neutrino double-electron capture (2νECEC) of ^{124}Xe and the neutrinoless double-β decay ($0\nu\beta\beta$) of ^{136}Xe [70]. The sections of this chapter will cover various aspects of the XENONnT experiment. Section 2.1 introduces the XENON Dark Matter Project history and context. Section 2.2 delves into the principles and technologies behind the dual-phase xenon TPC. Section 2.3 presents the design and implementation of the XENONnT experiment, while in Section 2.4 a complete overview of the backgrounds that characterize the main physics research is provided. The final section of the chapter (Sec. 2.5) is instead dedicated to the future prospects of the LXe-based DM research experiments.

2.1 The XENON Dark Matter Project

Initiated in 2005, the XENON program represents a series of groundbreaking experiments at the vanguard of DM research. Utilizing xenon-based dual-phase TPC, these experiments have significantly advanced the sensitivity in direct detection of WIMPs. The project is based at the INFN Laboratori Nazionali del Gran Sasso (LNGS) in Italy, a site uniquely suited for such sensitive experiments due to its location, providing substantial shielding from cosmic radiation. Figure 2.1 shows the evolution of the projects over the years, in terms of dimensions, active target mass, and the correspondingly reduced background level.

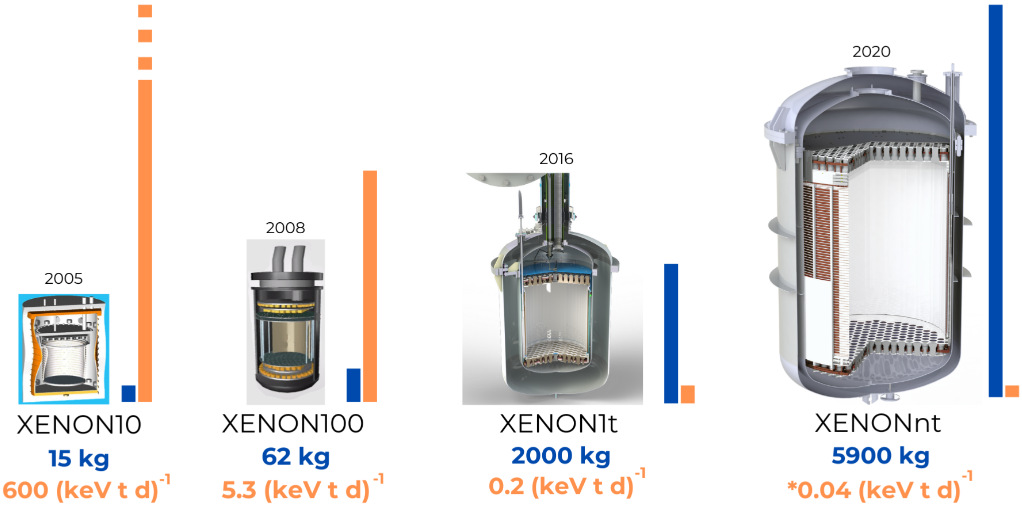

Figure 2.1: *Overview of the XENON program detectors, showcasing the TPCs of varying dimensions and with the construction year noted. Displayed in blue are the active LXe masses within the TPCs. The orange indicator represents the low-energy ER background level, set at* $\leq$ 20 *keV. The rate for XENONnT, marked with an asterisk, represents the targeted performance and purity goals of the experiment. Figure re-adapted from [71].*

XENON10 [72], the first of the series, was a milestone in DM detection technology. Operating with an active xenon mass of about 15 kg from 2005 until 2007, it was instrumental in validating the long-term operational viability of xenon-based TPCs. Notably, XENON10 established world-record upper limits on SI (and SD-neutrons) WIMP-nucleon cross-section, with minimum of 4.5×10^{-44} cm^2 [73] (5×10^{-39} cm^2 [74]) for WIMP mass of 30 GeV/c^2 at a 90% confidence level.

Building on this success, the XENON100 experiment [75] was installed in 2008 with an increased target mass of 62 kg. The experiment achieved a hundredfold reduction in background levels compared to XENON10, setting new upper limit records for the SI WIMP-nucleon cross-section at 1.1×10^{-45} cm^2 for 50 GeV/c^2 WIMP mass, while for SD WIMP-neutron (-proton) cross-section upper limits were set at 2.0×10^{-45} cm^2 (3.5×10^{-40} cm^2) for 55 (45) GeV/c^2 WIMP mass [76, 77], marking a significant stride in the quest for DM.

The transition to ton-scale TPCs was marked by the launch of XENON1T [78] in 2016, which operated until the end of 2018. With an active 2.0-tonne target mass of xenon, XENON1T pushed the boundaries of detection sensitivity, setting the most stringent limits on SI (SD) WIMP-nucleon cross-sections, with a minimum at 4.1×10^{-47} cm^2 (6.3×10^{-42} cm^2) for 30 GeV/c^2 WIMP mass with 1.3 tonne-year exposure [79, 80]. Its results not only reaffirmed the leading position of the XENON program in DM research but also expanded the scientific scope to explore new interaction channels and rare physics events [81, 82, 83, 84]. In 2019, the program evolved into its fourth phase with XENONnT (section 2.3). Starting the data acquisition at the end of 2020, XENONnT is designed to enhance the sensitivity by an order of magnitude compared to its predecessors. A picture of the experiment, in Hall B of LNGS, is shown in figure 2.2. The first results from XENONnT published in [85, 86], will be presented in the next chapters.

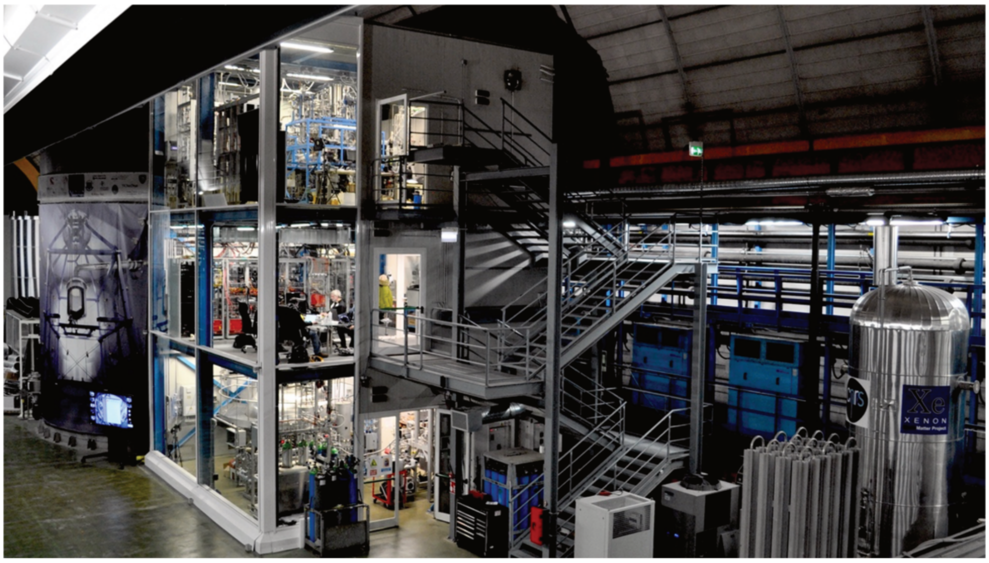

Figure 2.2: *A view of the XENONnT experiment located in hall B at LNGS. Prominently featured in the background is the water tank, serving both as a passive shield and an active water Cherenkov MV. At the heart of the water tank, the TPC stands as depicted on the overlaying poster. In the foreground, the service building is visible, housing the various subsystems of the experiment including cryogenics, Xe purification, distillation, recovery, and the DAQ system.*

2.2 Particle Detection in a Xenon Dual Phase Time Projection Chamber

2.2.1 Liquid Xenon

Liquid Xenon (LXe) serves as an exemplary medium for DM detection, but in general it offers many advantages for rare event searches. Its high atomic mass (A = 131) enhances the rate of spin-independent interactions (as seen in section 1.3.2 since the WIMP cross-section scales with A^2), while the presence of isotopes with non-zero spin, such as the ^{129}Xe (spin 1/2) and the ^{131}Xe (spin 3/2), allows for effective probing of spin-dependent interactions. Xenon natural abundance of stable isotopes (nine in total, all listed in table 2.1), including ^{134}Xe and ^{136}Xe, which undergo rare weak decays, makes it a valuable medium for studying these processes as well.

^{A}Xe	Abundance (%)	Half-life	Decay mode
^{124}Xe	0.095	1.8×10^{22} y	ECEC
^{126}Xe	0.089	stable	
^{128}Xe - ^{132}Xe	80.3	stable	
^{134}Xe	10.43	stable	
^{136}Xe	8.8	2.2×10^{21} y	$\beta\beta$

Table 2.1: *Natural xenon composition. Only two of the natural isotopes are unstable but with half-life greater than the age of the Universe. For the stable isotopes,* $^{128..131}$*Xe, the overall abundance is reported.*

When in the liquid phase, Xenon high density (2.96 g/cm^3) provides excellent self-shielding against external background, and its scintillation and ionization properties result in strong signal intensity. Furthermore, LXe can be liquefied at moderately cryogenic temperatures (triple point at 161 K), allowing for compact and scalable detector designs. When a particle interacts with a xenon atom, it transfers energy, leading to ionization and excitation. The resulting recoils can be classified into **electronic recoils** (ERs) and **nuclear recoils** (NRs), depending on whether the incident particle scatters off an electron or a nucleus. NRs tend to produce shorter, denser energy tracks compared to ERs due to the greater mass of the nucleus. In XENONnT, the detection relies on measuring scintillation and ionization signals generated by these energy deposits, while the energy converted to heat is not directly detected.

Figure 2.3 shows a schematic of how the deposited energy is partitioned among the three processes. The excitation and ionization of xenon atoms result

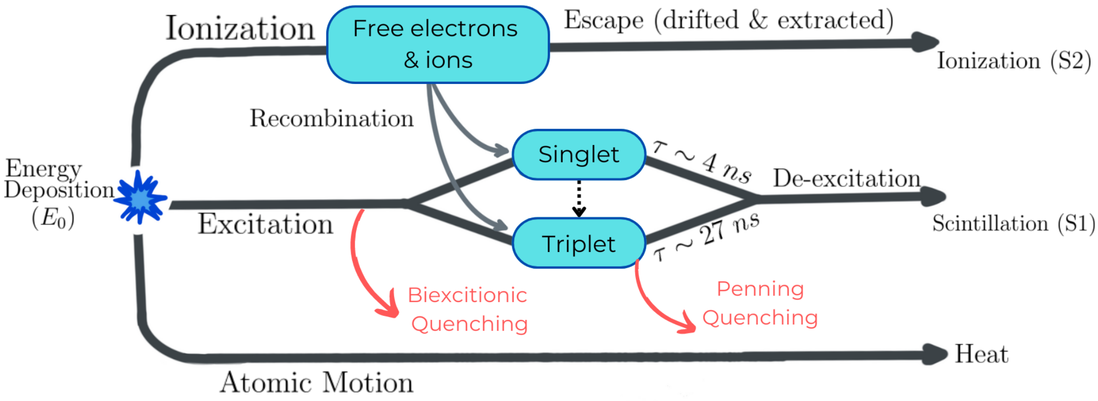
Ionization
Free electrons & ions
Escape (drifted & extracted)
Ionization (S2)
Recombination
Energy Deposition (E_0)
Singlet
$\tau \sim 4\ ns$
De-excitation
Scintillation (S1)
Excitation
Triplet
$\tau \sim 27\ ns$
Biexcitionic Quenching
Penning Quenching
Heat
Atomic Motion

Figure 2.3: *Energy depositions in LXe lead to the formation of observable scintillation and ionization signals, as well as to non-observable energy loss to heat. Atom excitation and ion-electron recombination form the prompt scintillation signal, referred to as S1. The ionization electrons are drifted and extracted by the application of electric fields, forming a proportional scintillation signal, S2. The dashed grey line depicts the process of superelastic collisions between electrons and singlet states, forming triplet molecular states. Schematic re-adapted from [87].*

in scintillation light, primarily in the ultraviolet spectrum, due to the de-exciting and recombining of xenon atoms and ions. Free electrons are also produced via ionization. In the first case, one starts with an excited xenon atom (Xe*) followed by the scintillation process:

$$\begin{aligned} \mathrm{Xe}^* + \mathrm{Xe} &\longrightarrow \mathrm{Xe}_2^* \\ \mathrm{Xe}^* &\longrightarrow 2\mathrm{Xe} + h\nu \end{aligned} \tag{2.1}$$

The second case instead involves ionized xenon atoms Xe$^+$.

$$\begin{aligned} \mathrm{Xe}^+ + \mathrm{Xe} &\longrightarrow \mathrm{Xe}_2^+ \\ \mathrm{Xe}_2^+ + e^- &\longrightarrow \mathrm{Xe}^{**} + Xe \\ \mathrm{Xe}^{**} &\longrightarrow \mathrm{Xe}^* + \mathrm{heat} \\ \mathrm{Xe}^* + \mathrm{Xe} + \mathrm{Xe} &\longrightarrow \mathrm{Xe}_2^* + Xe \\ \mathrm{Xe}_2^* &\longrightarrow 2\mathrm{Xe} + h\nu \end{aligned} \tag{2.2}$$

Notably, LXe is transparent to its scintillation light due to the specific wavelength emitted by these excimers, since dimers and atoms have different energy levels configuration. These processes are characterized by distinct decay times for the spin singlet (4 ns) and triplet (27 ns) states of xenon excimers (Xe$_2^*$), resulting in the same scintillation light of about 178 nm [88]. The ratio between the two states depends on the density distribution of the deposited energy and therefore varies between different particle types; for other liquid noble gases such as argon, with a difference in decay times much larger for singlet and triplet, this feature can be exploited to perform pulse-shape discrimination. In a xenon dual-phase TPC this is challenging because the difference in the lifetimes is smaller than the time resolution associated with the photosensors and their readout electronics.

2.2.2 Dual Phase TPC

The core of the XENONnT experiment is the dual-phase TPC employing liquid and gaseous xenon (LXe/GXe) to detect DM interactions. The operating principle of the dual-phase TPC is sketched in figure 2.4. When a particle interacts with the xenon target, it triggers the production of light and charge quanta. The prompt scintillation light signal, known as S1, marks the beginning of the event. Concurrently, the ionization process releases electrons that drift toward the gaseous xenon phase under an electric field. As these electrons approach the liquid-gas interface, they are accelerated by a stronger extraction field into the gaseous phase, generating a secondary, electro-luminescence signal called S2. This two-phase amplification is a distinctive advantage of the dual-phase TPC, enabling the detection of smaller charges and thereby lowering the energy threshold of the detector. The dual arrays of photomultipliers (PMTs), positioned at both ends of the TPC, detect these S1 and S2 signals. A series of electrodes ensures the uniformity of drift and extraction across the detector volume. The TPC design allows for measuring several interaction properties. The three-dimensional position of events can be reconstructed: the vertical (z) coordinate is derived from the drift time between S1 and S2, while the horizontal (x,y) coordinates are inferred from the S2 hit pattern on the top photosensor array. The TPC can also distinguish between Single-Scatter (SS) and Multiple-Scatter (MS) events, essential for discriminating signals from background events.

In XENONnT, the ratio between the S1 and S2 signals (light and charge quanta) plays a main role in discriminating between ERs and NRs. ER and NR events occupy distinct regions in the (S1, S2) parameter space, as shown in figure (2.5).

The corrected signals, denoted as cS1 and cS2, account for detector effects influencing the number of light and charge quanta collected compared to those produced in the interaction. These effects are quantified with the g1 and g2 parameters, obtained by studying the anti-correlation between S1 and S2

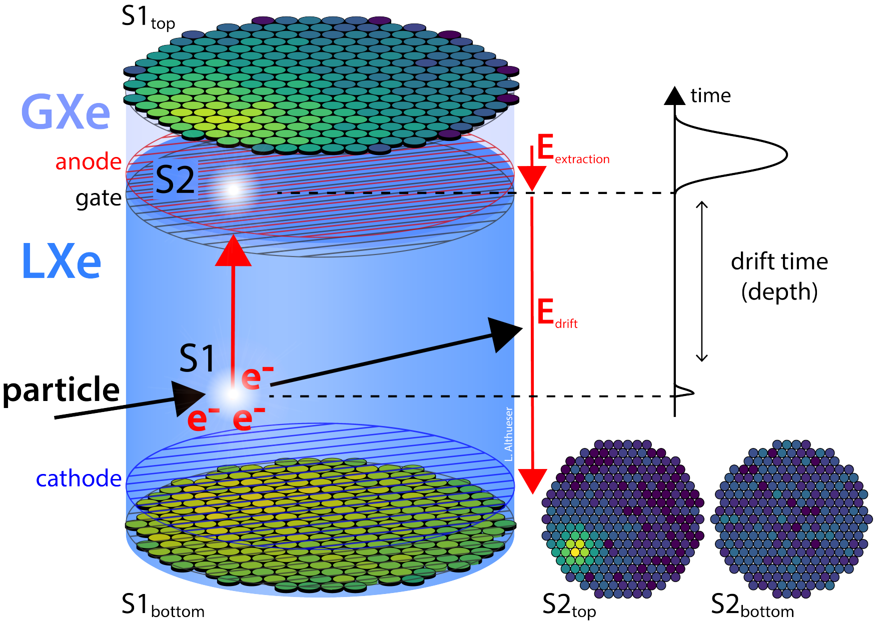

Figure 2.4: *Schematic illustrating a particle interaction within the XENONnT TPC. When a particle collides with the LXe, it imparts energy to either a xenon nucleus or an electron. This interaction results in immediate scintillation light, captured by the PMT arrays positioned at both the top and bottom of the TPC, known as the S1 signal. Additionally, the collision produces quasi-free electrons. These electrons are guided upwards to the liquid surface by the* E_{drift} *electric field. Here, a more intense field,* $E_{exctraction}$*, propels them into the GXe layer above. The ensuing interactions with xenon atoms in this layer generate a secondary scintillation signal, called S2. The horizontal (x, y) position of the interaction is deduced from the pattern of S2 detected by the top PMT array (illustrated in the bottom right), while the vertical (z) coordinate is determined by measuring the time interval between the S1 and S2 signals*

using different mono-energetic calibration sources. The Energy deposition from interactions is reconstructed with

$$E_{dep} = W \times \left(\frac{S1}{g1} + \frac{S2}{g2} \right) \tag{2.3}$$

where W is the averaged energy to produce either a scintillation photon or an ionized electron and stands at (13.7 ± 0.4) eV. While this formula is valid for ER events, in the case of NRs one has to consider the Lindhard factor that accounts for the signal quenching resulting from heat loss[1].

Due to the different yields, the light-to-charge ratio for NR differs from that for ER. For a given energy deposition in keV_{er} one has $(S2/S1)_{NR} < (S2/S1)_{ER}$. The ability to discriminate between ER and NR is quantified as the portion of

---

[1] Electronic recoil events lose almost all their energy through electronic excitation, whereas NR events also lose energy through elastic collisions with other atoms. While some of these interactions create further electron-ion pairs, most have energies below the ionization threshold.

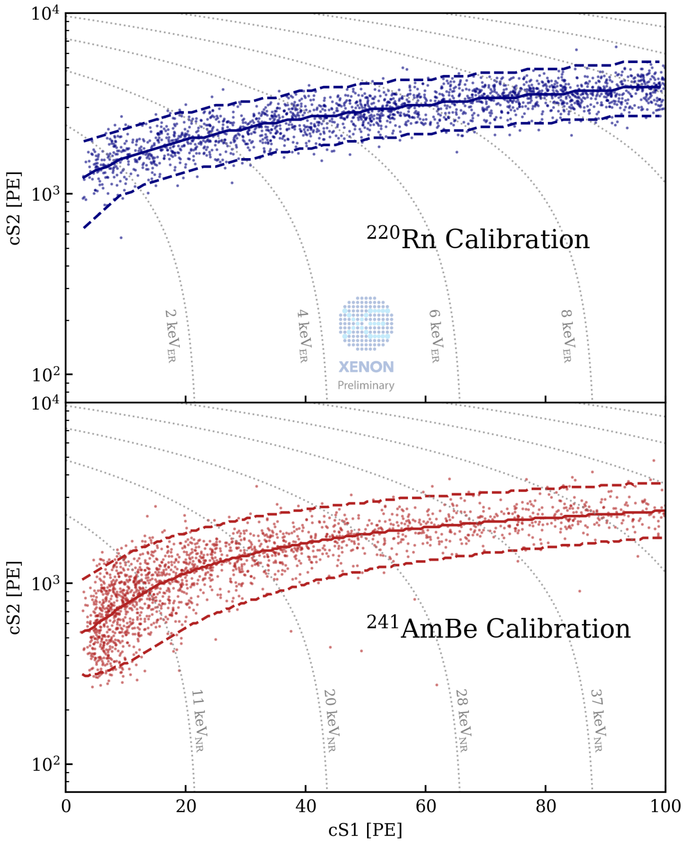

Figure 2.5: *Determination of ER (top - blue) and NR (bottom - red) bands in the (cS1 area, cS2 area) parameter space during XENONnT SR0 [86]. The ^{220}Rn and ^{241}AmBe calibration data were used to identify the bands, whose median (solid line) and $\pm 2\sigma$ percentile are depicted for both types of interaction. The dotted grey lines in the plots show the respective ER and NR energies.*

the ER band that falls below the median of NR band. This parameter, called ER-leakage, is energy-dependent and is modulated by the applied drift field. For instance, the higher the drift field, the better the separation between ER and NR events due to the different recombination processes involved. Concerning the electric field in the TPC, the drift field is defined at the bottom by a negatively biased cathode electrode, with the top marked by a grounded gate mesh. Above the gate electrode lies the anode, with the liquid-gas interface in between. Of the two PMT arrays, one is in the gaseous xenon at the top, and the other is immersed in liquid xenon at the bottom of the detector. The TPC ability to reconstruct interaction vertices in three dimensions and to select events within a defined fiducial volume (FV) significantly mitigates background interference from external sources.

2.3 The Experiment

The XENONnT experiment is installed in Hall B of the INFN LNGS. As the fourth phase of the XENON project, XENONnT has inherited much of its infrastructure from its predecessor, XENON1T, but with substantial advancements to address the ever-increasing challenges of DM research. XENON1T itself has been designed to also host its successor and this strategy allowed for a quick transition between the two experiments; the installation of the XENONnT detector systems was completed in 2020 in less than 1 year (some of the operations in which I have contributed, presented in section 3.3). The TPC is located at the center of the system. It is surrounded by Gd-loaded water within the reflective boundaries of the Neutron Veto (NV) detector, a new subsystem developed to reduce the radiogenic neutron background. Everything is installed inside the same cylindrical stainless steel tank built for XENON1T. The tank is instrumented with PMTs and acts as a passive shielding against environmental radiation, and as an active water Cherenkov Muon Veto (MV). While the MV and the NV will be extensively covered in the next chapter, as primary subjects of this thesis, in the following there is an overview of all the other key systems that are shown in figure 2.6.

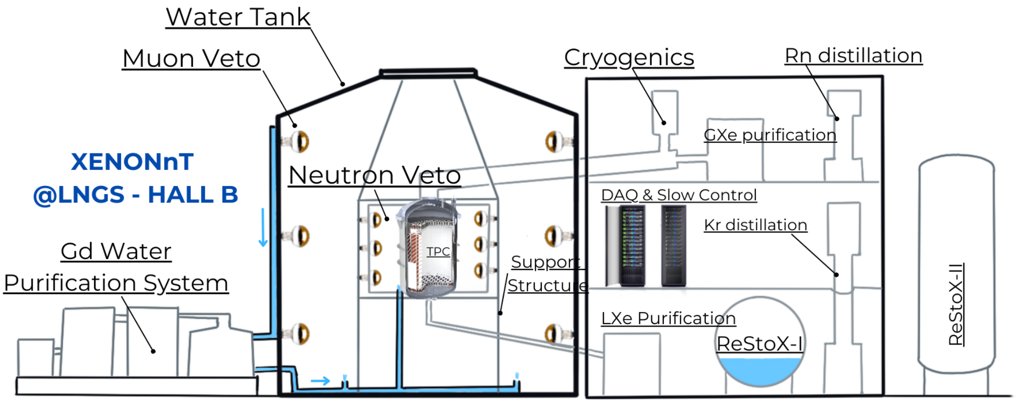
Water Tank
Muon Veto
Cryogenics
Rn distillation
GXe purification
XENONnT
@LNGS - HALL B
Neutron Veto
DAQ & Slow Control
Kr distillation
Gd Water
Purification System
TPC
Support
Structure
LXe Purification
ReStoX-I
ReStoX-II

Figure 2.6: *Schematic View of the XENONnT Experiment and its main subsystems.*

The XENONnT TPC

At the core of XENONnT lies the TPC, now housed within a new inner cryostat vessel, capable of holding a total of 8.6 tons of xenon at -98°C. Of this, 5.9 tons serves as the active detection medium inside the TPC, while the rest acts as a passive shield against external radiation sources. The (virtually) cylindrical active region of the TPC is 1613 mm high and about 1327 mm wide. A rendering of the TPC is shown in figure 2.7 The TPC walls are made of Polytetrafluoroethylene (PTFE) panels to maximize UV-photon reflection. It is equipped with 494 (253 at the top and 241 at the bottom) carefully selected Hamamatsu R11410-21 3-inch photomultiplier tubes (PMTs) [89], chosen for their low radioactivity and high efficiency in detecting xenon scintillation light. The cathode and gate electrodes are responsible for generating the drift field in the liquid xenon (LXe) phase. The cathode is placed in the bottom of the TPC, while the gate hovers close to the liquid-gas interface, separated by a distance of 1486 mm. Above the gate, in the gaseous xenon (GXe) phase, lies the anode, creating an extraction field over a gap of 8 mm. This configuration allows for an efficient transition of electrons from the liquid to the gas phase, where they generate the S2 signal. Additionally to these primary electrodes, there are two screening electrodes, to shield the photomultiplier tubes (PMTs) from the electric fields. These electrodes are made of stainless steel wires stretched across frames using oxygen-free[2] high conductivity (OFHC) copper pins. Additional wires are integrated into the anode and gate to counteract potential sagging. The TPC field uniformity is achieved through two concentric sets of OFHC copper field-shaping electrodes. These rings, interleaved vertically and spaced radially, ensure a consistent electric field

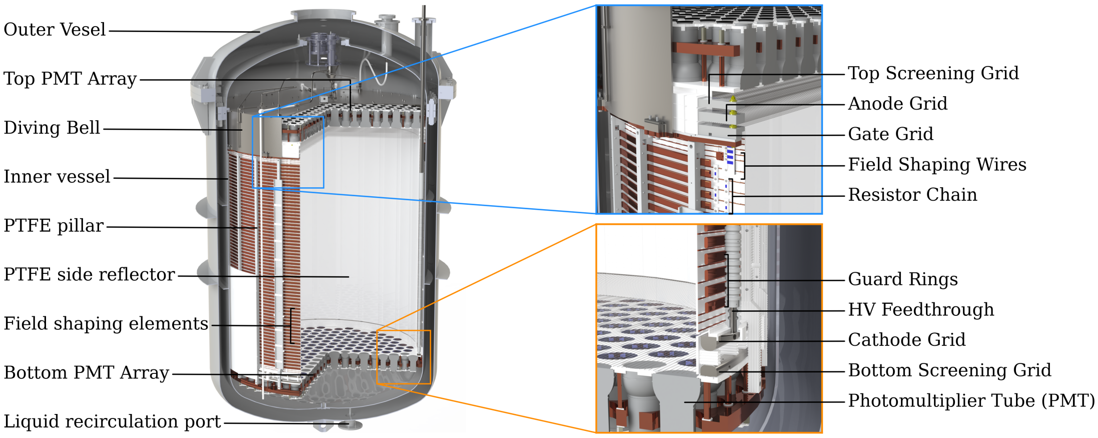
Outer Vesel
Top PMT Array
Diving Bell
Inner vessel
PTFE pillar
PTFE side reflector
Field shaping elements
Bottom PMT Array
Liquid recirculation port
Top Screening Grid
Anode Grid
Gate Grid
Field Shaping Wires
Resistor Chain
Guard Rings
HV Feedthrough
Cathode Grid
Bottom Screening Grid
Photomultiplier Tube (PMT)

Figure 2.7: *CAD rendering of the XENONnT dual-phase TPC. The zoomed insets show details about the field cage, the electrode at the top and bottom of the TPC, and the PMT arrays.*

---

[2] Oxygen must be avoided as it is an electronegativity impurity that can trap electrons and reduce the electron lifetime.

across the active xenon volume, crucial for the event reconstruction; by design the drift field of XENONnT was 200 V/cm, however during the commissioning phase of the experiment, a short circuit occurred between the cathode and the bottom screen electrode, limiting the voltage of the cathode. For the first science run (SR0), the electrodes were set to a voltage of 0.3 kV at the gate, 4.9 kV at the anode and −2.75 kV at the cathode. This resulted in an average electric drift field of 23 V/cm. In the construction of the TPC, thorough attention was paid to the selection of materials and cleanliness procedures to minimize background radiation. An intense screening campaign was essential to identify the most radio-pure materials to be used. Techniques such as gamma-ray spectrometry and inductively-coupled plasma mass spectrometry (ICP-MS) were employed to assess various materials including stainless steel, OFHC copper, PTFE and the PMTs. The target set was of a ^{222}Rn concentration of 1 μBq/kg, which guided not only the selection of low radon-emanating materials for all components in contact with xenon, but also a meticulous cleaning campaign.

Xenon Handling

The larger xenon volume required the development of new systems for xenon handling and purification, aimed at reaching and maintaining the desired purity and background levels. Specifically, the improvements included the introduction of a novel liquid xenon (LXe) purification plant and a radon distillation column, directly lowering the radon concentration in the xenon target. The xenon handling system consists of the following elements:

- **Cooling System**: The cooling and temperature control system of XENONnT closely resembles that of XENON1T; it is based on a "remote cooling" concept with a vacuum-insulated cryogenic pipe connecting the system to an external cooling station. It is complemented by a battery-powered backup LN2 cooling system, ensuring stability during short-term power outages.
- **Xenon Storage and Recovery**: XENONnT cryogenic plant includes two storage units, ReStoX and ReStoX2, capable of storing the entire xenon inventory. ReStoX, designed for XENON1T, can store up to 7.6 tonnes of xenon, while ReStoX2 can hold up to 10 tonnes at room temperature. They play a crucial role in xenon recovery, both in liquid and gas phases, offering rapid recuperation capabilities in emergencies.
- **Electronegative Impurity Removal**: The removal of electronegative impurities like O_2 and H_2O is critical for maintaining the TPC effectiveness since they can reduce, along the drift, the number of electrons available

for the charge signal. The gas purification system from XENON1T was supplemented with a new LXe purification system for XENONnT. The performance of these systems is quantified by the so-called electron lifetime, i.e. the average time before an impurity captures electrons. The electron lifetime achieved has exceeded all expectations, reaching up to <10 ms [86], whereas XENON1T achieved ~650 μs [79].

- **Krypton and Radon Removal**: Krypton and radon isotopes pose significant background risks for the detector. The decay of ^{85}Kr via beta emission, with an end-point (kinetic) energy of 687 keV, can contribute to the intrinsic background in the low-energy search region, while the emanation of ^{222}Rn from detector materials with a 3.8 days half-life, results in a distribution of its decay products within the whole LXe volume. Thus two additional systems, the krypton and the radon distillation, are employed to reduce the otherwise dominant source of background, dissolved in the xenon. The krypton column is responsible for distilling out the anthropogenic ^{85}Kr; it is based on a cryogenic distillation technique, exploiting differences in vapor pressures, and has been carried over from XENON1T. ^{222}Rn has a long decay chain with many radioactive daughter isotopes and constantly emanates from the detector materials (SS, cables, PTFE, etc.), thus requiring a continuous distillation. In XENONnT an online radon removal plant integrated into the LXe re-circulation loop effectively reduces radon concentration [90]; this allowed for a reduction of the ER background (of which as we will see in section 2.4, Rn is the dominant source) of a factor ~5 [91]. This plant is designed to distill both liquid and gaseous xenon phases, enhancing the overall purity of the xenon inventory.

Slow Control and DAQ

The SC system of XENONnT employs Programmable Automation Controllers (PACs) and industry-standard software (Cimplicity SCADA) for monitoring and controlling all the subsystems. The system has been expanded to accommodate new components like the LXe purification, radon distillation column, ReStoX-2 xenon storage, and NV (and its subsystems, as we will see in the next chapter). Enhancements in the SC system allow for more advanced automated operations, such as adjustments in cryogenics, PMT high voltage settings, and optical calibration sequences. All the monitored parameters are stored and used to define alarm conditions and notify users of any anomalies. The DAQ system of XENONnT is responsible for reading out data from the three sub-detectors (LXe TPC, NV, MV), for a total of 698 channels (or PMTs): 494 for the TPC, 84 for the MV and 120 for the NV. It is based on a quasi-triggerless acquisition logic, except for a digitization threshold. The data from all sub-detectors are directed to a unified storage system and processed in a user-friendly format for analysis. This setup ensures that data from all detectors is integrated seamlessly, facilitating the data analysis process.

Calibration Systems

The calibration systems play a crucial role in characterizing the responses of the TPC and outer detectors to various types of radiation. In particular, they are relevant to determine the ER/NR bands and reconstruct the position of the events and energy of the interaction (estimating the g_1 and g_2 parameters). The systems are classified into two kinds of calibrations: internal and external calibration methods. Internal calibration means that the radionuclides are directly injected into the xenon target, allowing for a uniform distribution of the source and thus a better characterization of the whole active volume of the TPC. Of course, this can be applied only for sources with a sufficiently fast decay time. The three sources used are:

- ^{83m}Kr: This metastable (m) isotope is introduced into the TPC via the xenon re-circulation system. It decays into 32.2 keV and 9.4 keV conversion electrons (with a half-life of 1.83 h), useful for calibrating mono-energetic lines close to the Region of Interest (ROI) of WIMP search defined by cS1 between 0 PE and 100 PE and cS2 between 126 PE and 12 589 PE. Regular calibrations with ^{83m}Kr monitor the stability of light and charge yields as well as electron lifetime.
- ^{220}Rn: Introduced into the TPC from an electro-deposited ^{228}Th source, ^{220}Rn decays yield β, γ and α particles. Its decay product, ^{212}Pb, offers a beta spectrum used for low-energy ER band characterization. Due to its relatively longer half-life, ^{220}Rn is typically used at the beginning or end of scientific runs.
- ^{37}Ar: Emitting X-rays at 0.27 keV and 2.8 keV, ^{37}Ar is used to characterize the detector response near the low energy threshold. Its long half-life of 35 days requires calibrations at the end of scientific runs, followed by its removal through distillation.

On the other hand, the External Calibrations consist of placing sources outside of the TPC, usually near the cryostat, to characterize specific regions of the TPC as well as the outer detectors. For instance, the calibration of the NV is one of the main topics of this work and will be extensively covered in the next chapters. In XENONnT we use three different systems:

- L-Shaped Beam Pipe: This system provides collimated neutron beams from a high-energy neutron generator. When combined with D_2O, it allows for low-energy neutron calibration, characterizing the NR band near the energy threshold.
- I-Belt Structure: Used to move a tungsten collimator with an ^{88}Y-Be source along the cryostat, emitting low-energy neutrons and γ-rays.
- U-Tubes: Two independent stainless steel tubes (called top and bottom tubes) run around the cryostat at different heights. They guide small external sources for characterizing the TPC and NV at different positions. Sources such as AmBe and ^{228}Th; these have been the main calibration systems employed so far in the experiment.

The Vetoes

The XENONnT experiment employs two veto systems, the MV and the NV, designed to significantly reduce background signals, respectively from muons and radiogenic neutrons, enhancing the detection sensitivity for WIMPs. This short paragraph serves as a brief overview of these systems, laying the groundwork for a more detailed discussion in the next chapter. The MV system [92] is built on a water tank filled with ultrapure water and equipped with 84 Hamamatsu R5912ASSY 8-inch PMTs. It serves two primary functions: as passive shielding against radioactivity from the surrounding rock and as an active veto against cosmic muons. The MV detects Cherenkov light, emitted by muons traveling through the water, with a high tagging efficiency of 99.5% for muons and 70% for secondary particles. The NV is situated between the cryostat and the MV. Its primary function is to veto neutrons scattering inside the TPC by detecting the neutron capture in water. Instrumented with 120 PMTs, the NV achieves a neutron tagging efficiency of ~68% with demi-water only. In future operations, doping the NV water with gadolinium (Gd) is planned, which is expected to increase neutron capture probability and the tagging efficiency up to 87%. **The Neutron Veto is a significant focus of my research, and its details will be presented in the following chapters, highlighting its importance and contributions to the experiment.**

2.3.1 Status of the Experiment

The journey of XENONnT began with the decommissioning of XENON1T in December 2018 and the preparation of the new TPC. Its assembly started in February 2020 in a dedicated cleanroom at LNGS. This process, detailed in [93], involved meticulous cleaning protocols to ensure the purity of the

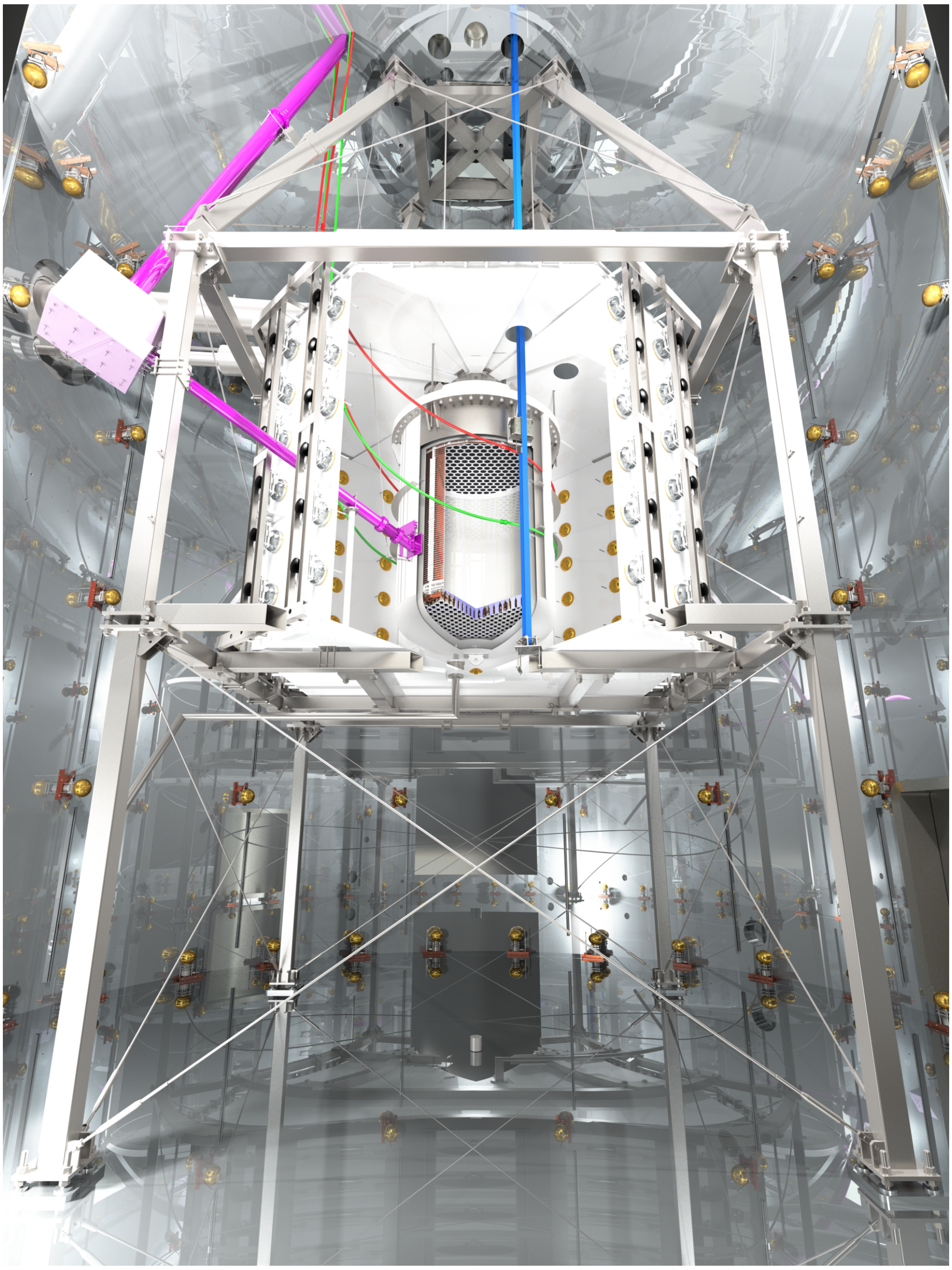

Figure 2.8: *CAD rendering showing the various components inside the XENONnT water tank, including the central cryostat, the NV, the MV, and the calibration systems. In blue is the I-belt, used for moving the tungsten collimator. In purple, the L-shaped beam for neutron calibrations, and in red and green, the two U-tubes that embrace the cryostat.*

detector. The assembly was completed in March 2020, after which the TPC was transported to the underground laboratory and integrated into the cryostat within a specially constructed cleanroom. Soon after the TPC installation, the construction of the NV and the refurbishment of the MV started. The intense work to which I actively contributed, is fully described in section 3.3. The finalization of the veto construction marked the transition from assembly to commissioning. During the commissioning of the TPC two significant issues were encountered. The first involved a short circuit between the cathode and bottom screen, which necessitated limiting the cathode voltage to -2.75 kV. The second issue, named *'hot-spot'* emerged while optimizing the top stack electrodes' high voltage. This phenomenon, characterized by bursts of single electrons, hindered stable operation. To address this, the anode and gate voltages were adjusted to +4.9 kV and +0.3 kV, respectively. Despite the lower field, stable conditions were achieved for the first scientific run, named Science Run 0 (SR0). SR0 started on July 6, 2021, and was concluded on November 10, 2021, achieving a total livetime of 97.1 days. Following SR0, after a few refurbishments and optimizations we went through the second science run (SR1), which began on May 19, 2022, and concluded in August 2023. This run yielded an exposure of nearly 200 days, providing a wealth of data for ongoing analysis. As the experiment moves forward, Science Run 2 (SR2) is currently in progress; in this phase of the experiment, the NV is operating with a $Gd_2(SO_4)_3$ concentration of 500 ppm. More details about each phase of the experiment will be found in Chapter 6.

2.4 Backgrounds

The WIMP signal is expected to be a single NR interaction in the active detector volume; this already gives a restriction on the event selection. Although ERs can be efficiently discriminated from NRs based on the S2/S1 ratio, leakage of the ER population can still produce events indistinguishable from WIMPs. Thus, a detailed understanding of both NR and ER background sources is required. This section stands as an overview of all the background sources relevant to the XENONnT main research channels, and is based on MC estimations presented in [91]. The background sources include the external radioactive isotopes in the detector materials and the dissolved ones in the xenon itself as well as the irreducible component arising from (solar, atmospheric, and supernova) neutrino interactions. A key strategy in reducing backgrounds is the use of a defined fiducial volume (FV) for the analysis. This FV is selected to effectively shield the core detector area from external backgrounds, primarily originating from the materials used in the detector construction. Although the materials for XENONnT were chosen through an extensive radioassay program, ensuring minimal radioactive contamination, this approach remains crucial in minimizing both ER and NR backgrounds.

2.4.1 Electronic recoil background

The dangerous ER events appear to be the events that are not rejected by the ratio of S1 and S2, since they show up in the signal region and can mimic the expected WIMP signal. In this section, we present all the sources taken into account to model the ER component, and table 2.2 summarizes the estimated contribution of each component.

- **Detector Components**: Radioactive decays within detector components, contribute to the low-energy background through single Compton scatters. External gamma radiation produced by these components forms an almost flat spectrum at energies below 200 keV. In XENONnT, the cryostat vessels and PMTs are the primary contributors to this background.
- **Radon** Radon-222 emanation from detector materials is significant due to its 3.8-day half-life, resulting in a uniform distribution within the LXe volume. The decay of ^{214}Pb, a product of the ^{222}Rn decay chain, contributes considerably to the ER background due to its beta-decay. Even if strong efforts have been made to reduce the ^{222}Rn level through careful material selection and the use of an online radon distillation column, achieving an improvement by a factor of 10 compared to XENON1T, it remains the largest contribution to the total rate in the ROI.
- **Krypton**: Traces of radioactive krypton-85 in the xenon target contribute to the intrinsic background. The ^{85}Kr undergoes beta decay, adding to the low-energy region. The concentration of krypton in the xenon target is minimized through dedicated distillation.
- **Xenon Isotopes**: Unstable xenon isotopes within the target, such as ^{136}Xe and ^{127}Xe, add to the background through their decay processes. The decay of ^{124}Xe through double electron capture, first observed in XENON1T [70], is now considered a new source of background specifically in the energy region of interest for WIMP searches. To estimate its contribution the measured half-life of 1.4×10^{22} y has been considered.
- **Solar Neutrinos**: the flux of neutrinos produced mainly through pp fusion and electron capture by ^{7}Be, interact with atomic electrons in the LXe target, leading to significant low-ER signals.

2.4.2 Nuclear recoil background

The SS NR background is the most dangerous for the WIMP search, having the same signature expected from the WIMP interaction. Here are the main sources of low energy NRs (Table 2.3 summarize all the estimated values):

Source	Rate $[(\mathrm{t\ y})^{-1}]$
Detector Radioactivity	25 ± 3
^{222}Rn	55 ± 6
^{85}Kr	13 ± 1
^{136}Xe	16 ± 2
^{124}Xe	4 ± 1
Solar Neutrinos	34 ± 1
Total	148 ± 7

Table 2.2: *Estimated ER background event rates in a 4 t fiducial volume. The energy ROI in which the event rates are integrated is (1, 13) keV [91]. The assumption for the ^{222}Rn activity concentration is of 1 μBq/kg and 0.1 ppt (mol/mol) for ^{nat}Kr/Xe. The background contributions from Xe isotopes are determined assuming the natural abundances of ^{136}Xe and ^{124}Xe.*

- **Radiogenic Neutrons** Radiogenic neutrons in the MeV range are produced through spontaneous fission (SF) and (α,n) reactions in detector materials. For heavy nuclei, the high Coulomb barrier suppresses the (α,n) interaction, so the neutron production is almost entirely due to SF. The highest (α,n) yields are from light materials, such as PTFE and the ceramic of the PMT stem [94]. For instance, the main contributions come from stainless steel cryostat, PMTs, PTFE components, and other materials close to the TPC, for the ^{238}U/^{226}Ra and the ^{232}Th/^{228}Th decay chains. The neutrons that interact in the active LXe, eventually exit from the TPC, and then they are captured in the NV volume; this results in a reduction of a factor ~ 8 in the estimated rate [3].
- **Cosmogenic Neutrons**: These neutrons, induced by cosmic muons interacting in the surrounding rock and concrete, are tagged using the active MV in the water tank. The rate of cosmogenic neutrons in the WIMP search region is already negligible but can be substantially suppressed thanks to the NV.
- **CEνNS**: Coherent elastic neutrino-nucleus scattering due to solar, atmospheric, and diffuse supernova neutrinos contribute to NR background [95]. Solar neutrinos affect the sensitivity to lighter WIMPs, while atmospheric and DSN neutrinos extend to higher energies. The expected rate of CEνNS is calculated, taking into account solar neutrinos (^{8}B+hep) [96] and the sum of atmospheric and DSN neutrinos.

---

[3] for a tagging efficiency of ~ 87%

Source	Rate $[(\mathrm{t\ y})^{-1}]$
Neutrons	$(4.1 \pm 2.1) \times 10^{-2}$
CEνNS (solar)	$(6.3 \pm 0.3) \times 10^{-3}$
CEνNS (Atm and DSN)	$(5.4 \pm 1.1) \times 10^{-2}$
Total	$(1.0 \pm 0.2) \times 10^{-1}$

Table 2.3: *Estimated NR background event rates in a 4 t fiducial volume. The energy ROI in which the event rates are integrated is (4, 50) keV. Table from [91].*

2.5 Future Prospects in LXe-based DM Research

The advancements in ultra-low background LXe detectors achieved with XENON1T, have opened up exciting avenues beyond DM research, such as probing rare processes like double electron capture decays and CEνNS. Current-generation experiments like XENONnT and LZ have significantly enhanced sensitivities across these research domains. However, they have yet to penetrate the "neutrino fog" limit in the spin-independent WIMP scattering parameter space (as shown in figure 1.7). This scenario paves the way for an even more ambitious project – the DARWIN observatory.

DARWIN [97], proposed as a 40-ton LXe active mass detector, aims to be the ultimate tool in DM detection, pushing the boundaries to the neutrino fog. Its design allows for a comprehensive search for neutrinoless double-beta decay, leveraging the natural xenon ^{136}Xe abundance. Additionally, DARWIN will refine measurements of the solar pp neutrino flux and extend its reach to other beyond-the-standard-model physics searches, making it a forerunner in the next decade of particle physics exploration.

Challenges are evident in such an ambitious project, primarily due to its size. It requires vast quantities of purified xenon, a suitably large underground lab, and novel materials and techniques for efficient operation. Further challenges lie in managing electrical fields within such large-scale TPCs, considering factors like electrode sagging as well as the material selection for detector construction, as they need to be structurally robust and extremely low in radioactive contaminants.

The use of traditional PMTs itself could significantly enhance background and raise concerns about their long-term stability in cryogenic conditions. Alternatives like Silicon Photomultipliers (SiPMs) offer advantages due to their lower radioactivity levels and compact size, making them suitable for large-scale applications as an alternative option.

For all these reasons and challenges, DARWIN would represent a quantum leap in the realm of DM detection and rare event searches, marking a transition to the next generation of LXe detectors.

3

The Neutron Veto of XENONnT

The Neutron Veto system is the central topic of my PhD research. This chapter offers a comprehensive discussion of the NV, highlighting its essential role in enhancing the sensitivity of the XENONnT experiment. Neutrons with energy in the range of a few MeV, originating from background radiation, pose a great risk to the sensitivity of the experiment, as they can mimic the NR signals expected from WIMPs. After mitigating the total ER background with the novel purification techniques discussed in the previous section, neutrons become an increasingly significant background component. There are mainly two sources of background neutrons: cosmogenic neutrons from high-energy muons, and radiogenic neutrons from materials through spontaneous fission or (α, n)-reactions. Cosmogenic neutrons are either induced by muons through the spallation of nuclei or as a product of an electromagnetic and hadronic shower. To reduce the cosmogenic neutron rate, the experiments of the XENON project have all been installed at the LNGS underground laboratory at a depth of 3600 m water equivalent. This reduces the muon flux by about 6 orders of magnitudes compared to the surface level; A conservative estimate of the muon-induced neutron flux in the LNGS cavern is $\sim 7.3 \times 10^{-10}$ n/(cm^{2}s) for E > 10 MeV [98], that is about 3 orders of magnitude lower than that of neutrons from concrete radioactivity, but their energy spectrum extends up to tens of GeV. The water tank itself serves on one hand as a passive shield against gamma radiation and neutrons emitted by the surrounding rock of the experimental cavern, but also contains two active veto systems. The outer part of the water tank acts as a water Cherenkov Muon Veto (MV); this system was already present in the previous XENON1T experiment. It is equipped with 84 Hamamatsu R5912-ASSY PMTs which are arranged in 5 rings mounted on the inner walls of the water tank. To improve the light collection efficiency the inner surfaces of the water tank are covered with a reflective foil (3M DF2000MA) which has a reflectivity larger than 99 % at wavelengths between 400 nm and 1000 nm. To suppress also the remaining neutron background due to detector materials, additional measures have been taken in XENONnT. As mentioned in the previous sections, all TPC materials were screened for their radio purity, and the overall material mass of the detector components was reduced. Furthermore, in XENONnT we installed the NV, a Gadolinium-loaded-Water Cherenkov Detector, designed to mitigate this challenge by effectively tagging neutrons through their capture on Gadolinium or Hydrogen, followed by gamma-ray emission, as deeply explained in section 3.1. **My PhD studies have been deeply focused on the NV, from its initial design stages, its installation, and operations during the science runs of the experiment**. This chapter delves into the design details of the NV (section 3.2) and its installation (section 3.3). The commissioning and the evaluation of initial performance before the science runs are presented in the next chapter. In the initial operation of the NV, only demineralized water was used and the NV already achieved an impressive neutron detection efficiency. In the second phase of the experiment, we dissolved the Gd salt through a dedicated plant presented in section 3.1.2.

3.1 Detection principle

The NV is a Gd-loaded water Cherenkov detector. It exploits the Cherenkov effect, a phenomenon discovered by Pavel A. Cherenkov [99], for which he received the Nobel Prize in 1958. This effect is widely used in high-energy physics, neutrino astronomy, and γ-ray astronomy. The Cherenkov effect arises when a charged particle travels through a dielectric and transparent medium at a speed greater than the phase velocity of light in that medium. This phenomenon has been exploited in various experiments like the Super-Kamiokande (SK) water Cherenkov detector [100]. The occurrence of Cherenkov radiation is due to the asymmetric polarization of the dielectric medium caused by the electromagnetic field of the fast-moving charged particle. When the particle velocity exceeds the phase velocity of light in the medium, it disrupts the symmetrical polarization, leading to the emission of coherent light waves that constructively interfere to form Cherenkov radiation, observable at a specific angle known as the Cherenkov angle θ_C; it can be expressed as:

$$\cos(\theta_C) = \frac{1}{\beta n} \tag{3.1}$$

where n is the refractive index of the medium. The minimum energy that a charged particle needs to emit radiation with this process in a specific medium is given by:

$$E_{th} = \frac{mc^2}{\sqrt{1 - \frac{1}{n^2}}}. \tag{3.2}$$

For neutron detection in the NV of XENONnT, this principle is crucial. Radiogenic neutrons may undergo single scatters within the TPC and escape it, losing kinetic energy predominantly through elastic collisions, mostly with hydrogen, before being captured. After the neutron capture, the nucleus is left in an excited state and it returns to the ground state emitting one or more γ-rays with energy in the range of a few MeV, which subsequently transfers its energy to electrons through Compton scattering. The recoil energy distribution of the electrons presents a peak at the maximal available kinetic energy which is given by [101]:

$$E_{max} = E_\gamma \left(\frac{2\gamma}{1 + 2\gamma} \right) \tag{3.3}$$

where γ is defined as $E_\gamma / m_e c^2$. Such peaks are known as *Compton edges*. As shown in figure 3.1, the electrons have still a ~ MeV energy, that is above the Cherenkov threshold (which is E_e^{th}(water) $\simeq$ 0.25 MeV).

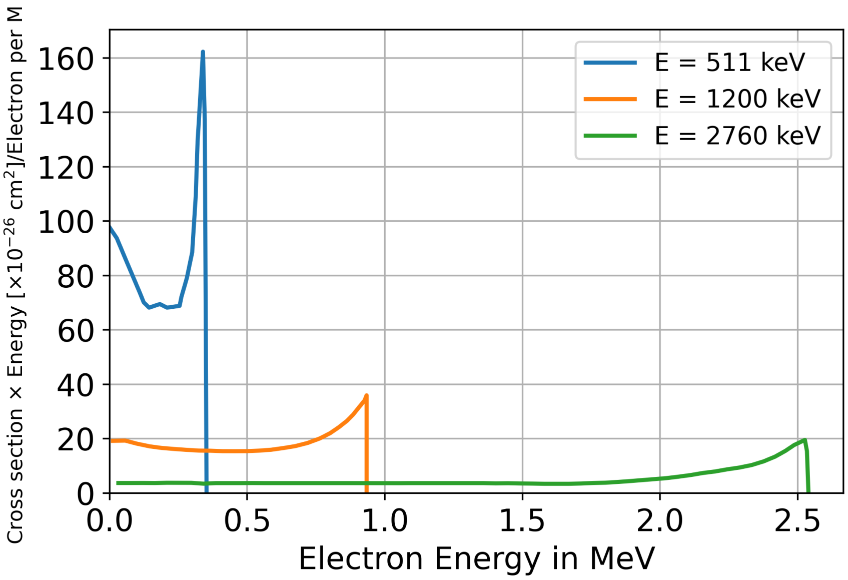

Figure 3.1: *Kinetic energy distribution of the recoil electrons after the Compton scattering by gamma rays of different energies. For MeV energy photons, the electrons have ~MeV kinetic energies. Plot re-adapted from [102].*

These high-energy electrons then emit Cherenkov light, detectable by the NV photomultipliers. The NV is delimited by reflective panels, where the Cherenkov photons undergo multiple reflections, effectively increasing the probability of their detection in the PMTs. In XENONnT, the NV was initially operated using demineralized water, leveraging the Cherenkov effect for neutron tagging through a delayed coincidence between the prompt S1 signal in the TPC and the delayed neutron capture signal in the NV. The emitted 2.22 MeV gamma-ray from neutron capture has a mean free path of about 30 cm in water, much larger than the mean free path of neutrons of ~10 cm; as reported by the water Cherenkov experiments of SK [100] and Sudbury Neutrino Observatory (SNO) [103] the neutron capture time is ~200 µs (with values of $(203.7 \pm 2.8)\ \mu s$ [104] and $202.35^{+0.87}_{-0.76}\ \mu s$ [103] respectively). To determine the number of photons produced, we use the Frank and Tamm differential emission formula:

$$\frac{d^2E}{d\lambda dx} = -\frac{\pi z^2 e^2}{\epsilon_0}\frac{1}{\lambda^3}\left(1-\frac{1}{\beta n(2\pi c/\lambda})^2\right) \tag{3.4}$$

thus, the spectrum of the number of photons emitted per unit path is given by

$$\frac{d^2N}{d\lambda dx} = \frac{2\pi z^2 \alpha}{\lambda^2}\left(1-\frac{1}{\beta^2 n\left(\lambda\right)^2}\right), \tag{3.5}$$

where z is the charge of the particle and α the fine structure constant. Considering a wavelength range of [250 nm, 700 nm] for a 2 MeV electron traveling approximately 1 cm in water with $n = 1.33$, around 500 photons are emitted. However, this estimate is based on the assumption that the entire 2.2 MeV energy of the gamma-ray is transferred to a single electron, leading to a faint signal. Furthermore in equation 3.5 there is a $\propto \lambda^{-2}$ which means that most of the radiation is emitted in the ultra-violet and blue regime. All these considerations have been taken into account when designing the NV, as presented in Section 3.2; for example, the NV PMTs have to be chosen to match as much as possible their Quantum Efficiency (QE) spectra and the Cherenkov spectrum.

3.1.1 Impact of Gadolinium

The addition of gadolinium to the water will further enhance the NV performance. It is dissolved in the form of a salt: Gd-sulfate octa-hydrate, specifically $Gd_2(SO_4)_3 \cdot 8\,H_2O$. Gadolinium ($^{A}_{64}$Gd) is a rare element on Earth. Its natural composition ^{nat}Gd consists of 7 isotopes. Their abundance ratio and the corresponding neutron capture cross sections are shown in Table 3.1. The Gd, in particular the ^{155}Gd and the ^{157}Gd isotopes, has a resonance state in the thermal energy region in the neutron capture reaction (Fig. 3.2). The capture process is resolved in the excitation of the Gd, which returns to the ground state emitting on average 3-4 γs [105]. The process for the ^{155}Gd reads:

$$n +^{155}\text{Gd} \rightarrow^{156}\text{Gd}^* \rightarrow^{156}\text{Gd} + \gamma \tag{3.6}$$

Isotope	Abundance (%)	σ [b]
^{152}Gd	0.2	735
^{154}Gd	2.18	85
^{155}Gd	14.8	60.9×10^3
^{156}Gd	20.47	1.8
^{157}Gd	15.65	25.4×10^4
^{158}Gd	24.84	2.2
^{160}Gd	21.86	1.4

Table 3.1: *Thermal neutron capture cross sections of the various Gd isotopes, with their natural abundance. The two isotopes which are exploited for their high (n, γ) cross section are the ^{155}Gd and ^{157}Gd. Table from [105].*

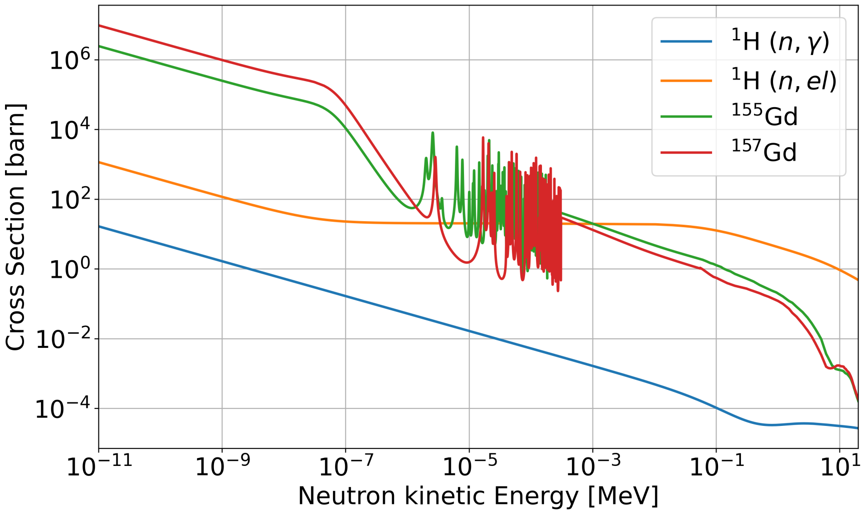

Figure 3.2: *Cross section of the interaction between neutrons and ^{1}H / ^{155}Gd / ^{157}Gd as a function of the neutron kinetic energy (MeV). The neutron-H interaction can occur as elastic scattering (orange line) or as (n, γ) (blue line). On the other hand the dominant process with the Gd isotopes is the (n, γ) (green and red lines). The cross-section for the Gd decreases with the energy but for values $\mathcal{O}$(10 eV) presents some resonant states. Data from IAEA ENDF Database [106].*

Thus the γ-ray energy can be calculated via mass difference:

$$E_\gamma = M(^{155}\text{Gd}) + M_n - M(^{156}\text{Gd}) = 8.54 \text{ MeV} \tag{3.7}$$

where M_n is the neutron mass, while $M(^{155}\text{Gd})$ and $M(^{156}\text{Gd})$ are the mass of ^{155}Gd and ^{156}Gd respectively. Similarly, for the process involving the ^{157}Gd isotope, the γ energy is 7.94 MeV. Since the 90s, Gd has found interesting applications in astroparticle physics experiments, in particular in neutrino detection through the inverse beta decay process:

$$\bar{\nu}_e + p \longrightarrow n + e^+ \tag{3.8}$$

and the neutron capture on protons:

$$n + p \rightarrow d + \gamma \text{ (2.2 MeV)} \tag{3.9}$$

and on Gadolinium. Indeed, it has become a common technique to dope liquid organic scintillator with a mass fraction of 0.1-0.2% of Gadolinium as, e.g., in the Double Chooz [107] and Daya Bay [108] experiments. More recently, it has been proposed to add Gd directly into water Cherenkov detectors. The Super-Kamiokande experiment has been doped with Gd in 2020 [109], to enhance its sensitivity to inverse beta decay of neutrinos, to search relic supernovae neutrinos. The advantages of using capture on Gadolinium instead of on Hydrogen are mostly two. First, the greater Q-value of the process guarantees a greater tagging efficiency. Furthermore, the neutron capture time in Gd-loaded water is reduced from $\sim 200\ \mu$s to $\sim 30\ \mu$s [1], allowing to use a shorter coincidence time window in the NV selection cut and in turn, losing a smaller fraction of livetime.

The XENONnT experiment is the first Dark Matter experiment employing the Gd technology to reduce the neutron background in a Gd-water Cherenkov NV. Gadolinium is added to water by dissolving Gd ultrapure salts like $GdCl_3$, $Gd(NO_3)_3$ and $Gd_2(SO_4)_3$. Since the chlorine in $GdCl_3$ causes unwanted corrosion and the nitrate in the $Gd(NO_3)_3$ tends to absorb part of the Cherenkov light spectrum, the Gd-sulphate $Gd_2(SO_4)_3$ results to be the best candidate when it is octahydrate ($Gd_2(SO_4)_3 \cdot 8\,H_2O$), to enhance its solubility. The final goal concentration of $Gd_2(SO_4)_3$ is 0.48% (500 ppm) which corresponds to about 0.2% (200 ppm) concentration in mass of Gd. Figure 3.3 shows the fraction of neutron capture on Gd as a function of the concentration of gadolinium sulphate. With a 0.2% concentration, the $\sim$ 90% of the neutrons are captured by the Gd, while the remaining part relies on the capture in water. The idea of adding Gd to the NV required a careful selection of materials because of the tendency of Gd, once added to water, to cause corrosion and accelerate the aging of materials. Consequently, Gd-soak tests have been conducted, to assess potential material deterioration and select the most suitable ones. These tests involve immersing detector components in Gd-water and studying the transparency of the corresponding solutions. Materials like stainless steel (AISI304), PTFE, and polyethylene are compatible with Gd-water solution, so they have been extensively used in the NV design. Furthermore, with Gd-water the XENONnT experiment requires a more advanced purification system than the simple one used with pure water. An external system is needed that handles both the purification of water enriched with Gd and the storage and recovery of gadolinium.

---

[1] For a Gd mass concentration of 0.2%.

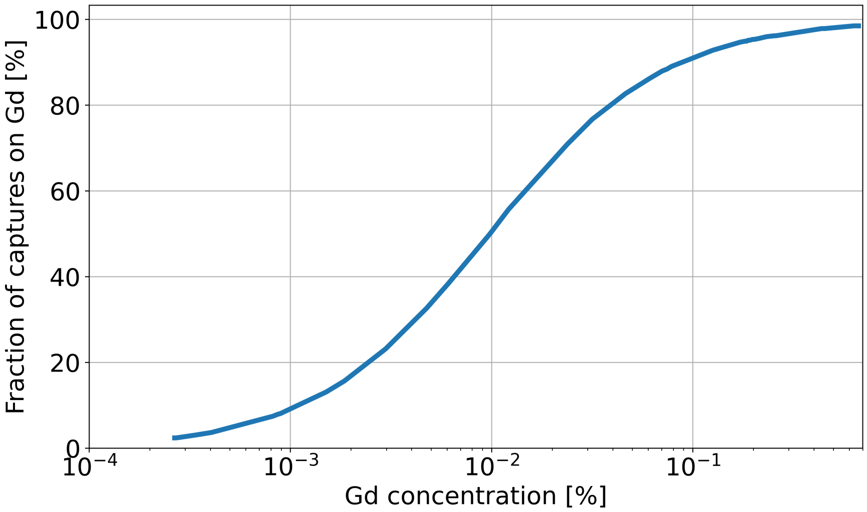

Figure 3.3: *Fraction of neutron captures on Gd as a function of the Gd concentration. With a* $\sim 0.1\%$ *in mass of Gd, the* $\sim 90\%$ *of neutrons are captured by the Gd, while* 10% *are captured by protons as shown in Eq.*(3.9)*. Plot re-adapted from [110].*

3.1.2 Gd-Water Purification System (GdWPS)

As highlighted in section 3.1, the Cherenkov emission process inherently produces a relatively small number of photons. This limitation places a significant emphasis on two aspects of the NV efficiency: the transparency of water to UV and optical photons, and the reflectivity of the detector walls. The latter is effectively addressed by employing highly reflective ePFTE panels. However, maintaining water transparency, equally crucial, requires a continuous purification process. Until October 2023 the NV has been operated with demineralized water. Thus, the Water Loop Plant (WLP), inherited from XENON1T, has been used. The WLP's primary role is to remove water-soluble ions and bacteria, which can significantly diminish water transparency, thus impacting the detector's optical performance. The system, though relatively simple, is equipped with a de-ionizing filter and sensors for measuring pressure, temperature, flow, and resistivity - the latter being a crucial indicator of water purity (with demineralized water at 25°C having a nominal resistivity of 18.18 MΩcm). The integration of Gd into the water presents several challenges: the WLP, while effective for purifying water, is unsuitable for Gd-Water, as it would remove the precious Gd ions. To overcome this problem, the **Gadolinium-Water Purification System (GdWPS)** has been developed. The GdWPS is designed to achieve three primary goals:

- Firstly, it ensures the successful integration and uniform dissolution of Gd sulfate into the water of the NV and, eventually, the MV.

- Secondly, the GdWPS is responsible for attaining and consistently maintaining the desired Gd sulfate concentration. This involves not only reaching the target concentration but also implementing continuous monitoring to ensure its stability over time.
- The third and final goal is to preserve the optical properties of the NV. The GdWPS purifies the solution, removing impurities that could adversely affect water transparency, which is vital for maintaining the system detection efficiency.

The design and operational strategy of the GdWPS were inherited from the EGADS (Evaluating Gadolinium's Action on Detector Systems) facility [111, 112], located in the Kamioka mine, as shown in figure 3.4). Its primary purpose was to establish that incorporating Gd into the SK detector would be both safe and effective. This successful model laid the groundwork for the development and implementation of the XENONnT GdWPS. [2]

Operating principles In the GdWPS, the process begins with the dissolution of Gadolinium into water, creating a solution enriched with Gd. This solution is then meticulously managed within the system. A key step involves the separation of the Gd-enriched solution from the Gd-depleted part. This separation is achieved using specialized filters designed for this purpose. Following this, an ion purification system comes into play, specifically targeting the Gd-depleted portion of the solution. This system is crucial as it removes impurities without causing significant loss of Gadolinium, a vital aspect of maintaining the efficacy and efficiency of the process.

Once the impurities are removed from the Gd-depleted solution, the next phase involves recombining it with the Gd-enriched part. This reintegration is carefully conducted to ensure uniformity in the solution. The final purification step employs filtration elements that are specifically chosen for their inability to absorb Gd ions. This careful selection is crucial as it allows the solution to be cleansed of impurities while simultaneously preserving the concentration of Gd-Sulfate. A picture of the GdWPS, is shown in figure 3.5.

The elements used by the GdWPS can be broadly classified into four key subgroups:

- **Circulation Elements** These components are the driving force behind the GdWPS, as they make the plant running and allow for adjusting

---

[2] **At the beginning of the third year of my PhD I spent three months onsite at Kamioka, to learn and get used to the techniques of Gd-water purification, and water transparency measurements.**

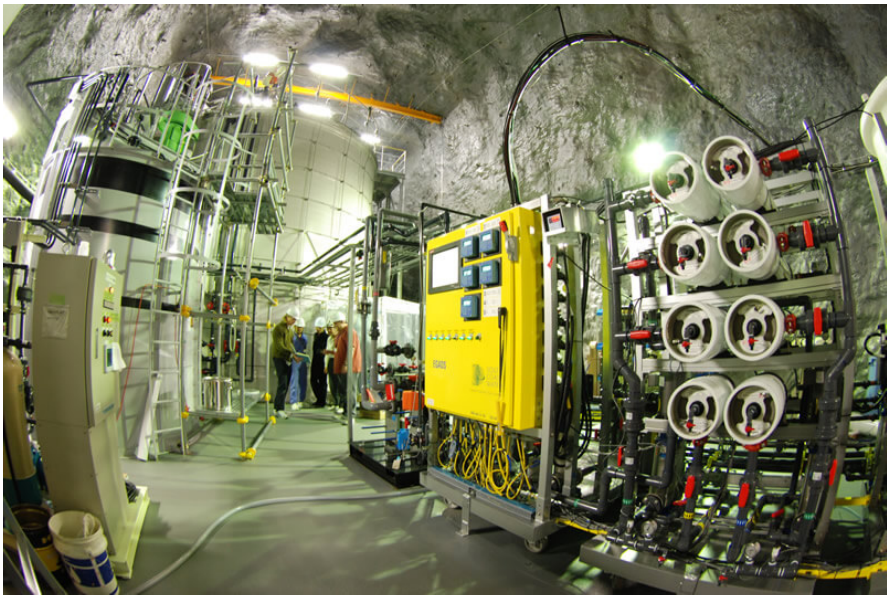

Figure 3.4: *Picture of the EGADS facility, in the Kamioka mine. Key features of EGADS include a 200-ton water Cherenkov detector equipped with 20-inch PMTs (of the SK model), a pre-treatment system with a 15-ton tank for dissolving and mixing* $Gd_2(SO_4)_3$ *into the water, a main Gd-water circulation system, and the UDEAL (**U**nderground **D**evice **E**valuating **A**ttenuation **L**ength) device for automatic measurement of water transparency. A primary objective of EGADS is to assess the transparency of ultra-pure water versus water doped with gadolinium sulfate. The monitor is performed with the dedicated UDEAL device. For the XENONnT NV, water transparency (coupled with the reflectivity of the panels) is monitored internally within the detector itself using a dedicated reflectivity monitor (section 3.4)*

pressures, temperatures, and flow rates; five pumps work in series to circulate water from the 700 m^3 XENON tank through various filtration and sensor-equipped branches. These branches converge at the mixing tank, a 2t stainless-steel container where Gd sulfate dissolution occurs. The water then returns to the XENON tank, maintaining a continuous purification loop at a target flow rate of about 3t per hour. A notable feature of the system is its ’bypass mode’, used during the commissioning phase to test the GdWPS without affecting the detector water quality. This mode connects the output of the last pump back to the first, creating an internal loop. The system pumps are complemented by manual and proportional solenoid valves, the latter being adjustable via the Slow Control system. These valves regulate flow and pressure, isolate system components for maintenance, and control pump intensity through a bypass line with a solenoid valve. Temperature control is managed by a dedicated chiller, placed between the first two pumps. The chiller aims to maintain the water temperature at around 12°C in the mixing tank to simplify the Gd

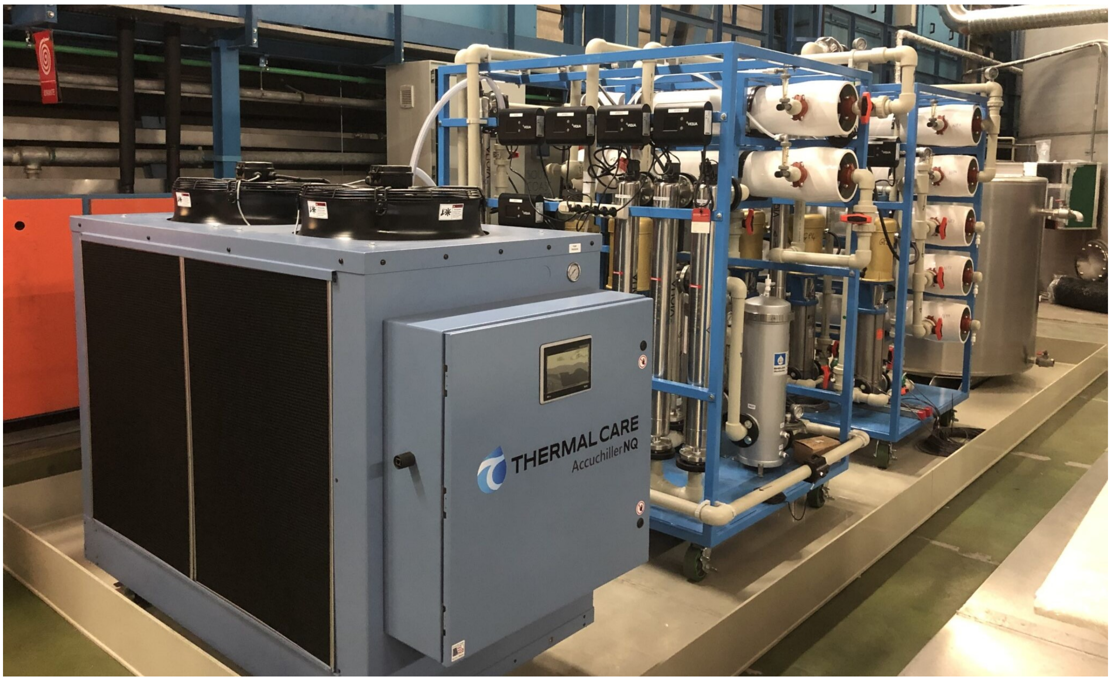

Figure 3.5: *Picture of the Gadolinium-water purification system, placed close to the 700 t XENON water tank.*

dissolution.

- **Gadolinium insertion system**: It is specifically designed for the introduction and dissolution of Gd-Sulfate into the GdWPS. This operation begins at the mixing tank, where the salt is thoroughly mixed and dissolved in water before being circulated throughout the plant. The salt is initially loaded into a specialized hopper at the external laboratory, sealed above ground and then transported to the underground laboratory. The next phase involves connecting the hopper to a pneumatic transfer system located above the mixing tank, connected via a flexible plastic pipe. The final step in the Gd salt insertion is the activation of a stirrer inside the mixing tank; it ensures that the sulfate is thoroughly mixed and dissolved in the water, essential for its effective distribution, and setting the stage for the subsequent steps of water purification within the GdWPS.
- **Purification elements** This complex process involves several stages, each targeting different types of impurities. Particulate matter is filtered out using static *particle filters*, effective against impurities larger than 20 micrometers. For smaller particles, *ultrafilters* play a crucial role. Unlike particle filters, Ultra-filters have a dual-output system, separating impurities and directing them to a reject line, while purified water passes through the product line. These Ultra-filters allow Gd ions to pass through the membrane and proceed to the product lines. The GdWPS employs two

ultrafilters, strategically placed at the input and output lines connecting to the XENON tank. Five *nanofilters* have the critical function of separating Gd-rich and Gd-depleted solutions. They operate similarly to ultrafilters but are designed to send all double-valence ions, including trivalent Gd ions, to the reject line. Of the five nanofiltration membranes, three are used in the first stage and two in the second stage, to progressively reduce Gd concentration. The efficiency of these nanofilters is measured by their ability to remove Gd ions from the main branch. In addition to these filtration systems, the GdWPS uses two types of resin contained in polymer beads within plastic tanks. The *De-Ionizing resin* (DI) is crucial for removing ionic impurities and is placed in the product line of the second nanofiltration stage, where Gd concentration is minimal. This placement is key to minimizing Gadolinium loss. The *Organic Removal Tank* (ORT) resin, on the other hand, does not capture Gd ions and is used to remove residual organic compounds, thereby enhancing water transparency. These resin tanks, connected via flexible pipes, can be easily bypassed for replacement or testing. To prevent the growth of organic impurities such as bacteria, the system employs ultraviolet irradiation through lamps. A total of six *UV lamps* are used in different parts of the plant, with some specifically placed before the DI and ORT resins for total Organic Carbon removal. These lamps inhibit organism growth with the cost of heating the system, thus the required use of a chiller to maintain optimal temperatures.

- **Sensors**: The GdWPS employs a range of sensors to monitor and control various aspects of the system. *Manometers*, both analog and digital, are installed at strategic points, including before and after each pump and around particle filters, to monitor the pressures within the plant. These pressure readings are crucial for indicating the proper functioning of the system and identifying when filters need replacement due to saturation. *Flow rate* meters are positioned in different branches of the GdWPS and provide essential data, contributing to the overall monitoring of the plant performance. These meters are particularly important for calculating the separation efficiency of the system, as they weigh ion concentrations. *Density meters*, are used to estimate the Gadolinium concentration within the system, as the density of the solution increases with higher Gd concentration. These meters are strategically placed in the main branch, both in the input line from the XENONnT tank and in the return line from the mixing tank, as well as in the reject line of the first nanofiltration stage where the highest Gd concentration is expected. Their functioning is based on the Coriolis effect, where fluid flow through a vibrating tube causes changes in vibration that can be detected and used to measure both flow rate and density. *Conductivity meters*, apply an alternating voltage to measure the resulting electric current, providing insights into the water purity levels and ion concentrations. These meters are placed in various parts of the system, including the reject and product lines of the nanofilters and after the DI resin tank. The conductivity values they provide are essential for understanding the ion concentration in different parts of the plant, with the highest conductivity expected in the first reject branch and the lowest after the DI resin, which removes most ions. *Temperature sensors* are also a key part of the GdWPS, integrated into the density and conductivity sensors. They are crucial for maintaining the optimal temperature for Gadolinium dissolution, **which is favored at lower temperatures**. Additional thermometers are placed at the top and bottom of the mixing tank, the site of Gd dissolution, to closely monitor temperature variations.

All the components of the system are schematized in the Piping and Instrumentation Diagram (P&ID), reported in figure 3.6.

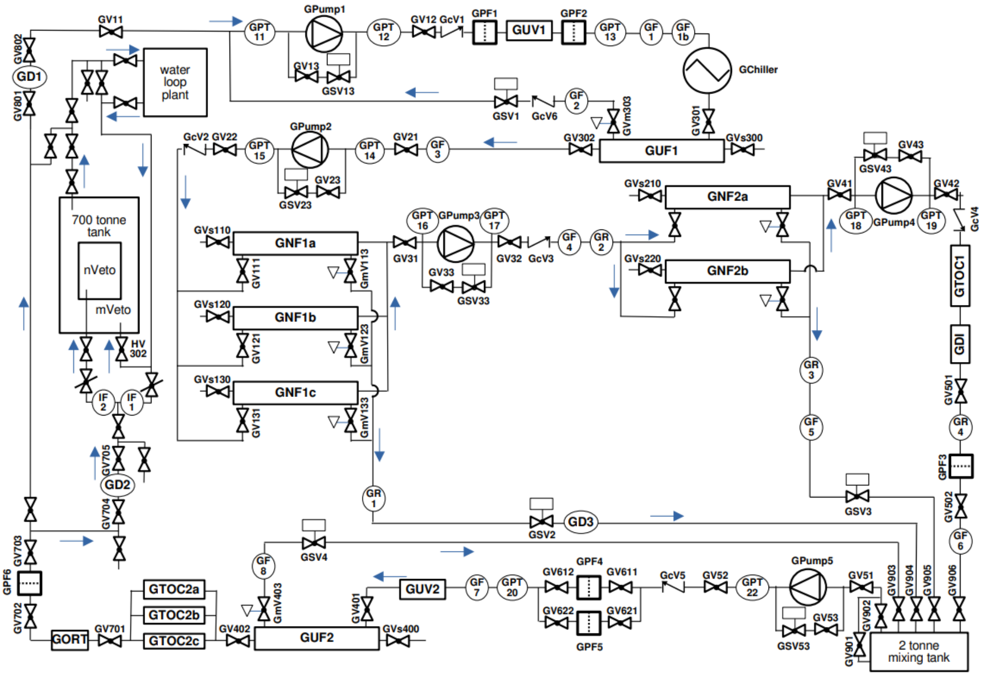
GV11
GPump1
GPT 11
GPT 12
GV12
GcV1
GPF1
GUV1
GPF2
GPT 13
GF 1
GF 1b
GChiller
GV802
GD1
GV801
water loop plant
GV13
GSV13
GSV1
GcV6
GF 2
GVm303
GV301
GPump2
GcV2
GV22
GPT 15
GPT 14
GV21
GF 3
GV302
GUF1
GVs300
GV23
GSV23
GV43
GSV43
GVs210
GNF2a
GV41
GV42
GPT 18
GPump4
GPT 19
GcV4
700 tonne tank
nVeto
mVeto
GVs110
GNF1a
GV111
GmV113
GPT 16
GPump3
GPT 17
GV31
GV32
GcV3
GF 4
GR 2
GV33
GSV33
GVs220
GNF2b
GTOC1
GVs120
GNF1b
GV121
GmV123
GDI
HV 302
GVs130
GNF1c
GV131
GmV133
IF 2
IF 1
GR 3
GV501
GR 4
GF 5
GV705
GD2
GPF3
GR 1
GSV3
GV502
GV704
GSV2
GD3
GF 6
GV703
GSV4
GF 8
GPF6
GPF4
GPump5
GTOC2a
GmV403
GUV2
GF 7
GPT 20
GV612
GV611
GcV5
GV52
GPT 22
GV51
GV903
GV904
GV905
GV906
GV702
GTOC2b
GV401
GV622
GV621
GV53
GV902
GORT
GV701
GTOC2c
GV402
GUF2
GVs400
GPF5
GSV53
GV901
2 tonne mixing tank

Figure 3.6: *Piping and Instrumentation Diagram (P&ID) of the GdWPS. All the relevant circulation elements (such as pumps and valves), filters, and sensors are reported.*

Current Status & Performances The commissioning phase of the GdWPS has been completed, ensuring the system readiness for the introduction of Gadolinium sulfate. This phase, primarily conducted with pure water, allowed for extensive testing of all the GdWPS components. Even without Gadolinium, the system demonstrated its efficiency in purifying water from various impurities. From May 2022 to the end of the year, the GdWPS operated alternately in bypass mode and connected to the XENON tank. This period was marked by a series of tests and modifications in preparation for the first Gadolinium insertion, which occurred in January 2023. Concurrently, the XENON tank underwent purification using the WLP. The first connection of the GdWPS to the XENON tank was made in July 2022. Following this, the optical properties of the NV were monitored using dedicated setups. Throughout the latter half of 2022, the GdWPS alternated between being connected to the water tank and operating in bypass mode, depending on various operational needs. Whenever the system was in bypass mode, the XENON tank continued to be purified using the WLP to maintain optimal optical performance. By the end of 2022, the system was fully primed for the inaugural insertion of Gadolinium salt. The plant operated in bypass mode, and the salt was added incrementally up to 15 kg. Several measurements were conducted to monitor the system response to the insertion. With 15 kg of salt in the system, the concentration reached the nominal value of 0.5%. The estimation of the separation efficiency of the GdWPS was approached using three distinct methods, each contributing to a comprehensive understanding of the system's effectiveness. The first method involved indirect measurement of ion concentrations through conductivity readings. This approach yielded a separation efficiency $\epsilon_{tot} = 99.6\%$. The second method employed a more direct approach, utilizing Inductively Coupled Plasma-Mass Spectrometry (ICP-MS) for precise measurement of ion concentrations. This technique resulted in a slightly higher separation efficiency of 99.85%. Additionally, the rate of Gadolinium salt loss was assessed following the re-connection of the DI resin to the system. This loss rate was estimated to be approximately 600 grams per day, corresponding to a separation efficiency of 99.68%. Furthermore, transparency measurements conducted through a dedicated setup, on samples of water from the plant, revealed a notable improvement in transparency compared to the solution prepared in the LNGS Chemistry Laboratory. The GdWPS managed to enhance the water transparency to levels nearly equivalent to that of demineralized water, with a difference in transmittance of less than 0.5%. Having demonstrated the efficiency of the system, the GdWPS is currently engaged in purifying the water of the Water Tank and stands ready to introduce high-concentration Gadolinium salt in preparation for the upcoming Science Run of the experiment.

3.2 Detector design

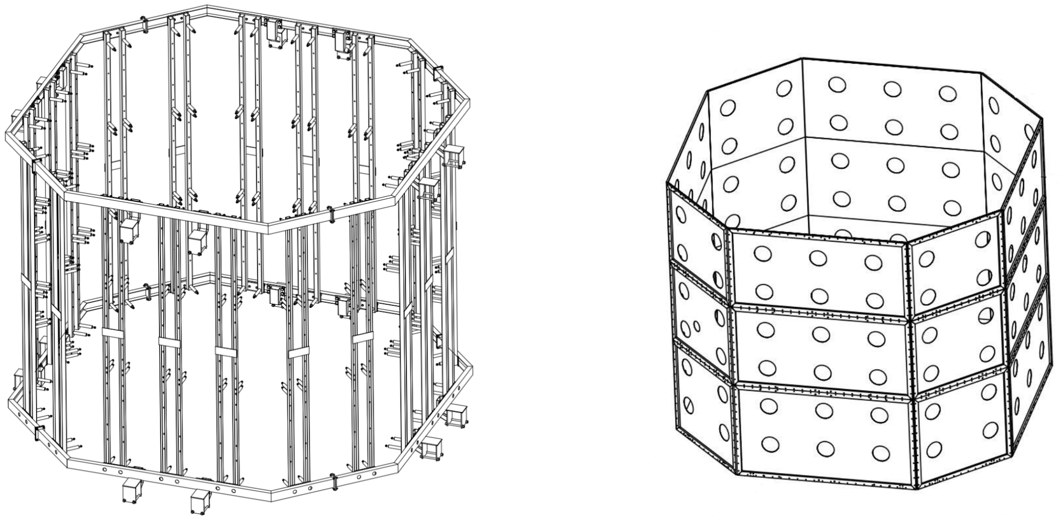
(a) **(b)**

Figure 3.7: *(a) Technical drawing of the NV support structure, showcasing also design of the supports for the reflective panels. (b) Technical drawing of the ePTFE panel assembly constituting the reflective surface of the NV.*

The NV is installed within a 700-tonne Water Tank that surrounds the cryostat containing the TPC. It forms a 33 cubic meter volume, enclosed by high-reflectivity panels made of expanded polytetrafluoroethylene (ePTFE). The NV shape is an octagonal prism, standing 3.16 meters in height. The octagon sides have two different widths, with wider ones measuring 2.02 m and narrower ones 1.22 m. The design decisions were driven by various key factors: the need to optimize neutron detection efficiency, the reduction of background induced by NV materials, as indicated by MC simulations, and the necessity to address practical constraints such as resolving interference from calibration system components and cryostat pipes. Additionally, the NV system had to be adapted to the pre-existing steel support structure of the cryostat. The stainless steel structure (Fig. 3.7a) is divided into four quarters, each containing the long side of the octagon and halves of the adjacent short sides. The upper part of the steel structure consists of two beams supporting a ring around the cryostat central pipe, to which the NV upper reflectors are anchored (they do not appear in the drawing of figure 3.7a). The lateral walls (Fig. 3.7b) are made up of 24 rectangular ePTFE panels, three for each side of the prism. Expanded-PTFE, chosen for its superior reflectivity, forms the NV reflective panels, which define the NV volume around the cryostat. These 1.5 mm thick panels outperform other materials in reflectivity, exceeding 99% for wavelengths over 300 nm. The ePTFE foils, held in place with plastic frames, are mounted on thin stainless steel bars anchored to the cryostat support structure. The NV floor (Fig. 3.8a) comprises several trapezoidal panels and two "free" reflective sheets, positioned 26 centimeters below the cryostat bottom dome. Its ceiling (Fig. 3.8b), inclined at 5 degrees, is constructed of five trapezoidal panels and five "free" sheets, anchored around the main pipe atop the cryostat dome. These "free" reflective sheet systems are necessary where there is interference with NV surfaces, particularly due to calibration elements and cryostat pipes already present during installation. In these cases, the reflective sheet will have a hole corresponding to such elements and a hinge to allow the reflective sheet sector to be closed. The ceiling features three additional openings to facilitate the insertion of a neutron generator and other equipment: these holes are the only openings where photons can travel between the NV and the outer MV volume. To enhance the system efficiency, the cryostat surface is also fully covered with the same ePTFE foils. The photon detection in the NV happens with 120 high quantum efficiency (QE), low-radioactivity 8" PMTs from Hamamatsu (R5912-100-10 WA-D30-SEL-Assy), designed for operation immersed in water. These PMTs are organized into 20 columns, each holding six PMTs spaced about 45 centimeters apart. The wide and narrow panels accommodate three and two PMT columns, respectively. The PMT bodies are mounted outside the NV, with only their glass windows extending into the NV volume; again, this solution aims at reducing the background from radioactivity. Figure 3.9 shows a CAD rendering of the NV, where all the various components can be identified. Additionally, the rendering

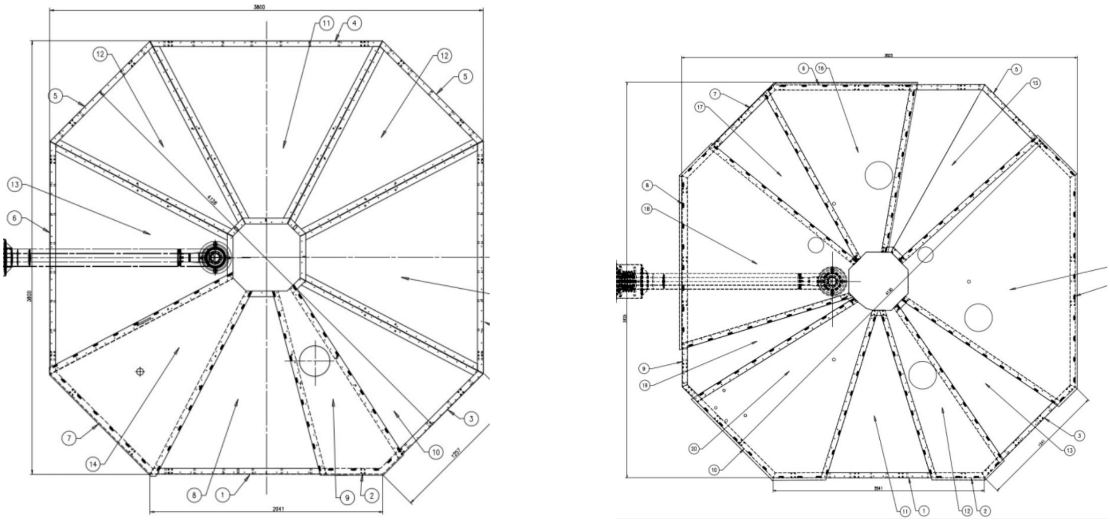

(a) **(b)**

Figure 3.8: *(a) Technical drawing of the ePTFE panels composing the NV floor. (b) Technical drawing of the ePTFE panels composing the NV ceiling.*

includes the detector calibration systems, described in Section 2.3.

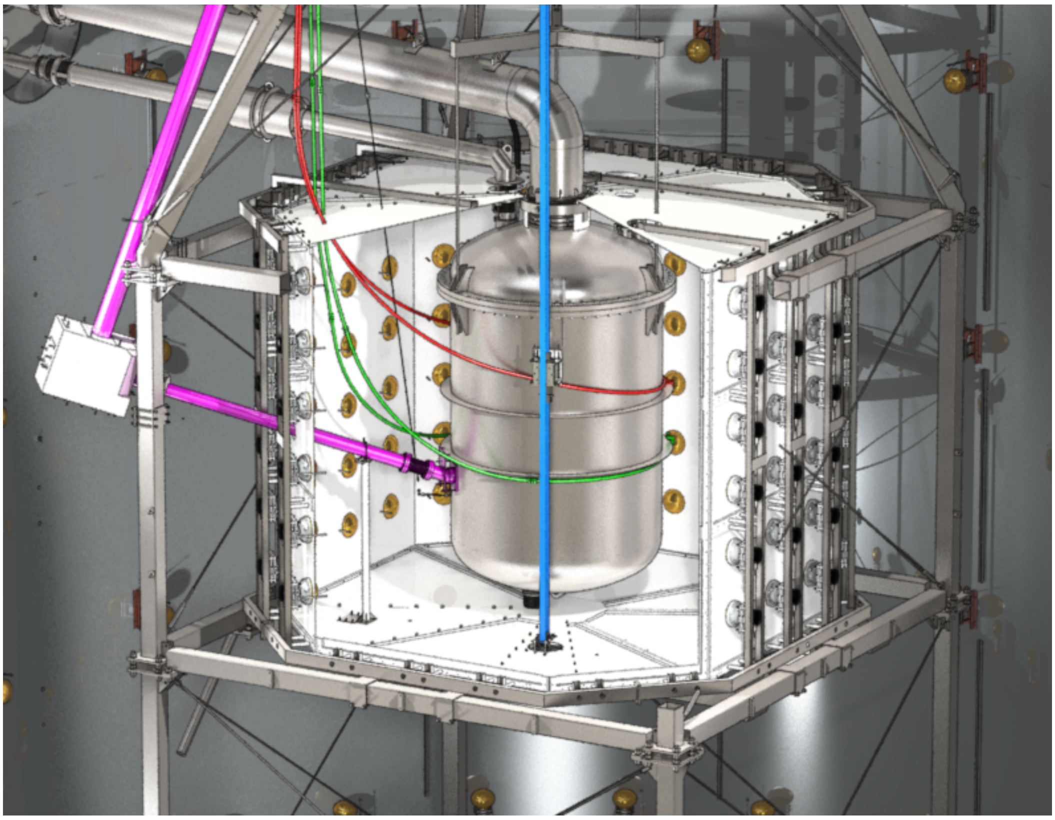

Figure 3.9: *CAD rendering of the NV installed in the center of the 700 t water tank: support structure (grey), reflector panels (white), 120 PMTs (yellow). The main components of the calibration system entering the NV are also shown: neutron generator pipe (purple), I-belt (blue), U-tubes (red and green). The reflector mounted to the cryostat has been deliberately removed in this CAD drawing.*

3.3 Installation

The installation of the NV began in July 2020, following the completion of the TPC work and its insertion in the cryostat. The first step in the NV installation involved covering the cryostat, which had been appropriately passivated and cleaned, with ePTFE foils, as shown in fig. 3.10a. They were precisely shaped to fit the entire surface of the cryostat. The ePTFE parts were fixed with studs previously welded onto the cryostat. Around the flange area, where the reflective sheet risked displacement, 12 polyethylene clamps were planned to exert radial pressure towards the upper dome. During the covering of the upper and lower domes, circular holes were made in the ePTFE segments to allow for the passage of the cryostat pipes. Additionally, the reflective sheet was further anchored around the two lateral rings of the cryostat using stainless steel straps. The cleaning procedure for the materials used in the installation was meticulous. The ePTFE rolls were processed in a clean environment in Bologna. After covering the cryostat, these reflective sheets were further manually cleaned[3] while the hardware, straps, and closures were cleaned in an ultrasonic bath.

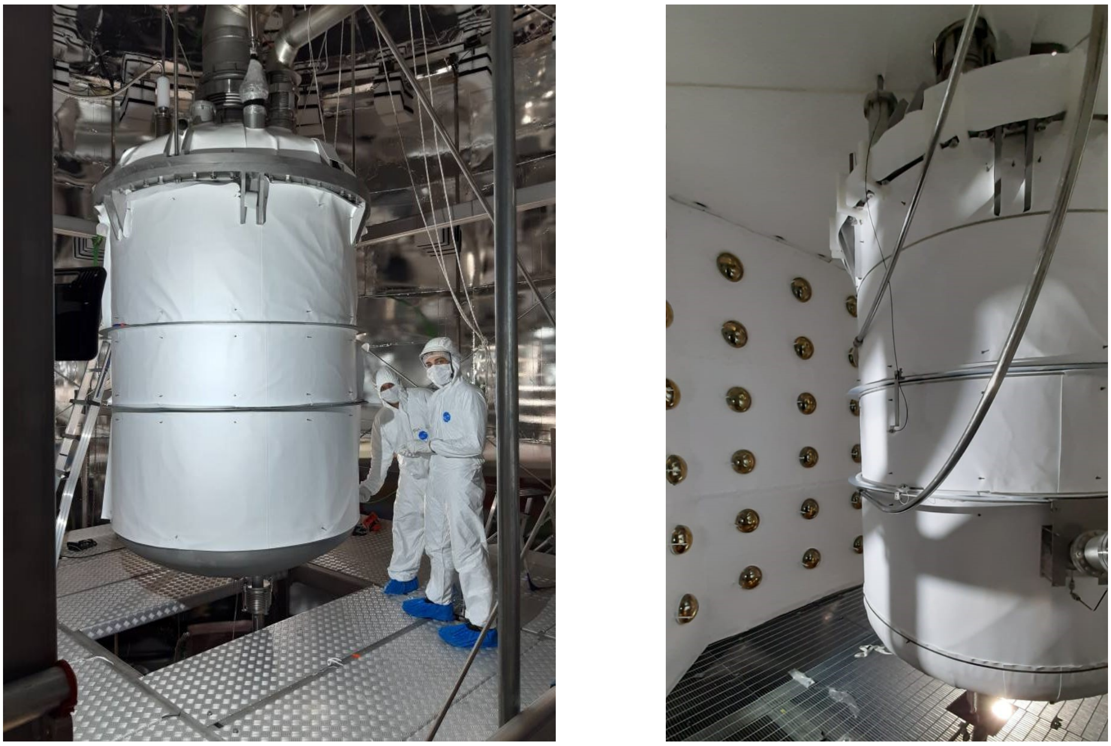

(a) (b)

Figure 3.10: *(a) Picture taken during the wrapping of the cryostat with the ePTFE foils. (b) Picture from inside the NV structure, during the installation of the NV lateral panels*

Once the cryostat was fully wrapped in ePTFE, the actual installation of the NV started. The initial step involved dismantling the existing floor around the cryostat and constructing a new octagonal floor, divided into slabs, specifically designed for the NV installation. The next major phase was the assembly of the stainless steel structure. This process began with the installation of the entire lower ring of the structure. Subsequently, the upper ring was installed, along with the columns. This procedure was repeated for the other three-quarters of the structure. Once the columns were in place, the transverse bars were installed, and the ring around the cryostat was mounted. The installation of the upper reflectors followed a specific sequence: first, the five trapezoidal segments were installed, and then the necessary polyethylene bars for anchoring the "floating" reflectors were put in place. Finally, these reflectors were anchored

---

[3] The cleaning of the foil was made just with demi-water, as we experienced, by using ethanol or isopropylic alcohol, a slow degradation of the sheets.

using special "tourniquets" mounted on the polyethylene bars and adjacent frames. An important step involved covering the internal pipes within the NV, particularly the calibration pipe for the neutron generator, with ePTFE. The assembly of the NV lateral walls started with the installation of one of the upper sectors, including mounting 4 (6) PMTs for the short (long) side of the octagon and securing the reflective panel to the support structure. This procedure was replicated for the middle and lower sectors. After each side assembly, the PMTs were covered with a light-tight cloth. Subsequently, the 30 meters of PMT cables and optical fibers were unrolled, guided through the support structure rails, and then along the cryostat structure to the Water Tank roof. Finally, once all the lateral surfaces were in place (Fig. 3.10b), the octagonal working floor was dismantled to allow for the installation of the lower reflectors. The view of the NV just before the installation of the floor is the one shown in the figure 3.11. This process involved installing six trapezoidal segments and the necessary polyethylene bars for anchoring the two "floating" reflectors, which were then

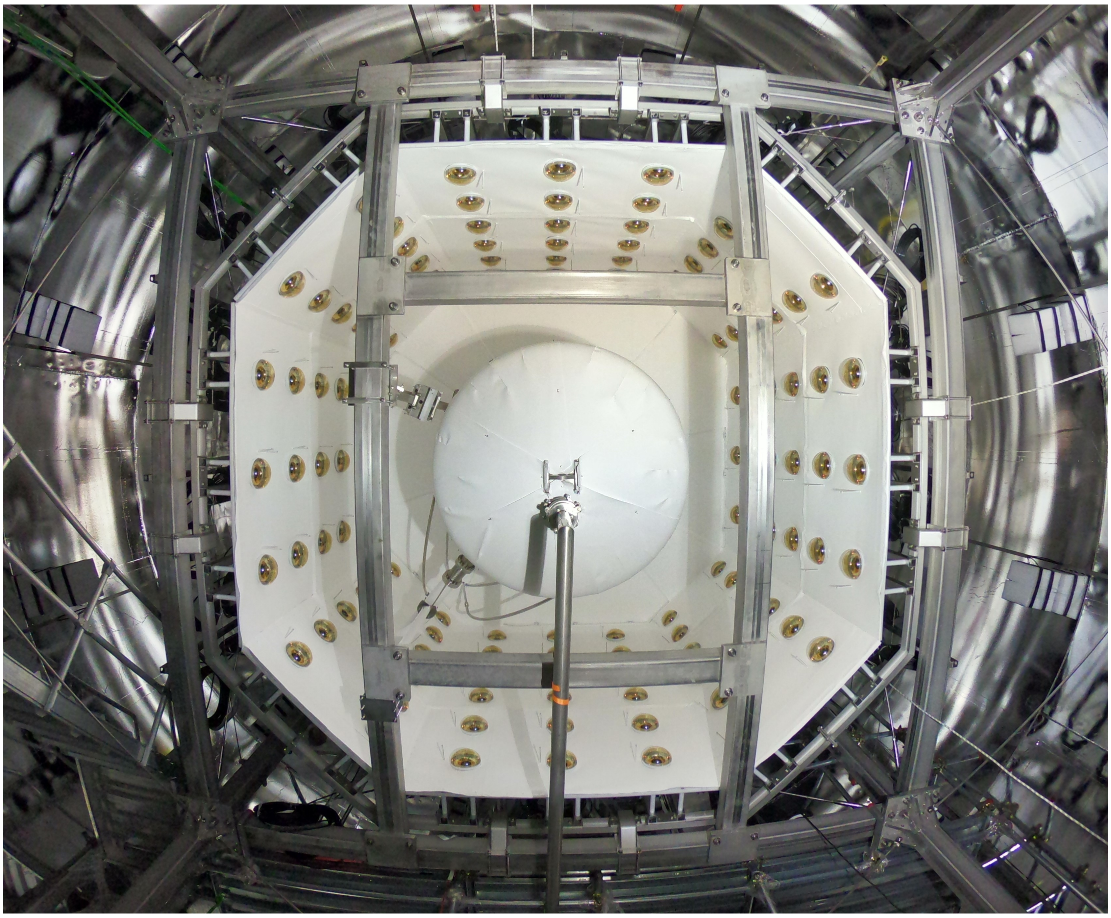

Figure 3.11: *View of the NV from below. The picture was taken before the installation of the NV floor panels.*

secured using tourniquets on the polyethylene bars and adjacent frames. The remaining steps involved driving the PMT cables outside the water tank. Here they were guided towards the DAQ room and cabled to the digitizers and the HV modules. The entire construction of the detector spanned several months, from July 2020 and until September 2020. Following the completion of the NV construction, subsequent operations focused on restoring the MV. The filling of the Water Tank with demi-water started in December 2020, marking the final steps in preparing the system for its commissioning.

3.4 Light Calibration Tool

The NV features several optical calibration tools to assess its optical performance and to evaluate the light response of the PMTs. This setup includes individual optical fibers directed to each PMT, a quartet of diffuser balls arranged around the TPC cryostat, and a specially designed reflectivity monitor system to illuminate the NV walls. A network of 120 individual optical fibers is used for characterizing and monitoring the single photoelectron response of every PMT. These fibers are optically coupled with the photocathode via diffuse reflection off a PTFE nozzle, which is mounted at the top of a PTFE rod that supports the fibers, as one can appreciate from figure 3.12 and 3.13.

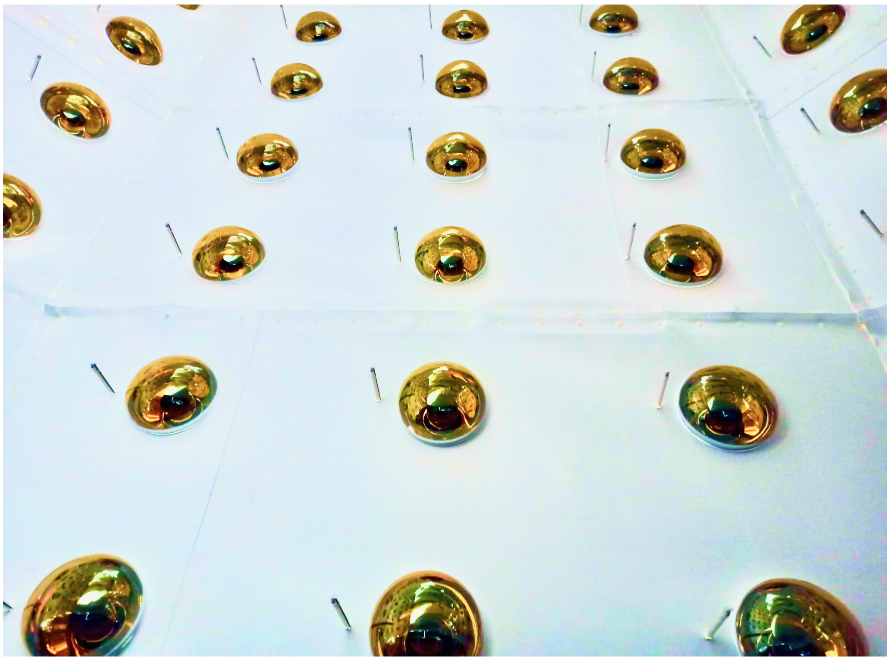

Figure 3.12: *Picture of the NV wall with the PMTs mounted, and the optical fibers coupled to each PMT through PTFE rods. Just as reference, the photocathode diameter is about 200 mm and the PMT is less than 300 mm long.*

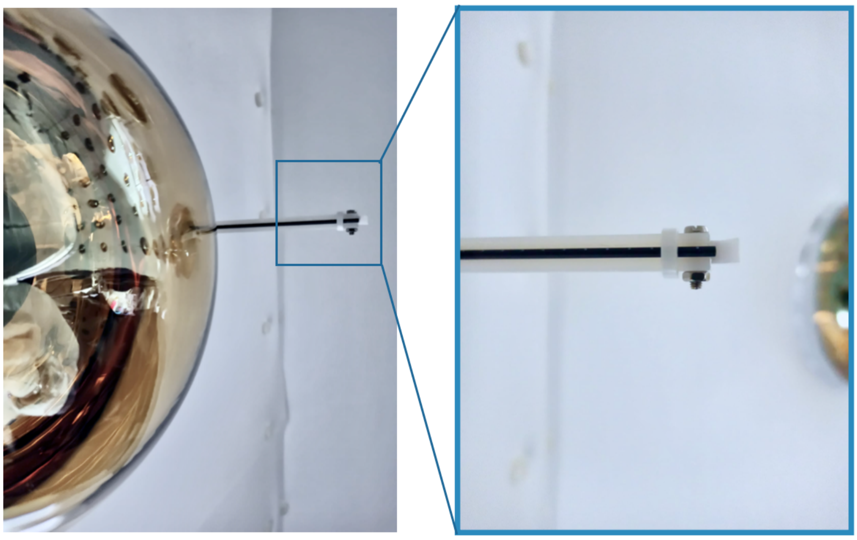

Figure 3.13: *View of the PTFE rod and nozzle coupled with the optical fiber. The light from the OF is reflected by the nozzle and hit the photocathode.*

The fibers extend outside the water tank, where they are connected to blue LEDs (470 nm). They are grouped into bundles of six, corresponding to each PMT column, resulting in 20 LED boxes, one for each column. The LEDs are controlled by three fast pulse generators, each offering 8 independent channels and a trigger output for the data acquisition system. Blue LEDs are chosen over lasers to facilitate calibration under low light conditions, enhancing the probability of single-photon interactions with the photocathode to probe the SPE response. For timing characterization and monitoring optical properties like water transparency and surface reflectivity of the NV, a system of four diffuser balls, illuminated by short laser pulses, is employed. They are positioned approximately 90 degrees apart around the cryostat, nestled between its two stiffening rings (Fig. 3.14). Each ball consists of a PMMA fiber within an SS306 steel cannula, leading into a quartz glass bulb filled with a mix of micro-glass bubbles and optical cement. The diffuser balls were thoroughly tested for isotropic light distribution and photon timing, with intrinsic time spreads ranging from 4 to 6 nanoseconds in air. They are operated using a picosecond laser with a 448±3 nm laser diode. An optical switch and attenuator enable individual operation and intensity adjustment of the laser light. The optical properties of the NV are also measured through a dedicated reflectivity monitor. Four optical fibers are installed to monitor the reflectivity of the ePTFE. Two fibers are pointed upward and the others downward. Each fiber channel can be selected individually using an optical switch. Pictures of the fiber heads of the reflectivity monitor mounted on the NV wall are shown in figure 3.15. Each quartz optical fiber (THORLAB UM22-200, polyimide coated) is housed

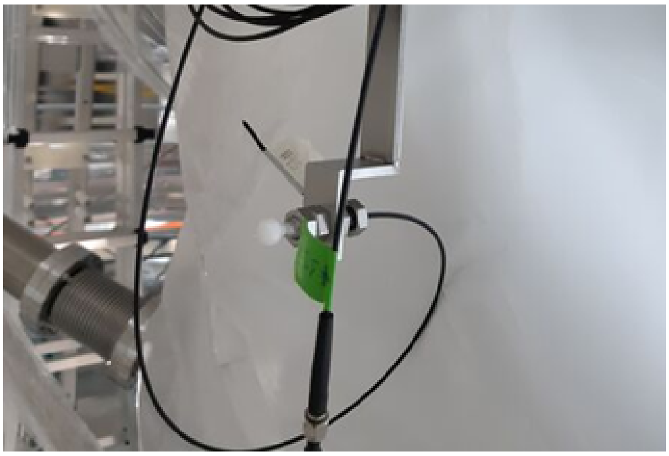

Figure 3.14: *Picture of one of the four diffuser balls installed in the NV. They are anchored to the cryostat stiffening ring.*

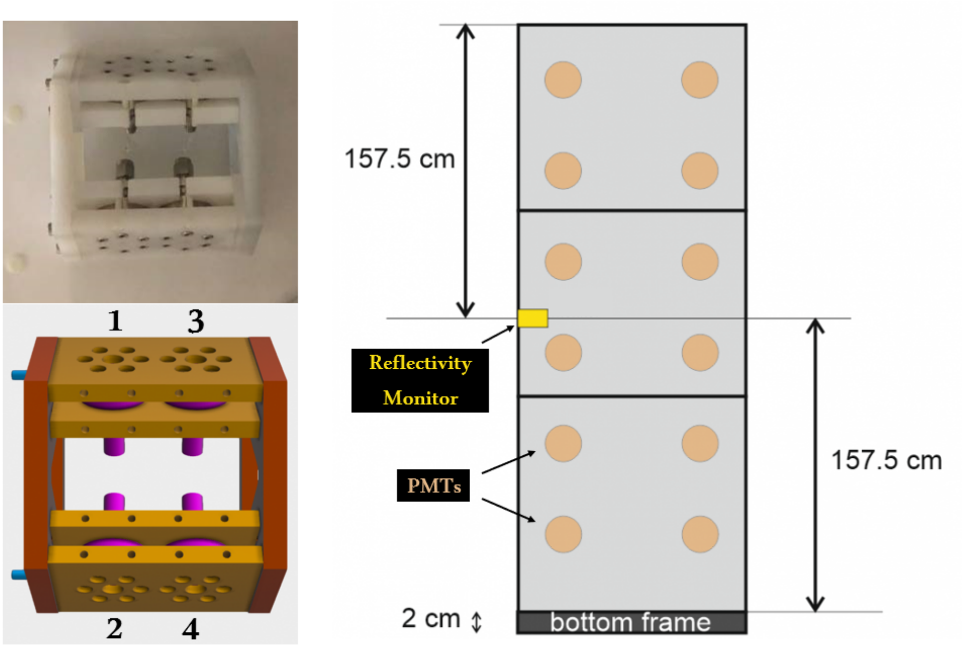

Figure 3.15: *Left: picture and CAD rendering of the support element for the Reflectivity Monitor, with the labels of the four channels: channels* 1 *and* 3 *look upward while channels* 2 *and* 4 *look downward. Right: position of the Reflectivity Monitor support on the lateral wall of the NV, compared to the PMTs positions*

in a stainless steel pipe. A picosecond laser (LDB-200, Tama electronics) with a wavelength of 375 nm is used to probe the more abundant shorter wavelengths of Cherenkov light and corresponding NV PMT quantum efficiency. The lasers in both setups, diffuser balls and reflectivity monitor, provide an external trigger signal for the data acquisition.

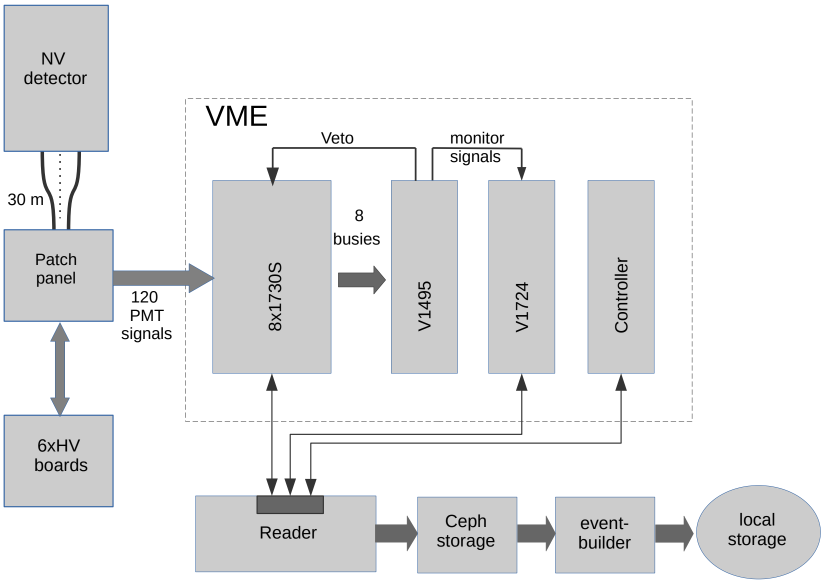

Figure 3.16: *NV DAQ scheme. PMT signals are digitized by the V1730S modules with a sampling rate of 500 MSamples/s. Data is read from the digitizers by the reader server and written to a common (Ceph) storage disk available to the event-builder processing. The busy logic and the acquisition monitor functionalities are handled by V1495 and V1724 modules, respectively. Schematic and caption from [113].*

3.5 Data Acquisition and Reconstruction

3.5.1 Electronics & DAQ

The primary purpose of the NV in XENONnT is to identify the neutron capture signals that contribute to the NR background events, which can mimic the interaction of a WIMP. The Cherenkov signal expected from neutron capture by hydrogen is very faint, with about 20 detected photo-electrons in total. Therefore, it is crucial to ensure high detection efficiency for each photon. In a trigger-based DAQ system, achieving this level of efficiency would typically require lowering the threshold on the number of PMTs that need to coincide to create a trigger, then reading all 120 channels. However, this approach would result in a large frequency of triggers and an increased volume of data, posing a challenge for the DAQ readout system. To address this, the NV DAQ is structured to operate in a **triggerless** data collection, defined on each single channel. A detailed block diagram of the NV DAQ system is presented in figure 3.16.

The NV DAQ capability to record both the shape and the timing of each PMT signal allows for data collection from fully independent channels, eliminating the need for a global trigger. As will be explained further, event building is performed in software post-data acquisition. This is done by using timestamps and observing coincidences between PMT signals to define events.

The readout of independent channels enables the capture of all PMT signals that exceed the digitization threshold, thereby allowing for a reduction in the energy threshold. To effectively identify neutron events, the electronics must be capable of processing signals ranging from 0.5 PE to about 100 PE, necessitating a broad dynamic range. The smaller signals, primarily due to single photoelectron from thermoionic dark rate, lasting about 100-200 ns, set the lower limit for the NV data throughput. In contrast, gamma and beta particles from neutron capture or radioactive decay in materials, as well as muons crossing the detector, produce waveforms that can last up to 10 μs (including afterpulses) across multiple channels. This requires a significantly higher rate of data collection. Therefore, the readout electronics must handle vastly different time acquisition windows and manage sharp peaks in the data rate. Moreover, the quick response (a few nanoseconds) of the PMTs used in the NV for single-pe detection necessitates a fast waveform digitizer for signal sampling. This high temporal resolution is essential to effectively separating multiple photons detected in the same channel, in the same waveform.

From the water tank, the 30-meter-long PMT coaxial cables are routed to the counting room, where the electronics, DAQ, and HV systems are located in a single rack. The high voltage is provided by the CAEN SY4527/A7435SP module, with the PMTs being powered with a positive HV of about +1.5 kV (with a current of ~3.5 mA).

The PMT signal cables are directly connected to the front-end electronics via a panel feedthrough. From the patch panel, the signal cables reach eight new-generation Digitizer boards (CAEN V1730S). Each board houses 16 input channels, each containing a 14-bit 500 MHz flash ADC. The input section is adapted to 50 Ω and set to 2 V. The V1730S digitizers operate using the Digital Pulse Processing for Dynamic Acquisition Window (DPP-DAW) firmware: each channel autonomously manages data acquisition in a **self-trigger mode**, recording the PMT waveform when its amplitude surpasses a pre-set threshold relative to the continuously computed baseline. The waveform recording continues until the signal falls below this threshold, with a time window of dynamic width. Most of the PMT channels, except for 10, have a self-trigger threshold set to 15 ADC counts corresponding to an amplitude of about 1.8 mV (~ 0.25 PE), the remaining more noisy ones are set to 20 ADC counts. Each pulse data frame, comprising a 48-bit trigger timestamp, a baseline, and variable-length waveform samples, is stored in a large channel memory buffer configured as a First-In-First-Out (FIFO) system. Pulses from different channels are recorded in separate buffer FIFOs. Data from these modules are transmitted through optical links to a CAEN A3818 PCIe card in the "Reader" server, depicted in Fig. 3.16, capable of handling up to 90 MB/s per link. If the memory reaches full capacity, a busy signal is activated, halting data acquisition until the memory status is cleared. An auxiliary board (CAEN V1495) stops data acquisition for all boards when one or more are busy, also providing a veto signal. This board generates two additional signals for the acquisition monitor, marking the start and stop of veto pulses. Notably, the NV DAQ system experienced no dead time during the science runs. Custom software has been developed for the NV V1730S boards, enabling block data transfers through the CAENVMElib and storing it on a Ceph storage device for online processing, including event building and definition. During the NV DAQ commissioning different run modes have been validated sustaining a data transfer rate of 90 MB/s on only one optical link. In the final setup used in the science run, the data rates are about 14 MB/s and 40 MB/s in the self-trigger and calibration modes respectively.

A key requirement for the XENONnT Data Acquisition system was the ability for its three DAQ subsystems (the TPC, MV, and NV) to function both independently and as a unified system. Despite sharing the same clock signal, the lack of synchronized start signals for the readout systems in each subsystem could lead to discrepancies in the timestamps recorded by the detectors. This would necessitate separate analyses for each subsystem. This approach was used in the XENON1T project, which involved only two subsystems. However, for XENONnT, to simplify the analysis flow, the DAQ was designed to enable the start signal from one subsystem to be directly transmitted to the others. This integration effectively combines the subsystems, allowing for direct comparison of timestamps across different detectors.

The subsystems can either be linked together based on the data collection requirements or operated independently. When operating in linked mode, the subsystems are managed as a single entity, and their data are merged at the readout stage for joint processing.

For time synchronization among its subsystems, the XENONnT DAQ uses a CAEN DT4700 clock generator module. The signals are then distributed within each VME crate via shorter clock cables, connecting adjacent digitizers. This setup ensures the temporal synchronization of the entire DAQ system. Time offsets within these clock chains have been manually calibrated to achieve synchronization that surpasses the temporal resolution of the digitizers.

Additionally, a GPS timing module distributes a 0.1 Hz trigger signal to specific digitizers in each DAQ subsystem. Each trigger is linked to a GPS timestamp, accurate to approximately 15 nanoseconds, adding another layer of time synchronization within the DAQ. This signal can also be used for absolute time synchronization with other experiments.

3.5.2 Data Processing

The processing of raw waveforms is managed by the event builder using two open-source Python software packages: `strax` and `straxen` [114, 115]. Strax offers a framework for setting up a processing chain for time-ordered, peak-like data, while straxen provides custom code specific for the XENONnT experiment. This processing system is built around `plugins`, which break down the processing chain into numerous small, logical steps. When a data chunk is retrieved from the digitizers, it undergoes online processing by a straxen thread on the XENONnT event builder machines.

The processing sequence for NV data begins with identifying *hits* in each of the `raw_record` pulses. The raw_records data type contains a fragmented (with a buffer size of 110 samples, i.e. 220 ns considering the time resolution of the NV digitizers) version of the recorded pulses. This data type is common to all three subdetectors; however, uniquely for the NV, `raw_records_nv` also contains a baseline field that stores the baseline estimated by the digitizer. A plot of a single PMT pulse is displayed in figure 3.17. Each pulse undergoes baseline correction and inversion by subtracting the average pulse height calculated from the initial 26 samples. Next, a hit-finder algorithm identifies PMT signals by detecting consecutive samples exceeding a fixed, PMT-specific threshold. For most channels, this threshold is 15 ADC counts, while channels with higher noise levels use 20 ADC counts, typically resulting in hits spanning three to five samples. Given the large dark count rate of the NV PMTs a software trigger plugin, based on a simple signal coincidence, is applied. The algorithm searches for a minimum number of n hits within a moving resolving time window ΔT. The settings of the software trigger were optimized to have a very high acceptance for neutron capture Cherenkov signals while keeping the pile-up due to PMT dark counts low. The resolving window was set to $\Delta T = 600$ ns, and a $n = 3$-fold coincidence. This method effectively reduces the volume of raw data further processed for the NV.

To capture each PMT signal tail, hits are extended by a fixed number of samples to the left (3 samples) and right (15 samples), forming a '`hitlet`', which is indicated in Fig. 3.17 as the orange-shaded region. Overlapping hitlets from the same PMT are first merged, then split at local prominences. Basic properties like amplitude, area, and shape parameters are then calculated for each hitlet. In particular, the area of the hit is converted from ADC Counts x Samples to PE (Photoelectrons) unit. The conversion factors are based on the weekly LED

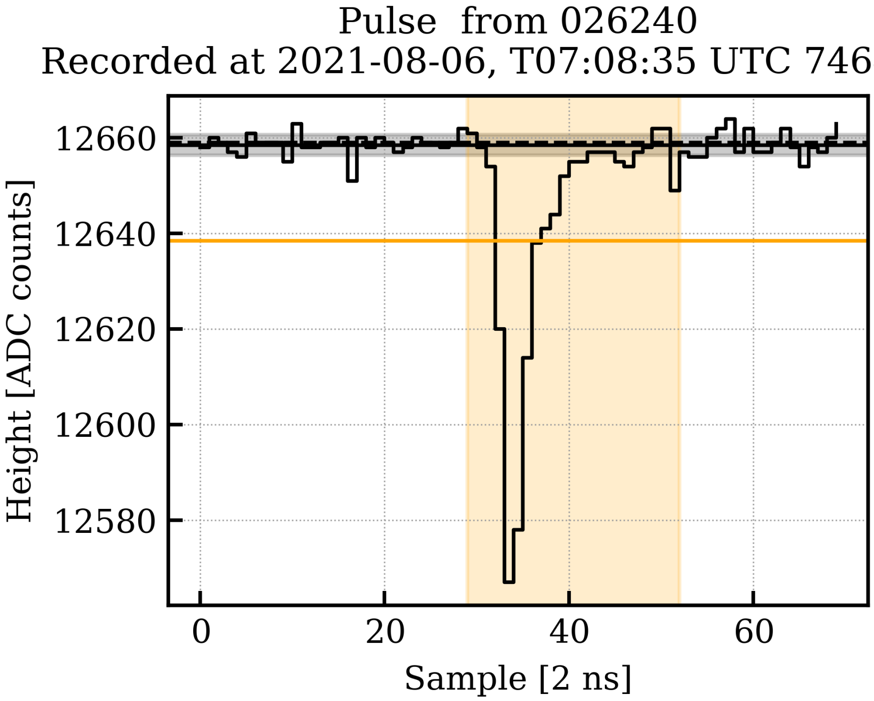

Figure 3.17: *Waveform of a SPE signal recorded in PMT 2054. The black solid and dashed lines represent the baseline of the waveform as estimated by the digitizer and processing software respectively. The black-shaded region indicates the baseline RMS. The orange horizontal line shows the hit-finder threshold which is set to 20 ADC counts above baseline. All consecutive samples below this line are marked as a hit. The orange shaded region indicates the hit including the left and right extension which is referred as to "`hitlet`" in the straxen framework.*

calibrations, and are queried from the *corrections database*.

Finally, hitlets are grouped into `events`, using a similar moving window coincidence as the software trigger, but with a narrower 200 ns window. Each event must contain at least 3 hitlets. Each event's start and end is then set according to the start and end of the first and last hitlet within the event. The time window was chosen based on the fact that the time distribution of a typical Cherenkov event for the NV follows an exponential distribution with a decay constant of ~60 ns as it is discussed in section 4.2.2. The PMT hit pattern and timing distribution of a typical NV neutron-capture signal are depicted in figure 3.18.

For each event, several characteristics are determined: the total signal area, the 'center time' (the area-weighted average arrival time of the hitlets), and a basic position reconstruction. The center time serves as an estimator for the optical decay constant, as measured by the reflectivity monitor and diffuser ball setup, but specifically for the spectrum of Cherenkov light. The position is estimated as an area-weighted average of all prompt hitlets recorded within the first 20 ns of an event, before any position information is lost due to diffuse

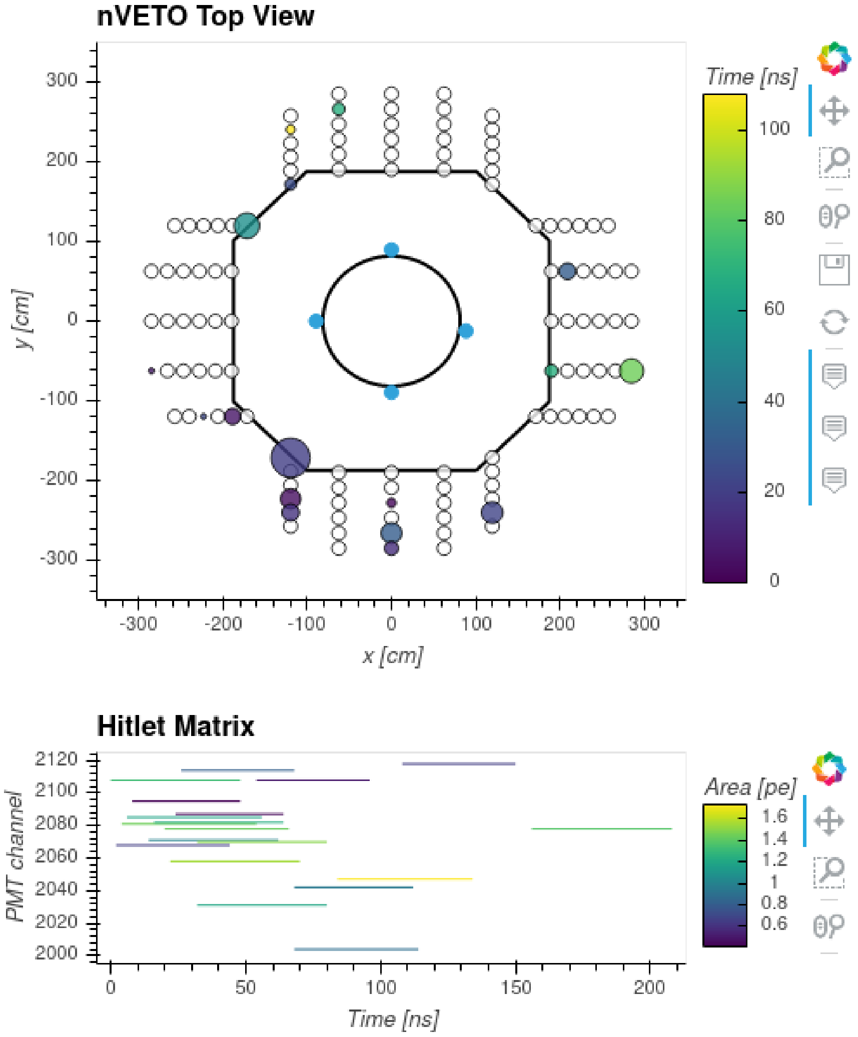

Figure 3.18: *Interactive event display of a neutron-capture event recorded during the AmBe calibration. The top figure shows a two-dimensional projection of the NV with the outer wall of the TPC cryostat shown as a black circle. The blue circles indicate the location of the four diffuser balls. The position of the NV reflector walls is displayed as a black octagon. Each circle next to the octagon represents one of the NV PMTs. The size of the dot indicates the integrated charge detected by the PMT in the displayed event. The color code encodes the arrival time of the detected photon. The bottom panel shows the arrival time of the individual hitlets for the given event, where the color code indicates the charge of each hitlet.*

reflection and photon propagation.

4

NEUTRON VETO CHARACTERIZATION AND PERFORMANCES

In this chapter, we delve into the analyses of the performances of the NV of the XENONnT experiment. The experiment life cycle is segmented into several distinct operational phases, each characterized by unique conditions and goals. So far we had: Commissioning, Science Run 0 (SR0), Post-SR0, and Science Run 1 (SR1), and currently we are in Science Run 2 (SR2). The differentiation of these phases is not merely a chronological division but a strategic approach to structure the analyses in an organized and coherent way. This structure allows us to trace the evolution of the NV performance, highlighting how each phase contributes to the overall understanding and refinement of the system. The transition from SR0 to Post-SR0, for example, provides valuable insights into the system response to extended operational stresses, as well as the adjustments implemented to enhance performance in preparation for Science Run 1. Table 4.1 outlines each phase, its start and end dates, duration, and the specific analyses conducted during these periods.

The photomultipliers (PMTs) are one of the key ingredients of the NV system, and their performances are inspected under the various operational conditions in these phases. In section 4.1 we explore the fundamental characteristics of the PMTs, their Single Photoelectron Models, and overall performances. This includes a deep dive into the Dark Rate, which is crucial for understanding the background noise and sensitivity of the PMTs; the SPE model and acceptance are analyzed to gauge the efficiency and reliability of the PMTs in detecting single photons, a key aspect to reach a low threshold in low-light conditions. Furthermore, the gain stability of the PMTs is examined to ensure consistent performance over the experiment duration. Key parameters related to light collection on PMTs, such as NV surface reflectivity and water transparency, are studied using dedicated optical calibration systems, and the results are

Phase	Start Date	End Date	Analyses / Operations
Commissioning	End of 2020	2021-05-01	Turning on the Experiment, Low-level analyses (PMTs and DAQ performances), background event rate
Science Run 0	2021-05-01	2021-12-10	Calibration of TPC and NV with AmBe source, Low-ER [85] - WIMP search [86]
Post - Science Run 0	2021-12-10	2022-05-19	Maintenance, Optimization of NV PMT High Voltages to enhance the SPE acceptance
Science Run 1	2022-05-19	2023-08-08	WIMP search (and other physics), Calibration of TPC and NV with AmBe source
Post SR1 and SR2	on-going		

Table 4.1: *Overview of experimental phases in XENONnT. It details the start and end dates of each phase, noting that the commissioning phase lacks precise dates due to the asynchronous commissioning of detectors (e.g., the TPC commissioning occurred while the NV was in its final step of installation - DAQ cabling etc.). The table also highlights the main research activities and operations conducted during each phase.*

presented in section 4.2.1. Finally, section 4.2.2 contains a detailed analysis of the background spectrum and rate observed during the data collection of the detector. The discussion centered on the NV detector itself, with its operational effectiveness quantified through the detection and tagging efficiency, is delegated to Chapter 5. These metrics are crucial in assessing the NV capability to accurately identify and measure neutron events.

4.1 The Neutron Veto PMTs

The PMTs play a crucial role in XENON detectors, acting as essential components across the different subsystems. The PMTs of each subsystem are specifically designed with distinct characteristics to fulfill a variety of requirements and operational conditions. In the NV, we use 120 8-inch Hamamatsu R5912-100-10 PMTs [116] (see Fig. 4.1), notable for their:

- Capability to be safely operated underwater;
- Coaxial cable design with separate grounding for signal and high voltage cable;
- High quantum efficiency (refer to Fig. 4.2);
- Low radioactivity levels (details in table 4.2);

- High Gain, with values around $1{\times}10^7$ at nominal HV.

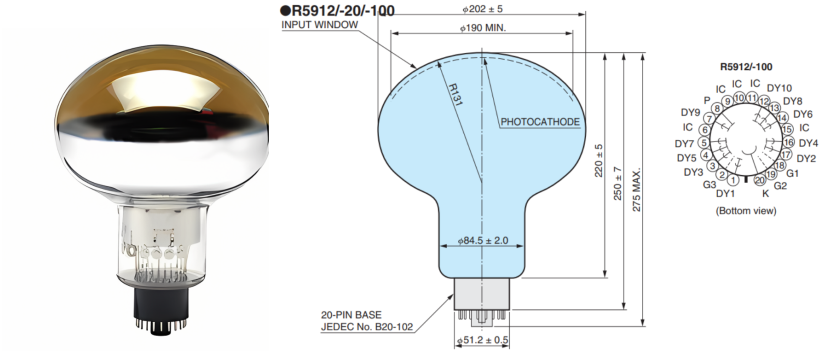
●R5912/-20/-100
INPUT WINDOW
ϕ202 ± 5
ϕ190 MIN.
R131
PHOTOCATHODE
220 ± 5
250 ± 7
275 MAX.
ϕ84.5 ± 2.0
20-PIN BASE
JEDEC No. B20-102
ϕ51.2 ± 0.5
R5912/-100
IC
IC
IC
DY10
P
DY8
DY9
DY6
IC
IC
DY7
DY4
DY5
DY2
DY3
G1
G3
G2
DY1
K
(Bottom view)

Figure 4.1: *(Left) Picture of a R5912 PMT. (Right) Schematic of the PMT and its socket structure. Both figures are taken from [117].*

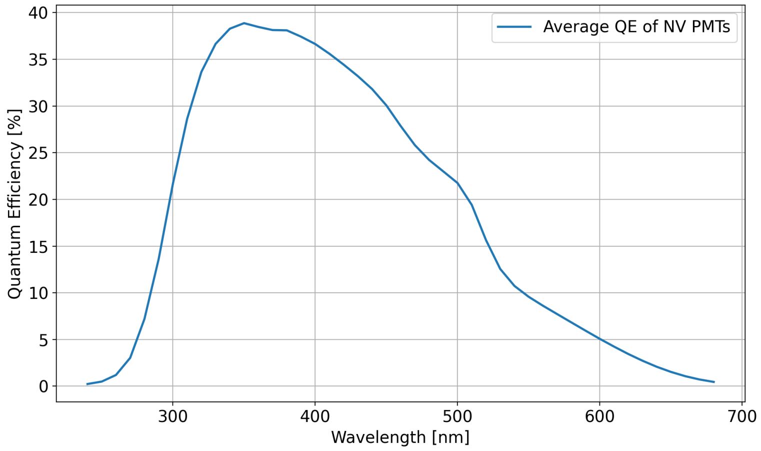

Figure 4.2: *Average quantum efficiency of the 120 PMTs. The maximum average value stands at* $\sim$ *39% for a wavelength of 350 nm.*

The strategic placement of the PMTs within the NV structure was determined through Monte Carlo simulations, aiming to optimize light collection efficiency and enhance overall neutron tagging efficiency. The selection process for the installed PMTs was grounded in extensive testing at LNGS. Here, we measured key parameters like gain, dark rate, afterpulses, optimal operating voltages, and timing characteristics. Of the 125 PMTs tested, 5 were designated as spares due to their comparatively lower performance. Further insights into the testing process and PMT selection are detailed in my master thesis [118].

In this section, we dig into the photomultipliers' characteristics; some aspects of the operating principle are presented to thoroughly understand the models

PMT Radioactivity [Bq/PMT]						
	Without glass		Standard glass		Low Rad. glass	
	Nominal	LNGS	Nominal	LNGS	Nominal	LNGS
^{40}K	0.6	0.08	4.7	2.4	0.8	0.6
U-series	<0.1	<0.05	2.4	2.26	0.4	<0.6
Th-series	<0.1	0.008	2.0	1.58	0.3	0.425

Table 4.2: *Comparison between the values of the PMT radioactivity reported by Hamamatsu [117] and measured with the Ge detector available at LNGS. In particular, the glass of two broken PMTs (featuring different glass materials) was isolated from the PMT body for the measurement. The values, expressed in [Bq/PMT], for the ^{40}K and the U/Th-series are shown. The employment of a low radioactivity glass in the NV PMTs mitigates the radioactive background. The uncertainties of the measured value, of less than 10%, are not reported in the table.*

used for describing the single photoelectron response of the PMTs.

4.1.1 Fundamental characteristics of PMTs

A PMT is a vacuum tube that transforms light signals into amplified electrical currents [119]. Its main components include:

- A *photocathode*, made of photosensitive material, converting light into an electron flux;
- An *electron-optical input system* focusing and accelerating the electron flux;
- An *electron multiplier* subsection or dynode string, comprising a series of secondary-emission electrodes known as *dynodes*;
- An *anode* collecting the electron flux to supply an output signal.

During operation, a high voltage creates a 'potential ladder structure' along the PMT. Incident photons with frequency ν and wavelength λ hitting a material with extraction potential Φ emit electrons via the photoelectric effect [120], with energy:

$$E = h\nu - \Phi \tag{4.1}$$

However, not all incident photons result in electron emission. The photoelectric conversion efficiency depends on the wavelength and the composition and thickness of the photoemissive material. The ratio

$$\eta(\lambda) = \frac{\text{number of released electrons}}{\text{number of incident photons}(\lambda)} \tag{4.2}$$

is called *Quantum Efficiency* (QE). The electron, once emitted, is focused and accelerated towards the first dynode. Here, it can emit secondary electrons via the secondary emission process. The number of electrons emitted in this manner is given by:

$$\delta = \frac{\text{number of secondary electrons emitted}}{\text{number of primary electrons}}, \tag{4.3}$$

which is called *secondary emission coefficient*. This process creates an electron cascade, culminating at the anode to produce a current, as a result of the amplification process. In discussing photomultipliers, we refer to specific parameters (usually found in datasheets) that summarize their efficiency and functionality under various conditions. This section aims to describe these fundamental characteristics of PMT operation, laying the groundwork for understanding the single photoelectron model we have developed.

Collection efficiency (CE) The CE is defined as the ratio of the number of photoelectrons that successfully reach the first dynode to the number of electrons initially emitted from the photocathode. This efficiency is intrinsically linked to the initial velocity of the electrons, which means it varies depending on the wavelength of the incident light. This parameter plays a significant role in determining the single photoelectron (spe) resolution of the PMT. The SPE resolution is crucial for accurately measuring low levels of light, as it impacts the PMT ability to distinguish between individual photon events.

Gain The gain (G) is defined as the ratio of the anode current I_{anode} to the cathode current I_k. In a PMT with an N-stage dynode multiplier, where each stage i has a gain g_i (determined by the CE of the i-th dynode α and the secondary emission coefficient δ), the anode current I_{anode} is expressed as:

$$I_{anode} = I_k \alpha \prod_{i=1}^{N} \delta = I_k \prod_{i=1}^{N} g_i. \tag{4.4}$$

Thus, the gain is given by:

$$G = \frac{I_{anode}}{I_k} = \prod_{i=1}^{N} g_i. \tag{4.5}$$

Usually, the multiplication region contains 10 to 14 stages with an overall gain of $\sim 10^7$. If the collection efficiency α of all stages approaches 100%, the gain becomes equal to the product of all the secondary emission coefficients. Fluctuations in gain can significantly impact the PMT performance, particularly in applications requiring high precision and sensitivity. Regular monitoring and calibration of the gain and voltage settings are essential to maintain PMT accuracy and reliability over time. Furthermore, this parameter is fundamental in the XENON data processing chain. As outlined in Section 3.5.2, the production of high-level data (hitlets and events) requires the normalization of signals area through the gain. This normalization ensures that the hit area is expressed in photoelectrons, allowing for the comparison of PMTs with different gains.

Dark Rate The background noise of the PMT, known as the Dark Current, is present even in total darkness conditions and it limits the detection of very low energy radiation. The observation of dark current typically reveals several pulses, characterized by a specific Dark Rate (DR). While factors like Field Effects, Leakage Current, and Background Radiation due to high energy particles and PMT material radioactivity do contribute to the dark current, it is the temperature variation that predominantly affects the dark rate and its potential changes over time, as the predominant contribution comes from Thermionic Emission of electrons from the photocathode and dynodes, with the dark pulses being of the SPE type.

4.1.2 SPE Models

When employing PMTs for the detection of extremely weak signals the concept of the SPE spectrum becomes crucial.

During the operation of the NV PMTs in the scientific runs of the experiment, we developed two distinct models to describe the SPE spectrum. In particular, in the period following Science Run 0, referred to as Post SR0, we focused extensively on investigating the phenomenon of electron sub-amplification within the PMT. The standard method for calibrating the SPE response of a PMT involves using a low-intensity light source, ensuring the generation of no more than a single photoelectron within the detector time resolution. The integrated signal spectrum is then fitted with a parameterized model of the SPE response to determine the mean and variance for each PMT. However, the challenge lies in selecting an appropriate model for the fit. Electron multiplication within the dynode chain is a complex process, and for a typical photoelectron originating at the photocathode, a standard Gaussian distribution is often assumed. Yet, more intricate models are employed to accurately depict the electron cascade process. Furthermore, a variety of sub-optimal photon and electron trajectories through the PMT are possible. These include scenarios where a photon bypasses the cathode to directly strike the first dynode, or a photoelectron inelastically backscatters off the first dynode or skips a dynode stage. Such trajectories often lead to under-amplified photoelectron signals, which may contribute significantly to the SPE spectrum. These under-amplified photoelectrons can constitute up to 20% of the SPE spectrum in some PMT models. Neglecting these can result in an underestimation of the number of detected photoelectrons and an inaccurate assessment of the resolution [121]. The true nature of the under-amplified component is often challenging to ascertain due to its substantial overlap with electronic noise contributions. Various authors have suggested incorporating additional terms into the single photoelectron response fit function, such as a falling exponential and extra Gaussian component [122, 123, 124]. However, the relative weight and shape of the under-amplified component can vary depending on the photocathode and dynode structure, and even among individual PMTs of the same model and gain. Consequently, constructing a parametrization of the single photoelectron spectrum that is universally applicable across a range of PMTs and conditions is a complex task, but without which it is not possible to accurately estimate the parameters that characterize the performance of the PMTs. The two SPE models presented in this section differ mostly in the description of the under-amplified electrons [119, 125]. In the first model, used in the preliminary phase of the experiment and during the first science run (SR0), the SPE component is made of two parts: fully amplified and partially amplified signals. The fully amplified component is described by a Normal distribution while a skew-Normal distribution is used to model the partially amplified component due to photo-electrons that are not fully amplified for different possible reasons: electrons partially depositing their energy in the first dynode, collection inefficiency on the second dynode, bad trajectories of electrons, and photons directly reaching the first dynode, etc. The probability distribution function (PDF) of the SPE component is hence the following [122]:

$$P_{SPE} = f_{FA} \cdot \mathcal{N}(\mu_{FA}, \sigma_{FA}) + (1 - f_{FA}) \cdot \mathcal{N}(\xi, \omega) \cdot \left[1 + \mathrm{Erf}\left(\alpha \frac{(x-\xi)}{\sqrt{2}\omega}\right)\right] \tag{4.6}$$

where the first part represents the Normal distribution with parameters μ_{FA} and σ_{FA} describing the fully amplified component which contributes to a fraction f_{FA} of the total SPE PDF, and the second one the skew-Normal distribution with location ξ, scale ω and shape parameter α modeling the partially amplified component. The parameters μ_{FA}, σ_{FA} and ξ are free parameters together with the fraction f_{FA} and the overall normalization while ω and α are constrained in the fit by σ_{FA} and σ_{PED}. Figure 4.3 shows a typical spectrum where are clearly visible a pedestal peak centered around zero, a valley followed by a second wider peak, due to fully amplified SPE signals, and by a decreasing structure due to double and multiple photo-electron (PE) events. We found that the pedestal peak is often described more accurately by the sum of two Normal functions with equal sigma (σ_{PED}) due to baseline instability. The multiple photo-electrons distributions are described by Normal functions whose mean and sigma are determined from the SPE distributions by applying the central limit theorem.

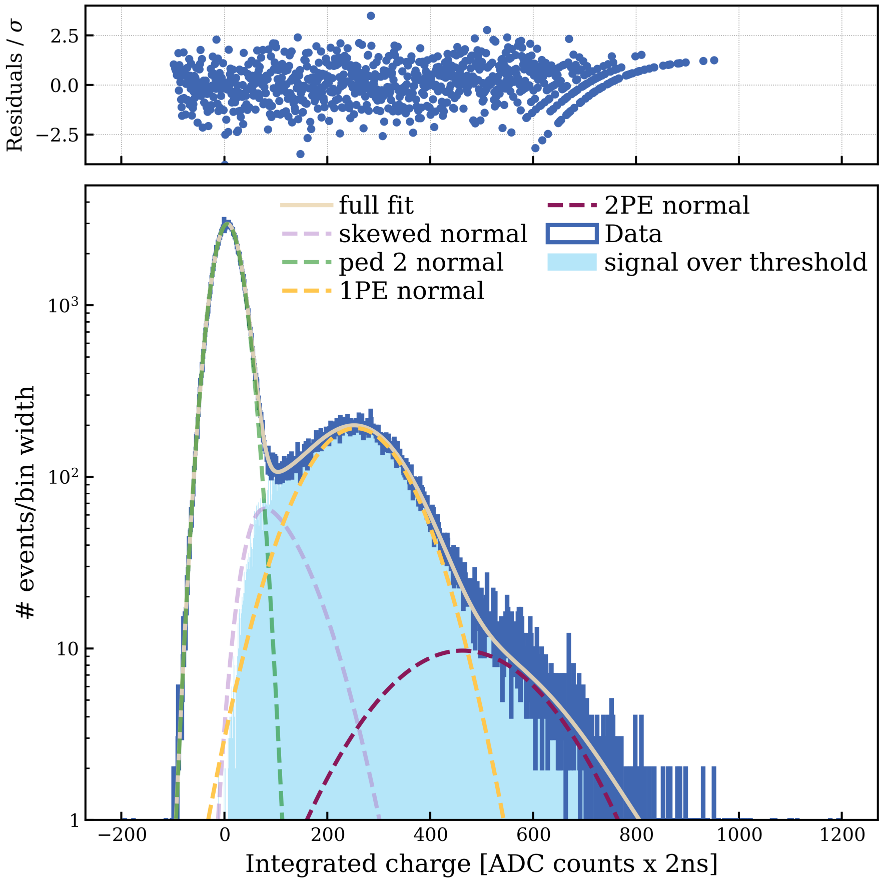

Figure 4.3: *Charge spectrum measured in one PMT during the LED calibration. The fit function with contributions of pedestal, single, and 2 photo-electrons is superimposed. The light blue full histogram corresponds to the signals surviving the digitizer's threshold, applied offline. In the top panel are shown the normalized residuals.*

Therefore only the normalization of these distributions are free parameters. During our LED calibrations we kept the LED light emission low, reducing the contribution of the multiple photo-electrons. In the second model, redefined for SR1, the SPE component is made by two structures as well. The fully amplified component is now described by a scaled Poisson distribution resulting from a discrete Poissonian process at the first dynode convoluted with the response of the remaining dynodes. It depends on the gain G_1 of the first dynode of the photomultiplier, the gain of the remaining dynode chain f (in ADC counts) with its fluctuations Σ, and on σ_{PED}:

$$P(x) = \rho \frac{e^{-\mu\rho}(\mu\rho)^{x\rho}}{\Gamma(1 + x\rho)} \tag{4.7}$$

where $\mu = G_1 \cdot f$ represents the mean of the distribution in ADC counts, and $\rho = \frac{G_1{,}f}{G_1{,}f^2+\sigma^2_{\mathrm{PED}}+G_1{,}\Sigma^2}$ is the scaling factor. By including the smoothing due to the amplification from the second dynode onward, the function describing partially amplified electrons can be described as the product of two smoothed step functions:

$$P'(x) = \frac{\left[1 + \mathrm{Erf}\left(\frac{x-\mu_L}{\sqrt{2}\sigma_L}\right)\right]\left[1 - \mathrm{Erf}\left(\frac{x-\mu_R}{\sqrt{2}\sigma_R}\right)\right]}{4(\mu_R - \mu_L)}, . \tag{4.8}$$

The parameters μ_L and μ_R represent the flex positions of the left and right distribution shoulders and are related to f and G_1, $\mu_L = f/2.25$ and $\mu_R = (G_1 + 0.375) \cdot f$, as determined from analytical calculations and simulations. The parameters σ_L and σ_R describe the smoothing of the left and right step functions: $\sigma_L = \alpha\sqrt{G_1 f^2 + G_1\Sigma^2 + \sigma^2_{\mathrm{base}}}$, $\sigma_R = \alpha\sqrt{\Sigma^2 + \sigma^2_{\mathrm{base}}}$, where α is a scaling factor close to unity determined from simulation. Figure 4.4 shows the same spectrum as in Fig. 4.3 but with the fit function originating from the second model.

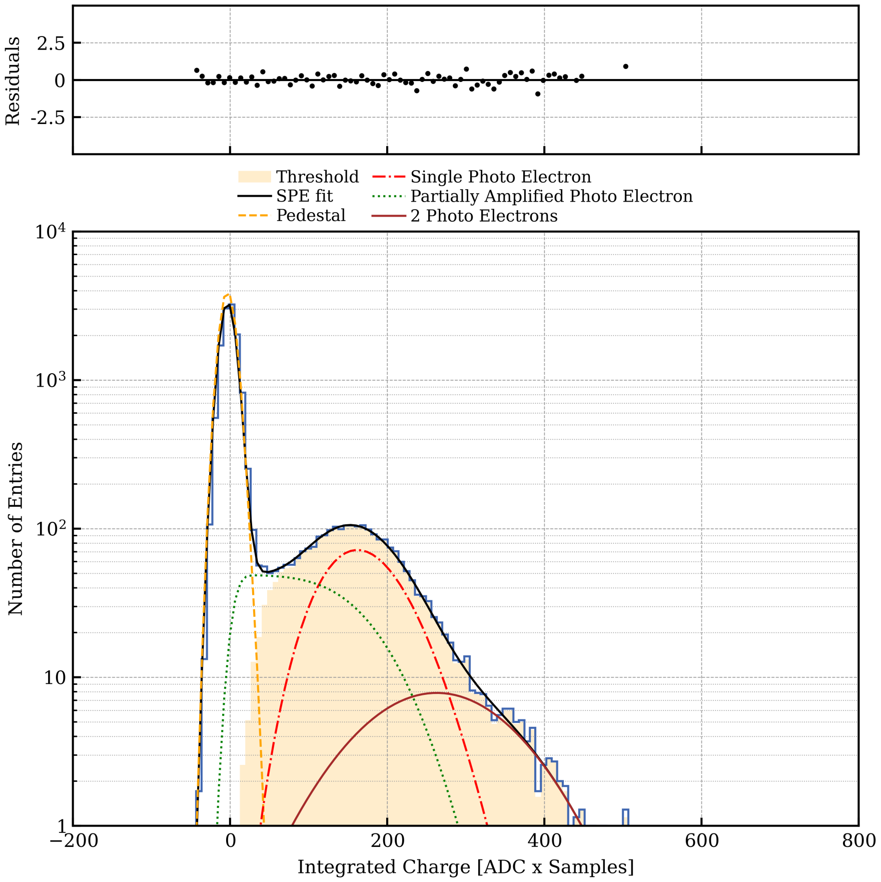

Figure 4.4: *Charge spectrum for one PMT during the LED calibration. The fit function with contributions of pedestal, single, and 2 photo-electrons is superimposed. The orange full histogram corresponds to the signals surviving the digitizer's threshold, applied offline. In the top panel are shown the normalized residuals.*

In both cases, from the fit of the spectra, the gain of the PMT is determined. The gain is defined as the mean value of the overall SPE component of the global fit, which includes the partially amplified contribution. Another important parameter that can be calculated from the fit is the SPE acceptance ε; it characterizes the ability to detect weak signals in the presence of a hardware acquisition threshold, as in the case of the self-trigger DAQ of the NV, and it is calculated from data as follows:

$$\varepsilon = \frac{N - \int [\mathcal{F}_{2PE}(x) + \mathcal{F}_{3PE}(x)]dx}{\int \mathcal{F}_{1PE}(x)dx}\,, \tag{4.9}$$

where N is the total number of events after applying the trigger threshold offline, and $\mathcal{F}_{nPE}(x)$ representing the n-photoelectron contributions of the fit function.

4.1.3 PMT Performances

During the data acquisition (mainly Science Runs, but also during the periods of maintenance) several relevant parameters of each of the 120 NV PMTs were monitored: average and standard deviation stability of the baselines, single hit rates (dark rate), gains, and SPE acceptance.

Baseline and Dark Rate Monitoring

Frequent PMT calibrations and measurements have consistently confirmed the stability of the detector conditions throughout the Science Runs. After resolving initial noise and bit flip issues in the digitizer firmware during the commissioning, the PMT baselines, calculated from the first 26 samples of the acquired waveforms from the self-triggered data, were found to be stable within $\sigma_{\text{base}} \approx 2.5$ ADC counts for the majority of PMTs. This stability is well below the average PMT threshold set at 15 ADC counts in the DAQ (Hardware trigger). Out of the 120 NV PMTs, during SR0 only two were excluded from the analysis due to fluctuating noise conditions, and 16 PMTs were set to a slightly higher threshold of 20 ADC counts, while on SR1 we managed to recover all the PMTs. The dark rate, i.e. the single hit rate of each NV channel, is determined from the number of peaks over threshold in the self-triggered data in a given time interval: it ranges from about 500 Hz to 1500 Hz depending on the PMT (Fig. 4.5), with an average rate of $\langle R \rangle_{\text{DC}} = (960 \pm 4)$ Hz. Figure 4.6 shows the sampled dark rate as a function of time during SR0 of some PMTs. A clear variation in time of the dark rate can be seen, correlated with the water temperature (red line in Fig. 4.6) inside the tank, which reflects the variations in the experimental hall underground at LNGS. This temperature dependence is compatible with the known temperature dependence of thermionic emission by bi-alkali photocathodes [119], but has no impact on the efficiency of the NV due to the high PMT coincidence requirement for its neutron tagging.

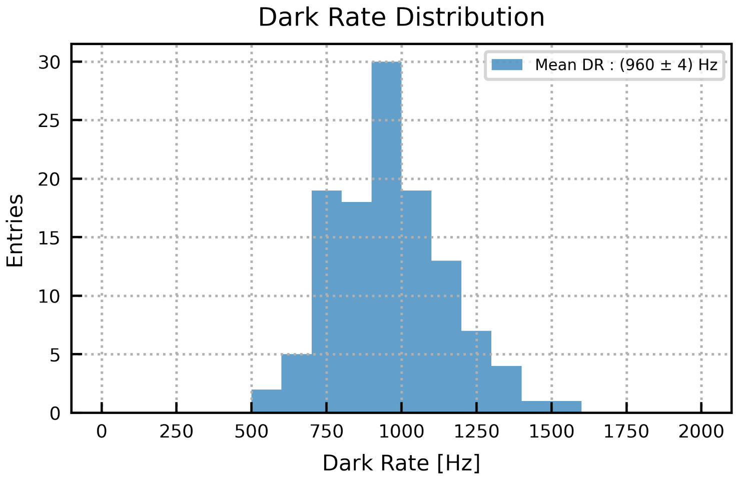

Figure 4.5: *Distribution of the Dark Rate of the 120 PMTs. The mean DR is* $\langle R \rangle_{\mathrm{DR}} = (960 \pm 4)$ *Hz.*

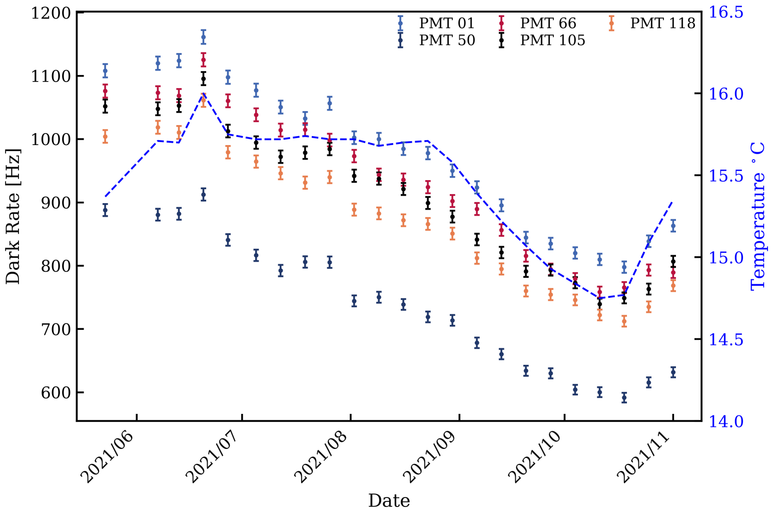

Figure 4.6: *Evolution of the dark rate of six PMTs during SR0. The temperature measured inside the demineralized water purification plant is shown with the blue-dashed line.*

For instance, for the event building, which utilizes a 3-fold coincidence requirement, this leads to an average event rate of approximately ∼ 150 Hz, with around ∼ 8 Hz attributed to accidental coincidences from PMT dark counts [126]. Increasing the threshold to a 5-fold coincidence and applying a 5 PE event area (defined as the sum of the integral of all the hits contributing to the event) threshold further reduces the event rate to about ∼66 Hz, reducing the contribution of accidental coincidences as well. This threshold condition is also utilized for the NV neutron tagging, as discussed in Chapter 5.

Gain Monitoring and SPE Acceptance

The gain of each PMT and the corresponding SPE acceptance is measured with dedicated light calibrations. Externally triggered LED calibration data are used to acquire events without any threshold (Section 3.4). Each acquired waveform is subtracted from its mean baseline value, and evaluated in a 30 samples window. Then the spectrum of each PMT is obtained by searching for the sample t_{max} with the maximum ADC value and integrating in a time interval of [-10,+20] samples (corresponding to 60 ns) relative to t_{max}. From the fit of the spectra, both PMT gain and SPE acceptance are determined. The gain is defined as the mean value of the overall SPE component of the global fit, which includes the partially amplified contribution. Figure 4.9 shows the gain values during SR0 for a selection of channels. Typical gain values are $\sim 7 \times 10^6$ with a stability better than 5%.

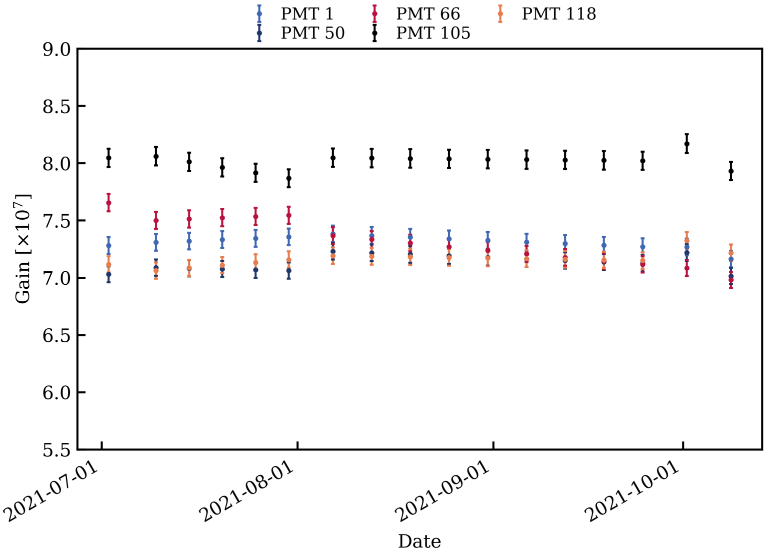

Figure 4.7: *Evolution of the gain of six PMTs during SR0. Some of the points are the result of the weekly LED calibration performed during SR0; in the case of missing runs, the gain values have been inferred through the Savitzky-Golay filter.*

Figure 4.8 shows the distribution of the SPE acceptance, calculated as in eq. 4.9, resulting in an average value of 91% and a standard deviation of 2.4%. Gains were estimated through weekly LED Calibrations, a routine developed after finely tuned parameters of the light sources during the commissioning of the experiment. Having a regular weekly calibration allowed us to obtain a clear trend of the PMT parameters in the scientific runs. For instances where calibrations failed or were skipped due to experimental needs, and to avoid considering non-physical gain fluctuations, we used a Savitzky-Golay filter [127] to obtain a smooth trend. The Savitzky-Golay filter is a widely used smoothing

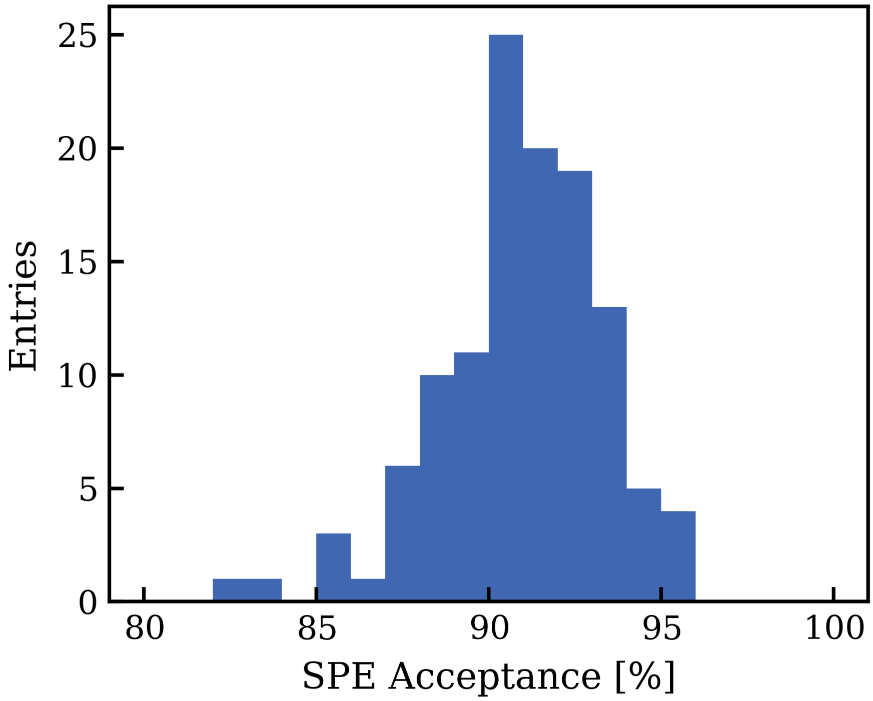

Figure 4.8: *Distribution of the SPE acceptance of the 120 NV PMTs.*

technique in signal processing that preserves underlying trends while reducing the impact of noise. It involves using a polynomial fit to locally approximate the data. The filter applies a window function that moves over the data points, fitting a polynomial within that window, and moves over the entire data series to produce a smoothed signal. In our cases, the window used is made of 3/4 points and the polynomial fit degree, which is typically 1 or 2 for most applications, was set to 1 (linear fit).

During the transition phase between the two Science Runs, we also changed the operating voltages of the photomultipliers to enhance the SPE acceptance, increasing it from 92% to over 96%. Generally, the voltage increase was about 200 V for all PMTs. The gain of the photomultipliers also increased, as shown in Fig. 4.9.

Figures 4.9 and 4.10 show the PMT monitoring during SR0 and SR1.

4.2 NV Optical Properties and Stability

In neutron capture events within the NV, Cherenkov photons undergo multiple reflections within the detector volume before potentially being detected by the PMTs. As we have already seen, the observed performance of the PMTs allows for excellent acceptance and good resolution of these photons. However, the dissipation of the light is also crucial, which can occur either as absorption by

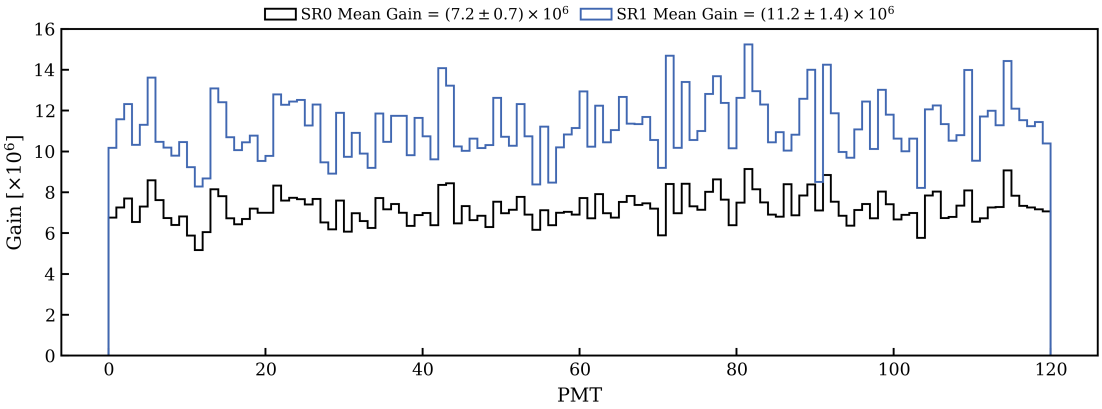

Figure 4.9: *Gain distribution for a SR0 and a SR1 LED calibration run. The mean gain for SR0 stands at* $\mu_G^{SR0} = (7.2 \pm 0.7) \times 10^6$ *while for SR1 stands at* $\mu_G^{SR1} = (11.2 \pm 1.4) \times 10^6$.

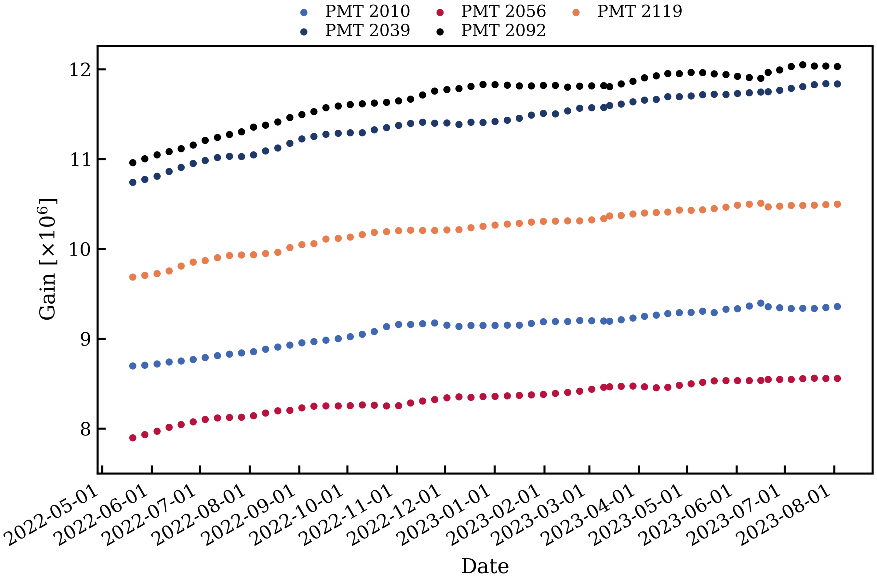

Figure 4.10: *Evolution of the gain of six PMTs during SR1. Some of the points are the result of the weekly LED calibration performed during SR1; in the case of missing runs the gain values have been inferred through the Savitzky-Golay filter.*

the water or due to insufficient reflection on the ePTFE surface that constitutes the NV. To accurately estimate these optical properties, the NV is equipped with two dedicated calibration systems: the Diffuser Ball and the Reflectivity Monitor (Section 3.4). These systems are crucial for assessing the light absorption and reflection characteristics within the detector, which directly impact the efficiency of photon detection. Additionally, estimating the background detected in the NV is essential for setting the lower energy threshold for the estimation of the neutron tagging efficiency. Under stable conditions, we expect the background to remain constant. Therefore, any fluctuations in the event rate could be attributed to variations in the sensitivity and detection efficiency of the detector itself. A good estimate of the background and overall detector conditions can be obtained by measuring the event rate with varying requirements for PMT coincidence. The details of these analyses are presented in the following subsections.

4.2.1 Transparency and Reflectivity

The optical properties of the NV, such as water transparency and wall reflectivity, along with its dimensions and active sensor area, are crucial in determining the size and shape of the detected Cherenkov signals. The reflectivity of the ePTFE as a function of the wavelength, shown in figure 4.11 has been measured when deciding the material to use for the NV walls. However we expect that due to impurity deposits on the walls, the reflectivity might deteriorate. Thus, to monitor the light collection efficiency of the NV and its stability over time, these optical properties must be consistently observed. This task is primarily accomplished using the reflectivity setup described in section 3.4, which allows for the injection of a fixed light signal into the detector. The spatial distribution of such a light signal from the reflectivity monitor channels is shown in Fig. 4.12. The time distribution of the injected photon signals follows an exponential distribution, with the decay constant determined by the optical properties. Figure 4.13 shows the summed distribution over all PMTs with only one reflectivity monitor channel turned on.

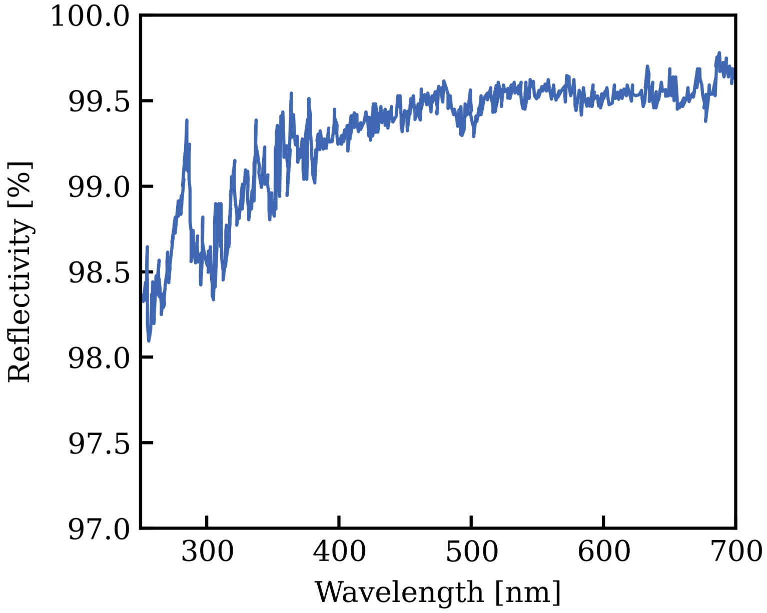

Figure 4.11: *Measurement of reflectivity of the ePTFE installed in the NV, as a function of the incident wavelength.*

The time constant from the reflectivity monitor runs can be determined using the following procedure. For a given run utilizing a specific optical fiber channel,

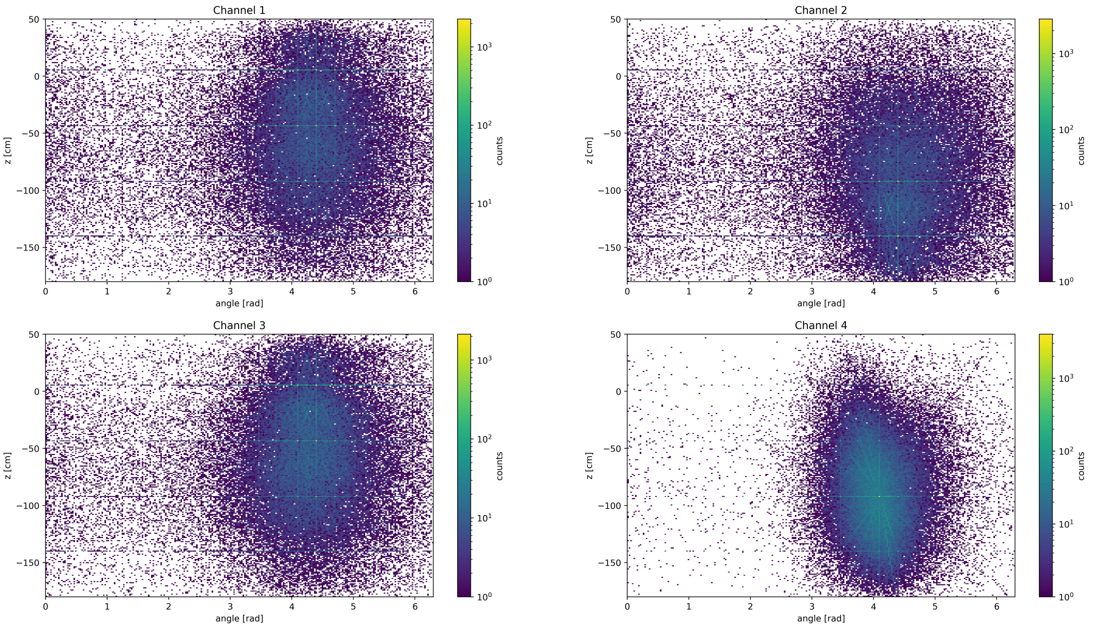

Figure 4.12: *Reconstructed average position of the detected events in the four channels of the reflectivity monitor.*

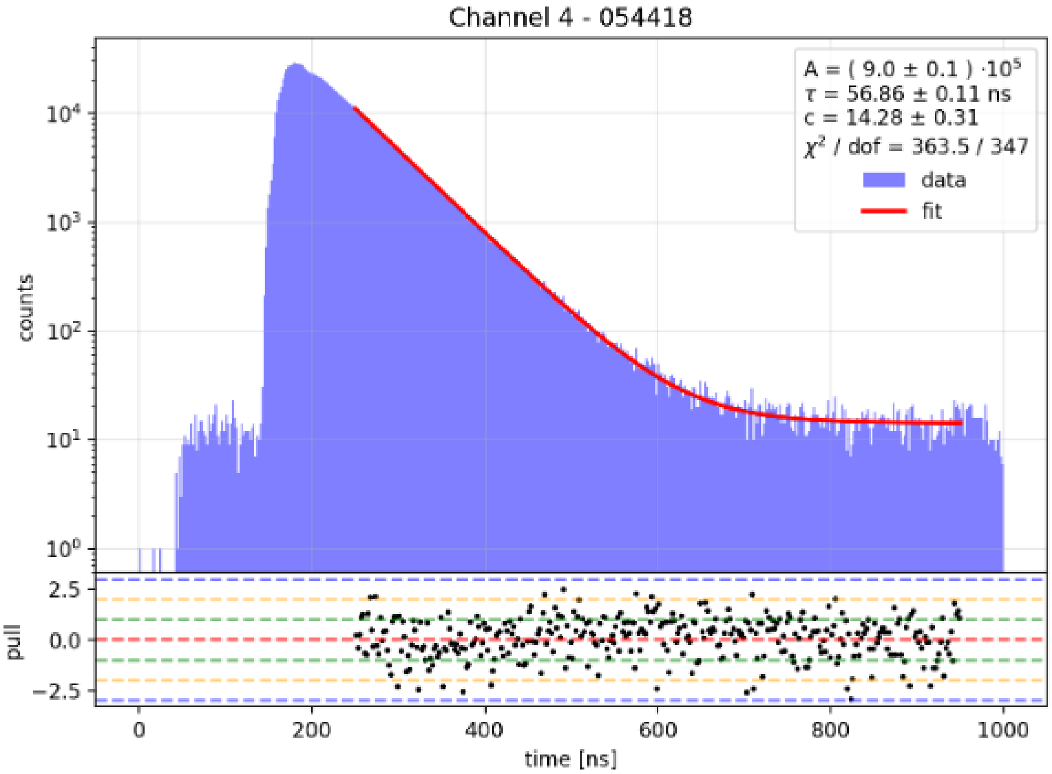

Figure 4.13: *Arrival time spectra of all PMTs for an injected light signal using one channel (the 4^{th}) of the reflectivity monitor. The solid lines show the best-fit model. The bottom panel indicates the residuals of the fit.*

the data recorded are from a series of time windows initiated at each trigger time. Within each time window, the `hitlets_nv` data are utilized: the time delays between the trigger time and each hit time are calculated and used to construct the distribution. The trigger time for each event is identified from the `raw_records_nv` data. This procedure has been encapsulated in a plugin that processes `raw_records_nv` and `hitlets_nv` data to produce a new data type named `ref_mon_nv`, similar to what is done for the gain analysis and the LED calibration. This new data type contains essential information for the reflectivity monitor analysis, comprising a series of hits where the PMT channel, the area, and its time relative to the preceding trigger are recorded. To ensure clearer timing distributions, several cuts have been applied before performing the exponential fits. At the single-hit level, a cut on the area keeps only hits with a minimum of 0.7 PE. This threshold is selected to filter out most nonphysical signals while preserving real signals. At the event level, another cut is applied to exclude events with a low number of contributing PMTs. This threshold is set to 7 PMTs. Once photons are diffusely reflected by the ePTFE walls, the distribution follows an exponential decay on top of a constant background:

$$R(T) = A \cdot \exp^{-t/\tau} + C. \tag{4.10}$$

The average time decay of the optical photon signal for the reflectivity monitor (λ = 375 nm) is found to be τ_{RM} = 57 ± 1 ns. Measurements conducted using the secondary system of diffuser balls have provided analogous results, with a difference in the decay constant (τ_{DB} = 63.9 ± 0.5ns), attributable to the different water transparency at the wavelength of the light source used in the diffuser balls (λ_{DB} = 448 ± 3nm), although further investigation on the discrepancy are ongoing. Given the excellent performances observed, ePTFE reflectivity and water transparency cannot be easily disentangled. Thus, the optical properties of the NV were monitored in terms of the optical decay parameter of injected light signals, τ. In principle, breaking this degeneracy can be done by deriving a model for the water absorption length from direct measurements, including them in the Monte Carlo simulation of the apparatus.

The time stability of the optical decay constant τ is shown in Fig. 4.14. A small decrease (< 0.5 ns, quantified also with a linear fit) can be observed over one year of operation, which does not significantly affect the light collection efficiency in the apparatus. The reflectivity monitor played an important role during the commissioning of the GdWPS, between the two Science Runs (Post SR0) in 2022. In this period there was the first connection of the GdWPS to the XENON water tank to purify its demi-water with various flow adjustments: runs for each optical fiber channel of the reflectivity monitor were conducted more frequently alongside the weekly calibration.

Also throughout this period, no significant decrease in the time constant

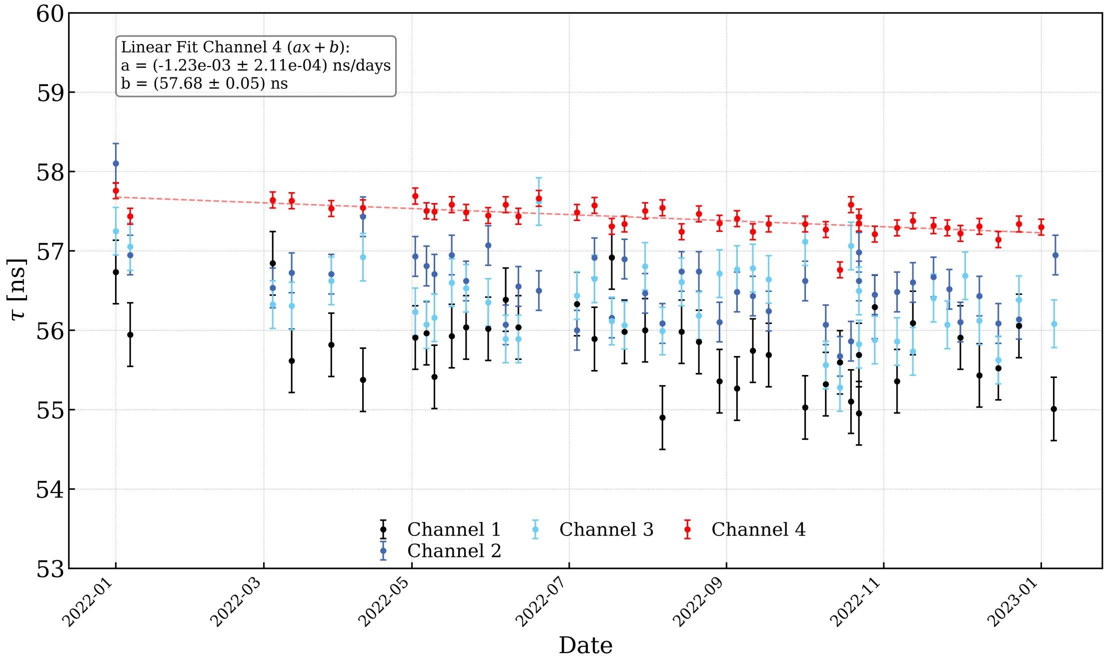

Figure 4.14: *Trend of the time decay parameter τ estimated from the fit of the time distribution in reflectivity monitor runs for the four different channels, in one year of data taking starting from the end of SR0. The linear fit performed on channel 4 data reveals a slightly decreasing trend of* < 0.5 *ns/y. However, this decrease does not significantly affect the light collection efficiency.*

was observed, suggesting that the connection of the GdWPS did not lead to a degradation of the NV performance. Again, On December 19, the system switched back to the normal WLP. Reflectivity monitor runs continued until January 2023. No significant decrease in the time constant was observed during this period either, indicating stable optical properties independent of the purification system employed. The same level of stability was also observed throughout SR1, with excellent consistency. During this period, monitoring was primarily conducted through channel 4 as it proved to be the most reliable, partly due to a better light transmission related to the hardware and its installation. The trend during SR1 is shown in Fig. 4.15

Figure 4.15: *Trend of the time decay parameter τ estimated from the fit of the time distribution in reflectivity monitor runs for the four different channels, during SR1.*

4.2.2 The Neutron Veto background events

The analysis of the event rate for different PMT coincidence requirements, chronologically the first analysis conducted after the detector activation during the commissioning phase, was crucial in estimating the initial performance of the

NV, specifically in terms of the background rate (when requiring several PMTs in coincidence). The event rate can be easily estimated thanks to the event-building plugin, described in section 3.5.2. Immediately following the filling of the water tank with demineralized water, we monitored the rate for 4-, 6- and 10-fold PMT coincidences. During this initial phase of detector commissioning, an exponentially decreasing trend in the rate was observed, as illustrated in Fig. 4.16. This trend is well modeled by an exponential plus a constant distribution analogue to (4.10). The resulting half-life, derived by averaging the fit parameters of the rates of 4-, 6- and 10-fold coincidence, yields (3.91 ± 0.02) days. This aligns with the hypothesis of decaying ^{222}Rn in the water, sourced directly from the Gran Sasso rock. Given the effectiveness of this monitoring approach in estimating performance, it was continued throughout the science runs. The expected plateau for the 10- and 4-fold rate served as a benchmark, providing a reference point for comparison with the collected data, and allowing to establish a procedure for the monitoring of the data quality. Figure 4.17 displays the trend throughout SR0.

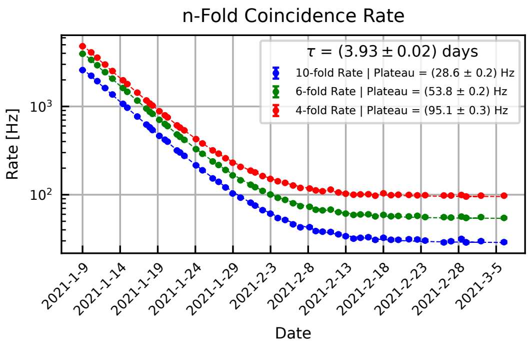

Figure 4.16: *Evolution of the 4-, 6-, and 10-fold coincidence rate during the commissioning of the NV. The trend has been fitted with an exponential function on top of a flat one. The obtained time decay constant is in agreement with the decay of Rn present in water at the beginning of the water tank filling.*

Upon inspection of the data quality, all data was accepted as no outlier run was observed, indicating a reliable data collection process with no significant deviations. A slightly decreasing trend in the 4-fold coincidence rate has been associated with the overall dark rate trend, which decreased during SR0, as explained in section 4.1.3. This drift was not observed in the 10-fold rate, suggesting it is related to accidental coincidences and uncorrelated hits on the PMTs rather than physical events. For SR1, the rate increased due to the enhanced PMT acceptance (increased up to ~ 95%) and to an increase in the dark rate, leading to a slightly higher rate of accidental coincidences. However, the trend remained stable over time as shown in figure 4.18, with fluctuations

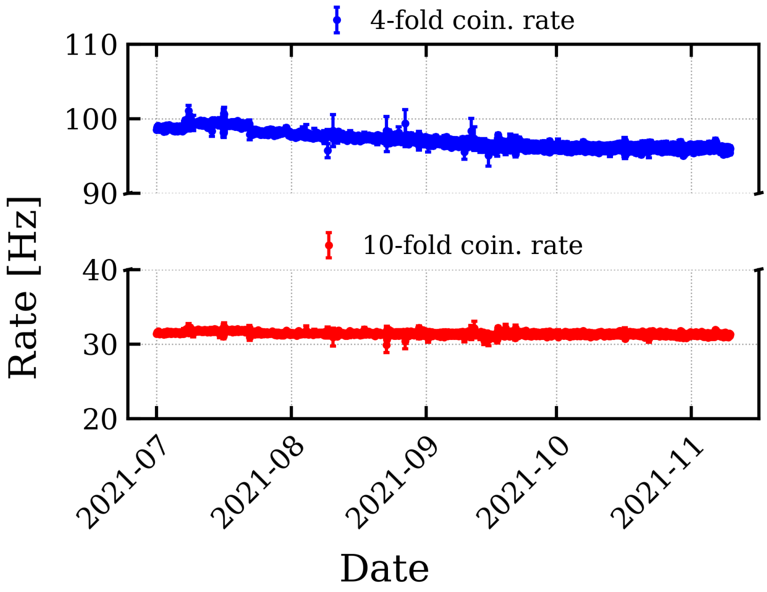

Figure 4.17: *Evolution of the 4- and 10-fold coincidence rate during SR0. Each point corresponds to a run. The 4-fold trend is slightly decreasing due to the PMT dark rate evolution. This plot also enters the NV data-quality selection.*

attributable to variations in the dark rate itself or to other operations affecting the DAQ ongoing.

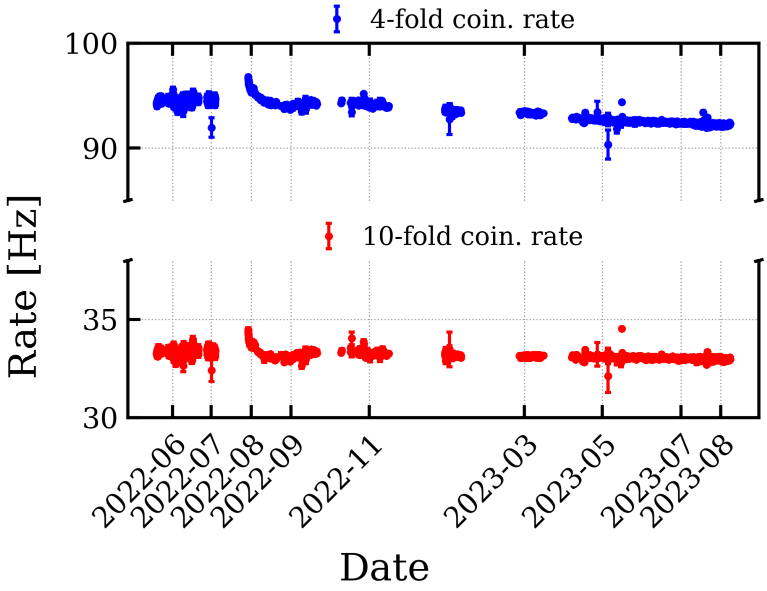

Figure 4.18: *Evolution of the 4- and 10-fold coincidence rate during SR1. Each point corresponds to a run. The 4-fold trend is slightly decreasing due to the PMT dark rate evolution. This plot also enters the NV data-quality selection. In this case, few outliers have been found in the data-taking period, which will be excluded from the analysis. For this plot only science runs have been considered; the empty periods are indeed related to detector calibration runs.*

The 10-fold coincidence rate, used as a benchmark threshold in the sensitivity study, reduces to around 30 Hz. This rate is primarily dominated by decays of various isotopes in the detectors' materials. We estimate that ~80% of the background in the NV originates from the NV PMTs. The typical spectrum of NV event area of background signals shows a fairly featureless distribution, as shown in Fig. 4.19, without any peak-like structure. To distinguish the various background contributions, an important parameter is the center-time of NV events. This is defined as the area-weighted average start time of the individual hitlets recorded within a single event. Figure 4.20 illustrates the distribution of the event center-time as a function of the event area, showcasing data from background runs (upper plot) and calibration runs with an AmBe source (lower plot), after bin-wise background subtraction. Within this distribution, five distinct components can be identified. The first component consists of events distributed almost vertically below approximately 20 PE, extending to large center-time values of about 500 ns. These events are observed exclusively in the background data and are likely the result of accidental coincidences (ACs) between PMT dark counts, as inferred from their hit patterns. The second and fourth components, present in both the background and calibration data plots, are attributed to Cherenkov signals. Notably, the fourth component forms a horizontal band around 60 ns, extending up to 60 PE in background data and up to 250 PE in calibration data. This characteristic center-time of approximately 60 ns is influenced by the NV optical properties, explained in section 4.2.1. For instance, the time distribution of Cherenkov photons within an event is modeled

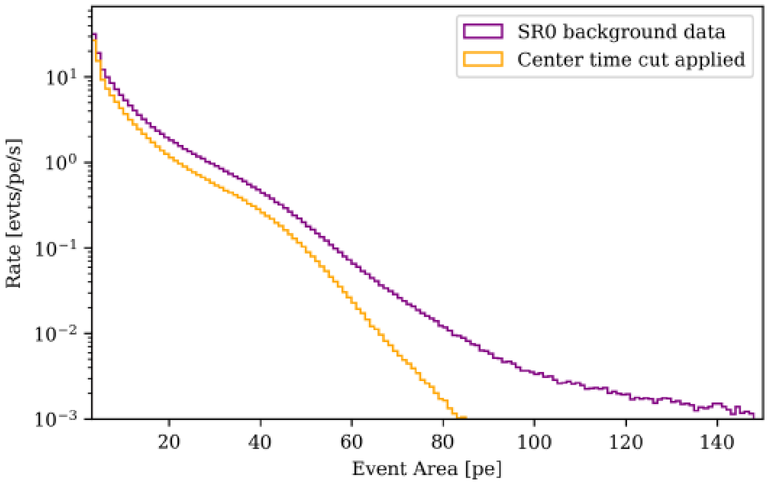

Figure 4.19: *Spectrum of background events in NV during SR0. The purple line represents all background signals with an area exceeding 3 PE and involving at least 3 PMTs. The orange curve further refines this selection to include only events within the central 95% contour of the center-time distribution in Fig. 4.20.*

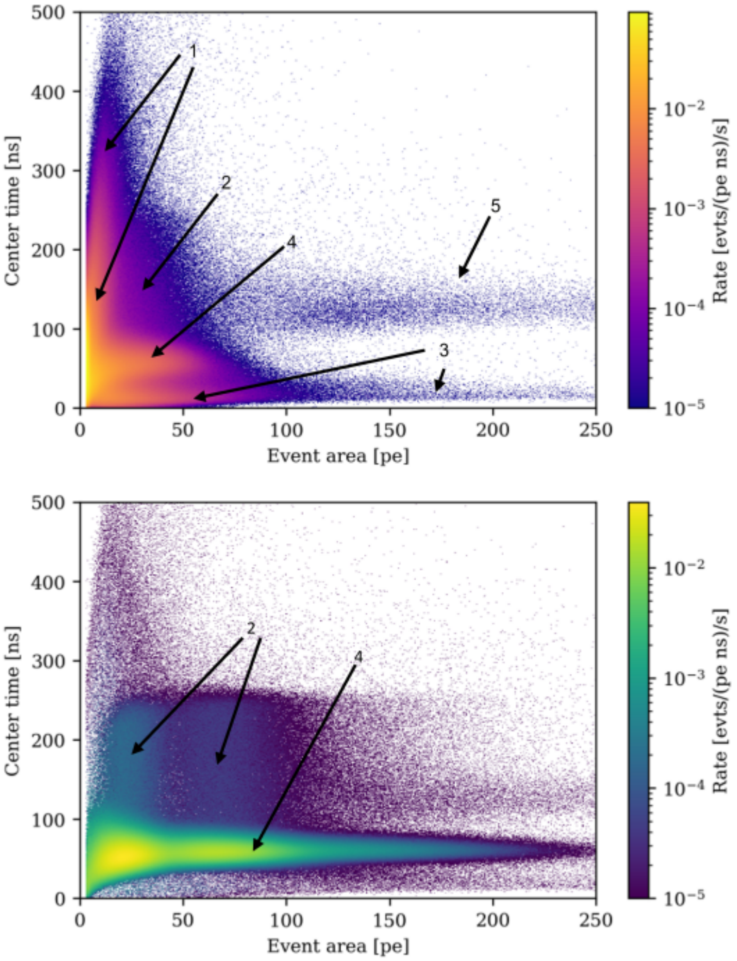

Figure 4.20: *Distribution of center-time vs. event area for NV events during SR0: The top figure presents the background data of the NV, while the bottom figure displays data from the AmBe calibration. The bottom figure has undergone bin-wise background subtraction based on the top figure. The background data can be categorized into five distinct components, two of which are also observable in the AmBe calibration data. The various contributions are associated to: (1) AC of PMTs' dark counts; (2 & 4) Cherenkov signals; (3) Afterpulses + Dark Counts or β-decays close to the PMT; (5) Un-identified background component. Plot from [126].*

by an exponential distribution, where the decay constant is shaped by factors such as detector size, water transparency, surface reflectivity, and photo-sensor coverage. The center-time value, serving as an estimator for the expectation value of this exponential distribution, corresponds to this decay constant. Moreover, the fourth component in the calibration data reveals two peak-like structures at event areas of approximately 20 PE and 80 PE, corresponding to the 2.22 MeV and 4.44 MeV γ-ray signals induced by the AmBe source. At smaller event areas, the center-time distribution broadens and becomes slightly asymmetric. Alongside the horizontal band, two column-like structures emerge at the positions of the full energy peaks, labeled as the second component in Fig. 4.20. These columns abruptly terminate at around 250 ns, forming an almost box-like structure, a behavior partially mirrored in the background data, albeit overlapping with the first component. These structures, as confirmed by dedicated MC simulations, are due to accidental pile-up between Cherenkov signals and PMT dark counts. The third component, resembling the regular Cherenkov signals' horizontal distribution but shifted towards smaller center-time values of about 20 ns, spans a broader event area range, akin to the AmBe calibration data. All these events share a commonality where a single PMT predominantly influences the event, as evident from Fig. 4.21. Therefore, the shape of these events is dictated by the signal shape of a single PMT, rather than the NV optical properties. At lower energies, these events are likely caused by PMT afterpulses accidentally paired with other dark counts. At higher energies, they are more likely dominated by Cherenkov signals due to β-decays within or near the quartz windows of the PMTs. Potential sources for such signals include β-decays within the chains of ^{232}Th, ^{238}U, and the β-decay of ^{40}K, identified during the material screening of the NV with the activities reported in Table 4.2. The final component, the fifth one, is observed at higher energies and center-time than those seen in the AmBe calibration data. This component of the background distribution is not yet fully understood. The typical hit pattern of these events does not suggest an artificial origin. The possibility of an accidental pile-up of two events is mostly discounted for two reasons. Firstly, the typical event window of about 200 ns and the high-energy background rate of around 30 Hz are insufficient to account for the observed event rate of approximately 10 mHz. Secondly, if this population were indeed caused by event pile-up, similar evidence would

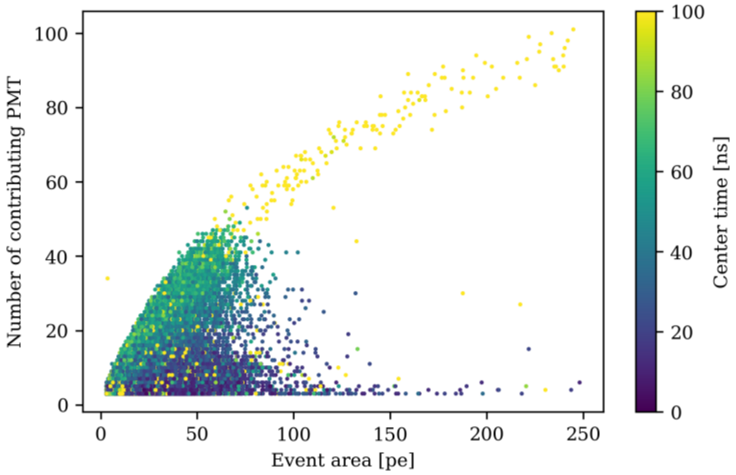

Figure 4.21: *Number of contributing PMTs Vs event area for SR0 NV background events, with the color scale representing the center-time parameter. Events with a smaller number of contributing PMTs typically belong to the third population of Fig. 4.20.*

be expected in the calibration data due to the higher overall rate in the detector. However, such evidence is absent. Therefore, it must be concluded that these events might have a genuine physical origin. To further probe the origin of these events, their spatial distribution was analyzed. As shown in Fig. 4.22, this distribution is notably localized compared to the uniform distribution of regular background events. The events predominantly originate from two different heights within the detector, spanning its full azimuth angle. A higher rate of events is observed between -50 cm < z < 50 cm than between -150 cm < z < -100 cm. This pattern suggests that the stiffening rings welded to the inner and outer TPC cryostat might be a contributing factor. These rings, located at specific z-positions, encircle the TPC cryostat and coincide with areas where higher background rates are observed in the TPC, contrasting with simulation predictions. In addition to these continuous distributions, a distinct cluster of events is noticeable at the position (5 rad, -120 cm) in Fig. 4.22, corresponding to the bottom of the beam pipe for the neutron back-scatter setup attached to the TPC cryostat. However, this spatial information alone does not fully explain the unique characteristics of the NV events. The observed shift towards larger center-times might be indicative of a pile-up of correlated events, such as a chained decay involving an isotope or state with a short lifetime. The event area distribution, shown in Fig. 4.23, reveals at least one peak-like structure with an average area of around 120 PE, corresponding to an energy of approximately 7 MeV[1]. If these events result from temporally correlated decays, one would expect to detect their constituents in a coincidence analysis between the TPC and NV, particularly if one of the decays involves a γ-ray capable of penetrating the

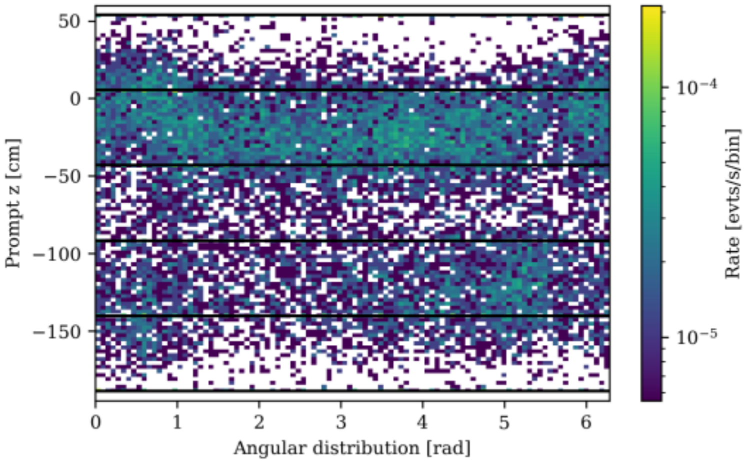

Figure 4.22: *Reconstructed position of the events of the 5^{th} component outlined in Fig. 4.20.*

---

[1] This correspondence between PE and MeV has been the results of NV Calibration with radioactive sources (AmBe) presented in the next chapter.

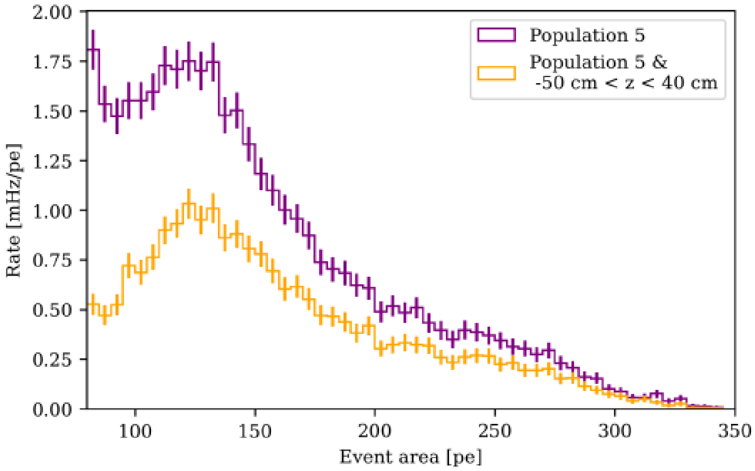

Figure 4.23: *Area distribution of the events of the* 5^{th} *component outlined in Fig. 4.20 before (purple) and after (yellow) the cut in the z-position shown in Fig. 4.22, which reveals a peak-like structure with an average area of around 120 PE.*

stainless steel cryostat. However, studies of the ER background using TPC-NV coincidence, conducted for the low ER analysis of XENONnT, did not identify any matching signals. This suggests that either the signals originate from a different source, or the decay constituents (such as β-decays or conversion electrons) cannot penetrate the TPC cryostat. Consequently, the higher activity observed in the TPC and the unusual background component in the NV might be unrelated or stem from different decays within the same chain. The similarity in their spatial reconstruction, however, challenges the mere coincidence hypothesis.

5

CALIBRATION OF NV EFFICIENCY

During the data acquisition phase of XENONnT, typically at the beginning of a Science Run, we conducted calibrations using neutron and gamma sources, with Americium-Beryllium (AmBe) and Thorium. The main calibration to understand the detector response to elastic interactions with xenon nuclei, crucial for the search for WIMP DM or CEνNS, is the nuclear recoil calibration of the TPC. This calibration is also effective in determining the NV tagging efficiency. The analysis of the calibration runs employs a novel coincidence technique between the NV and the TPC, that involves the simultaneous measurement of neutrons and gammas emitted from an AmBe source. In this chapter, there will be a discussion on the key characteristics of an AmBe source and the operational principles of the calibration technique. Neutrons serve as an excellent tool for studying the detector response to WIMP DM, as both result in elastic nuclear recoils when interacting with xenon. In general, neutrons also present significant challenges for XENONnT scientific goals; neutrons emitted from detector materials through spontaneous fission or (α, n)-reactions can enter the TPC fiducial volume, mimicking WIMP-like signals. While some neutron interactions can be differentiated from WIMPs due to their tendency for multiple scatters, identifying such multi-scatter events becomes challenging with small energy deposits. The NV role is to tag these neutrons by detecting the 2.22 MeV γ-ray released upon neutron capture on hydrogen (at least for this phase of operation with demineralized water), thereby mitigating this background source. To characterize this **tagging efficiency**, Section 5.3 delves into the calibration of the NV neutron response. The neutron **detection efficiency** of the NV, a measure of the probability of detecting a neutron after its emission, is introduced in section 5.4. This efficiency serves mainly as a benchmark for comparing the NV performance with other water Cherenkov detectors like SNO or SK. Additionally, the chapter includes a brief discussion on the use of a Thorium source (Section 5.1), which chronologically was the first calibration performed on the NV. Though of minor importance, this gamma source served as a reference for the future positioning of the AmBe source through the calibration pipes (U-tubes), and to have a preliminary estimation of the detector resolution to γs of energy close to the ones emitted after the neutron capture in water. The final section of this chapter (Section 5.5) introduces the NV Hitlet Simulator, an MC tool that has been developed and deeply used for the MC - Data matching, particularly in the contexts of the AmBe calibration. Once this matching is fine-tuned by adjusting the detector parameters in the simulation, we could estimate the NV performances under different detector conditions, i.e. in the presence of Gd at different concentrations.

5.1 Thorium Calibration

In February 2021, during the NV commissioning, we performed the first calibration (which was then repeated a few months later) of the NV using a ^{232}Th source. This source, encapsulated, was strategically maneuvered through the U-tubes of the detector, as illustrated in Figure 5.1. The primary objective of employing the Th source was to evaluate the spatial response of the NV to gamma emissions, achieved by relocating the source in the U-tubes. Within the decay chain of ^{232}Th

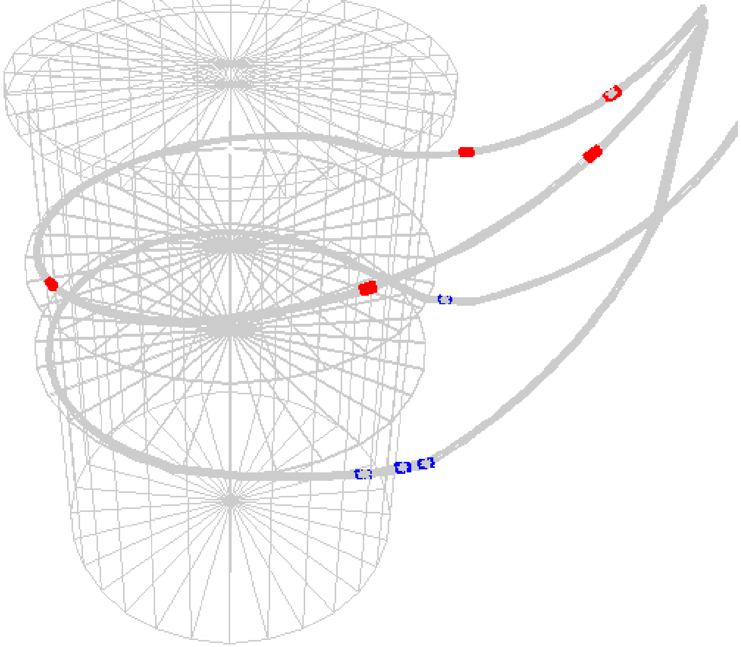

Figure 5.1: *Schematic of the U-tubes embracing the cryostat, as it results from the detector geometry implemented in the Geant4 simulation framework.*

there is ^{208}Tl, which predominantly emits a gamma ray of 2.6 MeV energy [128]. The interest in this gamma source in the NV context is linked to the gamma energy proximity to the energy released from the neutron capture in water (2.2 MeV), thus it allowed for a preliminary estimation of the NV resolution and of the characteristic timing associated with photon detection. Lastly, this allowed determining the source spatial positioning within the NV. Precise localization of the source is needed particularly for the neutron calibration, where also the distance from the TPC has to be taken into account. We refer to each position with the following nomenclature:

$$\text{ex: } \underbrace{\text{Bottom}}_{\substack{\text{Which of the}\\ \text{two tubes}}} \quad \underbrace{CW}_{\substack{\text{Insert orientation:}\\ \text{Clockwise}}} \quad \underbrace{6d9m}_{\substack{\text{Inserption Depth:}\\ \text{6.9 meters}}}$$

In Fig. 5.2 is shown the hit-map for one calibration run, highlighting the pattern that is seen by the PMTs, which allowed the position reconstruction, while figure 5.3 shows the event area distribution for one background run and for one thorium run; the latter is presented after the background subtraction, in order to appreciate the 2.6 MeV broad peak.

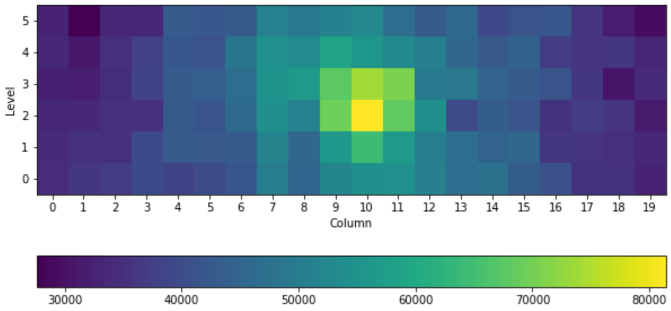

Figure 5.2: *Hit map for one Thorium run with the source located at the Bottom U-tubes (position CW6d). Each square/bin represents one NV PMT. We have 20 columns, each having 6 PMTs (called levels here). The color map represents the number of hitlets in 10 minutes of run.*

5.2 AmBe Calibration

5.2.1 AmBe Source

In the following, more details about the AmBe calibration source used in XENONnT will be provided. The AmBe source emits neutrons through the alpha-capture reaction ^{9}Be$(\alpha, n)^{12}$C, with ^{12}C either in the ground or first excited state. This is an attractive feature for a calibration source as the gamma-ray emitted when ^{12}C is on its first excited state can be used to cleanly identify neutron

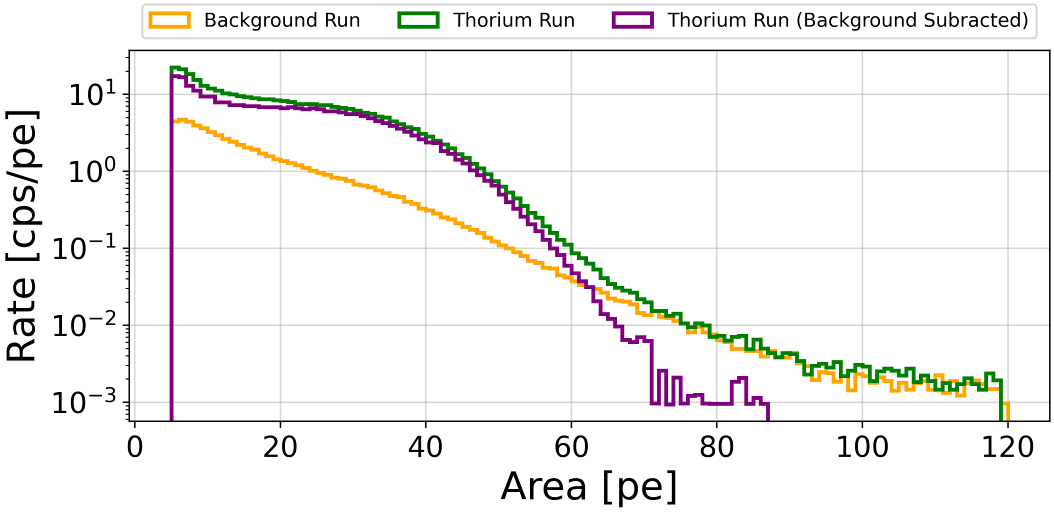

Figure 5.3: *Event area distribution for one background run (orange) and one Thorium run before (green) after (purple) the background subtraction.*

interactions in the NV or the TPC by the requirement of a tight coincidence between the two detectors. The alpha particles are emitted by ^{241}Am, decaying with a half-life of about 432.2 years into an excited state of ^{237}Np*, at an energy level of 60 keV. The alpha capture on ^{9}Be leads to a ^{13}C* nucleus, decaying by neutron emission into ^{12}C ground or excited states, the two most relevant ones being at 4.44 MeV and 7.65 MeV. A schematic of the involved energy levels is shown in Figure 5.4.

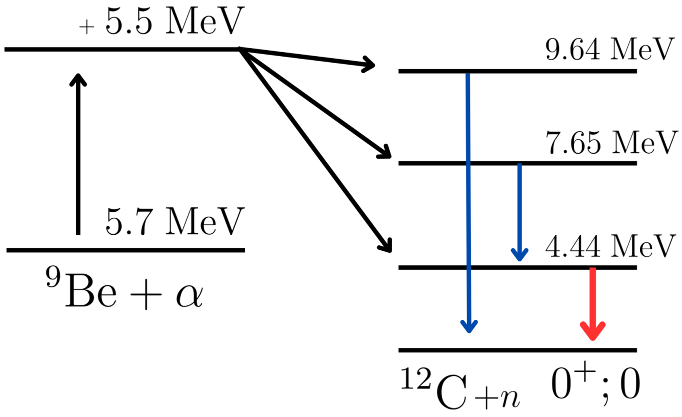

Figure 5.4: *Schematic of the energy levels involved in the ^{9}Be$(\alpha, n)^{12}$C reaction. The maximum kinetic energy of the ^{241}Am alpha particles is indicated by an additional energy level 5.5 MeV above the ground state of ^{9}Be. Blue arrows represent transitions via internal conversion, while the red arrow indicates a transition via gamma emission. The energy levels and the transition properties of ^{12}C are sourced from [129].*

The branching ratio of the various states depends on the alpha particle kinetic energy upon impacting the ^{9}Be nucleus, and this depends on the manufacturing of the source. Literature [130, 131, 132] typically cites a 60% branching ratio for the first excited state of ^{12}C, slightly lower than the 67% expected from neutron-production cross sections at ^{241}Am typical alpha energy of 5.5 MeV. Studies of the branching ratio performed during SR0 indicate a slightly lower branching ratio of about 50% for the source used in XENONnT. However, a precise knowledge of the branching ratio is not required for the calibration of the NV performance: the key information is that the presence of the gamma ensures that a neutron has been emitted so that the gamma can be used as a trigger for the neutron search. At the time of calibration, the source had a neutron rate of (159 ± 4) n/s estimated based on the decay rate measured in 2013 for XENON100 [133] and the half-life of ^{241}Am.

The neutron energy spectrum from AmBe (Figure 5.5) is continuous, with a maximum energy of around 11 MeV and an average one of about 4.5 MeV, though also these values depend on the source manufacturing. The spectrum features various peaks corresponding to the production cross-section.

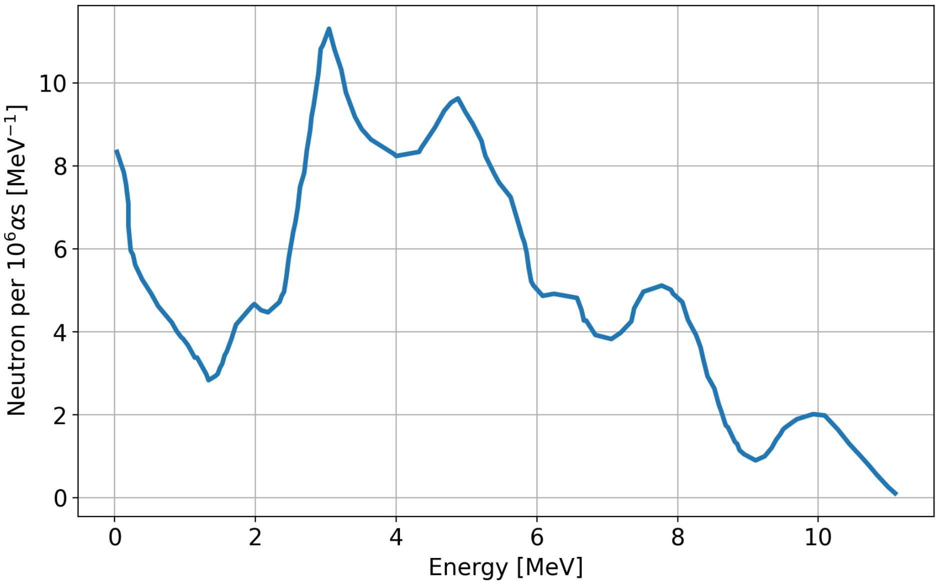

Figure 5.5: *The neutron energy spectrum of Am-Be source. Plot re-adapted from [130].*

AmBe serves as an alpha-neutron emitter for calibrating the single-scatter nuclear-recoil (SSNR) response of the TPC, as well as the NV efficiency in detecting neutron-capture signals and tagging SSNR signals. Calibration data was collected at three locations adjacent to the TPC cryostat at two different heights, with a fourth position inside the NV, at a similar distance with respect to both the cryostat and the lateral NV panels, to validate the NV response further.

5.2.2 AmBe Spectrum

Before delving into the tagging efficiency of the NV, a thorough understanding of the AmBe energy spectrum is needed. The goal here is to analytically describe the AmBe spectrum, determining also the overall source rate. This analysis is crucial for defining the selection boundaries for the 4.44 MeV γ-ray and for the next sections of this chapter. The development of a model to describe the AmBe data spectrum requires first a selection of a clean calibration sample. The selection criteria for NV events include the standard trigger conditions, i.e. a 3-fold coincidence within 300 ns. Before performing the fit of the energy spectra, two data quality cuts are applied. The first cut is based on the center-time versus area space. The center-time cut boundaries are depicted in Figure 5.6. The second cut uses the spatial distribution of NV events, determined by an area-weighted average over all PMTs active in the first 20 ns of an event. Figure 5.7 shows the spatial distribution for a specific source position, with the cut boundaries used.

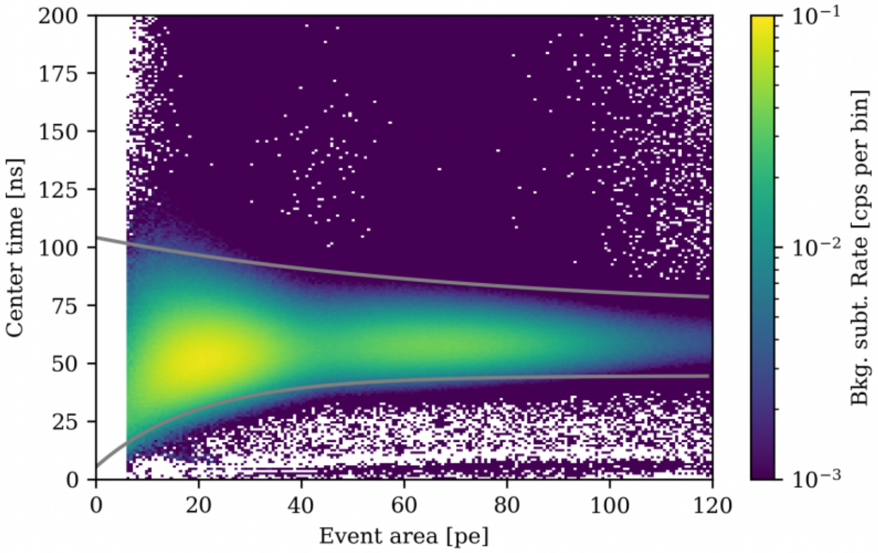

Figure 5.6: *Background subtracted spectra for the center-time cut space (left) for the top CW5d9m position. The gray lines indicate the boundaries of the center-time cut.*

In addition to these cuts, only events with an area larger than 5 pe are selected to further remove any accidental coincidence events due to PMT dark rate. After applying the cuts to the data of the given source position and background, a bin-wise background subtraction of the energy spectrum is computed. The energy spectrum before and after applying the cuts, as well as the result of the subtraction, are shown in Figure 5.8. The background-subtracted spectrum is

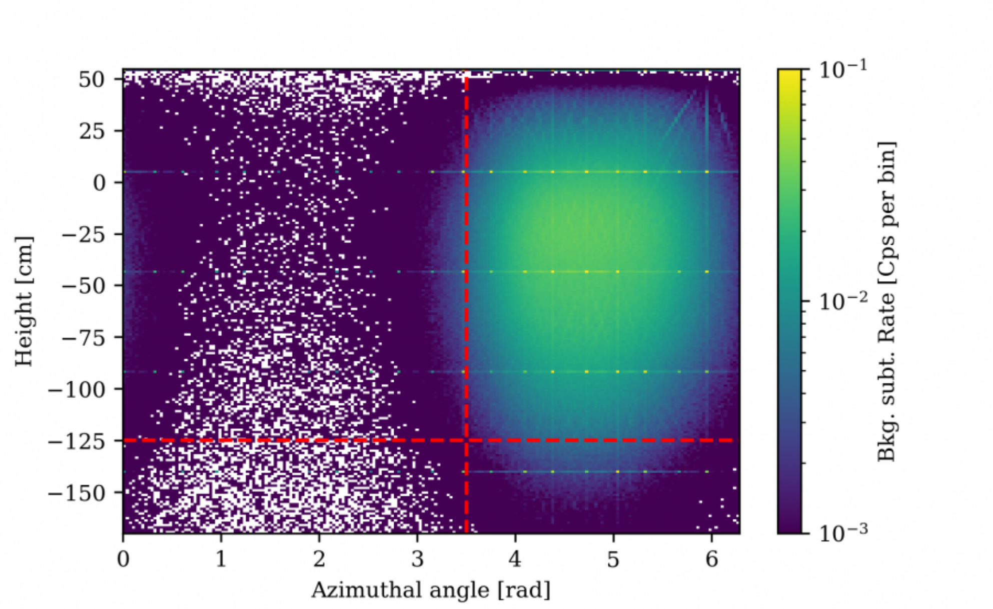

Figure 5.7: *Background subtracted spectra for the spatial cut for the top CW5d9m position. The red dashed lines show the cut boundaries for the spatial distribution. The center-time cut shown in figure 5.6 has been applied to obtain this plot.*

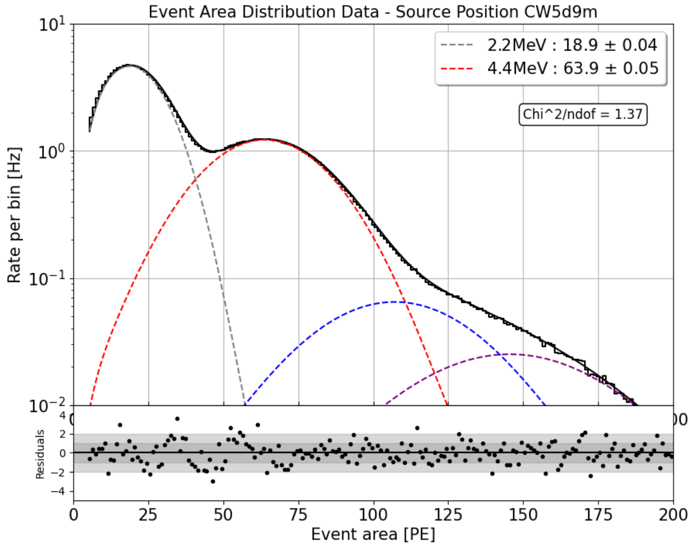

Figure 5.8: *Best fit of the NV AmBe energy spectrum taken at the bottom CW5d9m source position. The bottom panel shows the fit residuals. The individual fit components are also shown in different colors*

then fitted with the following function:

$$f(x; A_1, A_2, A_3, A_4, \mu_1, \mu_2, \mu_3, \mu_4, \sigma_{th}, \mu_{th}, s, o, c) = \\ N_{cdf}(x, \mu_{th}, \sigma_{th}) \cdot \left(\sum_{i=0}^{4} N(x, A_i, \mu_i, \sigma(\mu_i, s, o)) + c \right) \tag{5.1}$$

Here, $N(x, A_i, \mu_i, \sigma(\mu_i, s, o))$ represents a Normal distribution, and $N_{cdf}(x, \mu_{th}, \sigma_{th})$ is the cumulative of a Normal distribution, modeling the detector threshold. The width of each Normal distribution is constrained by an energy resolution σ, defined as:

$$\sigma(\mu, s, o) = \sqrt{\mu \cdot s + o} \tag{5.2}$$

where μ is the position of the corresponding peak. The energy resolution curve is motivated by the fact that each peak should follow Poisson statistics, with a σ proportional to the square root of the number of detected photons μ. Given the fact that a water Cherenkov detector has a rather high energy threshold, an additional offset term was added to the energy resolution. The fitting procedure, performed using a Least Squares method via the `iminuit` package [134], accounts for bin uncertainties estimated through Gaussian error propagation:

$$\Delta r_i = \sqrt{(\Delta N_{AmBe}/T_{AmBe})^2 + (\Delta N_{Bkg}/T_{Bkg})^2} \tag{5.3}$$

assuming that each bin in calibration and background data follows Poisson statistics and that the uncertainty on the total livetime is negligible. The best-fit result is depicted in Figure 5.8: the first peak is due to neutron captures on H (2.2 MeV gamma), while the second one comes from the 4.4 MeV gamma of C de-excitation. The observed spectrum high-energy tail is likely caused by neutron capture on ^{56}Fe. This broadening of this peak is attributed to the cascade of γ-rays with a total energy of 7.6 MeV released during the capture process. Such a cascade in a water Cherenkov detector, with a Cherenkov threshold of about 264 keV, results in a more pronounced spread of the full energy peak. Another potential source of high-energy gammas comes from higher-energy C de-excitation. This fit has been replicated for other source positions, showing similar results. Although the model described by (5.1) performed well, finding an accurate analytical model is challenging due to the high precision required by the high statistics of calibration data. The same model has been applied to fit the MC-generated AmBe spectrum, with its generation and analysis detailed in Section 5.5. Based on the estimates for A_1 and A_2 of the best fit it can be further seen that our AmBe source has a gamma/neutron ratio of about ~50 %, smaller than the typical values found in the literature; this may depend on the AmBe powder mixture. The absolute neutron rate is shown in Fig. 5.9, with also the fraction of high energy neutron capture events producing more than 60 pe events (i.e. the capture rate on ^{56}Fe) reported. The absolute rate of detected neutrons increases when moving away from the TPC, as the solid angle of the neutron-veto around the source position increases; on the other hand, the rate of captures on heavier nuclei decreases since fewer neutrons can reach the cryostat.

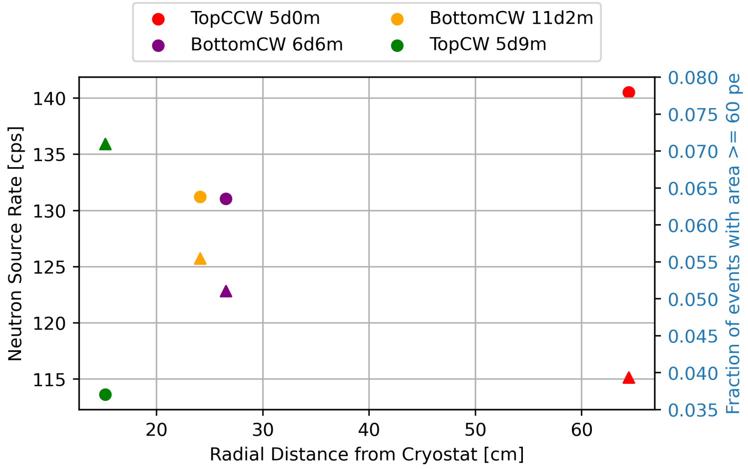

Figure 5.9: *Detected neutron rate (circles) and fraction of high-energy neutron capture events (triangles) as a function of the radial distance from the cryostat.*

5.3 Neutron Tagging Efficiency

Neutrons originating from materials within the detector pose a significant challenge to WIMP DM searches. Similar to WIMPs, these neutrons elastically scatter off the detector target nuclei, resulting in NRs that are indistinguishable from potential DM signals. In the XENON1T experiment, neutron signals were differentiated from DM by identifying multi-scatter events, where two or more interactions occur in quick succession within the detector's active volume. However, due to the substantial mass difference between xenon and neutrons, many neutrons simply backscatter off xenon nuclei and exit the sensitive volume without a second interaction. This is the reason why, in XENONnT, we built a (Gd) water Cherenkov neutron-veto to tag those neutrons in the water volume outside the cryostat.

This section focuses on estimating the neutron tagging efficiency, a crucial parameter of the NV. It quantifies the fraction of "dangerous" neutron signals in the TPC that are tagged by the NV, through the delayed coincidence with the 2.22 MeV signal due to neutron capture on hydrogen. The neutron tagging efficiency ζ, for a selected NR single-scatter sample, is defined as:

$$\zeta = \frac{\text{Number of neutron-capture events detected in the NV at a specific threshold}}{\text{Number of nuclear recoil single scatter events}} \tag{5.4}$$

The efficiency calculation is based on the AmBe calibration discussed in detail in section 5.2.1. The pattern of the events under study is schematized in figure 5.10.

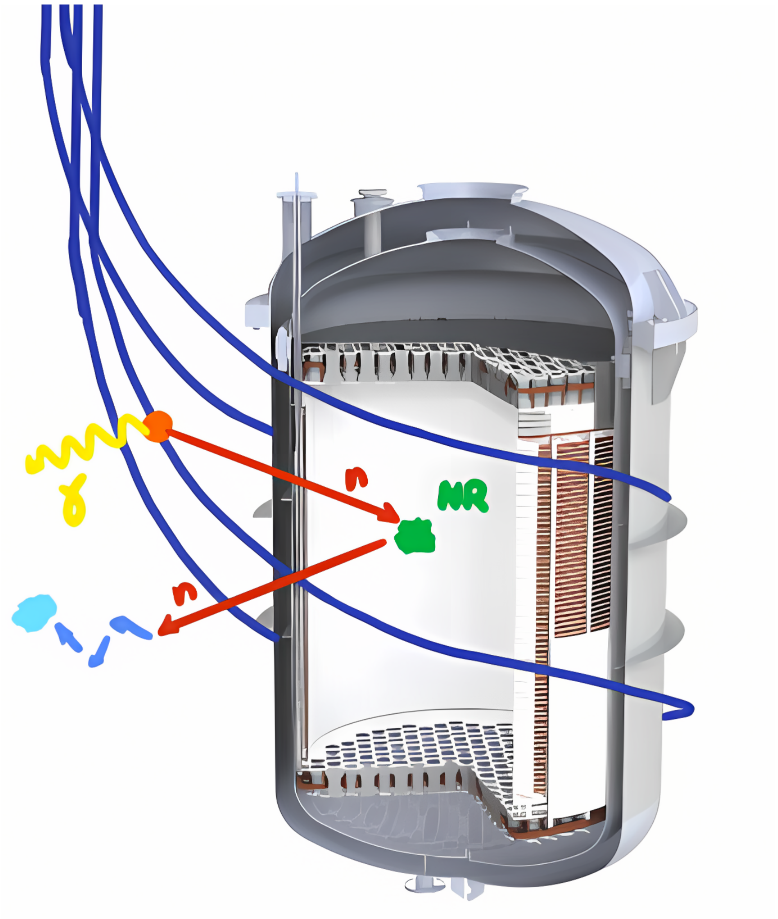

Figure 5.10: *Schematic showing the measurements of the NV tagging efficiency with the AmBe calibration. We search for the time-coincidence between the 4.4 MeV gamma in the NV (yellow) and the S1 signal of the NR in the TPC (green), then we look for the 2.2 MeV gamma of neutron capture in the NV (light blue).*

The signature is the same as the one expected from the neutron background, except for the position of the neutrons' origin and the additional 4.44 MeV γ-ray signal detected by the NV, employed to clearly identify NR single scatter events. According to its definition, the tagging efficiency relies on the selection thresholds set for NV events and the length of the time window, where delayed coincident signals are sought in the NV. These parameters must be optimized to balance the desired tagging efficiency against the loss in live time of the TPC due to accidental coincidences with background events in the NV.

The NR single-scatter events were selected by requiring a tight time-coincidence between the 4.4 MeV γ-ray signal recorded by the NV and the NR S1 signals detected in the TPC, using a 400 ns coincidence window. This coincidence selects well-reconstructed NR S1 signals with 99.9% purity. Additional data-quality cuts are applied to the TPC events to select only well-reconstructed single-scatter events, and only those NR signals found within the 90% contour of the NR band are used for the calibration of the NV tagging efficiency. These selected data are shown in Figure 5.11.

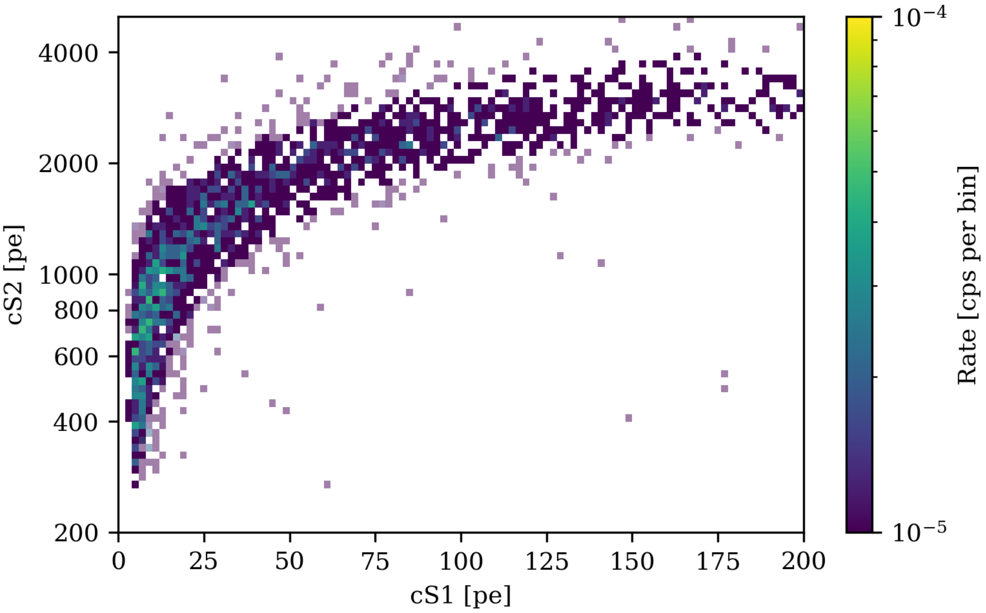

Figure 5.11: *cS2 versus cS1 space showing all NR single-scatter events within the 90 % contour of the NR band.*

To get the number of tagged NR interactions, it is necessary to identify all NV signals in coincidence with NR interactions. The coincidence, computed by a dedicated plugin inherited from the base coincidence for the event building, is built between the time of the S1 signal and the NV event, with the S1 signal acting as the trigger. The time window spans from -1000 μs to 2000 μs around the S1 and it is depicted in Figure 5.12. The spectrum exhibits a well-known structure marked by a pronounced peak at the center, followed by an exponentially decreasing distribution, all set on top of a flat plateau.

The central peak is populated by the 4.4 MeV γs in the NV detected in the selected time window. A closer look reveals additional minor peaks near the primary γ-peak, specifically around 2 μs and 8 μs. These are likely due to an increased background event rate in the NV, triggered by PMT afterpulses.

The exponential distribution is associated with radiative neutron capture signals on various materials, in particular hydrogen. The decay constant of this distribution is shaped by the effective capture time of all isotopes that capture neutrons and generate detectable signals inside the NV (for instance one has to take into account captures on other materials apart from hydrogen, e.g. ^{56}Fe in the SS). Finally, the plateau is given by random coincidences between the two detectors.

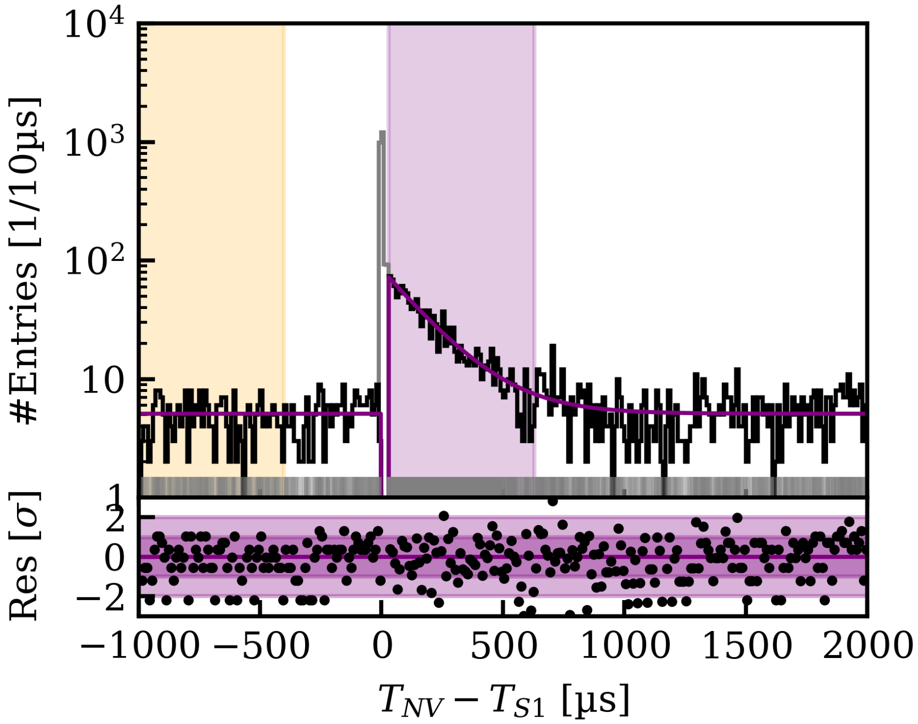

Figure 5.12: *Distribution of the time difference between NV events and the triggering single-scatter nuclear-recoil S1 signal in the TPC. The small gray vertical lines indicate the individual time differences. The purple line shows the best fit of the time distribution. The purple and orange areas indicate the ROI and background reference regions explained in the text. The black histogram shows a binned representation of the data whereas the gray-shaded part indicates bins excluded from the fit region. The bottom panel shows the residuals of the best fit with the binned data.*

To calculate the number of neutron capture signals detected by the NV, we compare the number of events within the purple region, spanning from 30 μs to 630 μs, against those in the orange reference region, set between -1000 μs and -400 μs. The boundaries of the purple region are strategically chosen to maximize the detection of neutron capture signals while being outside of the 0 μs to 30 μs range, contaminated by afterpulses. The area distribution of these selected events is shown in Figure 5.13. The events in the purple signal region exhibit a peak-like pattern, aligning with the general shape of the hydrogen neutron capture peak, as deduced from the best fit discussed in a previous section.

By integrating the data within the purple region and subtracting the counts from the orange background reference area, we can determine the number of tagged NR single scatter signals. This calculation directly informs us about the tagging efficiency for the chosen veto window of [30 μs, 630 μs). However, this specific window may not be entirely suitable for scientific data analysis,

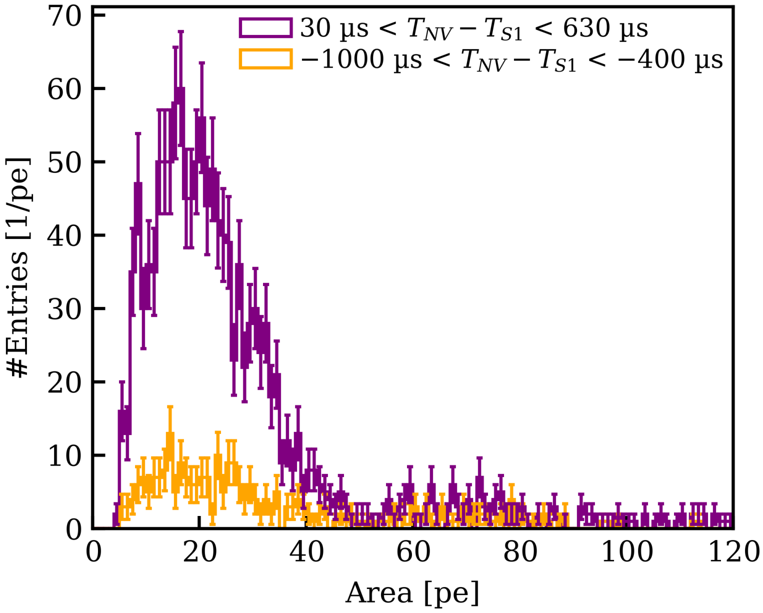

Figure 5.13: *Event area distribution for the signal (in purple) and background (in orange) reference region of Fig. 5.12. The error bars indicate the statistical uncertainties in each bin.*

as a significant portion of capture events are known to occur in the first 30 μs. Additionally, the total duration of the window used for the WIMP search is not 600 μs, since we want to minimize the detector deadtime. Therefore, to accurately compute the tagging efficiency, it is necessary to adjust the selection criteria and take into account additional corrections.

Firstly, to calculate the correction for the veto window, we use the cdf of an exponential distribution knowing its decay constant which is the one associated with radiative neutron capture. To estimate this we fit the entire time distribution, excluding the γ-peak and afterpulse region, using an extended unbinned log-likelihood method. Figure 5.14 displays the best fit, characterized by an exponential distribution superimposed on a uniform background. This fit was executed using an extended unbinned maximum-likelihood method. The decay constant of the exponential distribution, τ_C, results to be $(180 \pm 8)\mu$s. This value is lower than the expected ~ 200 μs for a pure water target, a discrepancy likely due to neutron captures on other isotopes like ^{56}Fe present in the cryostat materials.

This effect was further corroborated by systematically comparing the decay constant and the tail of the AmBe energy distribution (shown in Fig. 5.8), while varying the source distance from the cryostat. A neutron capture time of $(202.1 \pm 0.2)\mu$s, aligning well with measurements from other water Cherenkov detectors, was observed at larger distances from the cryostat.

The veto window correction factor, ϵ_{TW}, is estimated by comparing the

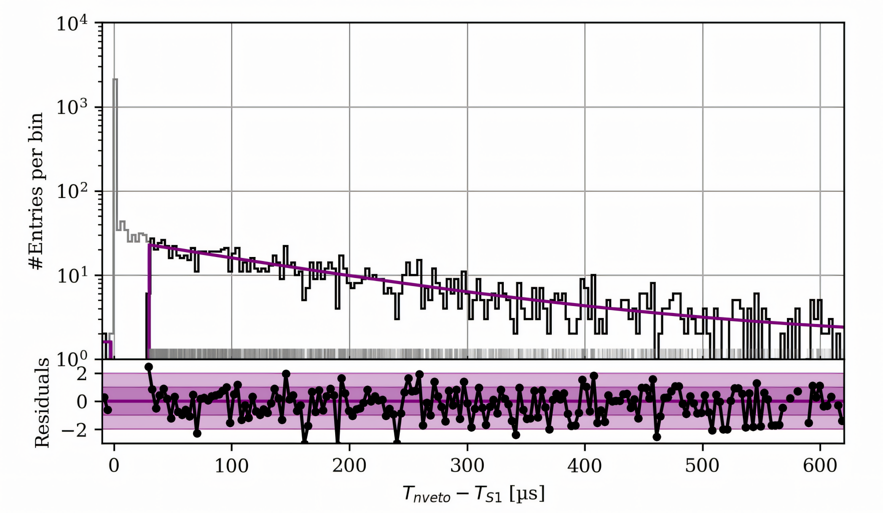

Figure 5.14: *Best fit of the hit time distribution in AmBe calibration runs, zoomed in the [0, 600] µs region. The gray part of the histogram indicates the data in the initial time region excluded from the fit represented by the purple line. The bottom panel shows the residuals of the fit.*

fraction of the exponential distribution covered by the purple time window in Fig. 5.12 to the respective veto window. Therefore, the correction is solely determined by the decay constant τ_C of the exponential distribution and is expressed as:

$$\epsilon_{TW} = \frac{\exp_{cdf}(t_1, \tau_C) - \exp_{cdf}(t_0, \tau_C)}{\exp_{cdf}(630\mu s, \tau_C) - \exp_{cdf}(30\mu s, \tau_C)} \tag{5.5}$$

where t_0 and t_1 denote the start and end of the veto window used for NV tagging in the science run.

Lastly, considering that the AmBe calibration was performed at only a limited number of locations around the cryostat, and given the differences in neutron energy distribution between AmBe and background neutrons, an additional geometrical correction factor, ϵ_{geo}, was calculated using Geant4 [135] simulations. The correction accounts for the spatial distribution of neutron sources intrinsic to the TPC and their neutron yields, as identified in the material screening results of the TPC components. This approach is similar to the one described in [136]. According to the simulations, approximately one-third of all background neutrons are estimated to originate from each of the following TPC components: the PMT ceramic stem, the PTFE walls, and the stainless-steel cryostat. The correction factor, ϵ_{geo}, is derived by comparing the simulated tagging efficiency for background neutrons against the efficiency for neutrons from the AmBe calibration. Although the simulated efficiency for AmBe is slightly higher than what was observed in the actual data, both results align within their statistical uncertainties. The simulations predict a tagging efficiency of (71 ± 1)% for an infinitely long tagging window. This is in close agreement with the (70 ± 3)% efficiency observed in the data using a 1200 μs long tagging window. The relative geometrical correction factor for radiogenic neutrons, ϵ_{geo}, is determined to be minimal, with a value of 1.01 ± 0.02. This indicates that the spatial distribution of the TPC intrinsic neutron sources has a negligible impact on the overall tagging efficiency of the NV system.

After calculating the number of neutron capture events and applying all correction factors, the tagging efficiency of the NV can be estimated with:

$$\zeta\left(t_0, t_1\right) = \epsilon_{\text{vw}}\left(t_0, t_1\right) \cdot \epsilon_{geo} \sum_{i=A_{\text{th}}}^{\infty} n_{\text{sig},i} - n_{\text{bkg},i} \tag{5.6}$$

where $n_{sig,i}$ and $n_{bkg,i}$ represent the number of neutron capture signals and background signals found in the i_{th} bin of Figure 5.13, respectively, for a specific n-fold coincidence requirement and an event area threshold A_{th}. The calculated tagging efficiencies for 250 μs and 600 μs windows are presented in Figure 5.15, requiring a 5-fold PMT coincidence, for different thresholds of the signal area in the NV.

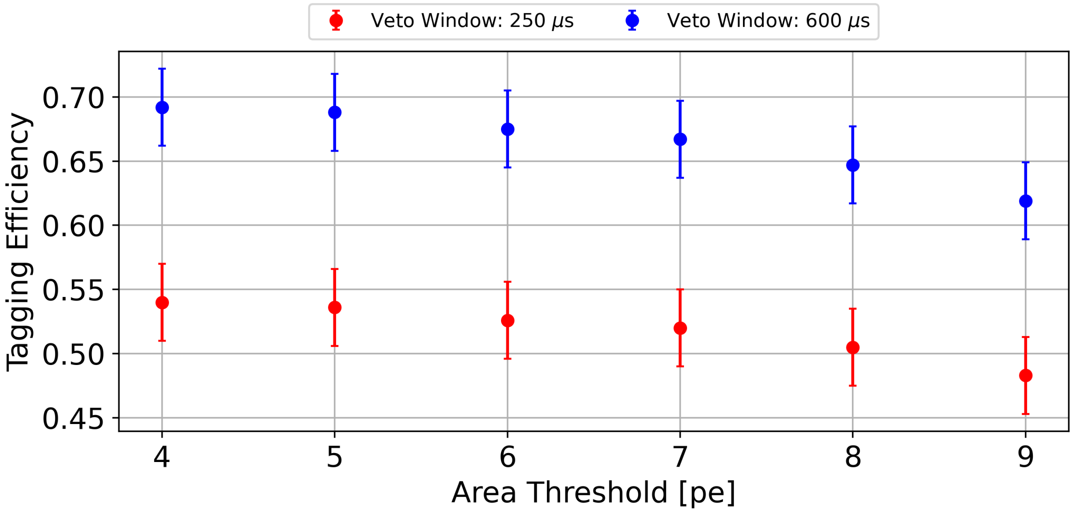

Figure 5.15: *Tagging efficiency of the NV in SR0. The red and blue data show the tagging efficiency for a 250 μs and 600 μs veto-window, respectively. In both cases, it was required that at least 5 PMTs contribute to an NV event.*

For the Science Run 0 (SR0), a neutron-tagging window of 250 μs was employed, along with an event area threshold of 5 PE and a 5-fold PMT coincidence requirement. This setup achieved a tagging efficiency of (53 ± 3)% with a livetime loss of 1.6%. The tagging efficiency for a longer, 600 μs window using the same threshold is (68 ± 3)%. The decision to use a smaller tagging window was based on the trade-off between deadtime and efficiency. The deadtime caused by NV tagging increases linearly with the window size, while the additional gain in tagging efficiency diminishes.

5.4 Detection Efficiency

Water Cherenkov detectors, like SNO or SK [103, 39], use neutron capture on hydrogen to recognize interesting signals, as the inverse-beta decay of electron anti-neutrinos, and to differentiate between signal and background. In addition to the neutron tagging efficiency, specific to WIMP search, another useful parameter is the "neutron-detection" efficiency η, which represents more generically the probability of detecting a neutron given the number of emitted neutrons. By definition, it is higher than the tagging efficiency, since the neutrons are not required to first make a signal inside the TPC before their capture, hence the solid angle for the neutron to reach the water and be captured is larger. The detection efficiency has been measured using the same AmBe calibration data as for the NV tagging efficiency, but exploiting a different event topology, shown in Figure 5.16.

To calculate the number of emitted neutrons, the TPC is used to trigger on the 4.44 MeV γ-ray, then we search for delayed coincident neutron capture events in the NV. After applying a series of data-quality cuts, all 4.44 MeV gamma signals within the 3σ contour of the full-energy ellipse were selected. As illustrated in Fig. 5.17, the selection of 4.44 MeV triggering events in the TPC can be considered background-free due to the significantly larger signal size of these events compared to other background signals in the TPC.

Following the selection of the 4.44 MeV gamma-ray events, the analysis steps used for determining the tagging efficiency are replicated. The first step involves selecting all coincident NV events within a time window ranging from -1000 μs to 2000 μs. The time spectrum of these events is then fitted using the same model adopted for the tagging efficiency. Unlike in the tagging efficiency study, only the time range between -0.1 μs and 0.1 μs is excluded from the fit, as the 4.44 MeV γ-ray is detected by the TPC and no significant increase in afterpulse rate is expected in the NV PMTs. The resulting time distribution and its best fit are depicted in Fig. 5.18. This figure illustrates the distribution of the time difference between NV events and the 4.44 MeV gamma-ray S1 signals recorded in the TPC. The color coding used in this plot is consistent with that in Fig. 5.12, providing a clear visual representation of the relationship between the NV events and the TPC-detected gamma-ray signals.

The neutron-capture constant τ_C was found to be $(194 \pm 4)\mu$ s, which is, not surprisingly, larger compared to the value obtained in the tagging efficiency

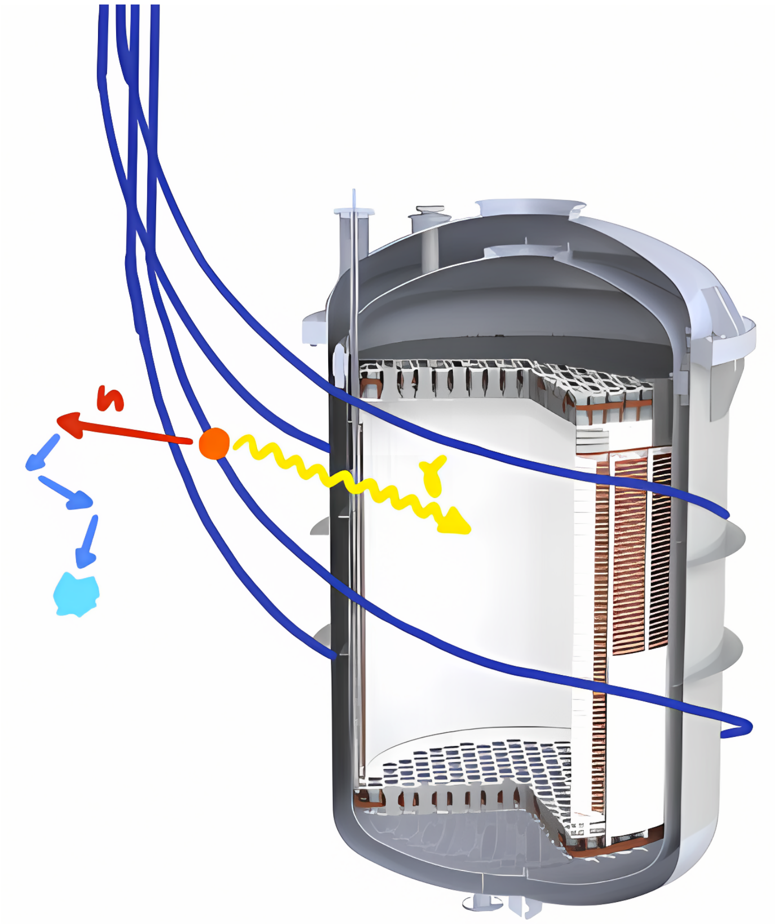

Figure 5.16: *Schematic showing the measurements of the NV detection efficiency with the AmBe calibration. We search for the 4.4 MeV gamma in the TPC (yellow), and then we look for the 2.2 MeV gamma of neutron capture in the NV (light blue).*

analysis, since the neutron is not requested to cross the stainless steel of the cryostat. The method for calculating the detection efficiency mirrors that of the tagging efficiency. It involves comparing the number of events in the purple region of interest with those in the reference region, as shown in Fig. 5.18. This approach yields a neutron-detection efficiency of (62 ± 1)% for a 250 μs long window. For a longer 600 μs window, the efficiency increases to (82 ± 1)%. As for the tagging efficiency, the detection efficiency has been calculated for the two windows and with different n-fold coincidence requirements; the results are presented in Figure 5.19.

Remarkably, these efficiency values are larger than those measured by other prominent water Cherenkov detectors, such as SNO [103] and Super-Kamiokande [104]. Thus the NV detection efficiency for the 600 μs window stands as the highest neutron-detection efficiency ever recorded in a water Cherenkov detector.

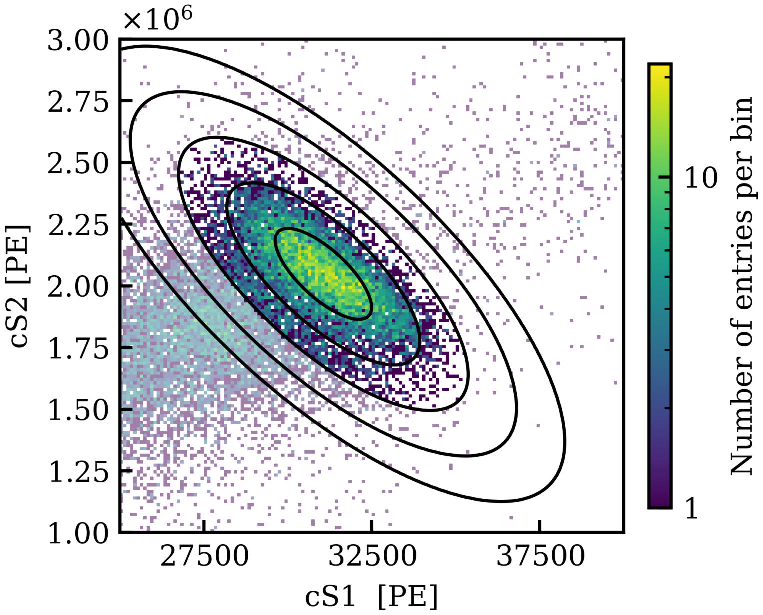

Figure 5.17: *Distribution in the corrected S1-S2 space of the full absorption of the AmBe* γ*-ray detected in the TPC. The black contours show the 1 to 5*σ *regions of the ellipse of the best fit. Only fully colored events inside 3*σ *were selected.*

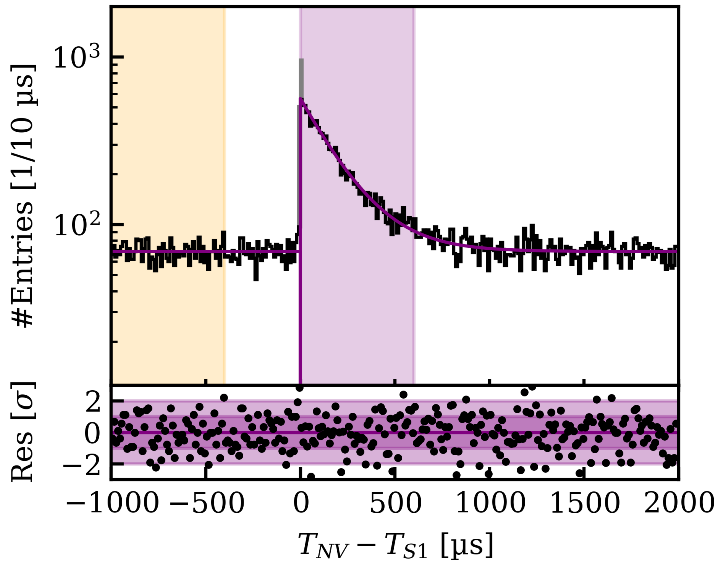

Figure 5.18: *Distribution of the time difference between NV events and the 4.44 MeV gamma-ray S1 signals recorded in the TPC. The color code is the same as in Fig. 5.12.*

5.5 MC-Data Matching - Hitlet Simulator

To complement the analytical model developed for the AmBe source components and to make predictions and extrapolations of tagging efficiency under different conditions, such as after the addition of the Gd salt, MC simulations can be

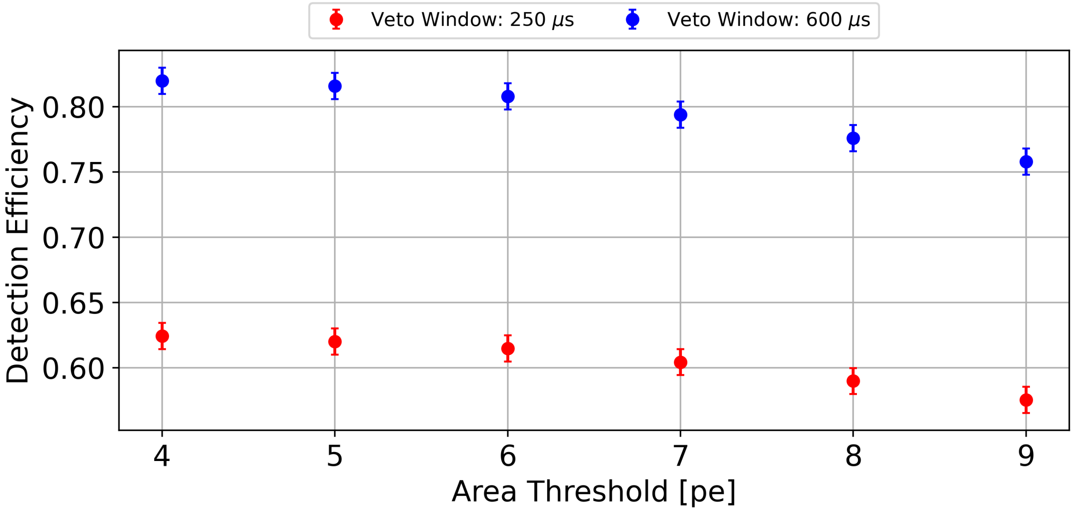

Figure 5.19: *Detection efficiency of the NV in SR0. The red and blue data show the detection efficiency for a 250 μs and 600 μs veto-window, respectively. In both cases, it was required that at least 5 PMTs contribute to an NV event*

employed. The aim is to adjust MC simulation outputs to align with observations from calibration data. Consequently, an effective event simulator, referred to as the "Hitlet Simulator" (HitSim), was developed during this work. The HitSim is designed as a fast and efficient simulator for generating NV hitlets and events (see section 3.5.2), assuming ideal delta-shaped PMT signals. The operational framework and methodology of HitSim are detailed in Figure 5.20 and are thoroughly discussed in the following.

The XENONnT detector is simulated with the Geant4 toolkit [135]. The MC framework is built upon the simulation package developed for XENON1T and described in [94]. The HitSim simulator processes "events" generated by Geant4, which takes care of particle generation and propagation through the detector volumes, energy deposition, and energy conversion processes, handled by dedicated physics lists; for example, radioactive decays are simulated via the `G4RadioactiveDecay` process list and the capture processes of neutrons at low energies (< 20 MeV) using the `G4NDL4.5` neutron library with thermal cross-sections. In the case of a neutron, Geant4 simulates its propagation through the water in the NV, the eventual neutron capture on hydrogen, the subsequent emission of a 2.22 MeV gamma-ray, the acceleration of electrons via Compton scattering, the production of Cherenkov radiation, and their tracking until the Cherenkov photons are either absorbed by the water or other materials, or hit the photocathode of the PMTs. To properly describe the situation with Gd-loaded water, a dedicated library has been added to generate the correct gamma emission after the neutron capture on Gd, leading to the production of several

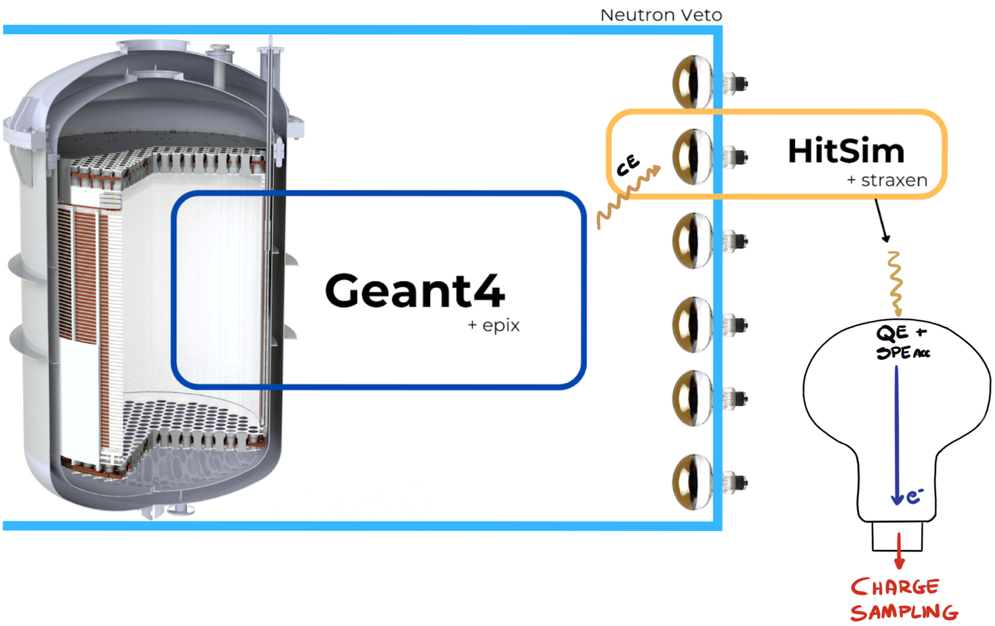

Figure 5.20: *Schematic of the concept and working principle behind the Hitlet Simulator. Geant4 takes care of all the physics processes to be simulated (blue box). Epix (Electron and Photon Instructions generator for XENON) [137] uses XENONnT Geant4 MC data to produce inputs to the TPC waveform-simulator (Wfsim) and thus to start the "processing"-chain of the simulated data into the TPC. Once the photon hits the PMT photocathode, the HitSim is used (orange box). In the HitSim, we determine if the photon is converted into a photoelectron and detected using the QE and the SPE acceptance of each PMT. For each photoelectron generated, the charge is sampled from a pre-defined PDF. The hits, with their charge in PE and their timing, are then clustered into straxen hitlets and events.*

gamma rays with a total energy of 7.9 or 8.5 MeV [138, 105]. For each Cherenkov photon, key information such as the time of impact on the photocathode, the PMT channel, and the photon wavelength are recorded in a Root TTree format. HitSim then reads these "PMT hits" from the corresponding TTree, with all the data being stored in array formats. The TPC uses a different simulator called Waveform-simulator (Wfsim), as it simulates for each hit the waveform recorded by the digitizer. In the NV HitSim, we use an effective approach neglecting the low-level information since they are not used in the analysis process (considering the PMT signal as a delta pulse). Going back to the HitSim working principle, to analyze the outcome of the MC simulation we need to convert the hit into straxen events; thus the simulated hits undergo a series of steps similar to those experienced by real photons in the detector. The initial stage involves converting all impinging photons into "detected" photons. This detection process in a PMT involves the conversion of photons into photo-electrons (PE) at the photocathode. The likelihood for the emission of a PE depends on its wavelength and is determined by the QE(λ) of the PMT. Once a PE is released, it must then be collected at the first dynode of the amplification stage. The efficiency of this collection is influenced by the PMT geometry and electric field and is quantified by the CE, as previously discussed in section 4.1.1. The overall probability of a single photon being detected is then represented by:

$$p_{det}(\lambda) = \text{Binom}(n = 1, p = \text{QE}_i(\lambda) \cdot \text{CE}) \tag{5.7}$$

In this equation, $\text{QE}_i(\lambda)$ represents the wavelength-dependent Quantum Efficiency of the i-th PMT channel.

The QE for each PMT is well-documented, thanks to measurements performed by Hamamatsu. Figure 5.21 illustrates the impact of applying the QE on the Cherenkov photon spectrum. The QE maximum is around 350 nm, but it is important to note that the emission of Cherenkov photons per unit wavelength is inversely proportional to the square of the wavelength, which shifts the region of maximal sensitivity to slightly below 350 nm. The wavelengths to which the NV is most responsive fall within approximately [300, 400] nm, with a significant portion of the Cherenkov spectrum, about 75%, contained within the [290, 440] nm range. The CE of each PMT is not precisely known and is thus treated as a free parameter to be determined through data-to-MC comparison. While the CE varies among PMTs, using a single average value is more practical, especially considering that the CE in this context encapsulates all potential uncertainties and discrepancies between the real detector geometry and the simulation, thus it

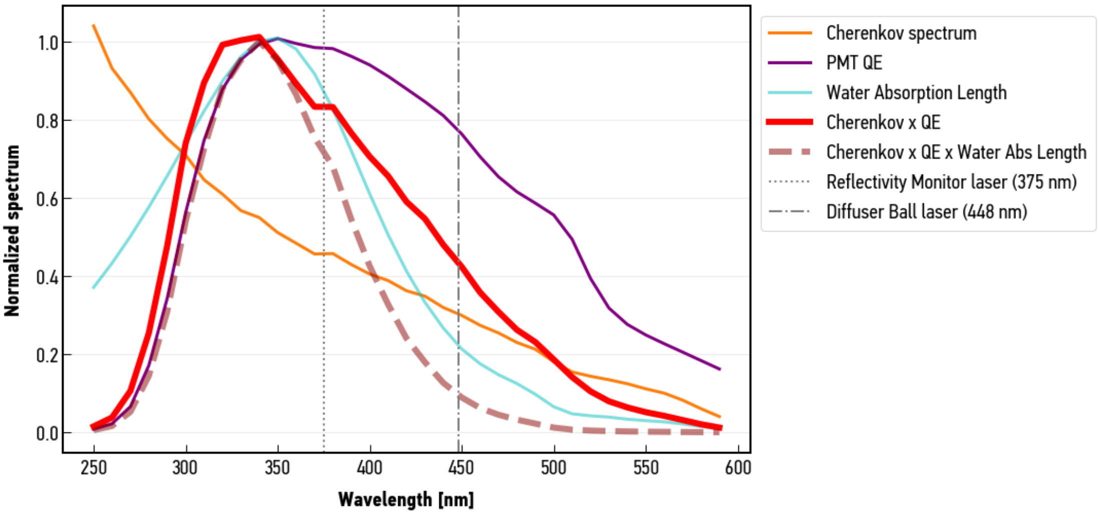

Figure 5.21: *Quantum efficiency curve of one PMT overlapped and convoluted to the energy spectrum of the Cherenkov photon hits from the Geant 4 output. The model of the water absorption length used in the simulation is also reported and is convoluted to the Cherenkov Spectrum and to the QE. The two dashed thin black lines refer to the wavelength of the Reflectivity Monitor and Diffuser Ball lasers used for the light calibrations.*

is not attributable only to the behavior of the PMTs. In simulating the detection process, it is also crucial to consider the hardware threshold of our DAQ (which is 15 ADC counts for most of the channels). This threshold impacts the SPE acceptance, which plays a role in determining whether a photon is detected by the PMT. The SPE Acceptance, determined through the dedicated LED calibrations, is factored into the photon detection probability formula, which is then modified to:

$$p_{det}(\lambda) = \mathrm{Binom}(n = 1, p = \mathrm{QE}_i(\lambda) \cdot \mathrm{CE} \cdot \mathrm{SPE}_{\mathrm{Acc.}}) \tag{5.8}$$

Once established whether the photon is detected or not, the next step in the HitSim process is to sample the charge for each detected hit. This is achieved by using the SPE model presented in section 4.1.2, derived from LED calibration data. For the development of the HitSim, we used the model developed for SR1, for its demonstrated robustness during the calibration campaign. The SPE model includes components for both under-amplified and fully amplified electrons. The under-amplified component is represented by a box function, while the fully amplified electrons are described by a Poissonian Gaussian distribution. However, it is important to note that due to the hardware threshold of our data acquisition system, not all under-amplified electrons are recorded. This limitation means that simply using the SPE model components might not accurately reflect the true charge distribution of detected photons in a self-triggered data acquisition.

To address this issue, the model for charge sampling in the HitSim incorporates a PDF that combines actual data distribution with the fit function. This hybrid approach accounts for the cut-off in the charge distribution caused by the ADC threshold, with the fit function modeling the theoretical charge distribution of the PE. The method is illustrated in Figure 5.22, which shows how the data distribution and fit function are merged to form the final PDF used for charge sampling in the HitSim. To simulate the two Science Runs of the experiment (SR0 & SR1), we used the corresponding SPE models.

After charge sampling, we obtain pseudo hits. The final step involves converting these recorded hits into hitlets with the corresponding straxen plugin. Each hitlet in this simulation is represented as a simple delta pulse, characterized by a single sample length and carrying information about time, PMT channel, and charge. The timing of these photons is relative to the simulated Geant4 events, so an additional time offset is applied to each group of hitlets. This offset can be distributed either uniformly to simulate well-separated events or according to a specific source rate to replicate event pile-up. The pseudo hitlets are then processed through the regular NV plugins to compute events and their properties.

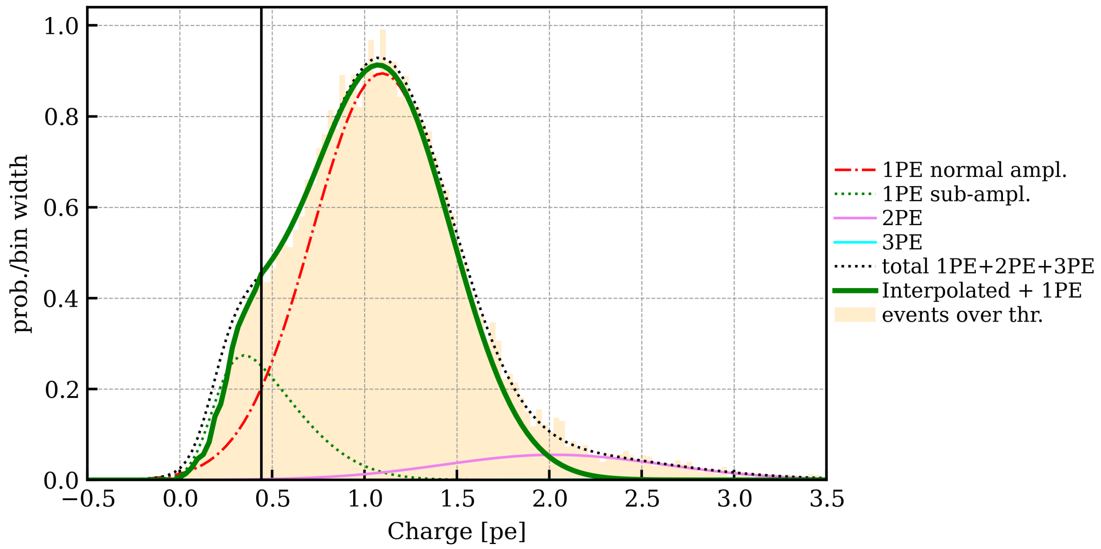

(a) Model used for SR0.

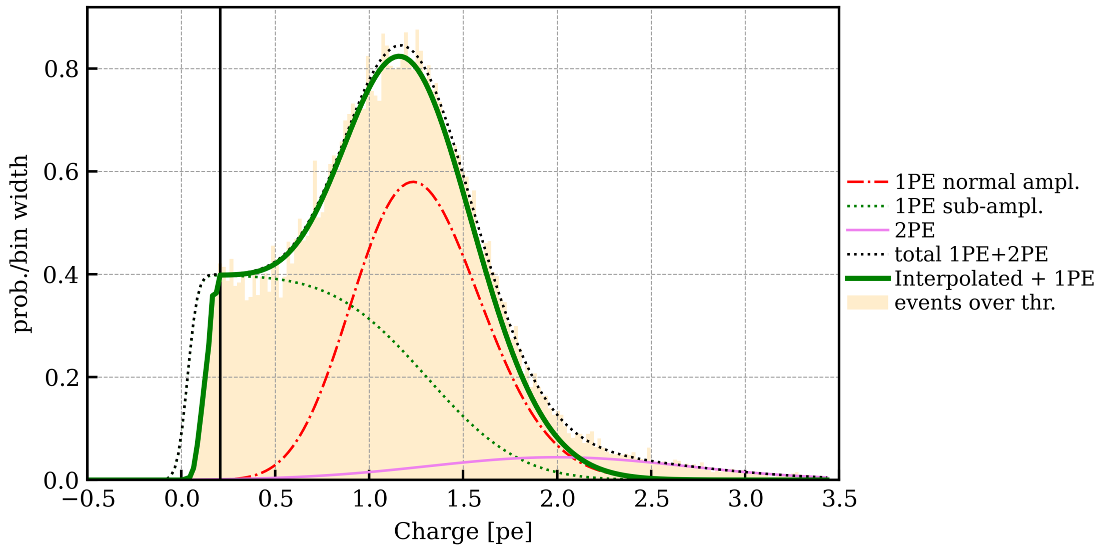

(b) Model used for SR1.

Figure 5.22: *Charge distribution used for the sampling in the HitSim for the two science runs. Both are a combination of the data with the 15 ADC count amplitude threshold applied (orange distribution) and of the SPE fit function (dashed thin black line). Up to the first intersection point (marked with the solid vertical line), the distribution follows the data, then it continues with the fit function. The final model is shown with the solid green line.*

The HitSim has been effectively used to estimate the CE based on the AmBe calibration datasets. In this way the CE is intended as an "effective CE" including not only the collection of photo-electrons at the first dynode, but also any other mis-modelling potentially present in the approach. For this purpose, the AmBe simulations were conducted with the source at the Top U-tube CW5d9m position, testing CE values ranging from 0.6 to 1. The event area distributions between the data and simulation were compared to determine the optimal CE value. A quantitative evaluation was performed by examining the positions of the 4.4 MeV and 2.2 MeV peaks expected in the AmBe calibration. Figure 5.23 and 5.24 illustrate the peak positions of the 4.4 MeV gammas (left) and the 2.2 MeV peak (right) for different CE values for the two science runs. From this analysis, it was determined that the most suitable CE value for accurately simulating the experimental data is 75% for SR0 and 87% for SR1.

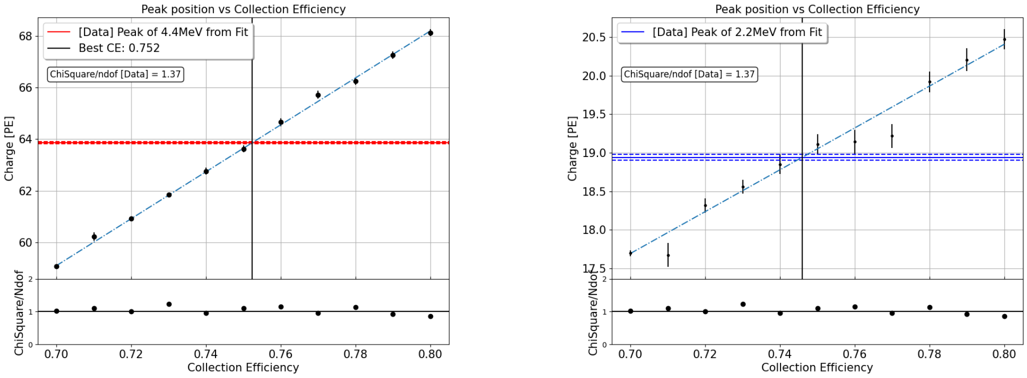

Figure 5.23: *Position of the 4.4 MeV (left) and 2.2 MeV (right) peaks in the simulated AmBe charge spectrum varying the Collection Efficiency in the range [0.7, 0.8]. From the intersection of the linear fit (dashed thin blue line) and the position of the peaks (red/blue lines) we determined the best CE for the match. The best CE from the two plots do not differ significantly; however, we decided to rely on the one inferred from the 4.4 MeV match since the data are less affected by the low-charge noise and threshold effects. In the bottom panels, the reduced χ^2 of the fit of the simulated spectra are shown.*

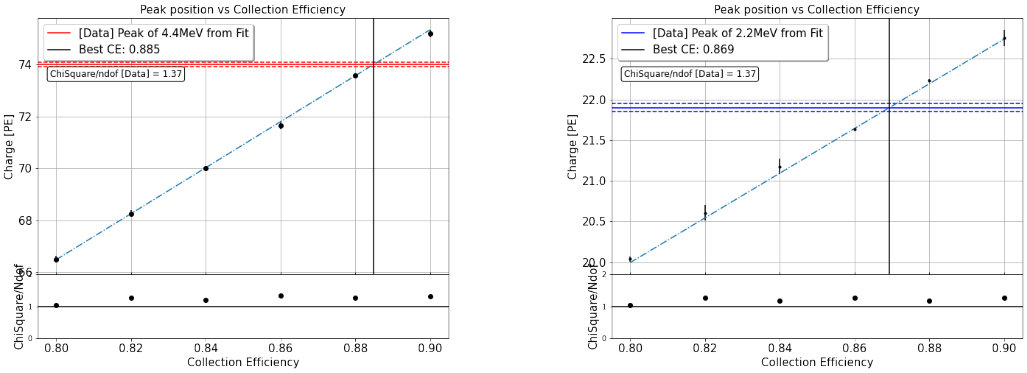

Figure 5.24: *Position of the 4.4 MeV (left) and 2.2 MeV (right) peaks in the simulated AmBe charge spectrum varying the Collection Efficiency in the range [0.7, 0.8] for SR1. The procedure to determine the CE is the same as the one reported in figure 5.23.*

With the CE determined, we can proceed to estimate the performance of the

NV and the expected tagging efficiency under varying detector conditions. The first comparison can be made on the event area distribution expected with the neutron captures on Gd; this has been done simulating AmBe source data in the Bottom CW6d0m position which is in the middle of the NV volume and in the Top CW7d8m position, which instead is close to the cryostat (as shown in the drawings in the left side of figures 5.25 and 5.26). The distributions for the water case and for the Gd-water configuration with a concentration of 500 ppm are shown in figure 5.25 and 5.26

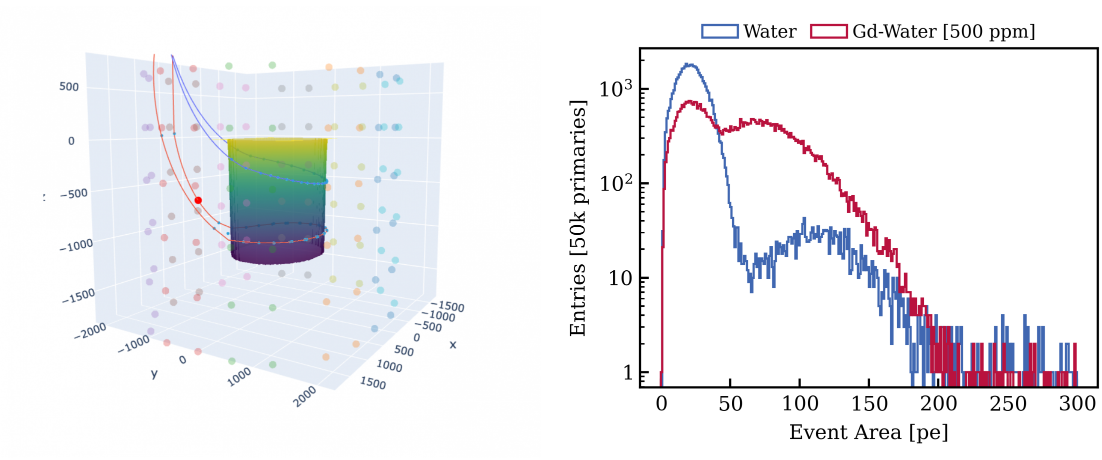

Figure 5.25: *(Left) Drawing of the U-tubes, the TPC and the NV PMTs with the position of the source indicated by the red dot. (Right) Event area distribution from simulated AmBe neutron captures events with the source located in the Bottom CW6d0m position and with the NV in the Water (blue) and Gd-Water [500ppm] (red) configurations. To highlight the impact of captures on Gd, the neutron emission without an associated 4.4 MeV γ are considered here. The number of generated primaries is the same for the two dataset.*

The Gd-capture events are expected to populate a region that overlaps with the reconstructed area of the 4.4 MeV gamma but with a larger spread distribution. This is expected given that, even if the Gd-capture emits a total energy of 8 MeV, this happens via the generation of 4 gammas of 2 MeV each, on average. By tracking down the information to the MC-truth (the output of Geant4) we can inspect the nature of the captures. From this, we see that in this configuration 62% of the captures occur on Gd while 35% on H (in agreement with the plot in figure 3.3)[1]; furthermore, there is an increase of the fraction of neutrons captured in the NV volume in the Gd-water case of about 0.8% for the position in the middle of the NV (Bottom CW6d0m), where most of the neutrons could be detected also in the demi-water case. The increase is much

---

[1] The remaining fraction is identified as "captures outside water", i.e. mostly on the SS of the support structure.

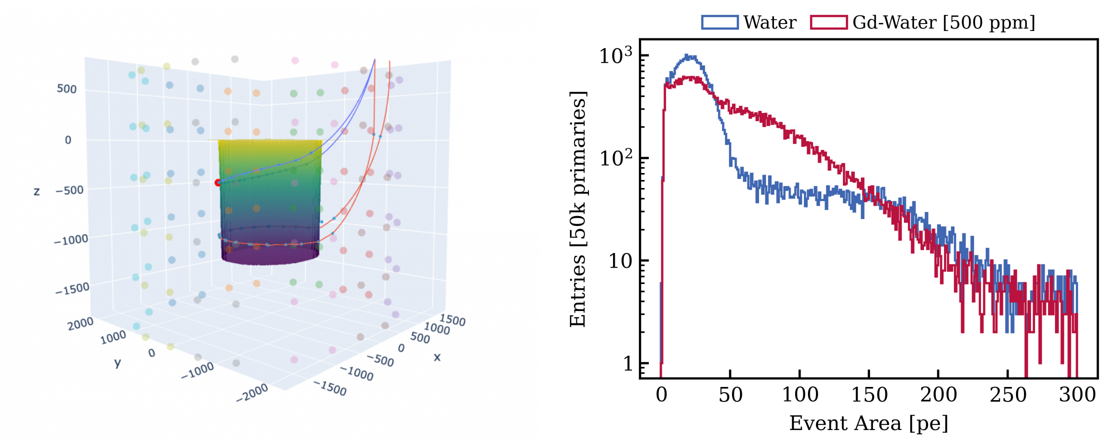

Figure 5.26: *(Left) Drawing of the U-tubes, the TPC and the NV PMTs with the position of the source indicated by the red dot. (Right) Event area distribution from simulated AmBe neutron captures events with the source located in the Top CW7d8m position and with the NV in the Water (blue) and Gd-Water [500ppm] (red) configurations. To highlight the impact of captures on Gd, the neutron emission without an associated 4.4 MeV γ are considered here. The number of generated primaries is the same for the two dataset.*

more significant (+16%) for the position close to the cryostat (Top CW7d8m). The impact of the Gd injection is visible also by studying the average capture times in the time distribution of the simulated events. This is shown in figure 5.27 for several positions and with a comparison with the Water case: in the positions close to the cryostat the typical capture time is reduced by more than a factor 2, from about 160 μs in demi-water to less than 80 μs with 500 ppm of GdSO.

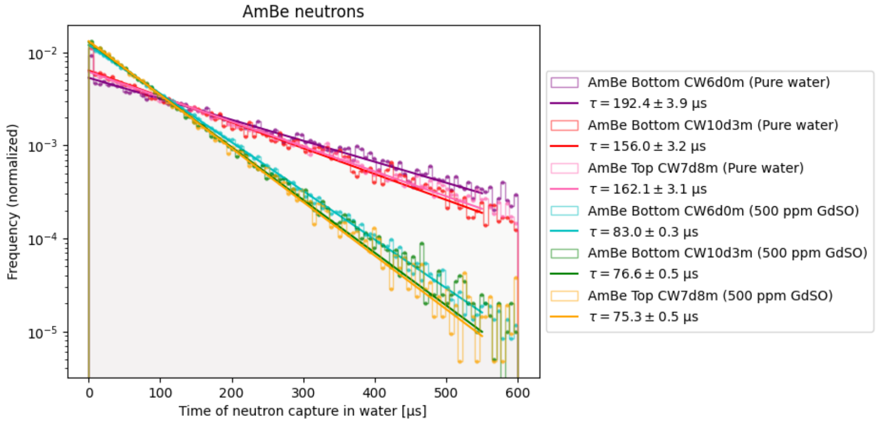

Figure 5.27: *Time distribution of the simulated neutron captures, identified by their flags in the MC-truth. The distribution is shown for several position and with a comparison with the pure-Water configuration; with the current Gd concentration we expect to halve the average capture time (estimated here with an exponential fit of the distribution).*

The improvement is also evident by simulating radiogenic neutrons from the cryostat (so in a position comparable with the Top CW7d8m AmBe source position) and computing the tagging efficiency for different thresholds, as displayed in figure 5.28 for various GdSO concentrations. As described in the next chapter, the NV is currently operated with a GdSO concentration of 500 ppm, corresponding to a Gd concentration of 0.02%. The results of the MC simulation predict that even in this configuration the tagging efficiency increases up to ~ 77%, reducing significantly (by a factor ~ 2) the background from radiogenic neutrons with respect to the results obtained in SR0 with demi-water.

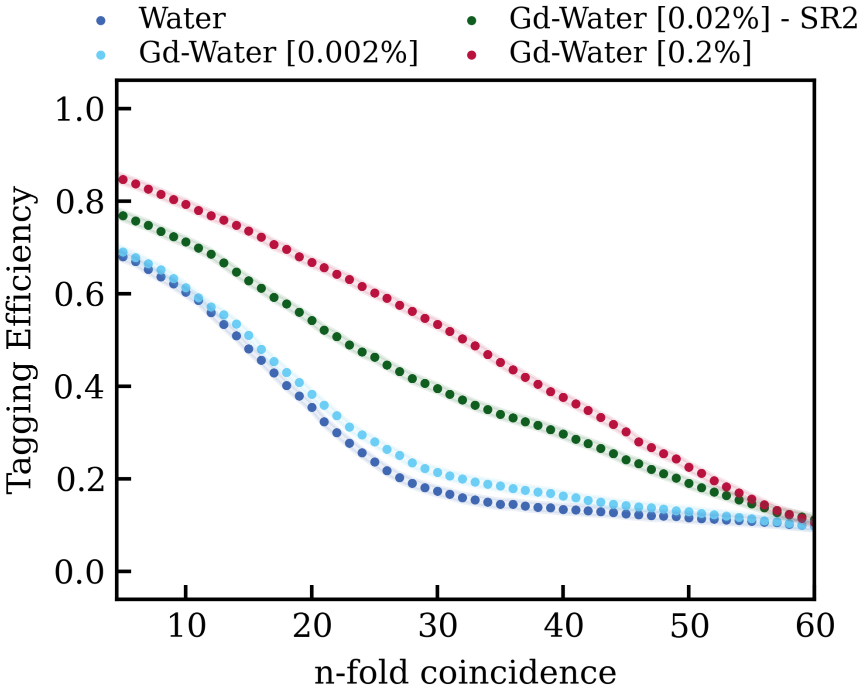

Figure 5.28: *Tagging efficiency computed from simulating radiogenic neutrons emitted from the cryostat, for different Gd concentrations as a function of the n-fold coincidence requirement . The NV selection cut used in the data analysis is applied.*

6

XENONnT DM SEARCH AND THE IMPACT OF THE NEUTRON VETO

In this chapter, we present the results of XENONnT during its first scientific run, on WIMP and Low-Energy ER searches [85, 86]. We also provide an outlook on the expected results in the second science run (SR1), still under analysis. The approach adopted for the WIMP analysis, the main focus of the XENONnT experiment, is that of a blinded analysis. This means that events within the region of interest (ROI) in the cS1 and cS2 space remain inaccessible until the analysis strategies, particularly the selection cuts, are finalized. Before proceeding to the "unblinding" of the WIMP ROI, the unblinding of all events tagged by the veto systems was conducted. Throughout this chapter, emphasis is placed on the contribution of the NV to the SR0 results, building upon the performances observed and presented in chapter 5. Finally, in addition to outlining the predicted results for SR1, the chapter will also touch upon the expected improvements in SR2. For SR2, an initial concentration of gadolinium has been introduced to enhance the NV tagging efficiency. The chapter begins with an overview of SR0, focusing on data acquisition, signal and background models, and the outcomes of the main research channels (Section 6.1). Special attention is given to the contribution of the NV in these searches (Section 6.1.3). Moving forward, a similar detailed overview is presented for SR1 (Section 6.2). However, only the anticipated results are showcased here, as the analysis is still ongoing. This section aims to provide a comprehensive understanding of the expected outcomes based on the current progress and data trends observed in SR1. Finally, the chapter concludes with a discussion of the upcoming steps towards SR2, particularly concerning the NV and its expected performances. This part will delve into the planned enhancements and modifications for the NV in SR2, including the introduction of gadolinium to improve neutron capture efficiency (Section 6.3).

6.1 Science Run 0

The data acquisition for the first Science Run (SR0) of XENONnT occurred between May 3, 2021, and December 10, 2021. During this period, blinded data were collected for a total of 97.1 days, along with weekly PMT calibrations, AmBe calibrations for studying the detector NR response, ^{220}Rn calibrations for the ER response, and ^{83m}Kr calibrations to obtain the correction map of the light- and charge-yield of the detector, as well as measuring the field distortion effects on the position of the S2 signals. Most of the blinded science data in SR0 were acquired in the **linked mode**, with the three detectors in time synchronization. However, at the beginning of the science run, 8.7 days of "unlinked" data were accumulated due to stability issues with the acquisition system. A portion of these data was later recovered for analysis through manual synchronization. As a result, the final corrected number for the livetime of SR0 considered for the analysis is 95.1 days, which, given a fiducial volume of (4.18 ± 0.13) tonnes, corresponds to a total exposure of (1.09 ± 0.03) tonnes × year. In the analysis of WIMPs many challenges were encountered in preparing cuts related to the shapes of S2 signals. Specifically, S2 signals reconstructed around the transverse wires of the gate and anode mesh were affected by local variations in the drift and extraction fields, leading to distortion in their peak shapes. This inhomogeneity in the drift field was partly due to the relatively small HV applied to the electrodes. Just before SR0, a short circuit occurred between the cathode and the bottom screening mesh. This incident limited the cathode voltage to -2.75 kV, while the gate was set to 0.3 kV, and the anode to 4.9 kV. As a result, the drift field was reduced to 23 V/cm, and the extraction field to 2.9 kV/cm. The voltage applied to the cathode and bottom screening mesh was capped at this value to prevent potential damage to the bottom PMTs. Additional rings surrounding the PTFE walls of the TPC were set to 650 V to mitigate the drift field inhomogeneity. The drift field was approximately 10 times smaller than the design goal of 200 V/cm, and the obtained electron extraction efficiency was (53 ± 3)%, instead of the design goal of 96%. The low extraction field also meant that the average single electron gain was (31.2 ± 1.0) PE/electron. As mentioned at the outset of this chapter, the data from SR0 was used for both the low-energy ER and WIMP searches. In the following sections, we will delve into these two analyses and their primary outcomes, with a particular emphasis on the contribution of the NV.

6.1.1 Search for New Physics in ER Data

The XENON1T low-energy ER search [139] observed an excess of events in the region of 1–7 keV that could potentially be attributed to tritium that emits a β-spectrum with a Q-value of 18.6 keV and a half-life of 12.3 yr. However, this excess could also be interpreted as physics Beyond the Standard Model (BSM), such as solar axions, solar neutrinos with an enhanced magnetic moment, and bosonic DM, which primarily includes Axion-like Particles (ALPs) and dark photon DM. To investigate this excess further, a similar analysis was conducted with XENONnT with an exposure of 1.16 tonne×years. XENONnT, with its advanced design and lower ER background, offered enhanced sensitivity in the energy range relevant to these observations.

The S1 and S2 responses to low-energy ERs were calibrated using two radioactive sources. Initially, ^{220}Rn was injected into the TPC in June 2021. Its beta-emitting daughter, ^{212}Pb, produces a uniform ER spectrum at low energies. Later, in December 2021, ^{37}Ar was introduced, primarily generating low-energy depositions, decaying through the emission of two mono-energetic lines at 2.82 keV and 0.27 keV.

The ROI for this analysis spans (1, 140) keV in reconstructed energy. The ER response in cS1-cS2 space, the ER-band, is shown in blue in Fig. 6.1.

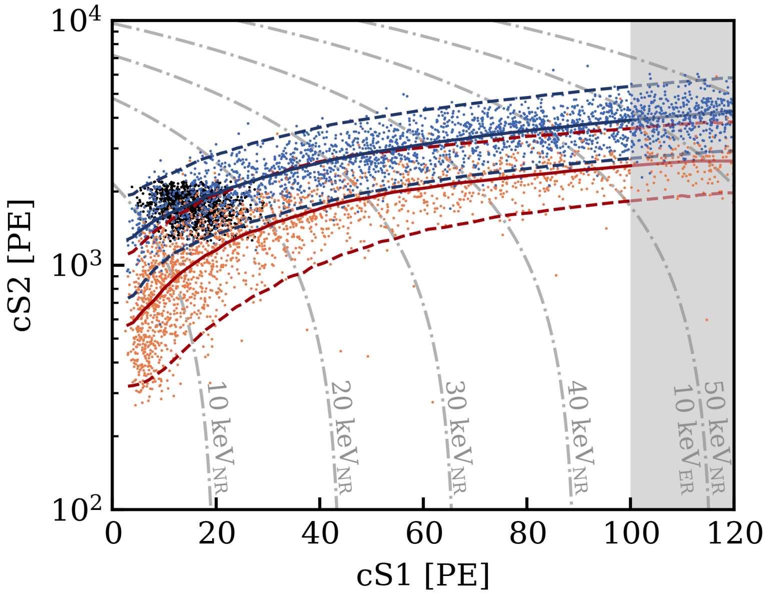

Figure 6.1: *NR and ER calibration data from ^{241}AmBe (orange), ^{220}Rn (blue) and ^{37}Ar (black). The median and the ±2 σ contours of the NR and ER model are shown in blue and red respectively. The gray dash-dotted contour lines show the reconstructed NR energy (keV$_{NR}$). Only the not-shaded events up to a cS1 of 100 PE are considered in the response model fits. Plot from [85].*

XENONnT achieved an ER background rate of $(15.8 \pm 1.3_{stat})$ events/(t·y·keV) in the (1, 30) keV energy region, setting a new benchmark for the lowest ER background rate in a DM search experiment. The blind analysis revealed no excess above the expected background, ruling out the previously hypothesized BSM interpretations of the XENON1T excess; figure 6.2 shows the data (and background-only fit) for both experiments, clearly showing the reduction of ER background and no excess in the low energy region of XENONnT.

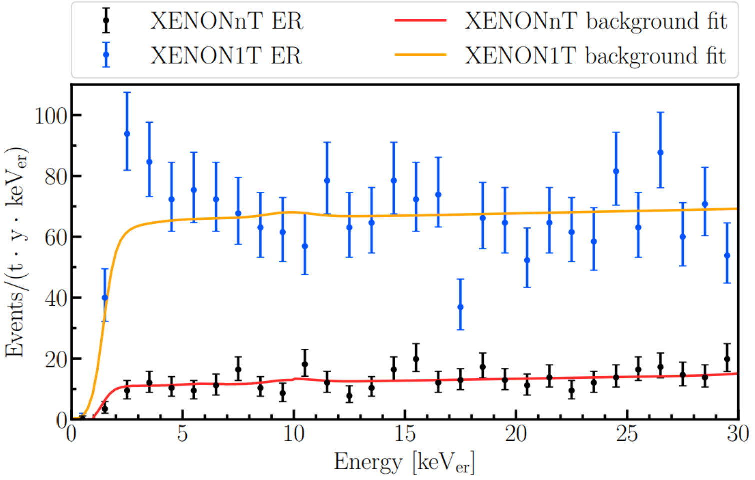

Figure 6.2: *ER background fits for XENONnT [85] and XENON1T [139]. The XENONnT ER background is ∼ 5× lower than that of XENON1T. No excess with respect to the background model is observed in the XENONnT data.*

Even if it was designed to mostly detect NR backgrounds, in this analysis the NV was used to reduce also part of the ER background. By excluding TPC events occurring within 300 ns of NV events, we effectively suppressed radioactivity background originating from the materials around the active LXe volume (TPC, PMTs, Cryostat). Certain isotopes, such as ^{60}Co and ^{208}Tl, emit gamma cascades detectable in both detectors. Tagging the corresponding S1 signal with a coincident NV signal allowed us to identify these events as background, thereby reducing the overall detector materials background for SR0 by about 10%. This method, requiring only a narrow coincidence window between the neutron-veto and TPC, did not significantly impact the total exposure, unlike the neutron-tagging used in the WIMP analysis. This procedure, while removing only a small fraction of events over the total ER background, demonstrates the very low threshold reached in the NV, and its potentiality in detecting $\mathcal{O}$(MeV) gamma rays.

Figure 6.3 illustrates the correlation between the energy observed in the NV and the one in the TPC for coincident events, highlighting the NV contribution. The figure includes:

- a 2D distribution of the observed light in the NV as a function of the

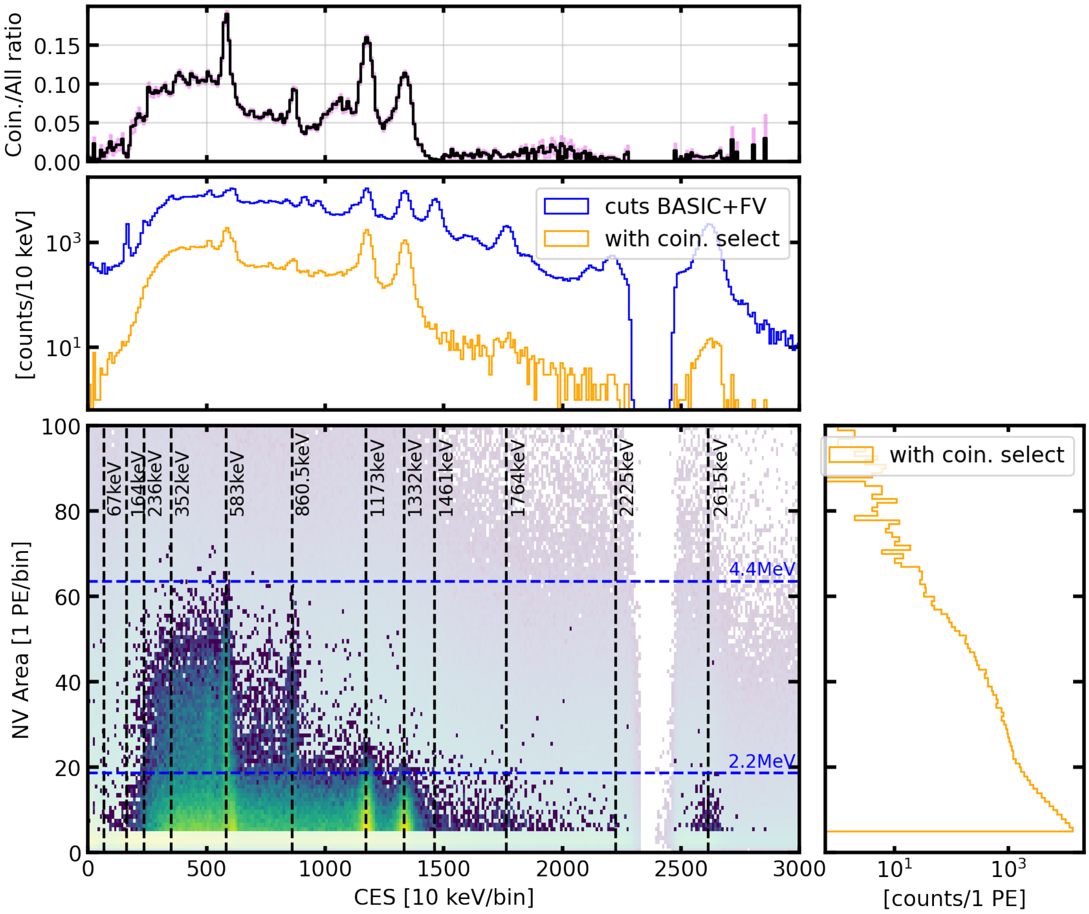

Figure 6.3: *Distributions of coincident ER events between TPC and NV. The cuts applied on the selection for TPC events are the standard ones (BASICS) and the Fiducial Volume (FV) cut. The selection of NV events requires a 3-fold PMT coincidence and a 5 PE threshold. The time window for coincidence is ±300 ns. The left-bottom plot is the 2D distribution of coincident events between TPC-NV (with energy in the TPC up to 3 MeV). The left-middle plot is the energy distribution of CES before (blue) and after (yellow) the NV-coincidence cut. The left-top plot is the ratio of the yellow and blue histograms in the left-middle figure, showing the fraction of ER events tagged by the NV. In the right plot, the projection of the NV-tagged event area is shown.*

observed energy in TPC, expressed as Combined Energy Scale (CES) using only coincident events;

- the distribution of light detected in the NV;
- the CES spectrum in the TPC with the standard selection cuts (in blue), and after applying the cut on the coincidence events with the NV (in orange).
- the ratio of tagged events as a function of the energy deposited in the TPC

In particular from this last plot, a detection probability > 10% is seen for the two γ lines of ^{60}Co (at 1173 and 1332 keV), and the 583 keV one of ^{208}Tl decay.

6.1.2 First Dark Matter Search with NR data

In this analysis, the focus is on detecting WIMPs, which are expected to primarily produce NRs in the detector volume. These NRs generally have fewer background sources compared to ERs.

The ROI for the WIMP search is defined within specific ranges of cS1 and cS2. The cS1 signal range is set between 0 and 100 PE, while the cS2 signal range is between 126 and 12600 PE. This selection criteria, combined with detection and selection efficiencies, correspond to an energy range of 3.3 to 60.5 keV$_{NR}$ with at least 10% total efficiency.

To maintain the integrity of the analysis, certain regions of the data were blinded. Specifically, events with ER energy below 20 keV$_{ER}$ and those within the contours of the ER and NR bands in cS1-cS2 space (see Fig. 6.1) were not accessible until the analysis procedure was finalized.

Several data quality cuts were applied to ensure well-reconstructed events were included, thereby reducing background. These cuts were optimized using calibration data and simulations with WFSim. Each event is required to have a valid S1-S2 pair, and multiple-scatter (MS) events are removed, as WIMPs are expected to produce only single-scatter (SS) NRs.

Events tagged by the MV are removed from the analysis, requiring a 1 ms veto window with a 5-fold PMT coincidence and a 10 PE event area threshold in the MV. Furthermore, a Gradient Boosted Decision Tree (GBDT) cut was developed to reduce accidental coincidences (ACs) - randomly paired S1-S2 signals. This cut, focusing on S2 area and shape, as well as interaction depth, reduces AC background by 65% while maintaining 95% signal acceptance. However, there are limitations caused by local variations in the drift and extraction fields, which primarily affect the S2 pulse shape modeling near the transverse wires of the TPC. This variation leads to different efficiencies and acceptances between the regions near the transverse wires and other regions within the TPC. Despite these differences, both regions are utilized in the analysis. The efficiency of detecting signals in the TPC is predominantly influenced by the efficiency of detecting S1 signals. This efficiency is assessed using WFSim, and cross-validated with a data-driven method. Both approaches show a high level of agreement, within 1%. At lower energy levels, the efficiency is primarily limited by the requirement for a 3-fold PMT coincidence. This requirement is crucial for confirming the presence of real events but limits the efficiency of the low-energy signals.

Figure 6.4 illustrates these efficiencies alongside the normalized recoil spectra for three different WIMP masses.

To reduce background noise from radioactive decay within the detector and

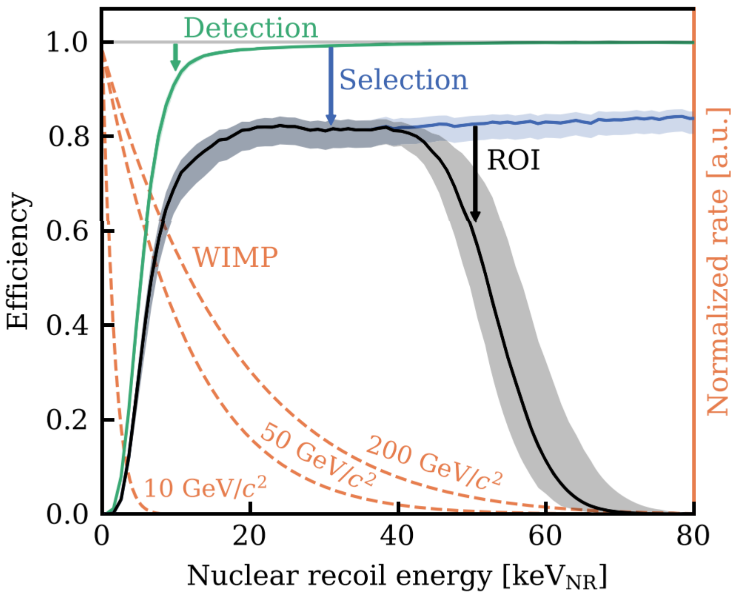

Figure 6.4: *Efficiency for detecting and selecting NR events in the WIMP search, plotted against NR recoil energy. The overall efficiency within the WIMP search region (black line) is primarily influenced by detection efficiency (green line) at lower energies and by event selection criteria (blue line) at higher energies, up to the boundary of the ROI. The normalized recoil spectra for WIMPs with masses of 10, 50, and 200 GeV/c^2 are depicted as orange dashed lines. Plot from [86].*

surface events (primarily associated to ^{210}Pb ERs), we have defined a FV whose total xenon mass, after accounting for systematic uncertainties related to field distortion corrections, is estimated to be (4.18 ± 0.13) t.

The background model for the XENONnT experiment comprises five distinct components: **radiogenic neutrons**, CEνNS, ERs, surface events, and ACs. The primary source of NR background is radiogenic neutrons, generated through spontaneous fission and (α,n) reactions in various detector materials. The neutron rate was initially estimated using a comprehensive detector simulation and then cross-checked against a data-driven method. This method employs a combined Poisson likelihood for both multiple-scatter (MS) and single-scatter (SS) events tagged by the NV, along with a simulation-driven MS/SS ratio validated with ^{241}AmBe data.

Within the WIMP blinded region, four events are tagged in total by the NV: three of them are MS and one an SS. This outcome is consistent with the MS/SS ratio from simulations, resulting in a total neutron background expectation of ($1.1^{+0.6}_{-0.5}$) events in SR0, which is a factor ~ 6 larger than simulation predictions. More details about the NV's contribution to the analysis are presented in the next paragraph.

The remaining NR background is predominantly due to CEνNS from ^{8}B solar neutrinos. The rate of this component is constrained by measurements of the ^{8}B flux, but the overall uncertainty is largely influenced by uncertainties in the detector response model. Regarding the impact of cosmogenic neutrons induced by muons, their contribution is already considered negligible as the estimate is less than 0.01 events following the MV tagging, even before accounting for the additional suppression provided by the NV.

After the unblinding, the ROI contained a total of 152 events, with 16 of these located in the blinded WIMP search area. These data are depicted in figure 6.5.

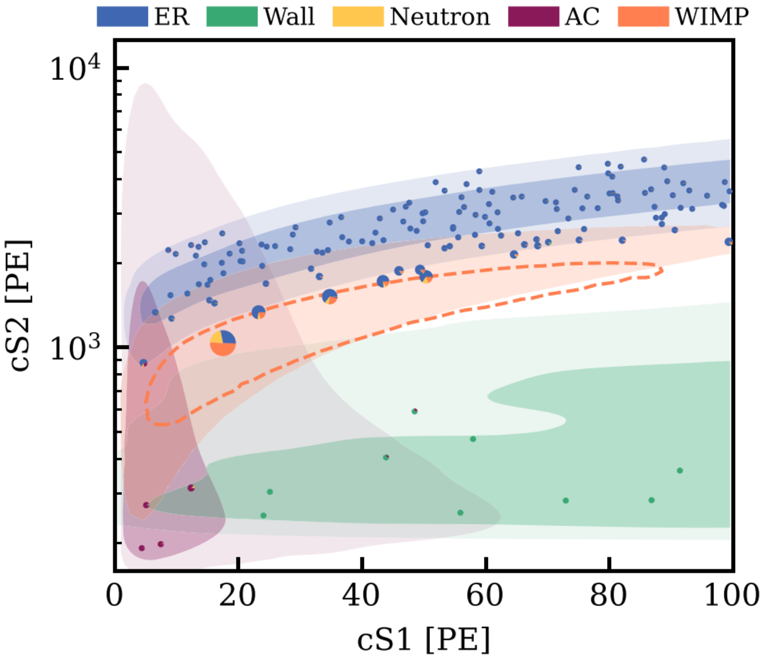

Figure 6.5: *Data from the WIMP search displayed in the cS1-cS2 space, where each event is visualized as a pie chart. These charts represent the fraction of the best-fit model at the event location, including the expected number of 200 GeV/c^2 WIMPs (shown in orange). The size of each pie chart is scaled to match the signal model prediction at that specific position. Background probability density distributions are illustrated as 1σ (darker regions) and 2σ (lighter regions) contours, as identified in the legend for ERs in blue, ACs in purple, and surface events (green, labeled as "wall"). The neutron background, indicated in yellow in the pie charts, shares a distribution similar to the WIMP signal, which is represented by the orange-filled area marking the 2σ region. An orange dashed contour outlines a signal-like region, designed to encompass 50% of a 200 GeV/c^2 WIMP signal, optimized for the highest signal-to-noise ratio. Plot from [86].*

The analysis for WIMP discovery revealed no significant excess (with a p-value ≥ 0.20, particularly for masses above 100 GeV/c^2). The derived limits on spin-independent interactions are illustrated in figure 6.6; the most stringent upper limit observed is 2.58×10^{-47} cm^2 at a WIMP mass of 28 GeV/c^2, at a 90% confidence level.

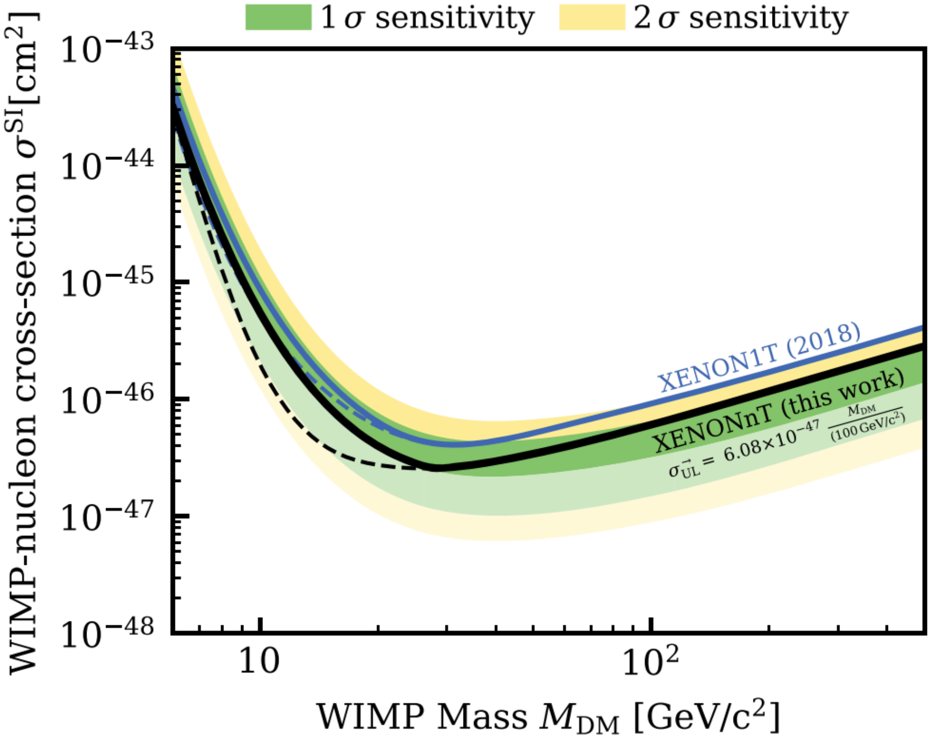

Figure 6.6: *Upper limit on the spin-independent WIMP-nucleon cross-section at a 90% confidence level (represented by the full black line) as a function of the WIMP mass. This limit is constrained to remain at or above the median unconstrained upper limit through a power constraint. The dashed lines depict the upper limit without the power constraint applied. The 1σ (green) and 2σ (yellow) sensitivity bands are illustrated as shaded areas, with lighter shades indicating the range of potential downward fluctuations. The result from the XENON1T experiment [79] is also included for comparison, shown in blue, with the same power constraint applied. Plot from [86].*

Figure 6.7 provides a comparison between these results and the recent findings of other competitor experiments, in particular considering the application of a power constraint consistent with the original PCL recommendation [140]. More details on how these limits are derived can be found in [86].

6.1.3 Impact of the Neutron Veto

To validate the neutron background model and its associated rate, an unblinding of all events tagged by the NV was conducted before the final unblinding. The background model was initially determined from Monte Carlo simulations informed on the results of material screening, as radiogenic neutrons are the dominant source. For SR0, the predicted background for single scatter (SS) events, after applying all data-quality cuts and the NV tagging, was estimated

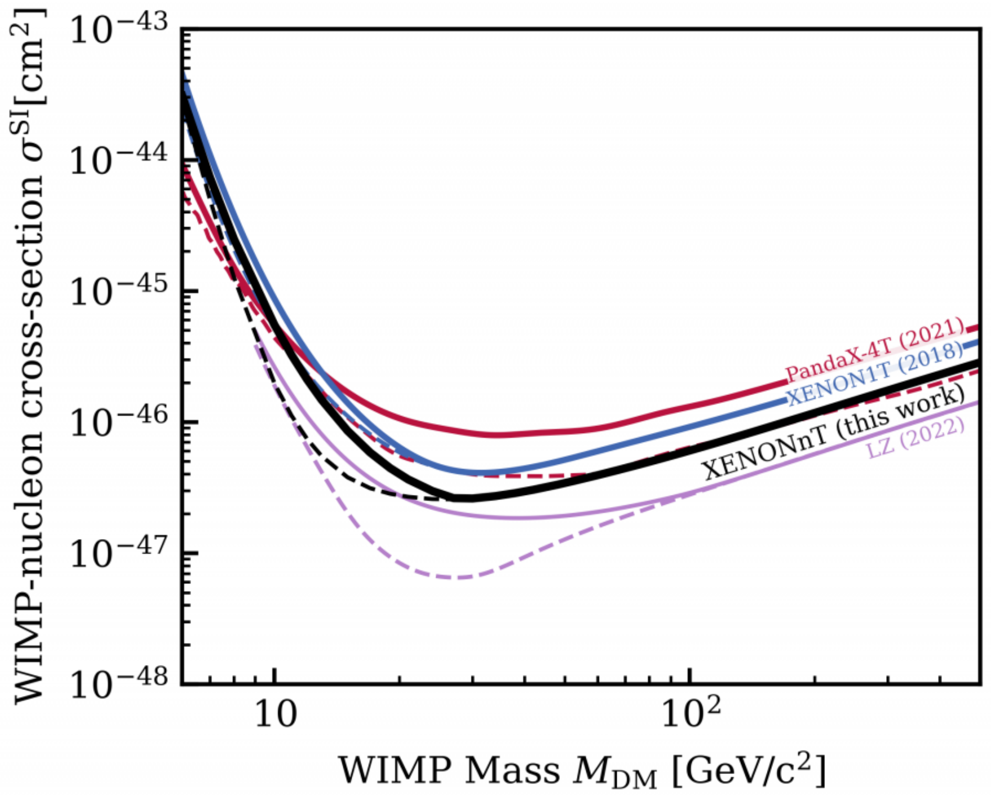

Figure 6.7: *Upper limits on SI WIMP-nucleon cross-section at 90% confidence level for this work (black lines), LZ [141] (purple lines), PandaX-4T [142] (red lines) and XENON1T [79] (blue lines). For PandaX and LZ, dashed lines represent their published result, for XENON results the dashed lines represent limits without a power constraint applied. Full lines for each experiment represent a limit that is power-constrained to always lie at or above the median un-constrained limit.*

to be 0.18 ± 0.06 (syst. [1]) ± 0.01 (stat.). Then, to validate the simulations, which on the other hand were crucial in determining the neutron yield from various materials and isotopes, as well as in estimating various selection efficiencies, the multiple-to-single scatter ratio of neutron interactions was determined. This ratio was found to be 2.2 for the data quality cuts used in SR0, a finding that was confirmed by the analysis of AmBe calibration data.

Figure 6.8 displays the same plot as in figure 6.5, but specifically focuses on events in the WIMP ROI that were tagged by either of the two vetos. As outlined in section 5.3, prior to unblinding the SR0 science data, a 250 μs veto-window was chosen for the NV, with a tagging efficiency of (53 ± 3)% and a livetime loss of 1.6%. Any TPC event with its primary S1 signal within the [-250 μs, 1 μs) window around an NV event center time is vetoed.

In the blinded region, three multiple-scatter and one single-scatter events

---

[1] mainly coming from uncertainties from material screening

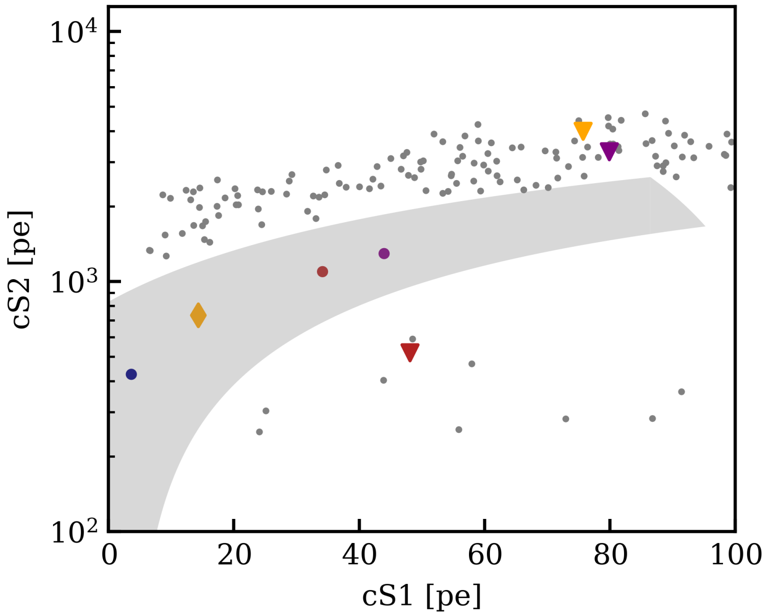

Figure 6.8: *NV-tagged events within the WIMP ROI from SR0 data are depicted here. Round markers symbolize multi-scatter events identified by the NV, while diamonds represent the single-scatter event that was tagged. The color coding of these markers corresponds to the event ID, consistent with the color scheme used in subsequent figures, specifically Fig. 6.9 and Fig. 6.10. The gray-shaded area highlights the blinded region of SR0, where neutron and WIMP signals are predicted to appear. Gray dots represent all events located within the WIMP ROI, but outside the blinded region. Additionally, events tagged by the NV that fall outside the blinded region are marked with colored triangles.*

were identified, aligning with the expected ratio for neutrons. Additionally, three events outside the blinded region were NV-tagged, consistent with the predicted accidental tagging rate of (2.5 ± 0.2) events. The four events within the blinded region exhibit characteristics highly indicative of neutron-induced signals, considering both the energy deposited in the NV and their temporal correlation with TPC signals, as depicted in Fig. 6.9.

The contour regions in Fig. 6.9 were numerically estimated using an exponential distribution for time delay and a normal distribution for the light detected in the NV, incorporating the best-fit values for the neutron capture time and the light signal at 2.2 MeV reported in section 5.4. The MS signal, marked by a red dot, is associated with two NV events. The first event falls within the 50% contour for neutron capture signals, while the second, delayed by 200 μs, suggests a larger energy deposit potentially from a daughter nuclei deexcitation in a spallation process. One event tagged by the muon-veto is also tagged by the NV, indicating a muon crossing the water tank, given its significant event area in both vetoes. Another event, with a smaller MV event area, likely represents an accidental coincidence between TPC and MV due to background, aligning with

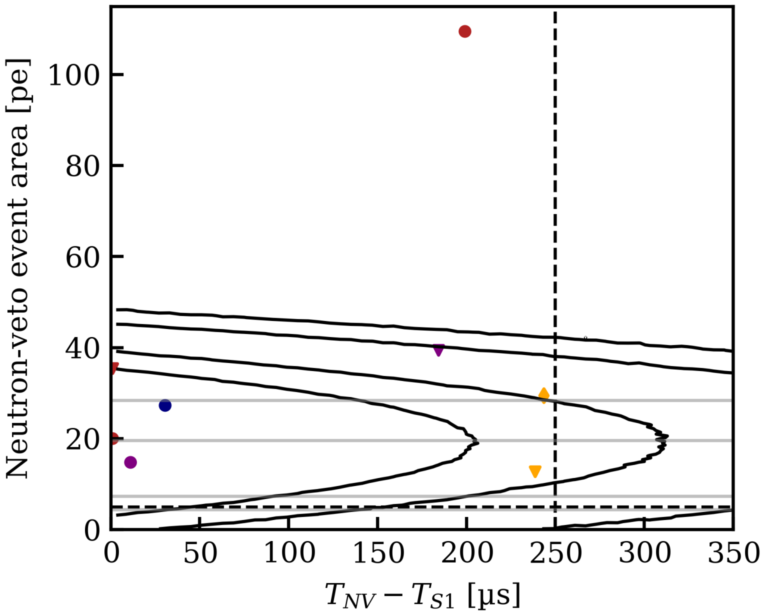

Figure 6.9: *Area of NV-tagged events plotted against the time delay between the S1 signal and the NV signal. Dashed lines represent the threshold and the duration of the tagging window implemented in SR0. Black contours and gray vertical lines delineate the 50%, 70%, 90%, and 95% quantiles for NV neutron-capture signals and background signals, respectively. These quantiles are derived from the purple and orange area distributions in Fig. 5.12, and the expected time distribution, which follows an exponential pattern for capture signals and a uniform distribution for background signals. The events are denoted using the same color coding and marker types as in Fig. 6.8.*

the expected accidental coincidence rate of (1.09 ± 0.09) events.

The fact that all TPC events within the NR band tagged by the NV are likely caused by neutron capture signals is also supported by the spatial correlation shown in Fig. 6.10.

The tagged SS event underscores the NV critical role in the XENONnT WIMP search, as it falls inside the WIMP ROI and would have passed all data quality checks otherwise. The observed ratio of multiple-to-single scatter events in the NV-tagged data matches simulation predictions. However, the overall neutron background rate is significantly higher than predicted, as all TPC events in the blinded region appear to be neutron-induced. The origin is this discrepancy is still under investigation: there are hints of a larger-than-expected background contribution in the Thorium chain from the stainless steel stiffening rings of the cryostat, which may be the source also of the increased neutron background. A precise estimation of this contribution is currently ongoing.

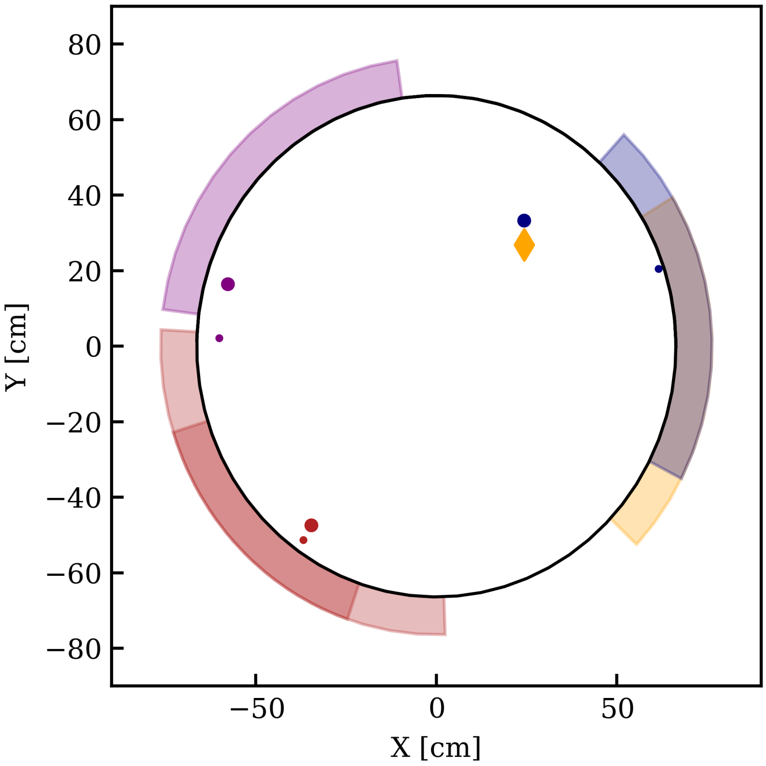

Figure 6.10: *Spatial correlation between TPC and NV events, with marker sizes representing the positions of the largest and second-largest S2 signals for each event. The color-shaded wedges depict the reconstructed azimuthal angle of the NV events, with the angular span of each wedge corresponding to the average 1 sigma contour of the AmBe calibration distributions. The red event is marked by two wedges, each corresponding to one of the NV events shown in Fig. 6.9.*

6.2 Science Run 1

Following the conclusion of Science Run 0 (SR0), preparations were made for the starting of a new Science Run, SR1. During this transitional phase, maintenance was primarily focused on the radon distillation columns, leading to an unprecedentedly low level of < 1 μBq/kg.

Regarding the NV, as mentioned in section 4.1.3, we made several enhancements to the PMT setup and analysis. Firstly, we developed a single photoelectron description model that improved the fitting of charge distributions in LED calibration signals, yielding more consistent results in terms of gains and acceptances. Secondly, this investigation led to increasing the voltage of the photomultipliers to enhance the acceptance and thus the detection efficiency of neutron capture signals in water. This naturally impacted the dark rate of the PMTs (and hence the accidental coincidences), with a non-worrisome increase given the low rate observed in SR0, namely $<$ 100 Hz with a 4-fold PMT coincidence requirement. The increase in voltage for the PMTs was about 200 V in each channel. Due to these changes in detector conditions, and to monitor the TPC performances, a new AmBe calibration was made in Spring 2022, in preparation for SR1. The analysis of AmBe data is analogous to that presented in 5.3. The tagging efficiency slightly increased, reaching (56 ± 2) % with a lifetime loss of 1.7% using a time-window of 250 μs, and (70 ± 2)% with a lifetime loss of 4.1% using a larger time-window of 600 μs; this increase is consistent with the increase in SPE acceptance of the PMTs. The estimate also includes an updated geometrical correction factor which was re-evaluated based on an updated neutron background model. SR1 began on 19^{th} May 2022 and ended on 8^{th} August 2023, resulting in a total exposure of ~200 days whose data is currently blinded until the final selection criteria and analysis steps will be finalized. With the increased neutron tagging efficiency and the larger exposure, the data-driven prediction on the neutron background obtained in SR0 will be cross-checked with tighter constraints. Having already clarified the excess in the low-ER region in XENON1T through the respective analysis in SR0 of XENONnT, SR1 analysis priority is again dedicated to WIMP search, with an increased sensitivity given by the larger exposure and the lower ER and NR backgrounds.

6.3 Towards Science Run 2

In the transition from SR1 to SR2 the key element is the addition of Gd-Sulphate Octahydrate (GdSO) salt into the water tank, finally making the NV a Gd-Water Cherenkov detector. The target Gd concentration was achieved in small steps. The insertion and dissolution of the salt are the focus of this section, together with the performances obtained with Gd.

During SR1, we completed the commissioning of the Gd-Water Purification System (GdWPS) (described in section 3.1.2): in particular, in this first phase its basic performances were tested by running it with demineralized water in a closed loop. Since July 2022, the 700 t of water of the main XENON tank, usually treated with the WLP, has been circulated through the GdWPS for several months with stable conditions in terms of pressure, flows, and temperature in the GdWPS. The water purified in the plant was inserted back into the XENON water tank through two inlet points: one at the floor of the water tank, and one directly inside the NV on its floor. The flux was split evenly, with about 25 l/min in each branch. The optical properties of the water were weekly monitored through reflectivity monitor runs: the average arrival time of photons at the NV PMTs showed a constant behaviour, close to 57 ns, demonstrating stable optical performances of the detector.

In January 2023, the GdPlant was run again in closed loop mode (with the main tank water purified through the WLP), to perform the first insertion of GdSO inside the plant. We added 15 kg of salt dissolved in the ~3 t of water inside the GdPlant, corresponding to the 5000 ppm concentration planned as the final one. The plant was operated for several months in this configuration to optimize the performances in terms of Gd separation efficiency at the nanofilter stages. In June 2023, we decided that the first insertion of GdSO in XENONnT would have happened at a reduced concentration, 500 ppm (10 times lower than the nominal one). This choice was made as a risk mitigation strategy, to test the system in the first phase without using the whole amount of salt. Referring to Fig. 3.3, the fraction of captures on Gd at this concentration is already significant, ~60%. For this reason, since June 2023 the concentration inside the GdPlant was reduced to 500 ppm, and the system has been run for the whole summer in this condition, providing very stable performances, with a negligible amount of GdSO lost after the two nanofiltration stages.

The insertion of GdSO in the Water Tank started in October 2023; the timeline of the entire operation is documented in figure 6.11 where the data rate of the NV DAQ is shown in response of each phase of the Gd-loading. The first step involved reintegrating the GdWPS into the water tank purification loop. Inside the GdWPS 1.5 kg of GdSO was present for its commissioning in a closed loop: this content was then inserted into the water tank on October 5, with the input flow split into the two entrance points of the water tank.

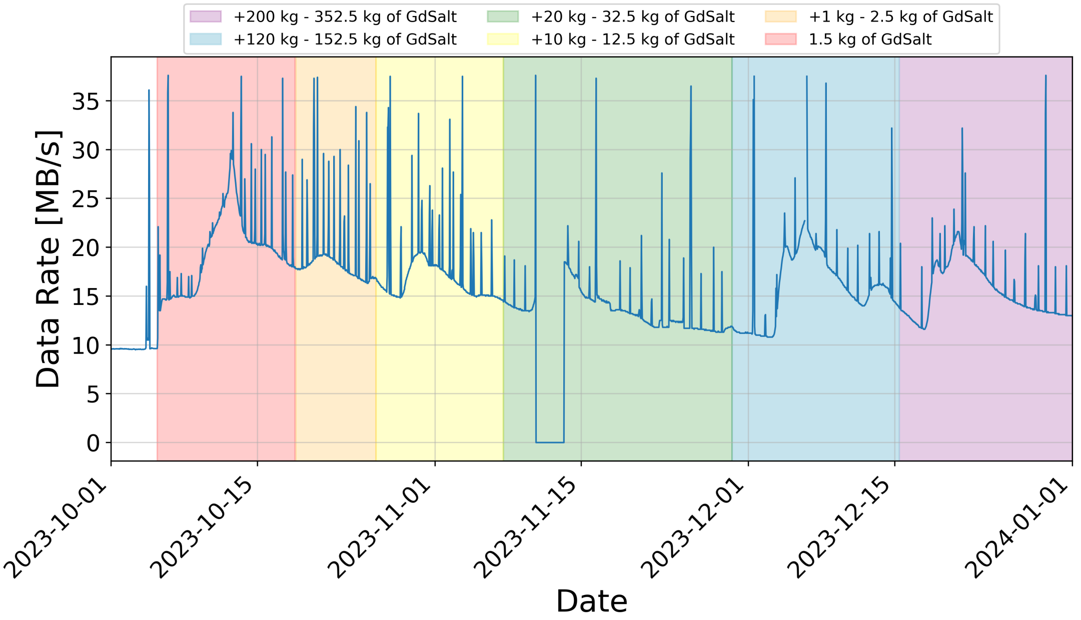

Figure 6.11: *Evolution of the data rate during the Gd-loading operations. This plot covers the entire timeline from the first loading of 1.5 kg in October 2023 up to the goal concentration achieved in December. Each step is represented by a different color. For the first loading only (red region), the Gd-Water injection occurred also directly in the NV. After observing a sudden increase in the rate, we decided to adopt in the following insertions a more gradual procedure by injecting the water only at the bottom of the water tank. Therefore, from the orange region onwards, the rate increase does not immediately follow the operation, but occurs a few days later, the time needed for the concentrated Gadolinium solution to also spread into the NV. Most of the spikes observed are associated with optical calibrations (using laser) to regularly monitor the optical properties during operations. These calibrations are linked to a constant rate of* ~ 30 *MB/sec, defined by the trigger rate that characterizes data acquisition. Some of the smaller spikes, however, are associated with regular AmBe calibrations. These lead to a more modest increase in the data rate, due to an increase in the rate of physical events.*

As soon as the operation began, a sudden increase in the data rate was observed across all 120 NV PMT channels, by approximately ~50% (as shown in Fig. 6.12). The data rate refers to the amount of incoming data to the DAQ server and, in the case of self-trigger acquisition, provides a preliminary estimate of the observed hit rate. The data rate has often been used as a monitor during operations on the NV, particularly to observe any increases in dark rate in the system.

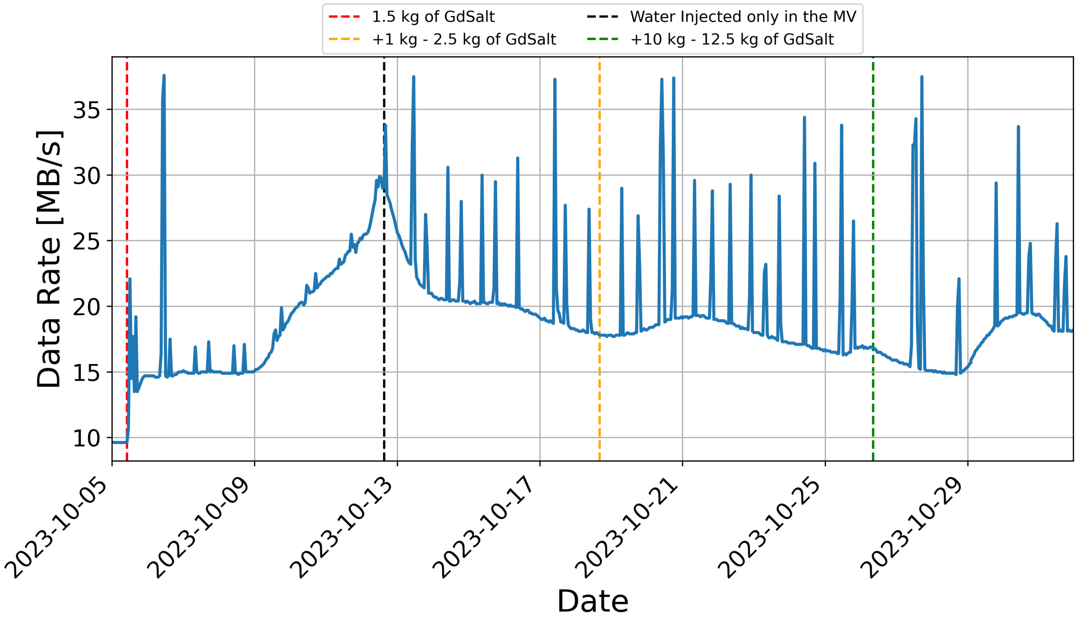

Figure 6.12: *Zoom of the plot in Fig. 6.11, corresponding to the initial steps of Gd loading into the water tank. In this plot, each step is identified by a colored vertical dashed line. In addition to the moments when Gd salt was added to the system, the plot also marks the time when the water injection into the NV was turned off to control the rapid increase in rate following the very first loading on October* 5^{th}.

This unexpected increase was investigated to understand its origin. A study on the multiplicity of these hits (i.e., varying the coincidence requirement) revealed that the increase mostly involved events with one or a few channels in coincidence, suggesting an increase in the light seen by each PMT, rather than an increase of background events from radioactivity, which would have produced > 10 photoelectrons in coincidence on several channels.

Following the sudden increase of October 5, the data rate continued to increase in the following days until Oct 12, when we closed the input line to the NV, inserting the solution only through the water tank floor. At this point the data rate started decreasing, reaching a level similar to the pre-insertion status in about 7-10 days. Once a relatively stable situation was achieved, it was decided to proceed with the insertion of new GdSO into the system, introducing the new solution only from the bottom of the water tank. Each addition of GdSO was followed by an increase, although lower, of the rate in the NV. The data rate in the NV throughout the whole Gd insertion period is shown in fig. 6.11. The detailed timeline of the various insertions of GdSO into the ~ 700 t of the water tank is reported in table 6.1. A similar but smaller data rate increase was observed in the MV PMTs.

The GdSO concentration inside the water tank was monitored by sampling

Date	Additional / Total GdSO mass	GdSO Concentration
Oct 5	Connection of the Water Tank to the GdWPS, with 1.5 kg of GdSO present	~ 2 ppm
Oct 18	+1 kg / 2.5 kg	~ 3.5 ppm
Oct 26	+10 kg / 12.5 kg	~ 18 ppm
Nov 7	+20 kg / 32.5 kg	~ 46 ppm
Nov 29	+120 kg / 152.5 kg	~ 218 ppm
Dec 15	+200 kg / 352.5 kg	~ 504 ppm

Table 6.1: *Sequence of GdSO insertion steps.*

the solution from dedicated pipes available to extract water at various points in the water tank, including inside the NV at its floor as shown in figure 6.13.

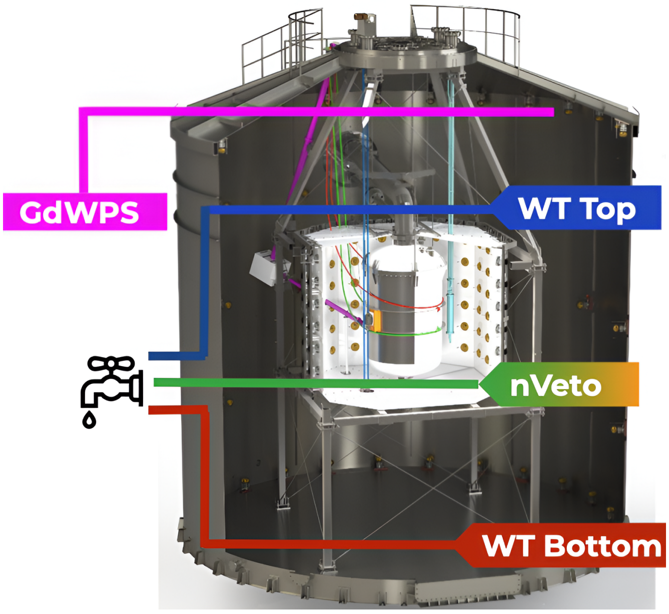

Figure 6.13: *CAD rendering of the water tank and NV with the sampling points where the Gd-water solution is extracted for further analyses. The 4 sampling points are reported with different colors, matching the scheme of figure 6.14. For the NV port there are two colors indicating that for those samples the measurements of the concentration are performed with two different methods (conductivity and ICP-MS). The flow of the Gd-Water is also reported. The GdWPS line is positioned on the top of the water tank since the solution flows in the GdWPS from that spot.*

The Gd concentration was measured directly through ICP-MS measurements, and indirectly by the conductivity. The behaviour of the concentration measured as a function of time is shown in figure 6.14, where also the expected value is reported.

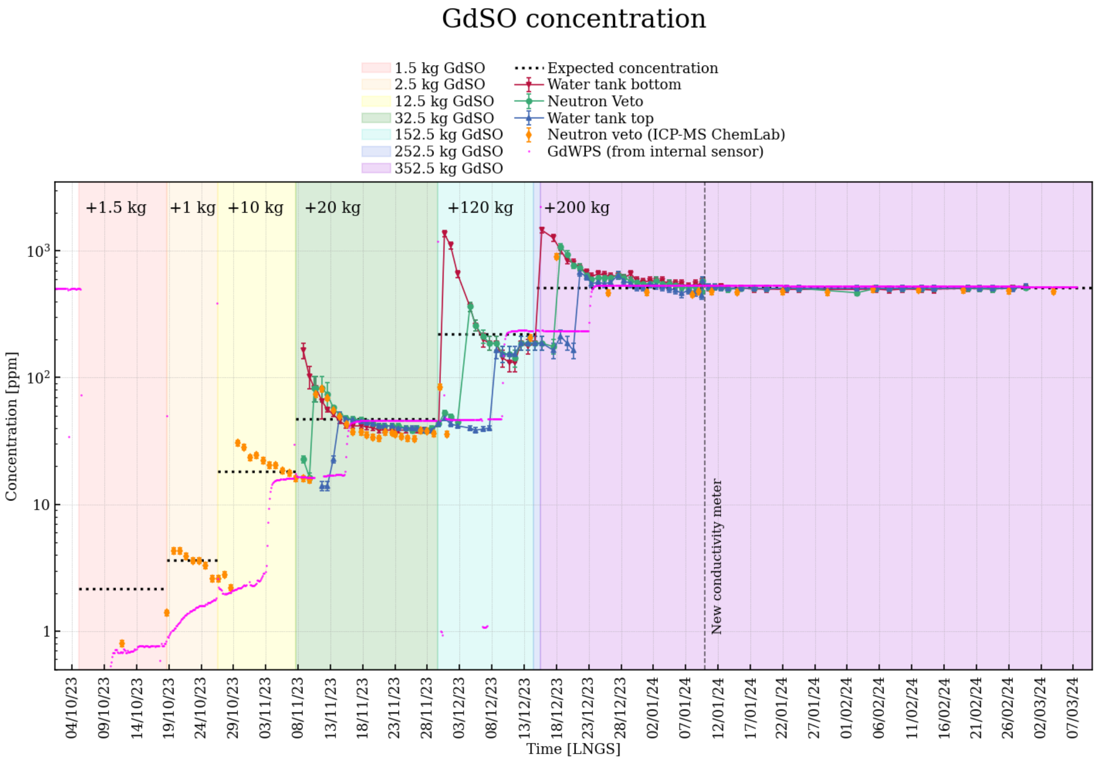

Figure 6.14: *Evolution of the measured Gd concentration of the solution extracted from various sampling points arranged as shown in figure 6.13. The different steps of Gd-loading are represented by various background colors. The expected values based on the amount of added GdSO are marked with the black dashed horizontal lines. The concentration was primarily estimated using the conductivity measured at the 4 sampling points. Additionally, the Gd concentration of the sample collected from the NV (green dots) was also measured using ICP-MS (yellow dots). The values estimated with these different methods agree with each other. The continuous trend outlined by the pink line represents the concentration measured directly with the conductivity sensors in the GdWPS. In this case, the delay between the insertion and the achievement of the concentration plateau is associated with the diffusion of the doped water throughout the water tank, since the system collects the water from the top of the water tank.*

The physical phenomena at the origin of the increased data rate at each GdSO insertion is not yet understood. However, the most likely hypothesis is the production of light when there is a variation in the GdSO concentration. The effect indeed has its origin in the whole volume of the solution, being detected in all channels inside the NV. Since the pH of the solution changes when inserting the GdSO, from 7 of the demineralized water to about 5.5 of the 500 ppm solution, it may be due to the formation of molecules of Gd^{3+} $(OH)^{-3}$. We plan to test this hypothesis in a dedicated setup at LNGS, monitoring the light emission of the GdSO solution inside a becker with a highly sensitive PMT inside a black box, varying the GdSO concentration in the solution.

To ensure that these operations were not adversely affecting the excellent performance achieved in the NV with the previous configuration, the water transparency and wall reflectivity were regularly checked using the reflectivity monitor (by studying the τ of the exponential distribution as detailed in section 4.2.1). The results of the reflectivity monitor trend are shown in figure 6.15.

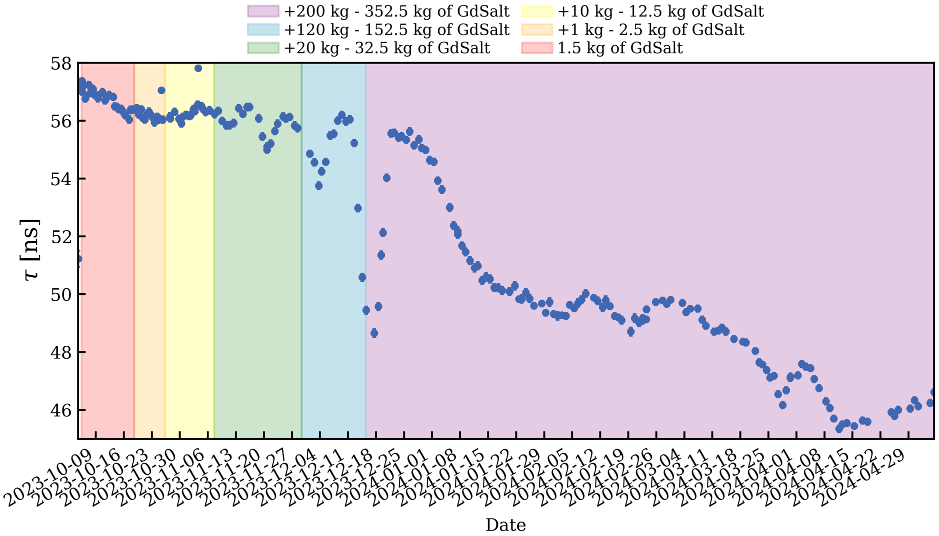

Figure 6.15: *Evolution of the average time parameter τ estimated from the fit of the time distribution of the daily reflectivity monitor runs taken during the Gd-loading operation. Each GdSO insertion step is marked by a different color.*

During the initial phases of Gd insertion, it was observed that τ is affected by the operations only when the GdSO concentration changes inside the NV, thus with a slight delay following the salt insertion into the floor of the water tank. However, the τ values returned to higher levels after a few days of re-circulation and purification through the GdWPS. After the last large injection of GdSO in mid-December, the optical properties inside the system started decreasing, reaching an almost stable behaviour after a few months. As it was expected from preliminary tests, the insertion of GdSO inside water indeed reduces the transparency of the medium, leading to an overall decrease in the light collection efficiency inside the NV of about 20%.

To monitor the effect of GdSO in water, we also performed regular AmBe calibration before, during, and after the Gd-insertion period, to measure the charge spectra with the source in the same position at the center of the NV (Bottom U-Tube CW6d0m). As shown in fig. 6.16, the light spectrum observed in the NV was analyzed with the same model described in section **??**, with the addition of a new gaussian to take into account the neutron captures on Gd (red solid curve). No significant differences in the charge spectra were observed until concentration of 50 ppm was reached, corresponding to 32.5 kg of Gd-salt, when the first captures on Gd were observed.From the position of each peak, in particular those related to the 2.2 and 4.4 MeV lines, as a function of time we can obtain a direct measurement of the reduction in light collection efficiency, while from the area under each gaussian curve we get the amount of captures on H and Gd.

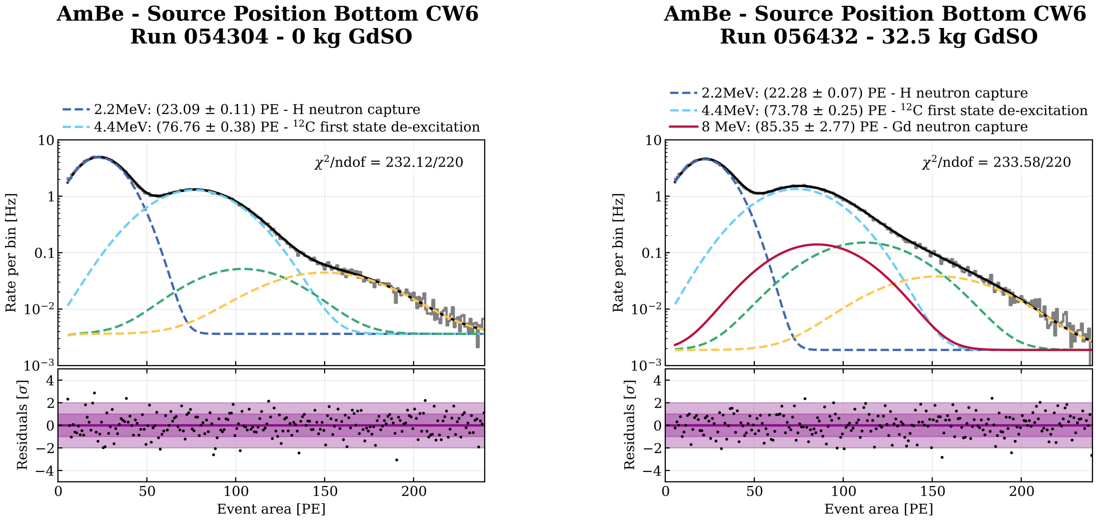

(a) *Demineralized water*

(b) *GdSO Concentration: 50 ppm*

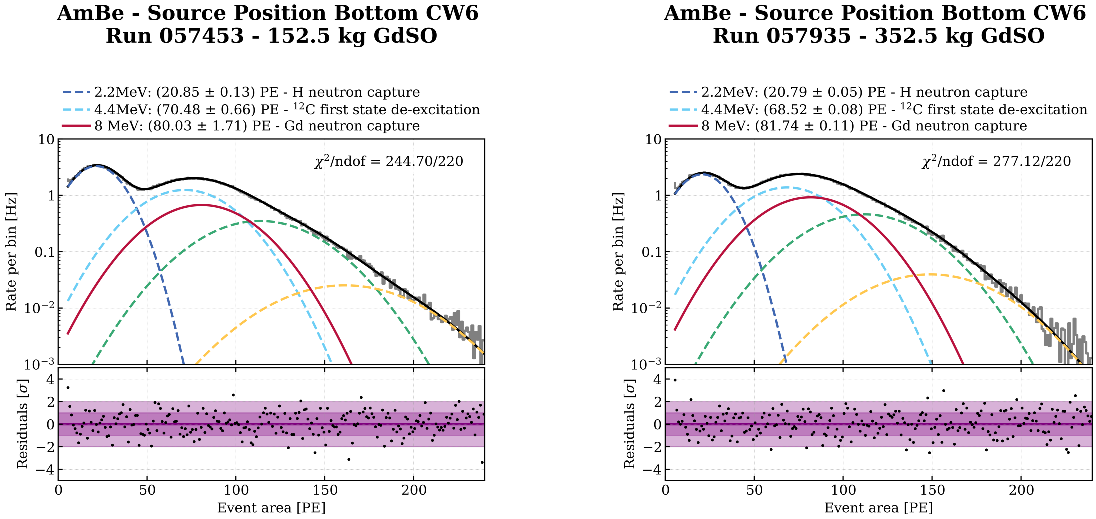

(c) *GdSO Concentration: 200 ppm*

(d) *GdSO Concentration: 500 ppm*

Figure 6.16: *Energy spectrum in the NV during AmBe calibration for different GdSO concentration - (a) Demineralized water (as the one already shown in figure 5.8) - (b) 32.5 kg of GdSO (corresponding to ∼ 50 ppm). (c) 152.5 kg of GdSO (corresponding to ∼ 200 ppm) - (d) 352.5 kg of GdSO (corresponding to ∼ 500 ppm). The bottom panels of all the plots show the fit residuals. The individual fit components are also shown in different colors. For all the plots with Gd an additional Gaussian component (shown in red solid line) has been added to take into account the contribution of neutron captures on Gd.*

The results are shown in figure 6.17: in the top panel we can see that the decrease in the optical properties is reflected in the shifted position of the peaks (both the neutron capture on H and the gamma from the de-excitation of ^{12}C). Currently, the light collection efficiency with 500 ppm of GdSO is about 80% of the one with demi-water. However, the number of events lost due to the 5 PE threshold is very small, at the level of a few percent. In the bottom panel, indeed, we show the capture rates on H, Gd and the total. The total neutron capture rate is basically unchanged, increasing by a few percent: this is due to the fact that in the center of the NV most of the events were already detected even in the case of demineralized water. Also, we can clearly see that most of the events move from the H-capture to the Gd-capture region when increasing the concentration of GdSO. At the final concentration, about 60% of the neutron captures happen on Gd, as predicted by MC simulations.

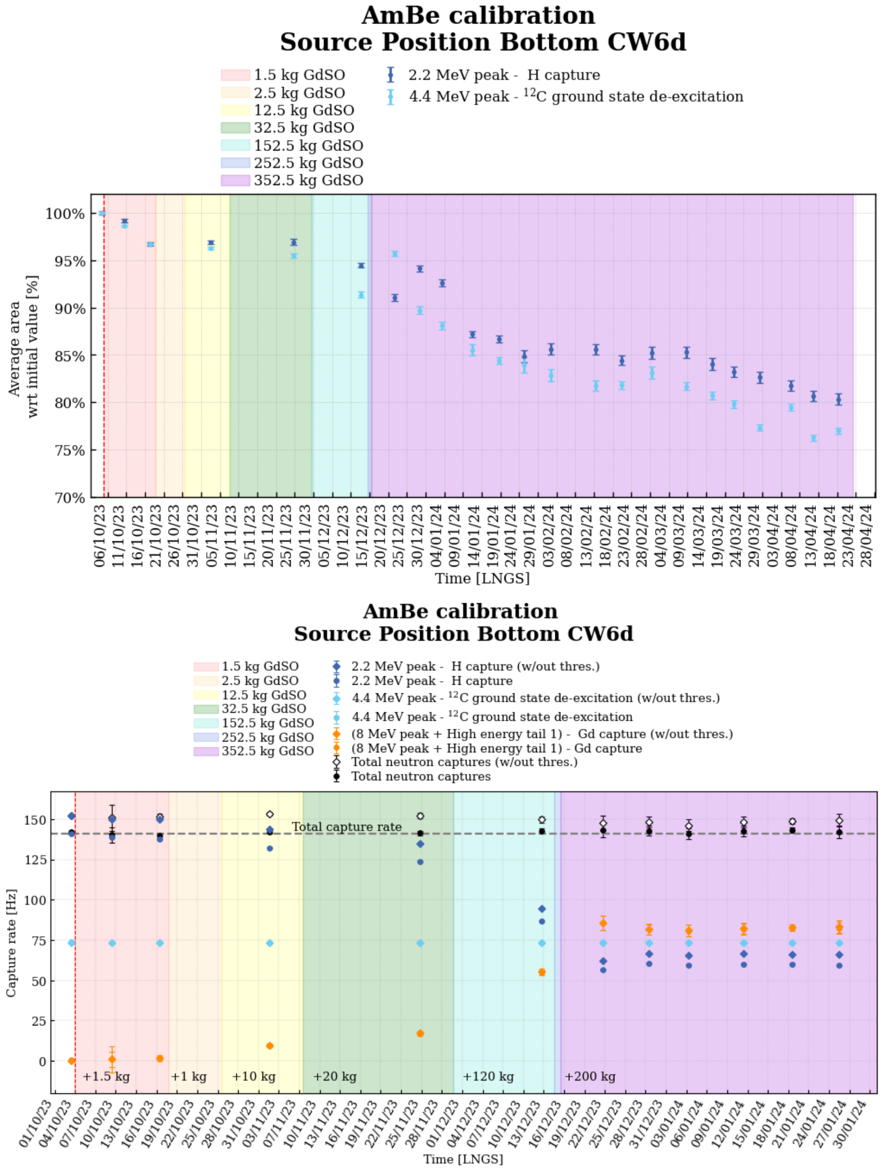

Figure 6.17: *(Top Panel) Time evolution of the mean values of the Gaussian corresponding to H captures and* ^{12}*C de-excitation, normalized to their initial value. (Bottom panel) Time evolution of the rate of n capture for H (blue), Gd (brown) and the* ^{12}*C de-excitation (light-blue). The open diamonds represent the values obtained without considering the threshold, while the solid points show the results above the 5 PE threshold. Also, the total number of captures (the sum of the H and the Gd captures) is shown for reference.*

To finally measure the neutron tagging efficiency with Gd, we use the AmBe calibration with the source positioned near the cryostat (Top CW7d8m), reproducing in the closest way the topology of the neutron background from the cryostat.

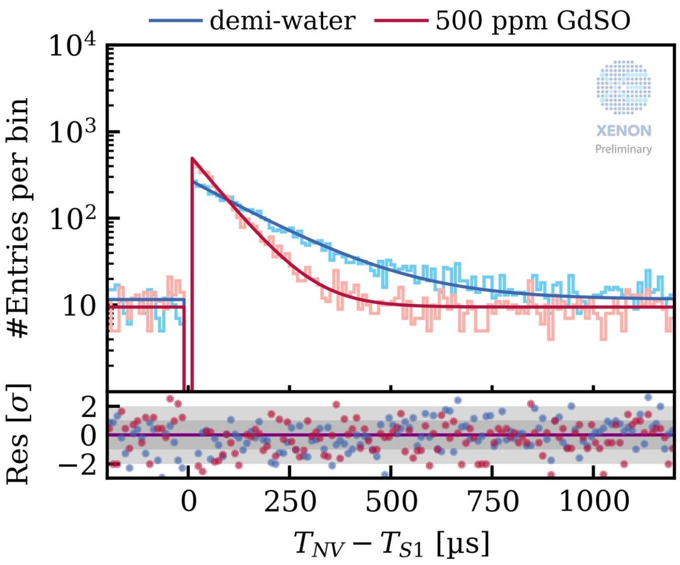

Figure 6.18: *Distribution of the time difference between the triggering nuclear-recoil S1 signal in the TPC and the neutron capture event in the NV: in demi-water (blue) and with 500 ppm of GdSO (red).*

The results are obtained with the same analysis described in section 5.3: as shown in figure 6.18, the capture time of neutrons is reduced due to the presence of Gd from (163 ± 3) μs in SR1 (demi-water) to (75 ± 2) μs in SR2 (Gd-water). In figure 6.19 the spectra in the NV are shown: about 60% of the neutron captures now happen on Gd rather than on H, as can be clearly seen by the second peak in the distribution of light collected in the NV. The resulting neutron tagging efficiency, shown in figure 6.20, inside a 250 μs time window, 5 PMTs in coincidence and a threshold of 5 PE, becomes 77% with 500 ppm of GdSO (it was 53% with demi-water in SR0), reducing the neutron background by a factor 2 compared to the results published in SR0.

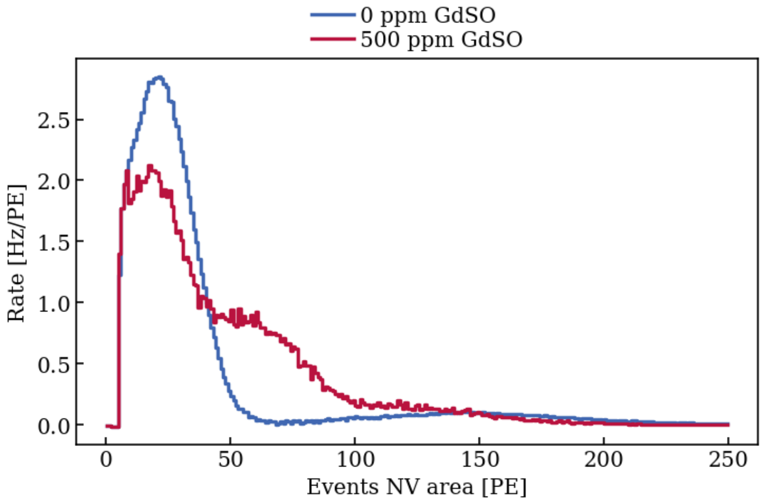

Figure 6.19: *Event area distribution of AmBe calibration after the 4.4 MeV γ subtraction (this contribution has been estimated with the usual fit described in 5.2.2), for demineralized water (blue) and 500 ppm GdSO-water solution (red).*

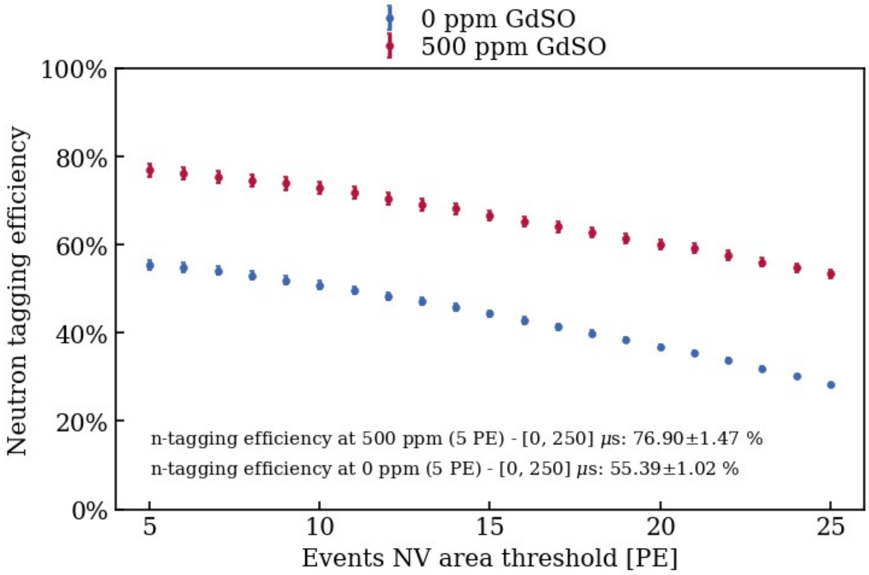

Figure 6.20: *Tagging Efficiency measured with an AmBe calibration with the source positioned close to the cryostat (Top CW7d8m). The tagging efficiency is displayed here for the time window of [0,250]μs which is the one used in Science Runs analysis (section 5.3). With the current configuration (500 ppm GdSO concentration, in red) we observe an improvement of $+\sim 24\%$ (absolute value) in the tagging efficiency with respect to SR0 with demi-water (blue).*

In conclusion, loading water with GdSO this new XENONnT science run will benefit from the reduced neutron background, where the MC predicts a reduction by a factor of 2 compared to the one obtained in SR0, as it was shown by the MC simulations presented in Fig. 5.28. The prediction is now confirmed by the data shown in figure 6.20. This will significantly improve the XENONnT sensitivity in the WIMP search.

7

SUMMARY AND OUTLOOK

More than a century has passed since F. Zwicky hypothesized the existence of dark matter, as evidence of unseen mass, to account for the discrepancy between measurements of the mass of the Coma Cluster made through dynamical means and the mass inferred from its luminous matter. Since then, a wide range of observations, both astronomical and cosmological, have increasingly supported the existence of dark matter. Despite its assumed presence, it remains one of the most intriguing mysteries of modern physics, drawing a plethora of experimental efforts to uncover the nature of this elusive component of the universe.

In the search for Weakly Interacting Massive Particles (WIMPs), currently regarded by the scientific community as one of the most promising dark matter candidates, dual-phase xenon Time Projection Chambers (TPC) have been at the forefront, setting the most stringent exclusion limits for a wide range of WIMPs' masses.

The XENON project at the INFN Laboratori Nazionali del Gran Sasso has been a pioneer in the ultra-sensitive and low background xenon-based dual-phase TPCs, with its current phase, XENONnT, that operates 5.9 t of LXe in its instrumented mass.

In a dual-phase TPC, scintillation (S1) and ionization (S2) signals are observed, from which the event position and energy can be reconstructed. These signals also enable precise discrimination between signal and background. WIMP-like signals are expected to be Nuclear Recoils (NRs), in contrast to the background-like signals typically associated with Electronic Recoil (ER) scatterings. XENONnT has reported the lowest ER background rate ever achieved among dark matter direct detection experiments [85] , approximately five times lower than the one obtained in XENON1T. This significant reduction was possible by decreasing the activity of ^{222}Rn to $< 1\ \mu$Bq/kg, which so far was the dominant background component. With the substantial reduction in ER background, radiogenic neutrons become an increasingly relevant threat to the sensitivity of

WIMP discovery, since they can interact with the xenon nuclei, leaving a signal in the TPC indistinguishable from the one expected from a WIMP. Neutrons, mostly emitted from spontaneous fission and (α-n) reactions in the detector materials, can undergo a single scatter NR in the TPC and then exit the cryostat undetected, as a WIMP signal. To address this challenge, in XENONnT it is implemented a Neutron Veto (NV): a dedicated detector designed to tag these neutrons and thus suppress this source of background. The XENONnT experiment, located in Hall B of LNGS, is immediately noticeable upon entering the experimental hall due to its prominent three-floor glass building. This building hosts all the ancillary systems of the experiment, including the xenon storage, the purification system, the Rn & Kr distillation columns and the data acquisition control room. Hidden behind this structure is the 10-meter-tall water tank. The experiment consists of three main detectors. The TPC is at the core, housed within the cryostat containing 8.6 tonnes of xenon, in total. The NV, the water Cherenkov detector consisting of an octagonal prism-shaped volume, surrounds the cryostat. Mounted on a light stainless-steel support structure are 120 photomultipliers and reflective ePTFE panels that optically separate the interior of the NV from the outer part of the water tank. On the latter, 84 photomultipliers are installed, constituting the Muon Veto. The working principle of the NV is as follows: neutrons interacting within the TPC may escape from the cryostat. Here, they are first moderated by water and eventually captured. The neutron capture process in pure water leads to the emission of a 2.2 MeV gamma, which in turn accelerates electrons through Compton scattering. These electrons emit Cherenkov radiation that, after multiple reflections within the internal volume of the NV, is detected by photomultipliers. To enhance the neutron tagging efficiency, $Gd_2(SO_4)_3 \cdot 8\,H_2O$ was dissolved in water. Gadolinium has the highest neutron capture cross-section of any element. Neutron capture on Gd is associated with the emission of photons (typically 3-4) with a total energy of ~8 MeV. However, the addition of Gd presents several challenges. One of the primary concerns is ensuring the compatibility of Gd with all the materials involved in the experiment. Any reactive interaction between Gd and these materials could potentially lead to corrosive damage, adversely affecting the optical properties of the detector. Another critical aspect revolves around the water purification system. The system design must not only preserve the transparency of the water but also prevent the inadvertent removal of gadolinium during the purification process. This necessitates a sophisticated purification system that not only maintains water transparency at a high standard, but also effectively separates the dissolved gadolinium salt before purification, ensuring that it is not discarded as waste. To address these challenges, a Gadolinium Water Purification System (GdWPS) has been designed and installed. This system boasts the capability to purify water while simultaneously achieving an appropriate gadolinium separation efficiency. The neutron detection efficiency of the NV is contingent upon its optical properties, such as the water transparency and surface reflectivity, and the single-photoelectron detection efficiency of the photomultiplier tubes. The PMTs used are the 8-inches Hamamatsu R5912, which feature a high quantum efficiency, low radioactivity, a gain of around 10^7, and high single-photoelectron acceptance (>90%). Throughout the data acquisition phase of the experiment, these PMTs are monitored weekly. So far, they have demonstrated performances that align with our expectations. To further optimize their performance, we have also adjusted the high voltages; an increase of approximately 200 V in the HV of the PMTs has enabled us to achieve a ~95% acceptance while maintaining a contained dark signal rate of <1 kHz. The monitoring of the PMTs, as well as the optical properties of the detector, is conducted through dedicated luminous calibration systems. Optical fibers, coupled on one end to each PMT and on the other to blue LEDs, facilitate the calibration of single-photoelectron response and gain. Additionally, we have four quartz optical fibers connected to a 375 nm wavelength laser, constituting the reflectivity monitor. This setup allows us to monitor the optical properties of the NV. Monitoring the decay constant of the exponential distribution of the detected signal arrival times ensures that the detector performance remains consistent throughout the data acquisition and during operations on the purification plant. These promising "low-level" performances correspond to equally exceptional "high-level" performances, parameterized in terms of the neutron tagging and detection efficiency. Both measure neutron detection efficiency, with the former associated exclusively with neutrons that have produced an NR-type signal in the TPC. To determine these metrics, we conducted calibrations using an AmBe neutron source. The signature of AmBe is characterized by the production of ^{12}C+n from ^{9}Be+α. The excited ^{12}C can decay to the ground state in ~50% of cases emitting a 4.4 MeV gamma. Whenever a 4.4 MeV gamma is detected, an associated neutron is also present. To estimate the tagging efficiency, we look for an NR event in the TPC and coincidentally search for the 4.4 MeV gamma in the NV. We then identify neutron capture events by subtracting the area distribution of a background run. The tagging efficiency, estimated in this manner with a 600 μs coincidence window and a requirement of 5-fold PMT coincidence, is (68 ± 3)%. For the detection efficiency, we search for all the events in the NV in coincidence with a 4.4 MeV gamma in the TPC. With the same requirements, the detection efficiency is (82 ± 1)% which, to our knowledge, is the highest neutron detection efficiency ever measured in a water Cherenkov detector. The experiment is currently taking scientific data. The first science run (SR0), which was concluded on December 2021, focused on analyzing low ER events to provide insights into the excess of events observed in XENON1T, as well as on WIMP analysis. For both studies, this work highlights the contribution of the NV in reducing the main backgrounds. With a total exposure of (1.09 ± 0.03) tonnes x year, no excess above the predicted background was observed in the region of interest for both searches. For the low ER analysis, this has allowed us to set stringent new limits on solar axions, enhanced neutrino magnetic moment, and bosonic dark matter, which were the main candidates to explain the excess seen in XENON1T. The blind analysis of nuclear recoil events in the WIMP search finds no significant excess, leading to a minimum upper limit on the spin-independent WIMP-nucleon cross-section of 2.58×10^{-47} cm^2 for a WIMP mass of 28 GeV/c^2 at a 90% confidence level [86]. Both the limit and the sensitivity for the full range of WIMP masses analyzed here improve on previous results obtained with the XENON1T experiment for the same exposure, and align well with the results of other competitor experiments as LZ, performing similar searches [141]. The role of the NV in this science run was crucial to directly measure and constrain the neutron background, by tagging single and multiple scatter events in the TPC, and by reducing its impact thanks to its high tagging efficiency. Following a maintenance period, the experiment transitioned to a second science run (SR1), ended on August 2023, where approximately 200 days of data was collected. In SR1, the voltages of the NV PMTs were adjusted, and AmBe calibrations were performed to verify the tagging efficiency with the new PMT acceptances. An increase of approximately ~3% in efficiencies compared to SR0 was observed, consistent with the increase of SPE acceptance of the PMTs. The analyses in the WIMP search are still ongoing, with an increased sensitivity expected due to the larger exposure and the lower ER and NR backgrounds.

The experiment is currently in data acquisition in a new science run, SR2. During the transition from SR1 to SR2, we completed the commissioning of the GdWPS, allowing the introduction of the first batch of Gd into the water tank. To reach the targeted concentration of 500 ppm which corresponds to 350 kg of GdSO, we followed several steps during which the optical properties and the PMT response were monitored. After some initial variations, the data rate returned to values similar to the situation before the Gd insertion. As expected, the optical properties showed an initial decrease, reaching a stable behaviour after a few months of running the solution through the dedicated GdWPS purification plant, with a light collection efficiency ~ 80% of the original one. The performance of the NV was monitored also thanks to neutron calibrations with the AmBe source, performed regularly during the Gd insertion. In addition to the peak due to neutron captures on H, the high-energy peak due to captures on Gd is clearly visible in ~ 60% of cases. The average neutron capture time is reduced due to the presence of Gd from (163 ± 3) μs in demi-water to (75 ± 2) μs with 500 ppm of GdSO in water. The tagging efficiency is measured with the AmBe source close to the cryostat: it results in (77 ± 3)% with 5-PMT coincidence and 250 μs window. This improvement reduces the neutron background by a factor of ~2 with respect to what was observed in SR0.

Tagging efficiency predictions at this Gd concentration were made possible through the use of a Hitlet Simulator, a tool capable of simulating the data processing chain; it includes the response of photomultipliers following a photon hit on the photocathode, up to the clustering of hits into events from which key information useful for analysis are constructed, such as charge, the temporal centroid of the event, and location. The Hitlet Simulator is one of the necessary steps to compare simulations with real data, and within the MC-chain, it stands immediately after the physical event simulation via Geant4. In Geant4, various physical processes and particle propagation within the geometric volume of the detector are simulated as faithfully as possible to reality. With a GdSO concentration of 500 ppm (corresponding to ~200 ppm of Gd in mass), ~60% of captures occur on Gd, and the estimated tagging efficiency is about 77% with 5-PMT coincidence and 250 μs window, in very good agreement with the measured results.

In summary, the work presented in this thesis describing the design, construction, commissioning and result of the XENONnT NV shows the excellent performance of this novel system, in terms of neutron detection capability, reduction of the neutron background, and impact on the XENONnT Science Runs for searches of WIMP and other rare events. The performances have been demonstrated both with demineralized water and with the very recent insertion of Gd in the system, allowing further improvement in the detector performance in the next Science run, with reduced neutron background and increased sensitivity. Gd-water Cherenkov detector technology is also promising to be used as an NV for future Dark Matter experiments like DARWIN/XLZD, where the xenon active mass will be increased up to 50-100 t, and the neutron background must be kept at a negligible level to maximize the sensitivity to WIMP search and finally reach the neutrino fog.

This page intentionally left blank.

BIBLIOGRAPHY

[1] F. Zwicky. "Die Rotverschiebung von extragalaktischen Nebeln". In: *Helv. Phys. Acta* 6 (1933), pp. 110–127. DOI: `10.1007/s10714-008-0707-4` (p. 5).

[2] F. Zwicky. "On the Masses of Nebulae and of Clusters of Nebulae". In: *Astrophys. J.* 86 (1937), pp. 217–246. DOI: `10.1086/143864` (p. 5).

[3] Vera C. Rubin and W. Kent Ford Jr. "Rotation of the Andromeda Nebula from a Spectroscopic Survey of Emission Regions". In: *Astrophys. J.* 159 (1970), pp. 379–403. DOI: `10.1086/150317` (p. 6).

[4] K. C. Freeman. "On the disks of spiral and SO Galaxies". In: *Astrophys. J.* 160 (1970), p. 811. DOI: `10.1086/150474` (p. 6).

[5] Yoshiaki Sofue. "Mass Distribution and Rotation Curve in the Galaxy". In: *Planets, Stars and Stellar Systems*. Springer Netherlands, 2013, pp. 985–1037. DOI: `10.1007/978-94-007-5612-0_19`. URL: `http://dx.doi.org/10.1007/978-94-007-5612-0_19` (p. 6).

[6] Edvige Corbelli and Paolo Salucci. "The Extended Rotation Curve and the Dark Matter Halo of M33". In: *Mon. Not. Roy. Astron. Soc.* 311 (2000), pp. 441–447. DOI: `10.1046/j.1365-8711.2000.03075.x`. arXiv: `astro-ph/9909252` (p. 6).

[7] Julio F. Navarro, Carlos S. Frenk, and Simon D. M. White. "The Structure of cold dark matter halos". In: *Astrophys. J.* 462 (1996), pp. 563–575. DOI: `10.1086/177173`. arXiv: `astro-ph/9508025` (p. 7).

[8] Yoshiaki Sofue and Vera Rubin. "Rotation curves of spiral galaxies". In: *Ann. Rev. Astron. Astrophys.* 39 (2001), pp. 137–174. DOI: `10.1146/annurev.astro.39.1.137`. arXiv: `astro-ph/0010594` (p. 7).

[9] Douglas Clowe, Anthony Gonzalez, and Maxim Markevitch. "Weak lensing mass reconstruction of the interacting cluster 1E0657-558: Direct evidence for the existence of dark matter". In: *Astrophys. J.* 604 (2004), pp. 596–603. DOI: `10.1086/381970`. arXiv: `astro-ph/0312273` (p. 7).

[10] M. C. Weisskopf et al. "An overview of the performance and scientific results from the Chandra X-ray Observatory (CXO)". In: *Publ. Astron. Soc. Pac.* 114 (2002), pp. 1–24. DOI: `10.1086/338108`. arXiv: `astro-ph/0110308` (p. 7).

[11] Douglas Clowe et al. "A direct empirical proof of the existence of dark matter". In: *Astrophys. J. Lett.* 648 (2006), pp. L109–L113. DOI: `10.1086/508162`. arXiv: `astro-ph/0608407` (p. 7).

[12] Albert Einstein. "Lens-Like Action of a Star by the Deviation of Light in the Gravitational Field". In: *Science* 84 (1936), pp. 506–507. DOI: `10.1126/science.84.2188.506` (p. 8).

[13] Matthias Bartelmann. "Gravitational Lensing". In: *Class. Quant. Grav.* 27 (2010), p. 233001. DOI: `10.1088/0264-9381/27/23/233001`. arXiv: `1010.3829 [astro-ph.CO]` (p. 8).

[14] Arno A. Penzias and Robert Woodrow Wilson. "A Measurement of excess antenna temperature at 4080-Mc/s". In: *Astrophys. J.* 142 (1965), pp. 419–421. DOI: `10.1086/148307` (p. 8).

[15] Joshua Frieman, Michael Turner, and Dragan Huterer. "Dark Energy and the Accelerating Universe". In: *Ann. Rev. Astron. Astrophys.* 46 (2008), pp. 385–432. DOI: `10.1146/annurev.astro.46.060407.145243`. arXiv: `0803.0982 [astro-ph]` (p. 8).

[16] N. Aghanim et al. "Planck 2018 results. VI. Cosmological parameters". In: *Astron. Astrophys.* 641 (2020). [Erratum: Astron.Astrophys. 652, C4 (2021)], A6. DOI: `10.1051/0004-6361/201833910`. arXiv: `1807.06209 [astro-ph.CO]` (pp. 8, 9).

[17] Karsten Jedamzik and Maxim Pospelov. "Big Bang Nucleosynthesis and Particle Dark Matter". In: *New J. Phys.* 11 (2009), p. 105028. DOI: `10.1088/1367-2630/11/10/105028`. arXiv: `0906.2087 [hep-ph]` (p. 9).

[18] Michael Kuhlen, Mark Vogelsberger, and Raul Angulo. "Numerical Simulations of the Dark Universe: State of the Art and the Next Decade". In: *Phys. Dark Univ.* 1 (2012), pp. 50–93. DOI: `10.1016/j.dark.2012.10.002`. arXiv: `1209.5745 [astro-ph.CO]` (p. 9).

[19] Jose A. R. Cembranos. "Modified gravity and dark matter". In: *J. Phys. Conf. Ser.* 718.3 (2016), p. 032004. DOI: `10.1088/1742-6596/718/3/032004`. arXiv: `1512.08752 [hep-ph]` (p. 9).

[20] Wayne Hu, Rennan Barkana, and Andrei Gruzinov. "Cold and fuzzy dark matter". In: *Phys. Rev. Lett.* 85 (2000), pp. 1158–1161. DOI: `10.1103/PhysRevLett.85.1158`. arXiv: `astro-ph/0003365` (p. 10).

[21] Bernard Carr, Florian Kuhnel, and Marit Sandstad. "Primordial Black Holes as Dark Matter". In: *Phys. Rev. D* 94.8 (2016), p. 083504. doi: `10.1103/PhysRevD.94.083504`. arXiv: `1607.06077 [astro-ph.CO]` (p. 10).

[22] Gerard Jungman, Marc Kamionkowski, and Kim Griest. "Supersymmetric dark matter". In: *Phys. Rept.* 267 (1996), pp. 195–373. doi: `10.1016/0370-1573(95)00058-5`. arXiv: `hep-ph/9506380` (p. 10).

[23] *Particle Dark Matter: Observations, Models and Searches*. Cambridge University Press, 2010 (p. 10).

[24] R. D. Peccei and Helen R. Quinn. "CP Conservation in the Presence of Instantons". In: *Phys. Rev. Lett.* 38 (1977), pp. 1440–1443. doi: `10.1103/PhysRevLett.38.1440` (p. 11).

[25] Francesca Chadha-Day, John Ellis, and David J. E. Marsh. "Axion dark matter: What is it and why now?" In: *Sci. Adv.* 8.8 (2022), abj3618. doi: `10.1126/sciadv.abj3618`. arXiv: `2105.01406 [hep-ph]` (p. 11).

[26] M. Milgrom. "A Modification of the Newtonian dynamics as a possible alternative to the hidden mass hypothesis". In: *Astrophys. J.* 270 (1983), pp. 365–370. doi: `10.1086/161130` (p. 11).

[27] Benoit Famaey and Stacy McGaugh. "Modified Newtonian Dynamics (MOND): Observational Phenomenology and Relativistic Extensions". In: *Living Rev. Rel.* 15 (2012), p. 10. doi: `10.12942/lrr-2012-10`. arXiv: `1112.3960 [astro-ph.CO]` (p. 11).

[28] S. W. Barwick et al. "Cosmic ray positrons at high-energies: A New measurement". In: *Phys. Rev. Lett.* 75 (1995), pp. 390–393. doi: `10.1103/PhysRevLett.75.390`. arXiv: `astro-ph/9505141` (p. 12).

[29] J. Abraham et al. "Properties and performance of the prototype instrument for the Pierre Auger Observatory". In: *Nuclear Instruments and Methods in Physics Research Section A: Accelerators, Spectrometers, Detectors and Associated Equipment* 523.1 (2004), pp. 50–95. issn: 0168-9002. doi: `https://doi.org/10.1016/j.nima.2003.12.012` (p. 12).

[30] H. Kawai et al. "Telescope array experiment". In: *Nucl. Phys. B Proc. Suppl.* 175-176 (2008). Ed. by Kwong Sang Cheng et al., pp. 221–226. doi: `10.1016/j.nuclphysbps.2007.11.002` (p. 12).

[31] P. Picozza et al. "PAMELA: A Payload for Antimatter Matter Exploration and Light-nuclei Astrophysics". In: *Astropart. Phys.* 27 (2007), pp. 296–315. doi: `10.1016/j.astropartphys.2006.12.002`. arXiv: `astro-ph/0608697` (p. 12).

[32] M. Aguilar et al. "First Result from the Alpha Magnetic Spectrometer on the International Space Station: Precision Measurement of the Positron Fraction in

Primary Cosmic Rays of 0.5–350 GeV". In: *Phys. Rev. Lett.* 110 (2013), p. 141102. DOI: `10.1103/PhysRevLett.110.141102` (p. 12).

[33] W. B. Atwood et al. "The Large Area Telescope on the Fermi Gamma-ray Space Telescope Mission". In: *Astrophys. J.* 697 (2009), pp. 1071–1102. DOI: `10.1088/0004-637X/697/2/1071`. arXiv: `0902.1089 [astro-ph.IM]` (p. 12).

[34] M. Ackermann et al. "The Fermi Galactic Center GeV Excess and Implications for Dark Matter". In: *Astrophys. J.* 840.1 (2017), p. 43. DOI: `10.3847/1538-4357/aa6cab`. arXiv: `1704.03910 [astro-ph.HE]` (p. 12).

[35] Stefano Profumo. "Dissecting cosmic-ray electron-positron data with Occam's Razor: the role of known Pulsars". In: *Central Eur. J. Phys.* 10 (2011), pp. 1–31. DOI: `10.2478/s11534-011-0099-z`. arXiv: `0812.4457 [astro-ph]` (p. 12).

[36] Lawrence M. Krauss, Mark Srednicki, and Frank Wilczek. "Solar System constraints and signatures for dark-matter candidates". In: *Phys. Rev. D* 33 (8 Apr. 1986), pp. 2079–2083. DOI: `10.1103/PhysRevD.33.2079` (p. 12).

[37] M. Ageron et al. "ANTARES: the first undersea neutrino telescope". In: *Nucl. Instrum. Meth. A* 656 (2011), pp. 11–38. DOI: `10.1016/j.nima.2011.06.103`. arXiv: `1104.1607 [astro-ph.IM]` (p. 12).

[38] M. G. Aartsen et al. "Search for annihilating dark matter in the Sun with 3 years of IceCube data". In: *Eur. Phys. J. C* 77.3 (2017). [Erratum: Eur.Phys.J.C 79, 214 (2019)], p. 146. DOI: `10.1140/epjc/s10052-017-4689-9`. arXiv: `1612.05949 [astro-ph.HE]` (p. 12).

[39] K. Choi et al. "Search for neutrinos from annihilation of captured low-mass dark matter particles in the Sun by Super-Kamiokande". In: *Phys. Rev. Lett.* 114.14 (2015), p. 141301. DOI: `10.1103/PhysRevLett.114.141301`. arXiv: `1503.04858 [hep-ex]` (pp. 12, 107).

[40] Michael B. Smy. "Hyper-Kamiokande". In: *Phys. Sci. Forum* 8.1 (2023), p. 41. DOI: `10.3390/psf2023008041` (p. 12).

[41] S. Adrian-Martinez et al. "Letter of intent for KM3NeT 2.0". In: *J. Phys. G* 43.8 (2016), p. 084001. DOI: `10.1088/0954-3899/43/8/084001`. arXiv: `1601.07459 [astro-ph.IM]` (p. 12).

[42] M. L. Ahnen et al. "Limits to Dark Matter Annihilation Cross-Section from a Combined Analysis of MAGIC and Fermi-LAT Observations of Dwarf Satellite Galaxies". In: *JCAP* 02 (2016), p. 039. DOI: `10.1088/1475-7516/2016/02/039`. arXiv: `1601.06590 [astro-ph.HE]` (p. 12).

[43] T. C. Weekes et al. "VERITAS: The Very energetic radiation imaging telescope array system". In: *Astropart. Phys.* 17 (2002), pp. 221–243. DOI: `10.1016/S0927-6505(01)00152-9`. arXiv: `astro-ph/0108478` (p. 12).

[44] B. S. Acharya et al. *Science with the Cherenkov Telescope Array*. WSP, Nov. 2018. ISBN: 978-981-327-008-4. DOI: `10.1142/10986`. arXiv: `1709.07997 [astro-ph.IM]` (p. 12).

[45] Leszek Roszkowski, Enrico Maria Sessolo, and Sebastian Trojanowski. "WIMP dark matter candidates and searches—current status and future prospects". In: *Rept. Prog. Phys.* 81.6 (2018), p. 066201. DOI: `10.1088/1361-6633/aab913`. arXiv: `1707.06277 [hep-ph]` (p. 13).

[46] Nishat Parveen. "The LUX-ZEPLIN dark matter experiment". In: *Astron. Nachr.* 342.1-2 (2021). Ed. by C. A. Zen Vasconcellos et al., pp. 423–430. DOI: `10.1002/asna.202113945` (p. 14).

[47] R. Agnese et al. "Projected Sensitivity of the SuperCDMS SNOLAB experiment". In: *Phys. Rev. D* 95.8 (2017), p. 082002. DOI: `10.1103/PhysRevD.95.082002`. arXiv: `1610.00006 [physics.ins-det]` (p. 14).

[48] G. Angloher et al. "COSINUS: Cryogenic Calorimeters for the Direct Dark Matter Search with NaI Crystals". In: *J. Low Temp. Phys.* 200.5-6 (2020), pp. 428–436. DOI: `10.1007/s10909-020-02464-9` (p. 14).

[49] J. Aalbers et al. "A next-generation liquid xenon observatory for dark matter and neutrino physics". In: *J. Phys. G* 50.1 (2023), p. 013001. DOI: `10.1088/1361-6471/ac841a`. arXiv: `2203.02309 [physics.ins-det]` (p. 14).

[50] Roxanne Turcotte-Tardif. "DEAP-3600 - Latest results from the largest liquid argon dark matter experiment". In: *PoS* ICRC2023 (2023), p. 1388. DOI: `10.22323/1.444.1388` (p. 14).

[51] P. Agnes et al. "First Results from the DarkSide-50 Dark Matter Experiment at Laboratori Nazionali del Gran Sasso". In: *Phys. Lett. B* 743 (2015), pp. 456–466. DOI: `10.1016/j.physletb.2015.03.012`. arXiv: `1410.0653 [astro-ph.CO]` (p. 14).

[52] D. S. Akerib et al. "First results from the LUX dark matter experiment at the Sanford Underground Research Facility". In: *Phys. Rev. Lett.* 112 (2014), p. 091303. DOI: `10.1103/PhysRevLett.112.091303`. arXiv: `1310.8214 [astro-ph.CO]` (p. 14).

[53] E. Aprile et al. "The XENON dark matter search experiment". In: *New Astron. Rev.* 49 (2005). Ed. by D. B. Cline, pp. 289–295. DOI: `10.1016/j.newar.2005.01.035` (p. 14).

[54] R. Bernabei et al. "The DAMA/LIBRA apparatus". In: *Nucl. Instrum. Meth. A* 592 (2008), pp. 297–315. DOI: `10.1016/j.nima.2008.04.082`. arXiv: `0804.2738 [astro-ph]` (p. 14).

[55] R. Bernabei et al. “First results from DAMA/LIBRA and the combined results with DAMA/NaI”. In: *Eur. Phys. J. C* 56 (2008), pp. 333–355. DOI: `10.1140/epjc/s10052-008-0662-y`. arXiv: `0804.2741 [astro-ph]` (p. 14).

[56] R. L. Workman et al. “Review of Particle Physics”. In: *PTEP* 2022 (2022), p. 083C01. DOI: `10.1093/ptep/ptac097` (p. 14).

[57] Julien Billard et al. “Direct detection of dark matter—APPEC committee report*”. In: *Reports on Progress in Physics* 85.5 (Apr. 2022), p. 056201. DOI: `10.1088/1361-6633/ac5754`. URL: `https://dx.doi.org/10.1088/1361-6633/ac5754` (p. 14).

[58] T. Prusti et al. “The Gaia Mission”. In: *Astron. Astrophys.* 595.Gaia Data Release 1 (2016), A1. DOI: `10.1051/0004-6361/201629272`. arXiv: `1609.04153 [astro-ph.IM]` (p. 15).

[59] Hai-Nan Lin and Xin Li. “The dark matter profiles in the Milky Way”. In: 487.4 (Aug. 2019), pp. 5679–5684. DOI: `10.1093/mnras/stz1698`. arXiv: `1906.08419 [astro-ph.GA]` (p. 15).

[60] Marius Cautun et al. “The Milky Way total mass profile as inferred from Gaia DR2”. In: *Mon. Not. Roy. Astron. Soc.* 494.3 (2020), pp. 4291–4313. DOI: `10.1093/mnras/staa1017`. arXiv: `1911.04557 [astro-ph.GA]` (p. 15).

[61] *mw-plot*. URL: `https://milkyway-plot.readthedocs.io/en/stable/` (p. 15).

[62] *galpy*. URL: `https://docs.galpy.org/` (p. 15).

[63] P. Salucci et al. “The dark matter density at the Sun’s location”. In: *Astron. Astrophys.* 523 (2010), A83. DOI: `10.1051/0004-6361/201014385`. arXiv: `1003.3101 [astro-ph.GA]` (p. 15).

[64] Anna-Christina Eilers et al. “The Circular Velocity Curve of the Milky Way from 5 to 25 kpc”. In: 871.1, 120 (Jan. 2019), p. 120. DOI: `10.3847/1538-4357/aaf648`. arXiv: `1810.09466 [astro-ph.GA]` (p. 16).

[65] Martin C. Smith et al. “The RAVE Survey: Constraining the Local Galactic Escape Speed”. In: *Mon. Not. Roy. Astron. Soc.* 379 (2007), pp. 755–772. DOI: `10.1111/j.1365-2966.2007.11964.x`. arXiv: `astro-ph/0611671` (p. 16).

[66] Jodi Cooley. “Dark Matter direct detection of classical WIMPs”. In: *SciPost Phys. Lect. Notes* 55 (2022), p. 1. DOI: `10.21468/SciPostPhysLectNotes.55`. arXiv: `2110.02359 [hep-ph]` (p. 16).

[67] Marc Schumann. “Direct Detection of WIMP Dark Matter: Concepts and Status”. In: *J. Phys. G* 46.10 (2019), p. 103003. DOI: `10.1088/1361-6471/ab2ea5`. arXiv: `1903.03026 [astro-ph.CO]` (p. 18).

[68] Ciaran A. J. O'Hare. "New Definition of the Neutrino Floor for Direct Dark Matter Searches". In: *Phys. Rev. Lett.* 127.25 (2021), p. 251802. DOI: `10.1103/PhysRevLett.127.251802`. arXiv: `2109.03116 [hep-ph]` (p. 19).

[69] M. Willers et al. "Direct dark matter search with the CRESST-III experiment - status and perspectives". In: *J. Phys. Conf. Ser.* 888.1 (2017), p. 012209. DOI: `10.1088/1742-6596/888/1/012209` (p. 18).

[70] E. Aprile et al. "Double-Weak Decays of ^{124}Xe and ^{136}Xe in the XENON1T and XENONnT Experiments". In: *Phys. Rev. C* 106.2 (2022), p. 024328. DOI: `10.1103/PhysRevC.106.024328`. arXiv: `2205.04158 [hep-ex]` (pp. 20, 36).

[71] Pietro Di Gangi. "The Xenon Road to Direct Detection of Dark Matter at LNGS: The XENON Project". In: *Universe* 7.8 (2021), p. 313. DOI: `10.3390/universe7080313` (p. 21).

[72] E. Aprile et al. "Design and Performance of the XENON10 Dark Matter Experiment". In: *Astropart. Phys.* 34 (2011), pp. 679–698. DOI: `10.1016/j.astropartphys.2011.01.006`. arXiv: `1001.2834 [astro-ph.IM]` (p. 21).

[73] J. Angle et al. "First Results from the XENON10 Dark Matter Experiment at the Gran Sasso National Laboratory". In: *Phys. Rev. Lett.* 100 (2008), p. 021303. DOI: `10.1103/PhysRevLett.100.021303`. arXiv: `0706.0039 [astro-ph]` (p. 21).

[74] J. Angle et al. "Limits on spin-dependent WIMP-nucleon cross-sections from the XENON10 experiment". In: *Phys. Rev. Lett.* 101 (2008), p. 091301. DOI: `10.1103/PhysRevLett.101.091301`. arXiv: `0805.2939 [astro-ph]` (p. 21).

[75] E. Aprile et al. "The XENON100 Dark Matter Experiment". In: *Astropart. Phys.* 35 (2012), pp. 573–590. DOI: `10.1016/j.astropartphys.2012.01.003`. arXiv: `1107.2155 [astro-ph.IM]` (p. 21).

[76] E. Aprile et al. "Dark Matter Results from 225 Live Days of XENON100 Data". In: *Phys. Rev. Lett.* 109 (2012), p. 181301. DOI: `10.1103/PhysRevLett.109.181301`. arXiv: `1207.5988 [astro-ph.CO]` (p. 21).

[77] E. Aprile et al. "Limits on spin-dependent WIMP-nucleon cross sections from 225 live days of XENON100 data". In: *Phys. Rev. Lett.* 111.2 (2013), p. 021301. DOI: `10.1103/PhysRevLett.111.021301`. arXiv: `1301.6620 [astro-ph.CO]` (p. 21).

[78] Elena Aprile. "The XENON1T Dark Matter Search Experiment". In: *Springer Proc. Phys.* 148 (2013). Ed. by David Cline, pp. 93–96. DOI: `10.1007/978-94-007-7241-0_14`. arXiv: `1206.6288 [astro-ph.IM]` (p. 22).

[79] E. Aprile et al. "Dark Matter Search Results from a One Ton-Year Exposure of XENON1T". In: *Phys. Rev. Lett.* 121.11 (2018), p. 111302. DOI: `10.1103/PhysRevLett.121.111302`. arXiv: `1805.12562 [astro-ph.CO]` (pp. 22, 31, 127, 128).

[80] E. Aprile et al. “Constraining the spin-dependent WIMP-nucleon cross sections with XENON1T”. In: *Phys. Rev. Lett.* 122.14 (2019), p. 141301. DOI: `10.1103/PhysRevLett.122.141301`. arXiv: `1902.03234 [astro-ph.CO]` (p. 22).

[81] E. Aprile et al. “Search for inelastic scattering of WIMP dark matter in XENON1T”. In: *Phys. Rev. D* 103.6 (2021), p. 063028. DOI: `10.1103/PhysRevD.103.063028`. arXiv: `2011.10431 [hep-ex]` (p. 22).

[82] E. Aprile et al. “Search for Coherent Elastic Scattering of Solar ^{8}B Neutrinos in the XENON1T Dark Matter Experiment”. In: *Phys. Rev. Lett.* 126 (2021), p. 091301. DOI: `10.1103/PhysRevLett.126.091301`. arXiv: `2012.02846 [hep-ex]` (p. 22).

[83] E. Aprile et al. “Emission of single and few electrons in XENON1T and limits on light dark matter”. In: *Phys. Rev. D* 106.2 (2022), p. 022001. DOI: `10.1103/PhysRevD.106.022001`. arXiv: `2112.12116 [hep-ex]` (p. 22).

[84] E. Aprile et al. “Searching for Heavy Dark Matter near the Planck Mass with XENON1T”. In: *Phys. Rev. Lett.* 130.26 (2023), p. 261002. DOI: `10.1103/PhysRevLett.130.261002`. arXiv: `2304.10931 [hep-ex]` (p. 22).

[85] E. Aprile et al. “Search for New Physics in Electronic Recoil Data from XENONnT”. In: *Phys. Rev. Lett.* 129.16 (2022), p. 161805. DOI: `10.1103/PhysRevLett.129.161805`. arXiv: `2207.11330 [hep-ex]` (pp. 22, 68, 119, 121, 122, 145).

[86] E. Aprile et al. “First Dark Matter Search with Nuclear Recoils from the XENONnT Experiment”. In: *Phys. Rev. Lett.* 131.4 (2023), p. 041003. DOI: `10.1103/PhysRevLett.131.041003`. arXiv: `2303.14729 [hep-ex]` (pp. 22, 27, 31, 68, 119, 125–127, 148).

[87] E. Hogenbirk et al. “Precision measurements of the scintillation pulse shape for low-energy recoils in liquid xenon”. In: *JINST* 13.05 (2018), P05016. DOI: `10.1088/1748-0221/13/05/P05016`. arXiv: `1803.07935 [physics.ins-det]` (p. 24).

[88] E. Aprile and T. Doke. “Liquid Xenon Detectors for Particle Physics and Astrophysics”. In: *Rev. Mod. Phys.* 82 (2010), pp. 2053–2097. DOI: `10.1103/RevModPhys.82.2053`. arXiv: `0910.4956 [physics.ins-det]` (p. 25).

[89] V. C. Antochi et al. “Improved quality tests of R11410-21 photomultiplier tubes for the XENONnT experiment”. In: *JINST* 16.08 (2021), P08033. DOI: `10.1088/1748-0221/16/08/P08033`. arXiv: `2104.15051 [physics.ins-det]` (p. 29).

[90] M. Murra et al. “Design, construction and commissioning of a high-flow radon removal system for XENONnT”. In: *Eur. Phys. J. C* 82.12 (2022), p. 1104. DOI: `10.1140/epjc/s10052-022-11001-9`. arXiv: `2205.11492 [physics.ins-det]` (p. 31).

[91] E. Aprile et al. "Projected WIMP sensitivity of the XENONnT dark matter experiment". In: *JCAP* 11 (2020), p. 031. DOI: `10.1088/1475-7516/2020/11/031`. arXiv: `2007.08796 [physics.ins-det]` (pp. 31, 35, 37, 38).

[92] E. Aprile et al. "Conceptual design and simulation of a water Cherenkov muon veto for the XENON1T experiment". In: *JINST* 9 (2014), P11006. DOI: `10.1088/1748-0221/9/11/P11006`. arXiv: `1406.2374 [astro-ph.IM]` (p. 33).

[93] E. Aprile et al. "Material radiopurity control in the XENONnT experiment". In: *Eur. Phys. J. C* 82.7 (2022), p. 599. DOI: `10.1140/epjc/s10052-022-10345-6`. arXiv: `2112.05629 [physics.ins-det]` (p. 33).

[94] E. Aprile et al. "Physics reach of the XENON1T dark matter experiment". In: *JCAP* 04 (2016), p. 027. DOI: `10.1088/1475-7516/2016/04/027`. arXiv: `1512.07501 [physics.ins-det]` (pp. 37, 110).

[95] J. Billard, L. Strigari, and E. Figueroa-Feliciano. "Implication of neutrino backgrounds on the reach of next generation dark matter direct detection experiments". In: *Phys. Rev. D* 89.2 (2014), p. 023524. DOI: `10.1103/PhysRevD.89.023524`. arXiv: `1307.5458 [hep-ph]` (p. 37).

[96] Aldo M. Serenelli, W. C. Haxton, and Carlos Pena-Garay. "Solar models with accretion. I. Application to the solar abundance problem". In: *Astrophys. J.* 743 (2011), p. 24. DOI: `10.1088/0004-637X/743/1/24`. arXiv: `1104.1639 [astro-ph.SR]` (p. 37).

[97] J. Aalbers et al. "DARWIN: towards the ultimate dark matter detector". In: *JCAP* 11 (2016), p. 017. DOI: `10.1088/1475-7516/2016/11/017`. arXiv: `1606.07001 [astro-ph.IM]` (p. 38).

[98] Dongming Mei and A. Hime. "Muon-induced background study for underground laboratories". In: *Phys. Rev. D* 73 (2006), p. 053004. DOI: `10.1103/PhysRevD.73.053004`. arXiv: `astro-ph/0512125` (p. 40).

[99] P. A. Cherenkov. "Visible radiation produced by electrons moving in a medium with velocities exceeding that of light". In: *Phys. Rev.* 52.4 (1937), pp. 378–379. DOI: `10.1103/PhysRev.52.378` (p. 41).

[100] Y. Fukuda et al. "The Super-Kamiokande detector". In: *Nucl. Instrum. Meth. A* 501 (2003). Ed. by V. A. Ilyin, V. V. Korenkov, and D. Perret-Gallix, pp. 418–462. DOI: `10.1016/S0168-9002(03)00425-X` (pp. 41, 43).

[101] W. R. Leo. *Techniques for Nuclear and Particle Physics Experiments: A How to Approach*. 1987. ISBN: 978-3-540-57280-0 (p. 42).

[102] Charlotte Meaker Davisson and Robley D. Evans. "Gamma-ray absorption coefficients". In: *Rev. Mod. Phys.* 24.2 (1952), pp. 79–107. DOI: `10.1103/revmodphys.24.79` (p. 42).

[103] M. R. Anderson et al. "Measurement of neutron-proton capture in the SNO+ water phase". In: *Phys. Rev. C* 102.1 (2020), p. 014002. DOI: `10.1103/PhysRevC.102.014002`. arXiv: `2002.10351 [physics.ins-det]` (pp. 43, 107, 108).

[104] Y. Zhang et al. "First measurement of radioactive isotope production through cosmic-ray muon spallation in Super-Kamiokande IV". In: *Phys. Rev. D* 93.1 (2016), p. 012004. DOI: `10.1103/PhysRevD.93.012004`. arXiv: `1509.08168 [hep-ex]` (pp. 43, 108).

[105] Kaito Hagiwara et al. "Gamma Ray Spectrum from Thermal Neutron Capture on Gadolinium-157". In: *PTEP* 2019.2 (2019), p. 023D01. DOI: `10.1093/ptep/ptz002`. arXiv: `1809.02664 [nucl-ex]` (pp. 43, 44, 111).

[106] IAEA. *Evaluated Nuclear Data File (ENDF) - Database Version of 2023-08-25*. 2023. URL: `https://www-nds.iaea.org/exfor/endf.htm` (p. 44).

[107] H. de Kerret et al. "The Double Chooz antineutrino detectors". In: *Eur. Phys. J. C* 82.9 (2022), p. 804. DOI: `10.1140/epjc/s10052-022-10726-x`. arXiv: `2201.13285 [physics.ins-det]` (p. 45).

[108] Jun Cao and Kam-Biu Luk. "An overview of the Daya Bay Reactor Neutrino Experiment". In: *Nucl. Phys. B* 908 (2016), pp. 62–73. DOI: `10.1016/j.nuclphysb.2016.04.034`. arXiv: `1605.01502 [hep-ex]` (p. 45).

[109] K. Abe et al. "First gadolinium loading to Super-Kamiokande". In: *Nucl. Instrum. Meth. A* 1027 (2022), p. 166248. DOI: `10.1016/j.nima.2021.166248`. arXiv: `2109.00360 [physics.ins-det]` (p. 45).

[110] Hiroyuki Sekiya. "Supernova neutrinos in SK-Gd and other experiments". In: *J. Phys. Conf. Ser.* 888.1 (2017), p. 012041. DOI: `10.1088/1742-6596/888/1/012041` (p. 46).

[111] Ll. Marti et al. "Evaluation of gadolinium's action on water Cherenkov detector systems with EGADS". In: *Nucl. Instrum. Meth. A* 959 (2020), p. 163549. DOI: `10.1016/j.nima.2020.163549`. arXiv: `1908.11532 [physics.ins-det]` (p. 47).

[112] Andrew Renshaw. "Research and Development for a Gadolinium Doped Water Cherenkov Detector". In: *Physics Procedia* 37 (2012), pp. 1249–1256. ISSN: 1875-3892. DOI: `https://doi.org/10.1016/j.phpro.2012.02.467` (p. 47).

[113] E. Aprile et al. "The triggerless data acquisition system of the XENONnT experiment". In: *JINST* 18.07 (2023), P07054. DOI: `10.1088/1748-0221/18/07/P07054`. arXiv: `2212.11032 [physics.ins-det]` (p. 61).

[114] *Strax*. URL: `https://strax.readthedocs.io/en/latest/` (p. 64).

[115] *Straxen*. URL: `https://straxen.readthedocs.io` (p. 64).

[116] A.Mancuso. *Misure di guadagno di fotomoltiplicatori per il Sistema di Veto di neutroni dell'esperimento XENONnT.* Alma Mater Studiorum - University of Bologna, 2016-2017 (p. 68).

[117] Hamamatsu. *Photomultiplier tube - R5912*. URL: `https://hep.hamamatsu.com/eu/en/products/R5912.html` (pp. 69, 70).

[118] A.Mancuso. *Neutron Veto of XENONnT: final construction design of the system and extensive study and calibration of the PMTs.* Alma Mater Studiorum - University of Bologna, 2018/2019 (p. 69).

[119] A. G. Wright. *The Photomultiplier Handbook*. Oxford University Press, 2017 (pp. 70, 73, 76).

[120] A. Einstein. ""The Photoelectric Effect"". In: *Annalen der Physik* Wiley-VCH Verlag GmbH & Co. KgaA (1905) (p. 70).

[121] R. Saldanha et al. "Model Independent Approach to the Single Photoelectron Calibration of Photomultiplier Tubes". In: *Nucl. Instrum. Meth. A* 863 (2017). Ed. by Guoqing Xiao, Hao Shen, and Guanghua Du, pp. 35–46. DOI: `10.1016/j.nima.2017.02.086`. arXiv: `1602.03150 [physics.ins-det]` (p. 73).

[122] Milind V. Diwan. "Statistics of the Charge Spectrum of Photo-Multipliers and Methods for Absolute Calibration". In: *JINST* 15.02 (2020), P02001. DOI: `10.1088/1748-0221/15/02/P02001`. arXiv: `1909.05373 [physics.ins-det]` (p. 73).

[123] P. -A. Amaudruz et al. "In-situ characterization of the Hamamatsu R5912-HQE photomultiplier tubes used in the DEAP-3600 experiment". In: *Nucl. Instrum. Meth. A* 922 (2019), pp. 373–384. DOI: `10.1016/j.nima.2018.12.058`. arXiv: `1705.10183 [physics.ins-det]` (p. 73).

[124] T Caldwell, S Seibert, and S Jaditz. "Characterization of the R5912-02 MOD photomultiplier tube at cryogenic temperatures". In: *Journal of Instrumentation* 8.09 (Sept. 2013), p. C09004. DOI: `10.1088/1748-0221/8/09/C09004`. URL: `https://dx.doi.org/10.1088/1748-0221/8/09/C09004` (p. 73).

[125] A. J. Dekker. *Secondary Electron Emission*. Macmillan Education UK, 1981. DOI: `10.1007/978-1-349-00784-4_17` (p. 73).

[126] Daniel Wenz. "Commissioning of the world's first water Cherenkov neutron veto and first WIMP dark matter search results of the XENONnT experiment". PhD thesis. Mainz U., 2023. DOI: `10.25358/openscience-9654` (pp. 77, 88).

[127] Abraham Savitzky and M. J. E. Golay. "Smoothing and Differentiation of Data by Simplified Least Squares Procedures." In: *Anal. Chem* 36 (1964), pp. 1627–1639. DOI: `10.1021/ac60214a047` (p. 78).

[128] Nuclear Data Section. *IAEA Nuclear Data Services*. URL: `https://www-nds.iaea.org/relnsd/ddep?NUCID=208TL&LSEQNO=0` (p. 94).

[129] Triangle Universities Nuclear Laboratory. *Nuclear Data Evaluation Project*. URL: `https://nucldata.tunl.duke.edu/nucldata` (p. 95).

[130] K.W. Geiger and L. Van Der Zwan. "Radioactive neutron source spectra from 9Be(α, n) cross section data". In: *Nuclear Instruments and Methods* 131.2 (1975), pp. 315–321. ISSN: 0029-554X. DOI: `https://doi.org/10.1016/0029-554X(75)90336-5` (p. 96).

[131] J. Scherzinger et al. "Tagging fast neutrons from an ^{241}Am/^{9}Be source". In: *Appl. Radiat. Isot.* 98 (2015), pp. 74–79. DOI: `10.1016/j.apradiso.2015.01.003`. arXiv: `1405.2686 [physics.ins-det]` (p. 96).

[132] I et al. Murata. "Neutron and gamma-ray source-term characterization of AmBe sources in Osaka University". In: *Progress in Nuclear Science and Technology* 4 (Jan. 2014), pp. 345–348. DOI: `10.15669/pnst.4.345` (p. 96).

[133] E. Aprile et al. "Response of the XENON100 Dark Matter Detector to Nuclear Recoils". In: *Phys. Rev. D* 88 (2013), p. 012006. DOI: `10.1103/PhysRevD.88.012006`. arXiv: `1304.1427 [astro-ph.IM]` (p. 96).

[134] *iminuit*. URL: `https://pypi.org/project/iminuit/` (p. 99).

[135] *Geant4*. URL: `https://geant4.web.cern.ch/` (pp. 105, 110).

[136] E. Aprile et al. "XENON1T Dark Matter Data Analysis: Signal and Background Models and Statistical Inference". In: *Phys. Rev. D* 99 (11 June 2019), p. 112009. DOI: `10.1103/PhysRevD.99.112009`. URL: `https://link.aps.org/doi/10.1103/PhysRevD.99.112009` (p. 105).

[137] *Epix*. URL: `https://github.com/XENONnT/epix` (p. 111).

[138] Tomoyuki Tanaka et al. "Gamma-ray spectra from thermal neutroncapture on gadolinium-155 and naturalgadolinium". In: *PTEP* 2020.4 (2020), p. 043D02. DOI: `10.1093/ptep/ptaa015`. arXiv: `1907.00788 [nucl-ex]` (p. 111).

[139] E. Aprile et al. "Excess electronic recoil events in XENON1T". In: *Phys. Rev. D* 102.7 (2020), p. 072004. DOI: `10.1103/PhysRevD.102.072004`. arXiv: `2006.09721 [hep-ex]` (pp. 121, 122).

[140] Glen Cowan et al. "Power-Constrained Limits". In: (May 2011). arXiv: `1105.3166 [physics.data-an]` (p. 127).

[141] J. Aalbers et al. "First Dark Matter Search Results from the LUX-ZEPLIN (LZ) Experiment". In: *Phys. Rev. Lett.* 131.4 (2023), p. 041002. DOI: `10.1103/PhysRevLett.131.041002`. arXiv: `2207.03764 [hep-ex]` (pp. 128, 148).

[142] Yue Meng et al. “Dark Matter Search Results from the PandaX-4T Commissioning Run”. In: *Phys. Rev. Lett.* 127.26 (2021), p. 261802. DOI: `10.1103/PhysRevLett.127.261802`. arXiv: `2107.13438 [hep-ex]` (p. 128).